



# Modeling and simulation of two-phase flow turbulent combustion in aeronautical engines

Bastien Rochette

## ► To cite this version:

Bastien Rochette. Modeling and simulation of two-phase flow turbulent combustion in aeronautical engines. Physics [physics]. Institut National Polytechnique de Toulouse - INPT, 2019. English. NNT : 2019INPT0059 . tel-04167247

HAL Id: tel-04167247

<https://theses.hal.science/tel-04167247>

Submitted on 20 Jul 2023

**HAL** is a multi-disciplinary open access archive for the deposit and dissemination of scientific research documents, whether they are published or not. The documents may come from teaching and research institutions in France or abroad, or from public or private research centers.

L'archive ouverte pluridisciplinaire **HAL**, est destinée au dépôt et à la diffusion de documents scientifiques de niveau recherche, publiés ou non, émanant des établissements d'enseignement et de recherche français ou étrangers, des laboratoires publics ou privés.



Université  
de Toulouse

# THÈSE

En vue de l'obtention du

## DOCTORAT DE L'UNIVERSITÉ DE TOULOUSE

Délivré par :

Institut National Polytechnique de Toulouse (Toulouse INP)

Discipline ou spécialité :

Energétique et Transferts

---

Présentée et soutenue par :

M. BASTIEN ROCHETTE

le mardi 25 juin 2019

Titre :

Modeling and simulation of two-phase flow turbulent combustion in  
aeronautical engines

---

Ecole doctorale :

Mécanique, Energétique, Génie civil, Procédés (MEGeP)

Unité de recherche :

Centre Européen de Recherche et Formation Avancées en Calcul Scientifique (CERFACS)

Directeur(s) de Thèse :

M. THIERRY POINSOT

M. OLIVIER VERMOREL

Rapporteurs :

M. FABIEN HALTER, UNIVERSITE D'ORLEANS

M. RONAN VICQUELIN, CENTRALESUPELEC GIF SUR YVETTE

Membre(s) du jury :

M. FRÉDÉRIC GRISCH, INSA ROUEN, Président

M. DENIS VEYNANTE, CNRS PARIS, Membre

Mme BENEDICTE CUENOT, CERFACS, Membre

M. OLIVIER VERMOREL, CERFACS, Invité

M. STEPHANE RICHARD, GROUPE SAFRAN, Invité

M. THIERRY POINSOT, CNRS TOULOUSE, Membre



---

## Abstract/Résumé

Nowadays, more than 80% of the energy consumed on Earth is produced by burning fossil fuels. Alternative solutions to combustion are being developed but the specific constraints related to air transport do not make it possible to currently power engines without introducing a technological breakthrough. These findings explain the research activity to improve the knowledge and the control of combustion processes to design cleaner, and more efficient aeronautical engines. In this framework, Large Eddy Simulations (LES) have become a powerful tool to better understand combustion processes and pollutant emissions. This PhD thesis is part of this context and focuses on the models and numerical strategies to simulate with more accuracy turbulent gaseous and two-phase reacting flows in the combustion chamber of aeronautical engines. First, a generic and self-adapting method for flame front detection and thickening has been developed for the TFLES model, and validated on several academic configurations of increasing complexity. This generic approach is then evaluated in the LES of a laboratory-scale burner and compared to the classical thickening method. Results show a more accurate thickening in post-flame regions. Second, from the analysis of 1-D homogeneous laminar spray flames where the dispersed phase has a relative velocity compared to the carrier phase, two analytical formulations for the spray flame propagation speed have been proposed and validated. The agreement between the overall trend of both the measured/estimated spray flame speeds demonstrates that the model and its parameters correctly take into account the main physical mechanisms controlling laminar spray flames. Finally, the state-of-the-art TFLES models were tested on complex turbulent gaseous and two-phase reacting configurations. The pros and cons of these models were investigated to contribute to the understanding of the mechanisms related to turbulent combustion, and to propose a LES modeling strategy to improve the fidelity of reactive simulations.

De nos jours, plus de 80% de l'énergie consommée sur Terre provient de la combustion de combustibles fossiles. Des solutions alternatives à la combustion sont en cours de développement mais les contraintes spécifiques liées au transport aérien ne permettent pas actuellement d'alimenter des moteurs sans introduire de rupture technologique. Ces résultats expliquent les activités de recherche visant à améliorer les connaissances et le contrôle des processus de combustion afin de concevoir des moteurs aéronautiques plus propres et plus efficaces. Dans ce cadre, les Simulations aux Grandes Echelles ("Large Eddy Simulation" LES) sont devenues un outil puissant pour mieux comprendre les processus de combustion et les émissions de polluants. Cette thèse s'inscrit dans ce contexte et se focalise sur les modèles et stratégies de calcul afin de simuler avec plus de précision les écoulements réactifs turbulents gazeux et diphasiques dans la chambre de combustion des moteurs aéronautiques. Tout d'abord, une méthode générique et automatique pour la détection et l'épaississement du front de flamme a été développée pour le modèle TFLES, et validée pour plusieurs configurations académiques de complexité croissante. Cette approche générique est ensuite évaluée dans une simulation LES d'un brûleur de laboratoire et comparée à la méthode d'épaississement classique. Les résultats montrent un épaississement plus précis dans les régions post-flammes. Dans un second temps, à partir de l'analyse de flammes laminaires 1D diphasiques homogènes où la phase dispersée a une vitesse relative comparée à la phase porteuse, deux formulations analytiques pour la vitesse de propagation de ces flammes ont été proposées et validées. La concordance entre les vitesses de flammes mesurées et estimées démontre que le modèle et ses paramètres prennent correctement en compte les principaux mécanismes physiques contrôlant ces flammes diphasiques. Enfin, les modèles TFLES les plus récents ont été testés sur des configurations de flamme turbulente gazeuse/diphasique complexes. Les avantages et les inconvénients de ces modèles ont été étudiés afin de contribuer à la compréhension des mécanismes liés à la combustion turbulente et de proposer une stratégie de modélisation par LES pour améliorer la fidélité des simulations réactives.

---

## Remerciements

Je voudrais tout d'abord remercier les membres du Jury: Ronan Vicquelin et Fabien Halter d'avoir relu et évalué ce manuscrit, Frédéric Grisch et Denis Veynante de les avoir rejoints au CERFACS pour assister à la soutenance et animer une séance de discussion constructive et pleine de perspectives.

J'aimerai ensuite remercier mes encadrants, Bénédicte Cuenot, Olivier Vermorel, Thierry Poinsot, Eleonore Riber et Stéphane Richard qui m'ont apporté leur expérience, de l'autonomie et du recul afin de mener à bien ces travaux.

Mes remerciements vont aussi à l'ensemble des membres de l'équipe CFD dans laquelle l'entraide et la bonne humeur font du CERFACS un lieu agréable et privilégié où travailler. Je remercie également l'équipe administration, en particulier Marie et Nicole, pour leur aide précieuse, mais également l'ensemble de l'équipe CSG dont l'efficacité redoutable nous facilite grandement la vie.

Je ne manquerai pas non plus de remercier la team LBM et la team kite pour tous ces bons moments passés ensemble, les voyage, weekend et RTT-kite, avec une mention particulière pour Flo, sa bonne humeur et ses blagues dès l'ouverture de la porte du bureau.

Finalement, je tiens à remercier ma famille et plus particulièrement Laura pour son soutien et sa confiance au quotidien.

# Contents

## Part I: General context

<b>1</b>	<b>General context</b>	<b>1</b>
1.1	Introduction . . . . .	3
1.2	Helicopter engines . . . . .	3
1.3	Combustion chambers . . . . .	5
1.4	Liquid fuel injection . . . . .	5
1.4.1	Atomization phenomena . . . . .	6
1.4.2	Characterization of a liquid spray . . . . .	7
1.5	Place and role of numerical simulation . . . . .	8
<b>2</b>	<b>Spray/combustion/turbulence interactions</b>	<b>11</b>
2.1	Introduction . . . . .	11
2.2	Interaction between a non-reactive spray and turbulence . . . . .	11
2.2.1	Preferential segregation . . . . .	11
2.2.2	Evaporation and mixture . . . . .	12
2.2.3	Turbulence modulation . . . . .	12
2.3	Interaction between turbulence and combustion . . . . .	13
2.3.1	Flame speed . . . . .	13
2.3.2	Definition of stretch . . . . .	15
2.3.3	Effect of stretch on flame speed . . . . .	15
2.3.4	Effect of flame fronts on turbulence . . . . .	18
2.4	Interaction between a spray and a laminar flame . . . . .	18
2.4.1	Two-phase combustion regimes . . . . .	18
2.4.2	Two-phase flame propagation mechanisms . . . . .	21
2.4.3	Two-phase laminar flame speed . . . . .	23
2.5	Interaction between spray, combustion and turbulence . . . . .	25
2.5.1	Characterization of a turbulent reacting spray . . . . .	25
2.5.2	Identification of the combustion regime . . . . .	25
2.5.3	Turbulent spray flame stabilization process . . . . .	26
2.5.4	Numerical simulation of a turbulent reacting spray . . . . .	29
2.6	PhD thesis objectives and manuscript outline . . . . .	34
2.6.1	Development of the AVBP code . . . . .	34
2.6.2	PhD thesis objectives . . . . .	34
2.6.3	Manuscript outline . . . . .	34

**Part II: Turbulent spray flames equations and models** 35

<b>3</b>	<b>Turbulent reacting gaseous flow equations and models</b>	<b>37</b>
3.1	Conservation equations for reacting flows . . . . .	37
3.1.1	Basic concepts of turbulence and combustion . . . . .	37
3.1.2	Generalities on combustion . . . . .	38
3.1.3	Conservation equations for reacting flows . . . . .	42
3.2	LES filtering, equations and models . . . . .	44
3.2.1	LES filtering . . . . .	44
3.2.2	Chemistry modeling in LES . . . . .	47
3.2.3	LES premixed turbulent combustion models . . . . .	48
<b>4</b>	<b>Evaporating spray equations, models</b>	<b>57</b>
4.1	Lagrangian deterministic approach . . . . .	57
4.1.1	Lagrangian set of equations . . . . .	57
4.1.2	Coupling with the Eulerian gaseous phase . . . . .	57
4.2	Macroscopic models for an isolated droplet . . . . .	58
4.2.1	Dynamic of an isolated droplet . . . . .	58
4.2.2	Evaporation of an isolated droplet . . . . .	60

**Part III: Application of the turbulent gaseous combustion models** 67

<b>5</b>	<b>Influence of chemical schemes, numerical method and dynamic turbulent combustion modeling on LES of premixed turbulent flames</b>	<b>69</b>
5.1	Introduction . . . . .	69
5.2	Chemistry description . . . . .	70
5.2.1	A two-step scheme for propane-air flames . . . . .	70
5.2.2	An analytically reduced scheme (22 species) for propane-air flames . . . . .	71
5.2.3	Comparison of two-step and ARC schemes on premixed laminar flames . . . . .	71
5.3	The TFLES model for flame/turbulence SGS interactions . . . . .	73
5.4	Second and third-order LES convection schemes . . . . .	74
5.5	The VOLVO experiment . . . . .	75
5.5.1	Experimental configuration . . . . .	75
5.5.2	Numerical setup . . . . .	77
5.6	Results . . . . .	79
5.6.1	Influence of the turbulent combustion model . . . . .	79
5.6.2	Influence of chemistry description and numerical scheme . . . . .	82
5.6.3	Discussions . . . . .	90
5.7	Conclusion . . . . .	91

**Part IV: Turbulent two-phase combustion modeling and simulations**

<b>6 A generic and self-adapting method for flame detection and thickening in the TFLES model</b>	<b>95</b>
6.1 Introduction . . . . .	95
6.2 The generic thickening approach . . . . .	96
6.2.1 Front detection . . . . .	96
6.2.2 Front thickening . . . . .	96
6.2.3 Asymmetric thickening . . . . .	98
6.2.4 Flame thickness estimation . . . . .	99
6.3 Validation . . . . .	100
6.3.1 Laminar cases . . . . .	100
6.3.2 Turbulent case . . . . .	107
6.3.3 CPU costs . . . . .	111
6.4 Conclusions . . . . .	112
<b>7 Effect of relative velocity on the flame speed and structure of laminar spray flames</b>	<b>113</b>
7.1 Introduction . . . . .	113
7.2 Chemistry description . . . . .	114
7.3 Numerical setup . . . . .	115
7.3.1 Configuration . . . . .	116
7.4 Results . . . . .	116
7.4.1 Spray flame structures . . . . .	116
7.4.2 Determination of the laminar two-phase flame speed . . . . .	124
7.4.3 Spray flame speed of the test cases . . . . .	125
7.5 Conclusions . . . . .	128
<b>8 Turbulent two-phase combustion simulations</b>	<b>129</b>
8.1 The HERON experiment . . . . .	129
8.1.1 Experimental configuration . . . . .	129
8.2 Numerical setup . . . . .	132
8.2.1 Chemistry description . . . . .	134
8.3 Numerical results . . . . .	134
8.3.1 Flow characteristics . . . . .	134
8.3.2 Non-reacting case . . . . .	135
8.3.3 Reacting case . . . . .	139
8.4 Application of the new generic thickening approach . . . . .	149
8.5 Conclusion . . . . .	155

**Part V: Conclusion and perspectives**

159

<b>9 Conclusion and perspectives</b>	<b>161</b>
--------------------------------------	------------

**Part VI: Bibliography**

163

# I General context

<b>1</b>	<b>General context .....</b>	<b>3</b>
1.1	Introduction	
1.2	Helicopter engines	
1.3	Combustion chambers	
1.4	Liquid fuel injection	
1.5	Place and role of numerical simulation	
<b>2</b>	<b>Spray/combustion/turbulence interactions ....</b>	<b>11</b>
2.1	Introduction	
2.2	Interaction between a non-reactive spray and turbulence	
2.3	Interaction between turbulence and combustion	
2.4	Interaction between a spray and a laminar flame	
2.5	Interaction between spray, combustion and turbulence	
2.6	PhD thesis objectives and manuscript outline	



# General context

## 1.1 Introduction

In today's industrial society, more than 80% of the energy consumed on Earth is produced by burning fossil fuels. However, exhaustion of natural resources on the one hand and the impact of human being on the environment on the other hand (global warming, pollutant and noise emissions, etc.) both place energy conversion through combustion in the center of actual major preoccupations. This finding has been globally recognized for few years and in this context of fuel depletion, growing pollution and global Earth warming, regulations are adopted by many countries to impose a drastic reduction of pollutant emissions and fuel consumption. As an example, the flightpath 2050 plans a reduction of 75% in CO<sub>2</sub> emissions per passenger kilometer, 90% in NO<sub>x</sub> emissions and 65% in noise emission perception. Moreover, alternative solutions to combustion, more environmentally friendly and more sustainable, are being developed and are gradually representing a higher part of global energy production, especially for automotive transportation. But the specific constraints related to air transport do not make it possible to currently power engines with an alternative source of energy to the combustion of hydrocarbons without introducing a technological breakthrough. Indeed, aeronautical propulsion requires a weight/power ratio and an endurance that only thermal propulsion with liquid fuel is able to provide, especially because of the high energy density of fuel compared to other methods of energy storage (battery, battery with hydrogen, nuclear propulsion, etc.). These findings explain the research activity to improve the knowledge and the control of combustion processes to design cleaner, and more efficient aeronautical engines.

In this framework, numerical simulations have become a powerful tool. Indeed, during the past decades, the advances in computing resources and simulation methods allow sophisticated simulations at industrial scale leading to better understanding of combustion processes and pollutant emissions. This PhD thesis is part of this context and focuses on the combustion chamber of aeronautical engines as well as the development of numerical methods to simulate with more accuracy the internal reacting flow of this last one.

## 1.2 Helicopter engines

As an illustrative example, Fig. 1.1 displays a cut of the Ardiden III helicopter engine, showing its main parts.

The process to generate power follows a Brayton cycle [1]:

- First, air is drawn into the compressor and undergoes an **isentropic compression**. The compressor provides a steady flow of pressurized air to the combustion chamber. Designing compressors is fraught with compromises primarily because of the need to deliver different flow rates depending on the power required. It is relatively easy to design a compressor that is very efficient under one specific set of conditions, but it may become very inefficient under other conditions. In practice it may be better to design a compressor which is a little less efficient, but which maintains that efficiency over a wide range of flow rates.

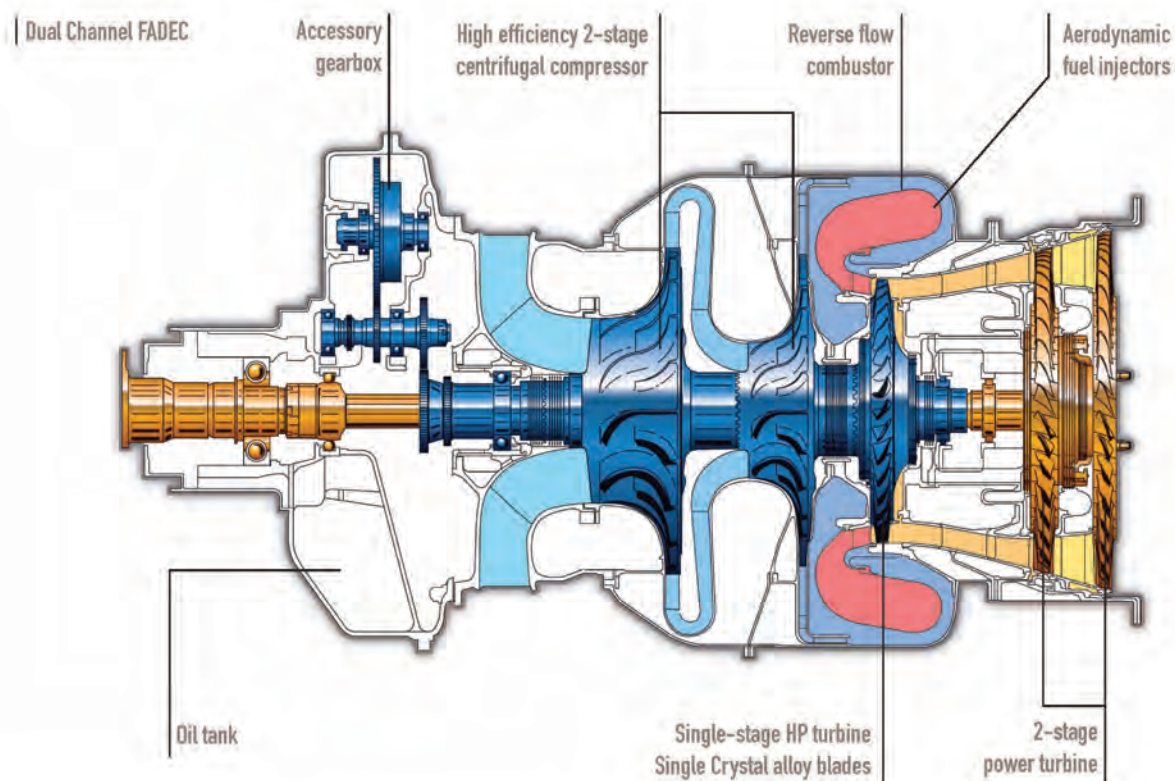


**Fig. 1.1.** Mid-plane cut of the Adriden III, Safran Helicopter Engine. Source: [www.helicoptermaintenancemagazine.com](http://www.helicoptermaintenancemagazine.com)

### 1.3 Combustion chambers

---

- Then, compressed air goes through the combustion chambers where fuel is sprayed in and burned through an **isobaric combustion**. The charge temperature increases and the gas expands but it cannot overcome the pressure of the compressor and must flow onwards. The expansion results in the burnt gases flowing much faster than the flow rate through the engine.
- Finally, the hot flow encounters first the High Pressure turbine coupled to the compressor, then the two stages of Low Pressure turbine (linked to the rotor through the transmission) to convert the burnt gases energy into shaft power following an **isentropic expansion**. Some of the resulting work is wasted driving the compressor, but the remainder is available to drive the rotor. The power turbine is the most highly stressed part of the engine as, like the compressor, it has to operate at high RPM but with the additional problems of working with high temperature of the burnt gases and at higher power. Like compressors, turbines may have cascaded stages with stator vanes between. The power turbine extracts power from the gas flow by reducing its velocity, pressure and temperature. This power is then provided to the rotor that converts shaft power into thrust.

As engines turn too fast for rotors, reduction gearing will be needed to transmit engine power to the various rotors and accessories. The primary functions of the transmission are to deliver the shaft power and to transmit the thrust to the hull. Secondary functions of the transmission include driving the tail rotor and vital services such as hydraulic pumps and generators. Note that there must be an autorotation clutch that allows a failed engine to stop while the rotors carry on turning. In some machines the transmission also drives cooling fans.

In this work, only the processes taking place in the combustion chamber are studied. For this reason, the compressor and the turbine will not be taken into account.

### 1.3 Combustion chambers

The gas turbine is a continuous flow engine and relies on a delicate equilibrium that must be maintained. As far as the combustion chamber is concerned, there are two related problems to be overcome. The first is that the velocity of flame propagation in kerosene is very slow compared to the air velocity from the compressor, which can be as high as hundred meters per second. If directly exposed to compressor flow, the flame would literally be blown out.

The second problem is that, to produce the desired temperature rise, the overall chamber air/fuel ratio must normally be around 50, which is well outside the limits of flammability for air-hydrocarbon mixtures (kerosene will only burn efficiently at an air/fuel ratio of about 15:1).

The Ardidén III combustion chamber (illustrated in Fig. 1.2) has been designed to overcome these problems.

The incoming air from the compressor is slowed down and redressed in the axial direction by the diffuser. While bypassing the combustion chamber, a part of this flow is deviated by several holes:

- The injector and primary air holes feed the flame located in the primary zone.
- The dilution holes decrease the burnt gas temperature to avoid blade damages of the turbine.
- Films and multi-perforated walls create a layer of fresh air that limits the heat fluxes to the walls of the combustion chamber.
- The elbow finally relieves the flow from the combustion chamber and ensures a thermal homogenization of the mixture before entering the high-pressure turbine.

### 1.4 Liquid fuel injection

The processes of liquid atomization and evaporation are of fundamental importance to the behavior of a gas turbine combustion system: liquid fuel must be vaporized to burn with air

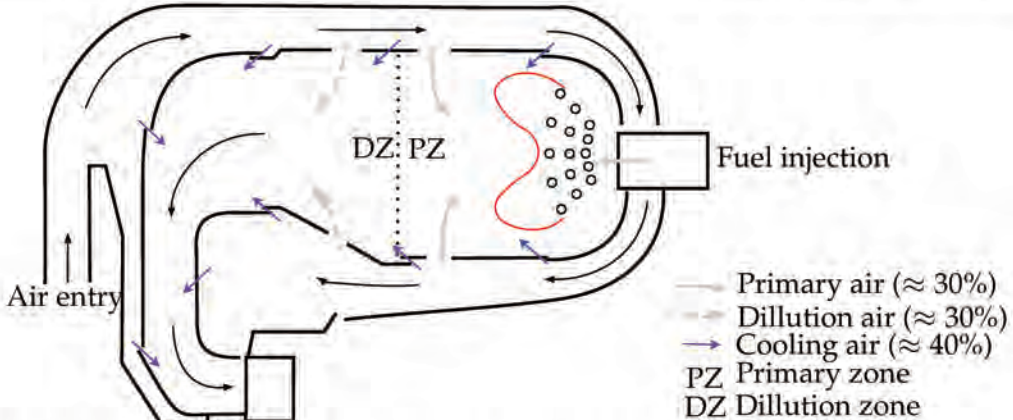


Fig. 1.2. Sketch of the Ardiden III reverse-flow combustion chamber (adapted from [2]).

incoming in the combustion chamber [2]. Standard fuels are not sufficiently volatile to produce vapor in the amounts required for ignition and combustion unless they are atomized into a large number of drops. The smaller the drops, the more the evaporation of the liquid and the mixing between fuel and air are fast, aiming the more homogeneous mixture as possible. Moreover, the combustion of the liquid fuel must be complete to ensure the efficiency of the engine, and the penetration length of the spray must be as short as possible to maximize the compactness of the combustion chamber. To achieve these goals, three injection types are usually encountered in helicopter engines:

- **Pre-vaporized injection:** liquid fuel is roughly sprayed in an elbow tube immersed in the hot environment of the combustion chamber. The thermal transfer through the walls of the injection system leads to a pre-vaporization of the fuel before it reaches the outlet of the tube. A fresh air flux is also injected inside the tube to prepare a premixed mixture.
  - **Centrifugal injection:** in-house injection system developed by Safran Helicopter Engines (SHE). It consists in the atomization of the fuel through its centrifugation with a highly rotating pierced wheel. The rotation of the wheel is achieved with the shaft of the engine.
  - **Pre-filming airblast injection:** A liquid film is generated with two counter-rotating co-axial jets. This widely used system is suitable for high air pressure and generates a small droplets directly injected into the combustion chamber. This technology has the advantage to create a central recirculation zone stabilizing the flame close to the injector.
- In this PhD thesis, only direct injection is studied: the fuel is directly injected inside the combustion chamber and strongly interacts with the reacting flow.

#### 1.4.1 Atomization phenomena

The physical phenomena leading to the atomization of a liquid sheet into a cloud of small droplets are represented in Fig.1.3.

The primary atomization consists in the disintegration of a liquid sheet into big pockets of liquid. The disintegration process comes from an instability at the surface of the liquid sheet. This instability, usually due to high strain between the liquid/gas interface, grows until the detachment of large drops and ligaments. The secondary atomization corresponds to the disintegration of both ligaments and large drops into smaller droplets. This atomization process is the result of a competition between aerodynamic forces destabilizing the surface of the big drops, and surface tension forces tending to maintain the liquid structures together. The more the velocity between the gaseous flow and liquid structures is high, the thinner the spray.

In this thesis, we will only be interested in the physical phenomena that occur after the complete atomization of the spray, without considering the complexity associated with the injection method and atomization mechanisms. We therefore consider a spray initially formed

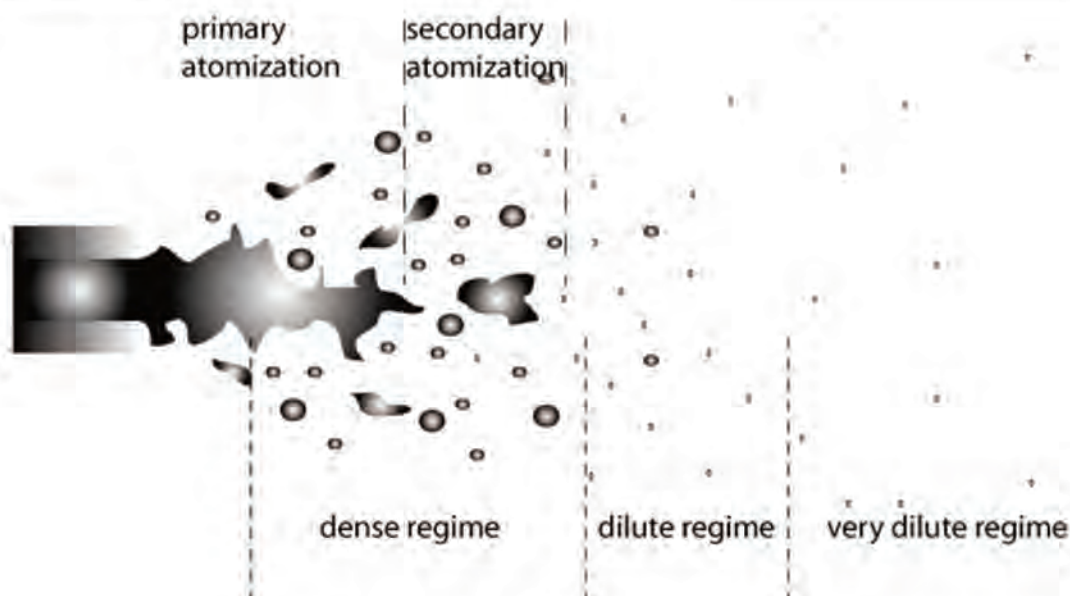


Fig. 1.3. Phenomenology of the atomization of a spray [3]

of small droplets, which may be considered spherical due to surface tension forces.

#### 1.4.2 Characterization of a liquid spray

One of the most common method to characterize the density of a spray consists in measuring the local proportion of liquid volume relatively to the gaseous volume, as well as the mass fraction associated to the spray. These data are respectively the liquid volume fraction  $\alpha_l$  and the liquid mass fraction  $M_l$  [4]:

$$\alpha_l = \frac{V_l}{V_{tot}}, \quad (1.1)$$

$$M_l = \frac{m_l}{m_{tot}}, \quad (1.2)$$

where  $V_l$ ,  $V_{tot}$ ,  $m_l$  and  $m_{tot}$  are respectively the liquid and total volume, and the liquid and total mass. These numbers are used to classify the spray/gas flows:

- $\alpha_l > 10^{-1}$ : **very dense spray.** The interactions between the liquid structures, and between the liquid and gaseous phases are preponderant. Inter-particle collisions are the most important contributions to the particle motion.
- $10^{-4} < \alpha_l < 10^{-1}$ : **moderately dense spray.** The interactions between neighboring droplets significantly decrease, but are still existing.
- $\alpha_l < 10^{-4}$  and  $M_l > 10^{-2}$ : **diluted spray.** Inter-droplets phenomena such as collisions and interactions between neighboring droplets are reasonably neglected. Droplets are considered as isolated and are separately treated. However, the interactions between liquid/gaseous phase must be taken into account since the inertia of the liquid mass is not negligible.
- $\alpha_l < 10^{-4}$  and  $M_l < 10^{-2}$ : **very diluted spray.** The interaction between the liquid/gaseous phase are neglected because of the low inertia of the liquid.

At the outlet of an injector, the density of the spray quickly decreases due to the liquid expansion and the droplets turbulent dispersion. Therefore, sprays in aeronautical burners are often considered as diluted.

This work focuses on the diluted regime zone located after the secondary breakup zone. Only diluted and very diluted flows are considered. Thus, inter-particle collisions are ignored

two-way coupling with the carrier fluid is considered. The principal physical phenomenon taking place in this type of flows is the particle dispersion due to the turbulence.

A spray composed of several droplets diameter is called **Polydisperse**, and represents most of the diluted sprays. However, generating a cloud of droplets of the same diameter is interesting to avoid polydispersity effects. Such **monodisperse** sprays are often studied for academic cases.

## 1.5 Place and role of numerical simulation

Fluid mechanics appears in the *XIX<sup>th</sup>* century, thanks to the French engineer Claude Navier and the Irish mathematician George Stokes, who independently established the set of equations characterizing the velocity and pressure of a fluid surrounding an object. These equations are well-known under the name of Navier-Stokes equations. Computational fluid dynamics (CFD) arises from the simultaneous development of numerical methods discretizing Navier-Stokes equations and the computational performances in the 60s. Before CFD, all fluid dynamics studies were experimentally achieved with wind tunnels.

Since its start, CFD did not stop being more and more used in the conception phase of aerodynamic shapes and the development of internal processes occurring inside engines. Indeed, the initial conception stage usually requires the manufacture and the study of many prototypes exploring several optimization ideas. Most of the time, using numerical simulations for this step costs less.

The accuracy of numerical results has been improved by the on-going development of models introducing more and more physical phenomena of increasing complexity. The intensive use of CFD helps in the optimization of gas turbines, while reducing their conception cost and time. Moreover, the influence of individual parameters on the industrial device performances is rather simple to perform using CFD.

However, CFD can not totally replace experimental investigations for several reasons. First, even today models are not always capable to predict with accuracy the physical phenomena occurring inside a device. The second issue concerns the feasibility of numerical simulations in an industrial framework.

There are three main strategies regarding CFD simulations:

- **Direct Numerical Simulation (DNS)**, which completely solves flow dynamics up to the smallest scales. DNS does not require modeling, but is computationally very expensive. Furthermore, simulating two-phase flows can quickly become prohibitive. Therefore, DNS is not applicable today to real industrial configurations, but only to limited canonical test cases, providing a great understanding of many types of flows.
- **Reynolds Averaged Navier-Stokes Simulation (RANS)**, which only solve the mean flow field [5, 6]. The balance equations for mass-weighted averaged quantities are obtained by averaging the instantaneous balance equations. The averaged equations require closure models for the turbulent dynamics of the flow. The greatest advantage of RANS lies in its low computational cost. However, this approach is not suitable for the simulation of unsteady or transient flows.
- **Large Eddy Simulation [7, 8]**, solves the largest scales of the flow up to a certain length-scale, and models by means of subgrid models the smaller scales. The balance equations are obtained by spatially filtering the instantaneous equations. The size of this filter determines the size of the scales that are solved and those that are modeled, providing information about the transient phenomena. This approach is very suitable for unsteady flows simulations and is more affordable than DNS while being more accurate than RANS, allowing the numerical simulations of industrial configurations [9, 10].

In the near future, the increasing accuracy level and efficiency of high fidelity numerical simulations will make CFD a powerful tool accessible by the industry. It will be used on the

## 1.5 Place and role of numerical simulation

one hand for further optimization of industrial systems, and on the other hand, for the study of operating points that are not experimentally accessible because of flight conditions that are too complicated to reproduce or too intrusive measurements... Moreover, the amount of data available from a simulation is much more important than the one that are difficult to measure in the experiment.

The main objective of this PhD thesis is to improve the accuracy of turbulent spray combustion models in the framework of a high fidelity CFD code. In the next chapter and in order to define more precisely the objectives of this research work, the physics of turbulent spray combustion is analyzed in detail and a view of the state-of-the-art is given.



# Spray, turbulence and combustion interactions

## 2.1 Introduction

For a typical engine, the most efficient way to store the fuel is in liquid form since at the same temperature and pressure conditions the density of the liquid is almost a thousand times higher than the one of the gas. Injecting liquid fuel inside a combustion chamber where the flow is turbulent and at high temperature leads to several multi-physics interactions. Two-phase turbulent combustion involves a large number of phenomena related to three main fields: turbulent flows, reactive flows and two-phase flows with phase change. Each of these areas has been the subject of research for more than a century, and are still leaving many open questions. Inside the combustion chamber and as observed in Fig. 2.1, these three types of flow are coupled, increasing the understanding complexity.

First consider a single-phase turbulent reacting flow. The vortices generated by turbulence affect the properties of the flame by changing its local structure through stretch and shear and generate an intense local mixture of the multi-species gas. This mixture directly influences the combustion regime. On the other hand, the burnt gases reduce the turbulence because of their high viscosity, but also increase the local turbulence through their expansion.

The injection of liquid fuel inside the combustion chamber leads to new additional multi-physics interactions: depending on the droplet diameter the turbulent flow modifies the repartition of the fuel. This leads to a heterogeneous mixture and thus to different combustion regimes. On the other hand, the wake generated by a droplet increases the local turbulence through drag. Finally, droplets modify the flame structure and propagation properties whereas the heat released by the flame contributes to the evaporation of the liquid fuel. All these phenomena are strongly coupled and need to be correctly modeled to accurately simulate turbulent spray flames.

In the following, key notions about the different interactions between the spray, combustion and turbulence are presented. First, the interaction between a non-reactive spray and turbulence is detailed in Sect. 2.2, then the interaction between spray and combustion in a laminar regime is presented (Sect. 2.4), whereas the interaction between a flame and turbulence is described in Sect. 2.3. Finally, spray/combustion/turbulence interaction is assessed in Sect. 2.5.

## 2.2 Interaction between a non-reactive spray and turbulence

### 2.2.1 Preferential segregation

When interacting with turbulence, particles may be either drawn into dense clusters or dispersed by deterministic eddy motions [11]. This phenomenon produces highly non-uniform concentration distributions [12] and is called preferential segregation or inertial clustering since it is caused by the difference of inertia between a particle and the fluid. The effect of turbulence on the droplets trajectory is characterized with the Stokes number  $St$ , comparing the inertia of the droplet to a turbulent characteristic time:

$$St = \frac{\tau_p}{\tau_g}, \quad (2.1)$$

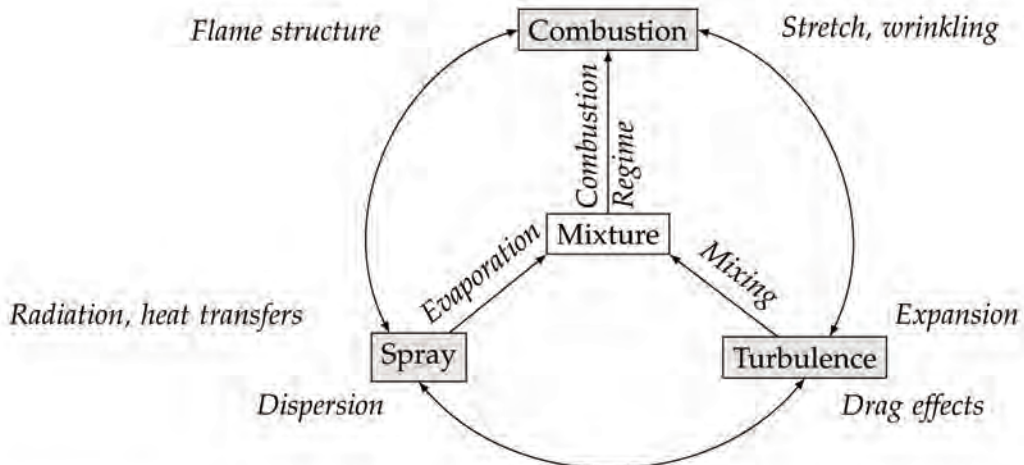


**Fig. 2.1.** Sketch representing the main physical fields and interactions in two-phase turbulent combustion.

where  $\tau_p$  is a characteristic time of the droplet inertia, and  $\tau_g$  is a characteristic time of the turbulent gaseous carrier-phase. As the ratio  $St$  approaches zero, the particles tend to be like fluid elements and to exactly follow the gas flow. As  $St$  increases to values much greater than one, the particles then follow ballistic trajectories and are only influenced by the largest, most energetic eddies. In the particular case of near unity Stokes numbers, inertia prevents the particles from following vortex streamlines and results in particles being centrifuged away from vortex cores, thus preferentially concentrating in areas of low vorticity and high strain rate (Fig. 2.2).

### 2.2.2 Evaporation and mixture

In industrial applications where evaporating polydisperse sprays are injected in combustion chambers, the inertia of the particles varies. Due to this wide range of Stokes numbers, the preferential concentration leads to a heterogeneous mixture where high fuel mass fraction regions are observed. In addition to this heterogeneity, when the droplets evaporation timescale ( $\tau_{ev}$ ) is very short, droplets quickly evaporate and few of them are located far from the injection. On the contrary if the droplet lifetime is long, droplets are located further downstream in the chamber. These phenomena generate a high variation of vaporized fuel and equivalence ratio.

### 2.2.3 Turbulence modulation

The turbulence in a flow containing very small liquid volume fraction ( $\alpha_l \ll 1$ ) and small droplets ( $d_p < \eta_k$ ) is nearly unchanged and similar to a single-phase flow. On the contrary, at higher  $\alpha_l$  or  $d_p > \eta_k$ , additional mechanisms of turbulence production, distortion, and dissipation become important, and the turbulent stresses can be either reduced or increased [11]. This is called turbulence modulation. For diluted sprays, three mechanisms contributing to turbulence reduction can be identified:

- The enhanced inertia of the particle-laden flow.
- The increased dissipation arising from particle drag.
- The enhanced effective viscosity of the particle-laden fluid.

On the contrary, turbulence can be enhanced in two different ways:

- The enhanced velocity fluctuation due to wake dynamics and self-induced vortex shedding.
- The buoyancy-induced instabilities due to density variation arising from preferential



**Fig. 2.2.** Laser-sheet image of  $St = 0.6$  particles in homogeneous turbulence, illustrating preferential concentration [13].

particle concentration.

Each of these phenomena modifies the distribution of the turbulent kinetic energy of the flow compared to the classical scenario of the turbulent Kolmogorov cascade, and the length scale at which these different mechanisms are active varies. Thus, compared to unladen turbulence, the suspended particles can simultaneously augment and suppress turbulence over a different range of scales, and the overall modulation depends on parameters characterizing the strength of the different mechanisms such as the particle-to-turbulence length scale ratio, the particle Reynolds number and the particle-to-fluid density ratio.

## 2.3 Interaction between turbulence and combustion

### 2.3.1 Flame speed

For a one-step irreversible chemical scheme, a premixed flame may be described with the progress variable  $c$  defined as:

$$c = \frac{T - T_f}{T_b - T_f} \quad c = \frac{Y_F - Y_f^f}{Y_F^b - Y_F^f}, \quad (2.2)$$

which describes the progression from fresh gases ( $c = 0$ ) to burnt gases ( $c = 1$ ). The fuel mass fraction and temperature are  $Y_F^f$  and  $T_f$  respectively in the fresh gases and  $Y_F^b$  and  $T_b$  in the burnt gases. Under unity Lewis number and adiabaticity assumptions, the two definitions of Eq. 2.2 are equivalent and a single balance equation for the progress variable is sufficient to describe a steady flame:

$$\frac{\partial \rho u c}{\partial x} = \frac{\partial}{\partial x} \left( \rho D \frac{\partial c}{\partial x} \right) + \dot{\omega}_c, \quad (2.3)$$

where  $\dot{\omega}_c$  is the reaction rate. When working in the phase space based on the reduced temperature or the reduced mass fraction, the flame structure is easily analyzed. An iso- $c$  surface may be used to localize the flame front. Equation 2.3 may be rewritten in a propagative form:

$$u \cdot \nabla c = \frac{1}{\rho} \left[ \frac{\nabla \cdot (\rho D \nabla c) + \dot{\omega}_c}{|\nabla c|} \right] |\nabla c| = S_d |\nabla c|, \quad (2.4)$$

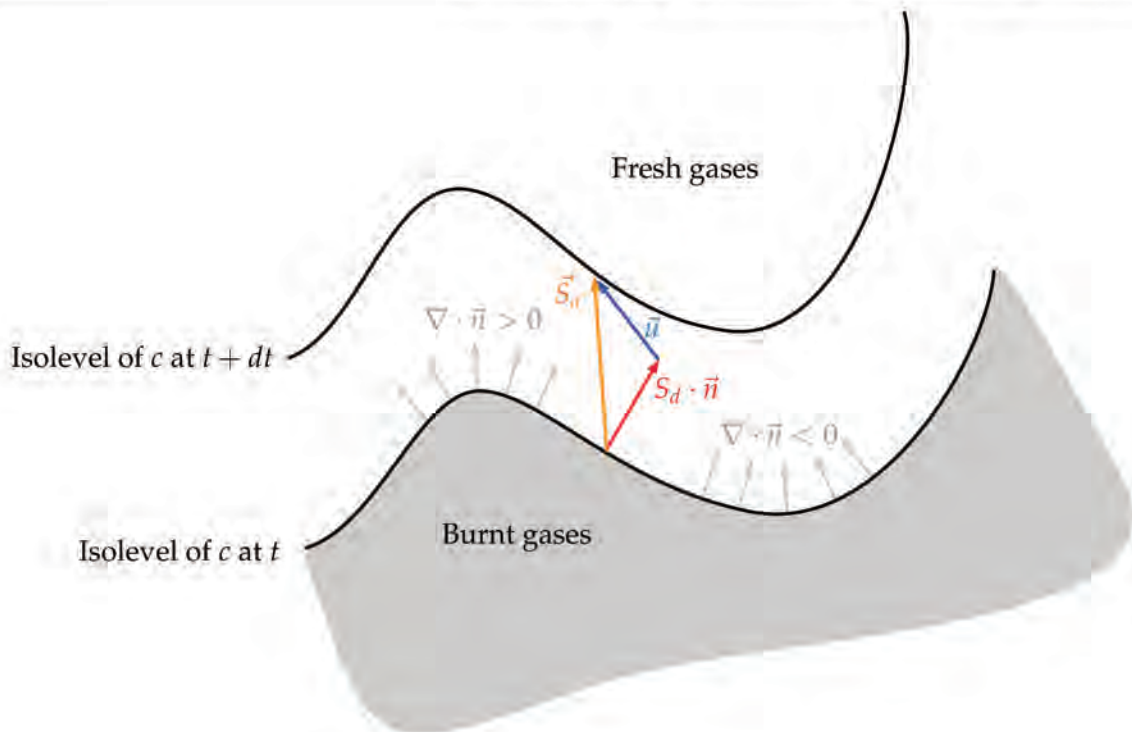


**Fig. 2.3.** Sketch representing the curvature and the flame speed of a turbulent wrinkled flame front.

where the displacement speed  $S_d$ , corresponding to the flame front speed relative to the flow, may be decomposed into three contributions:

$$S_d = S_n + S_t + S_r$$

$$S_d = \frac{1}{\rho |\nabla c|} \frac{\partial}{\partial n} (\rho D \nabla c) - D \nabla \cdot \vec{n} + \frac{1}{\rho |\nabla c|} \dot{\omega}_c, \quad (2.5)$$

where  $S_n$  is the normal molecular diffusion component,  $S_t$  is the tangential diffusion component depending on the local mean curvature  $\nabla \cdot \vec{n}$  of the iso- $c$  surface, and  $S_r$  is the reaction rate component.

The absolute flame front velocity  $\vec{S}_a$  at which a point on the iso- $c$  surface  $c = c_f$  must move, may be written in terms of unburnt gas velocity  $\vec{u}$  and the displacement speed  $S_d$  as follows:

$$\vec{S}_a = \vec{u} + S_d \vec{n}. \quad (2.6)$$

As illustrated in Fig. 2.3, the difference between the flame front velocity  $\vec{S}_a$  and the flow velocity  $\vec{u}$  is the displacement speed  $S_d \vec{n}$  which takes into account the effects of the flow on the flame structure itself.

Another definition of the flame speed is based on the speed at which reactants are consumed and corresponds to the consumption speed  $S_c$ :

$$S_c = -\frac{1}{\rho_f Y_F^f} \int_{-\infty}^{\infty} \dot{\omega}_F d\vec{n}. \quad (2.7)$$

Note that at any location on an iso- $c$  surface, the local gradient of  $c$  defines the normal to the flame front:

$$\vec{n} = -\frac{\nabla c}{|\nabla c|}, \quad (2.8)$$

where  $\vec{n}$  is oriented into the fresh reactants.

Turbulent flame speed  $S_T$

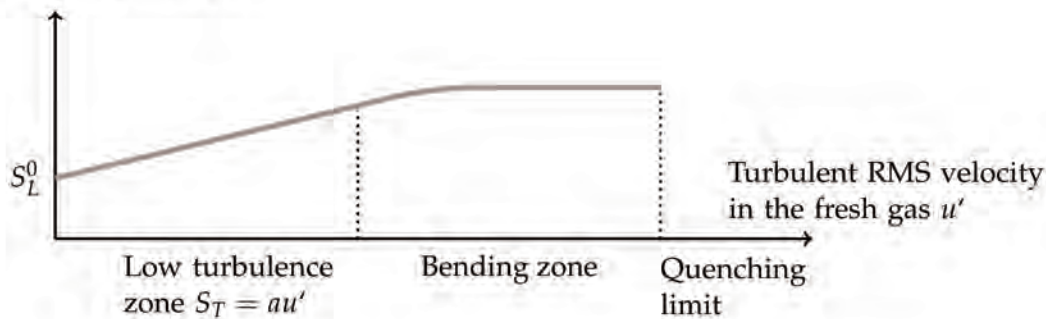


Fig. 2.4. Sketch representing the variations of the turbulent flame speed with the fresh gas turbulent RMS velocity  $u'$ .

### 2.3.2 Definition of stretch

The main effect of turbulence on combustion is to increase the combustion rate. This is achieved through an increase of the flame surface area: the flame front is wrinkled by vortices. For premixed flames, the increase of the combustion rate leads to an increase of the turbulent flame speed. Several correlations between the fresh gases RMS (Root Mean Square) velocity  $u'$  and the turbulent flame speed  $S_T$  exists [14, 15, 16, 17]. All show the same trend, displayed in Fig. 2.4:  $S_T$  first increases linearly with  $u'$ , then levels off ("bending effect") before total quenching occurs for too intense turbulence. The increase of turbulent flame speed  $S_T$  is due to the increase of total flame surface  $A_T$ , allowing higher consumption rate. When a flame front propagates in a non-uniform flow, the changes of flame surface is due to strain and curvature effects [18]. These changes are measured by the flame stretch, defined as the time derivative of the fractional rate of a flame surface element  $A$  [19, 20]:

$$\kappa = \frac{1}{A} \frac{dA}{dt}. \quad (2.9)$$

A negative  $\kappa$  means that the flame surface is reduced, whereas a positive  $\kappa$  indicates an increasing flame surface.

According to both  $\vec{u}$  and  $S_d$ ,  $\kappa$  can be decomposed into a tangential strain rate contribution and a term accounting for the effect of flame front curvature:

$$\kappa = \underbrace{-\vec{n}\vec{n} : \nabla \vec{u}}_{\text{Tangential strain rate}} + \underbrace{S_d \nabla \cdot \vec{n}}_{\text{Curvature}} \quad (2.10)$$

where  $\vec{n}$  is a normal to the flame front pointing by convention towards the fresh gases and  $\vec{n}\vec{n} : \nabla$  is the gradient operator normal to the flame surface. The term  $\nabla \cdot \vec{n}$  has a simple physical interpretation: it is the curvature of the flame front.

For a pocket of fresh gases surrounded by burnt gases, the contribution  $S_d \nabla \cdot \vec{n}$  in Eq. 2.10 is negative: flame propagation decreases stretch and diminishes the flame surface.

On the contrary, for a spherical flame,  $S_d \nabla \cdot \vec{n}$  is positive: the flame propagation increases stretch and flame surface.

From Eq. (2.10), the rate of change of the flame surface area is obviously related to both the flow aerodynamics and the shape of the flame surface. The orientation of flame fronts relatively to velocity gradients is a critical parameter for flame stretch: only velocity gradients in the flame tangent plane induce flame stretch.

### 2.3.3 Effect of stretch on flame speed

If the flame is stretched (i.e curved, strained or both), flame speed may take different values and be more difficult to evaluate, both experimentally and numerically. In the limit of small

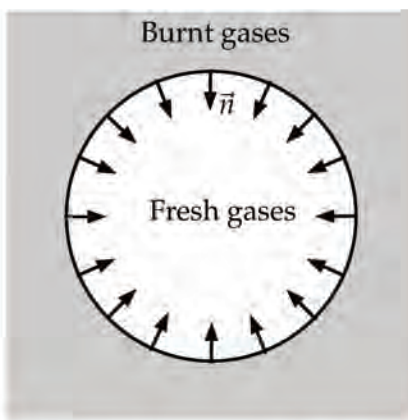


**Fig. 2.5.** Sketch representing the curvature of a pocket of fresh gases in burnt gases.

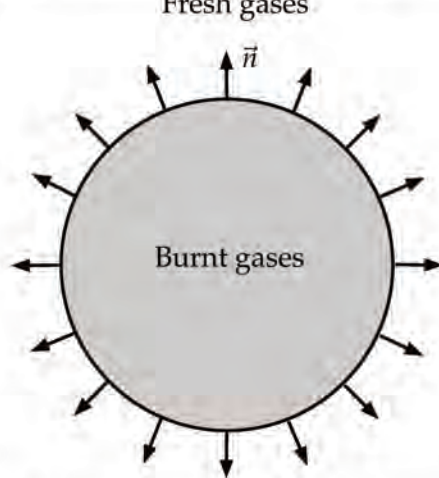


**Fig. 2.6.** Sketch representing the curvature of a spherical flame.

strain and curvature terms, the impact of  $\kappa$  on the displacement speed and consumption speeds may be expressed with a linear relationship ([18, 21, 22, 23, 24]):

$$\frac{S_c}{S_L^0} = 1 - M_a^c \frac{\kappa \delta_L^0}{S_L^0}, \quad (2.11)$$

$$\frac{S_d(0)}{S_L^0} = 1 - M_a^d \frac{\kappa \delta_L^0}{S_L^0}, \quad (2.12)$$

where  $M_a^d = L_a^d / \delta_L^0$  and  $M_a^c = L_a^c / \delta_L^0$  are Markstein numbers for the displacement and the consumption speeds respectively, whereas  $L_a^d$  and  $L_a^c$  are the corresponding Markstein lengths.  $\delta_L^0$  and  $S_L^0$  are respectively the laminar flame thickness and the laminar flame speed. Various expressions are found in the literature for the Markstein numbers. As an example for constant viscosity, lean, single-step flames with variable density, Clavin and Joulin [25] give:

$$M_a^d = \frac{L_a^d}{\delta} = \frac{T_2}{T_2 - T_1} \ln \left( \frac{T_2}{T_1} \right) + \frac{1}{2} \beta (Le_F - 1) \frac{T_1}{T_2 - T_1} \int_0^{\frac{T_2 - T_1}{T_1}} \frac{\ln(1+x)}{x} dx, \quad (2.13)$$

$$M_a^c = \frac{L_a^c}{\delta} = \frac{1}{2} \beta (Le_F - 1) \frac{T_1}{T_2 - T_1} \int_0^{\frac{T_2 - T_1}{T_1}} \frac{\ln(1+x)}{x} dx, \quad (2.14)$$

where  $\beta = (T_2 - T_1) T_a / T_2^2$  measures the activation energy,  $T_a$  is the activation temperature,  $T_1$  is the fresh gas temperature and  $T_2$  is the burnt gas temperature.

Note that the displacement speed is defined on the fresh gas side. The two Markstein lengths differ, showing that the displacement speed and the consumption speed are impacted by stretch.

The expression  $K_a = \kappa \delta_L^0 / S_L^0$  corresponds to the Karlovitz number. Flame quenching is expected when  $\kappa$  becomes of the order of the inverse of the flame time  $\tau_c$ , i.e., when the Karlovitz number is of the order of unity.

When a flame is stretched, two mechanisms are competing: the flame is fed with more fresh gases because fuel mass fraction gradients are increased, but it is also more intensely cooled due to the increase of the temperature gradients. Species and temperature gradients are competing, even more in presence of heat losses (especially radiative losses). Therefore, the Lewis number of the limitant reactant, measuring the ratio between heat and species diffusivities becomes a critical parameter for stretch effects. If for example the limitant reactant

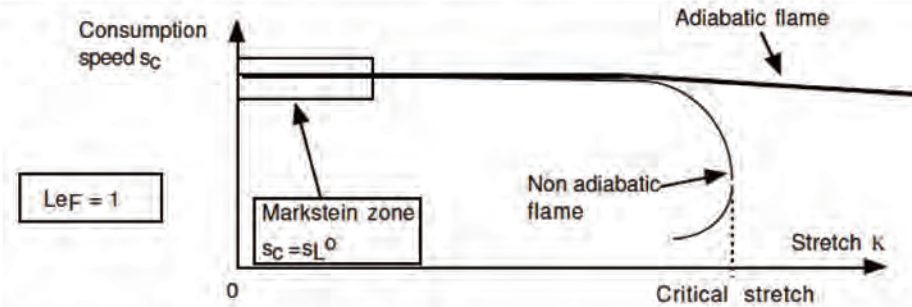


**Fig. 2.7.** Sketch representing the effects of stretch on a laminar flame front at  $Le_F = 1$ : zero  $L_a^c$  Markstein length ([26]).

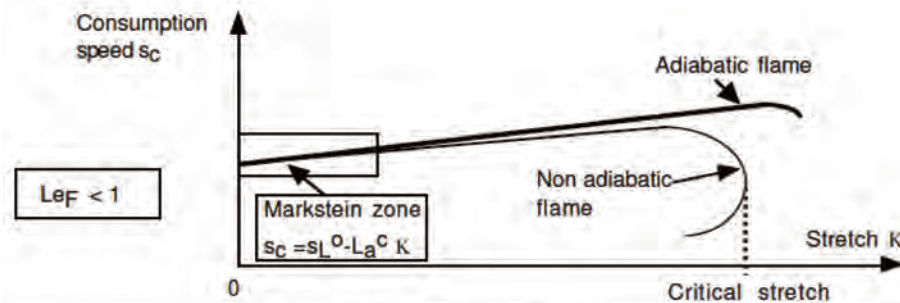


**Fig. 2.8.** Sketch representing the effects of stretch on a laminar flame front at  $Le_F < 1$ : negative  $L_a^c$  Markstein length ([26]).

is the Fuel and  $Le_F = 1$  (Fig. 2.7), the consumption speed of the flame is almost insensitive to strain for low strain values: it remains constant over a wide range of strain rates because both species and temperature gradients increase in the same proportion. The only effect is that the flame becomes thinner when strain increases. When  $Le_F < 1$  (Fig. 2.8) and for low values of strain, the reaction rate increases when strain increases.

On the other hand if  $Le_F > 1$  (Fig. 2.9), the heat release decreases with increasing strain. Note that the heat losses control the existence of a turning point in the curves where the flame gets suddenly quenched. In practice, when studying turbulent flame fronts, it is much more difficult to analyse the effect of stretch on the flame due to the unsteady and local nature of turbulence. The effect of this last one on the flame speed depends on the sign of the stretch which changes a lot along the wrinkled flame front. Moreover, stretch values also depend on the choice of  $c$  in Eq. 2.8.

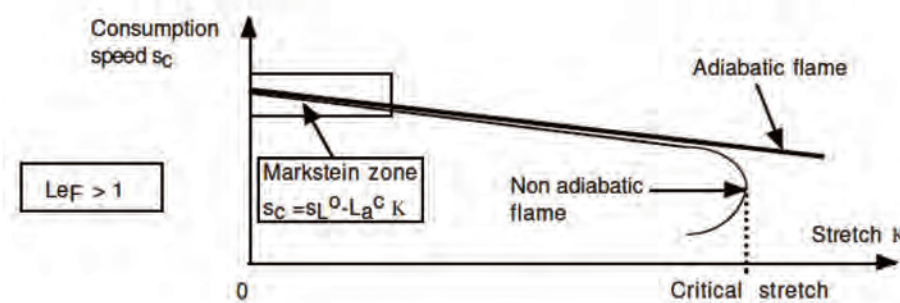


**Fig. 2.9.** Sketch representing the effects of stretch on a laminar flame at  $Le_F > 1$ : positive  $L_a^c$  Markstein length ([26]).

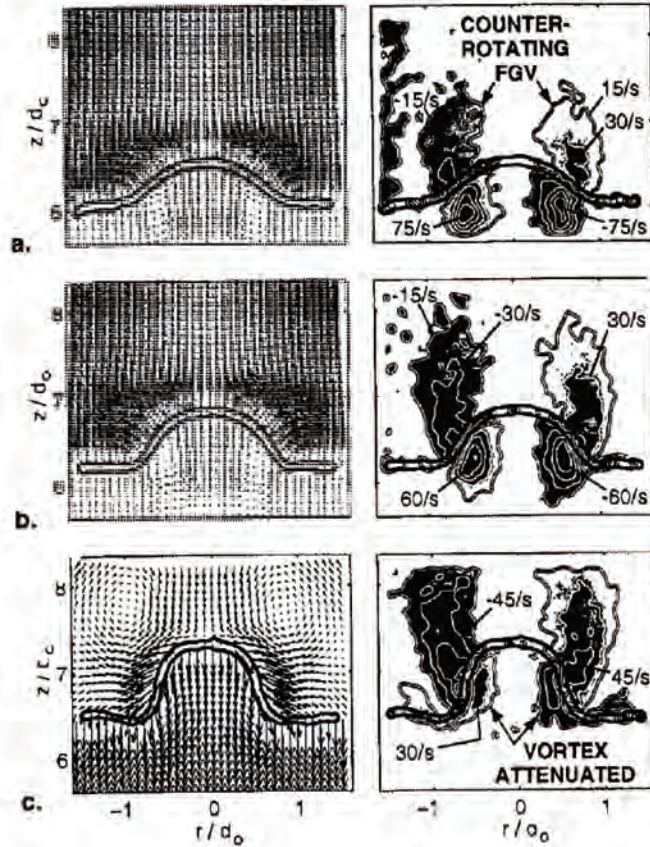


**Fig. 2.10.** Velocity (left) and vorticity (right) fields measured during the interaction of a weak toroidal vortex with a planar flame, at three successive times, a,b and c [27]. A counter-rotating flame generated vortex (FGV) is observed when the vortex crosses the flame front.

#### 2.3.4 Effect of flame fronts on turbulence

The flame also modifies the turbulent flow field. The increase of temperature from one side to the other of the flame front leads to an increase of the kinematic viscosity ( $\nu_{air} \propto T^{1.7}$ ) and therefore local Reynolds numbers. For a flame with a temperature ratio  $T_2/T_1 = 8$ , the Reynolds number is about 40 times smaller in burnt than fresh gases, leading to a relaminarization of the flow. On the other hand, the flow is accelerated through the flame front due to the burnt gases expansion, modifying the turbulent flow field:  $u = u_1 + S_L^0(\rho_2/\rho_1 - 1) = u_1 + S_L^0(T_2/T_1 - 1)$ . Vorticity is also generated because of pressure and density gradients (baroclinic torque). These mechanisms have been experimentally investigated by Muller *et al.* [27]. They have convected a toroidal vortex through a planar laminar premixed flame (Fig. 2.10). For low turbulence intensities, a counter-rotating flame generated vorticity was observed. On the other hand, strong vortices cross the flame front and remain almost unaffected.

### 2.4 Interaction between a spray and a laminar flame

#### 2.4.1 Two-phase combustion regimes

The combustion process involves chemical reactions which only take place in the gaseous phase [28]. Thus, the evaporation of liquid fuel is a necessary step for the combustion to occur. Droplets may evaporate, upstream, inside or downstream (and even all in one) of the flame front. The location of the evaporation process depends on several parameters such as the evaporation characteristic time, the liquid injection velocity or the distance between injection and the flame front (pre-evaporation distance), and determines the level of interaction between

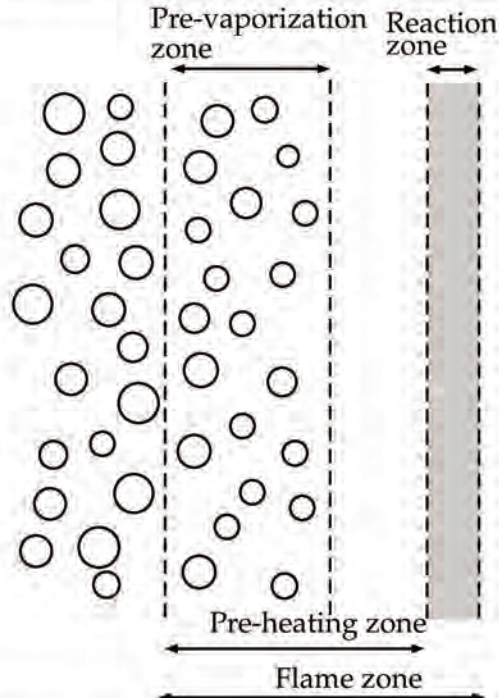


Fig. 2.11. Sketch representing the pre-evaporation mode.

the spray and the flame.

Three interaction levels are observed:

- **Pre-evaporation (Fig. 2.11):** droplets have enough time to completely evaporate before reaching the reaction zone. The spray and combustion are thus spatially uncorrelated and the combustion takes place in the single-phase regime which only depends on the gaseous fuel repartition in the chamber.
- **Homogeneous two-phase combustion (Fig. 2.12):** the spray reaches the reacting zone and is both dense and homogenous enough to continuously provide vaporized fuel to the flame. The level of interaction is intermediate compared to the pre-evaporation regime. The flame thickens as the droplets pass through the flame front. Note that if the mixture is rich, the combustion process may stop due to a lack of oxidizer, and droplets evaporate without burning behind the reaction zone.
- **Heterogeneous two-phase combustion (Fig. 2.13):** the flame is located in between the spray which strongly modifies the combustion regime. Additional combustion regimes arise such as the group combustion or the isolated droplet combustion. The spray and the combustion are strongly coupled.

These different combustion modes may be classified as a function of a dimensionless number,  $G$ , which is the ratio between the droplet evaporation rate and the diffusion rate of hot gases within the droplet cloud [29]. When convection is more important than diffusion,  $G$  is approximated as follows:

$$G \approx 5 \frac{N_p^{2/3} \delta_{r_f}}{\delta_{d_s}}, \quad (2.15)$$

where  $N_p$  is the number of droplets in the cloud,  $\delta_{r_f}$  is a characteristic diffusion flame radius [30] and  $\delta_{d_s}$  is the mean droplet spacing. The combustion regimes characterized by  $G$  are represented in Fig. 2.14 [29]. For large  $G$ , the spray is very dense and diffusion inside the cloud is low, only the droplets located at the periphery of the cloud evaporate. The flame envelopes the whole cloud of droplets. It is referred to as external sheath combustion. For diluted spray regimes, where  $G \ll 1$  droplets are far from each other and the evaporation rate increases

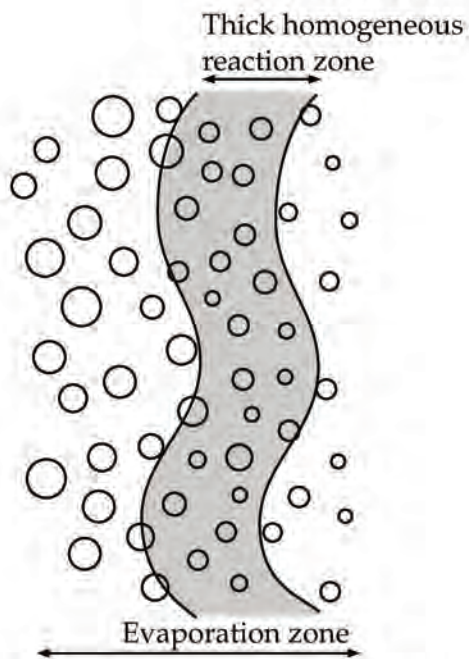


Fig. 2.12. Sketch representing the homogenous mode.

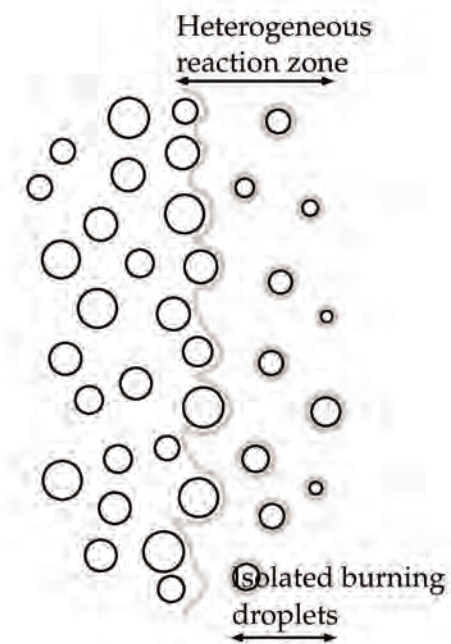


Fig. 2.13. Sketch representing the heterogeneous mode.

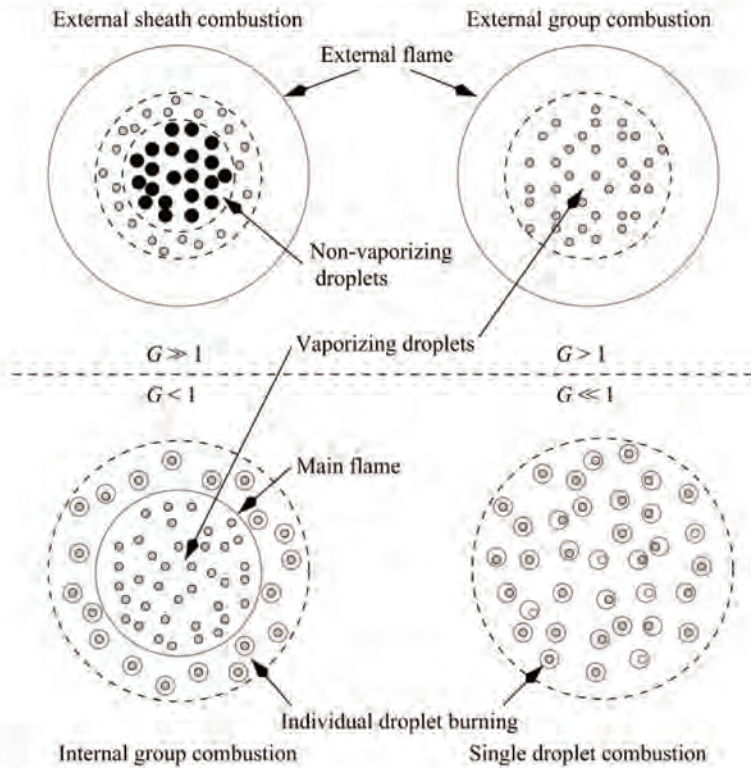


Fig. 2.14. Combustion modes of a droplet cloud [29, 31, 32].

due to hot gases diffusion. Separated flames surround each droplet, which burns individually. Intermediate regimes exist between these two extremes: for  $G$  slightly higher than one, the flame surrounds the whole cloud of droplets and hot gases diffusion is high enough to vaporize the droplets located at the center of the cloud. When  $G < 1$ , the center of the cloud burns in an external combustion regime and the droplets located at the periphery burn in an isolated manner.

#### 2.4.2 Two-phase flame propagation mechanisms

Considering the diluted spray as a whole (and not only as isolated burning droplets), one can observe the flame passing from one drop to another. Many propagation mechanisms of a flame in a cloud of droplets exist. These mechanisms introduce a great disparity in the intensity of the spray/flame interaction, ranging from homogeneous to heterogeneous combustion (Fig. 2.2). Three academic configurations are mainly used to study these mechanisms in a laminar regime [33, 34]:

- A drop stream corresponds to a set of monodisperse drops which are aligned and injected at regular intervals.
- A drop array corresponds to a regular assembly of drops formed at the crossings of the fibers of a two-dimensional or three-dimensional mesh.
- A two-phase counter-flow flame corresponds to a countercurrent flow in which a flame is stabilized and supplied by a spray. This configuration is suitable for parametric studies. Thanks to these configurations, it is easier to observe the propagation mechanisms of the flame, to analyze the influence of different parameters on the phenomena taking place in between droplets, and to provide experimental data such as two-phase flame speed.

From a drop array study, Umemura *et al.* [35] proposed a classification of the different flame propagation modes in a spray (Fig. 2.15).

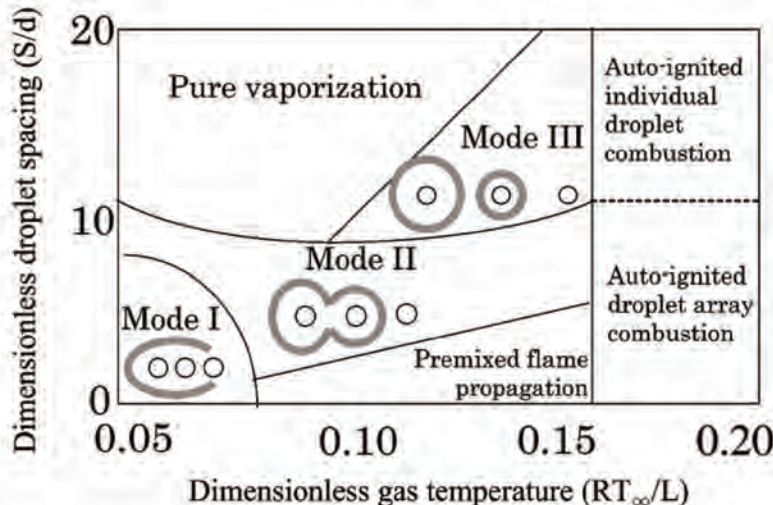
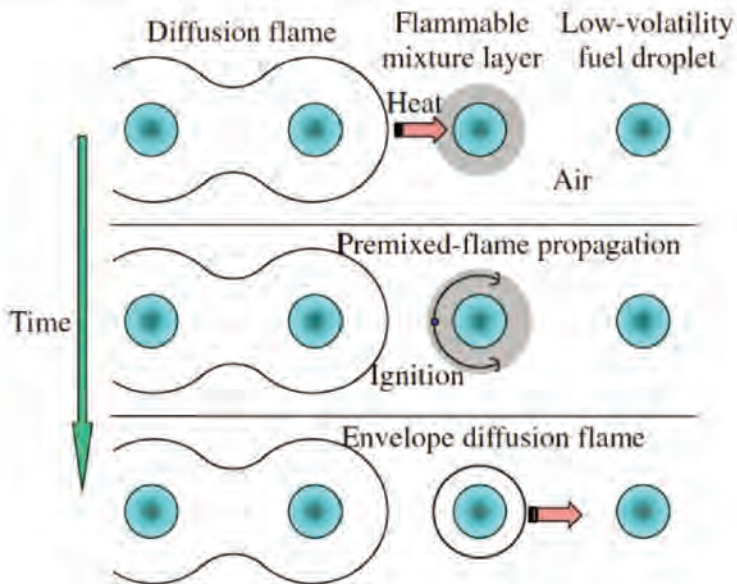


Fig. 2.15. Inter-droplet flame propagation mode map [35].

These propagation modes are function of both, a temperature made dimensionless with the heat vaporization of the liquid fuel  $L_v$ , and the space in between droplets  $S$  made dimensionless with the diameter of the droplets. For a high temperature ( $RT_{\infty}/L_v > 0.15$ ), droplets self-ignite individually through individual (high values of  $S$ ) or collective (small values of  $S$ ) envelop flames. For lower temperature ( $RT_{\infty}/L_v < 0.15$ ), the ignition is ensured through a the propagation of the flame in between droplets. Several propagation modes arise:

- **Propagation of a homogeneous spray flame** ( $S/d < 3$  and  $0.07 < RT_{\infty}/L_v < 0.15$ ): for small droplet spacing, the combustible gas mixture layers of neighboring droplets combine each other to form a continuous combustible gas mixture layer. As a result, a premixed flame may propagate through the continuous combustible gas mixture layer at a relatively small speed. This propagation process is close to the one of a purely gaseous premixed flame, to which is added the effects of preheating and evaporating droplets. Compared to a purely gaseous case, the two-phase homogeneous flame is usually thicker [36] and its laminar flame speed may be much different (even higher) as it will be shown in Sect. 2.4.3.
- **Mode I:** This inter-droplet flame propagation mode appears when the droplet spacing is shorter than the isolated droplets maximum flame diameter and results in a group combustion regime. The temperature of the mixture is no longer high enough to sufficiently vaporize the droplets of fuel. These conditions are not suitable for a premixed flame to propagate anymore. However, the envelop flame of the first droplet may encompass a cold neighboring drop because of the small inter-droplet distance. Due to its increasing evaporation rate, this second droplet becomes a new source of fuel. This allows the flame front to envelop a group of droplets. Mode I causes the formation of a diffusion flame encompassing several drops in a group combustion regime.
- **Mode II:** When the inter-droplet spacing increases, the envelop flame surrounding the first droplet is not big enough to encompass the neighboring drops. However, due to its proximity with other droplets, the flame front of the first spherical flame may propagate around the neighboring droplet, and as well as with the next one. This results into a flame encompassing several droplets.
- **Mode III:** When the inter-droplet spacing still increases, the flame heats the nearby droplets until their auto-ignition. This has been observed by Mikami *et al.* [37, 38] in an experimental study of a drop stream: the proximity of the flame heats the mixture surrounding nearby droplets until their self-ignition. From the ignition point, a triple flame propagates from one side of the droplet to the other until creating a new enveloping



**Fig. 2.16.** Sketch representing the propagation of a flame in a drop stream [38] (mode III).

flame (Fig. 2.16). These spherical flames are distinct from one another.

- **No propagation:** the energy provided by a droplet is not sufficient to auto-ignite neighboring droplets.

#### 2.4.3 Two-phase laminar flame speed

Knowing the flame speed is essential for the understanding of key issues such as flame stabilization or ignition. However, the liquid phase may significantly change the propagation properties of a two-phase flame [39, 40, 41, 42, 43]. Numerous researchers have worked on this subject. One of the first studies was carried out by Williams [44]. He derived an analytical solution for two distinct cases: either all the droplets are evaporated before reaching the flame front, or each droplet burns with a diffusion flame around it. Later, various studies were dedicated to mono- or poly-dispersed spray combustion [45, 46, 47]. In most of these studies, the carrier and the disperse phases are injected at the same velocity and the gaseous mixture initially contains some fuel vapor to stabilize the flame. The presence of droplets leads to a modification of the local equivalence ratio. For a polydisperse spray without relative velocity between the liquid and gaseous phase, analytical approaches exist to estimate the two-phase laminar flame speed. For example, Greenberg *et al.* [48] have proposed a formula to obtain the laminar propagation speed of a heterogeneous and poly-disperse spray using sectional approach [43, 49, 50].

Experimental studies also investigate heterogeneous two-phase flame propagation without relative velocity. Umemura *et al.* [35] observed an inter-droplet spacing threshold maximizing the flame propagation speed. This distance is close to the diameter that would have the flame around an isolated droplet in the same conditions. Mikami *et al.* [51] also observed that the flame propagation speed for the modes II and III is controlled by the self-ignition delay of the droplets composing the spray. Ballal and Lefebvre [41] experimentally pointed out the effect of the mean droplet size on the laminar spray flame speed for lean and stoichiometric mixtures, showing that increasing droplet diameter reduces the laminar flame speed. They also proposed a correlation to evaluate the laminar spray flame speed according to inlet liquid injection properties. However, this expression was shown inappropriate either for rich mixtures, or for a large range of droplet diameters [52]. For rich mixtures, Hayashi *et al.* [53] observed

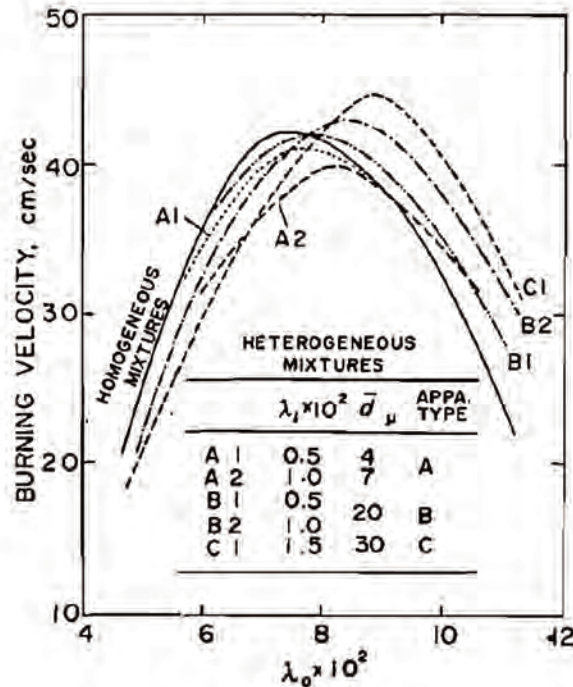


Fig. 2.17. Comparison of the burning velocities obtained for several droplets diameter (ethanol mixtures) [53]. The continuous line corresponds to the gaseous premixed flame.

the existence of an optimum droplet size that results in an enhanced laminar flame speed compared to gaseous premixed flame (referred as homogeneous mixtures in Fig. 2.17). This phenomenon was first associated to an increase of the flame surface that comes from the impact of the droplets on the flame front. Another explanation introduces an effective fuel-air ratio which accounts for the unvaporized and incompletely mixed fuel. The resulting reacting mixture may then burn close to stoichiometry, leading to high flame propagation speed.

The increase of the flame speed for overall rich two-phase flames has also been numerically observed in one-dimensional laminar premixed spray flame simulations [52, 54, 55]. Neophytou *et al.* [52] have shown that the two-phase laminar flame speed is maximum when the "effective" equivalence ratio seen by the flame (defined as the local equivalence ratio located at the maximum of heat release) is close to 1. Réveillon *et al.* [56] have stated that this effective equivalence ratio depends on the ratio between a liquid to gas transfer characteristic time, and a flame characteristic time. To estimate this effective equivalence ratio, Réveillon *et al.* [56] proposed to analyse the ratio  $D_v = \tau_{ev}/\tau_c$ , where  $\tau_{ev}$  is an evaporation time and  $\tau_c$  is the pre-heating time of the flame corresponding to the ratio between the thermal flame thickness and the gaseous laminar flame speed [26]. A short evaporation delay ( $D_v \ll 1$ ) corresponds to a quick evaporation of the droplets in the flame front and to an effective equivalence ratio equal to the initial total one:  $\phi_{tot} = \phi_g + \phi_l$ . On the contrary, if  $D_v \gg 1$ , the quantity of oxidizer decreases quicker than the fuel supply. The effective equivalence ratio is low, leading to a low flame speed. Flame speed can also be accelerated by chemical effects [52] or by gas expansion due to evaporation (adding local mass to the gas phase).

However no clear theoretical framework has been proposed in the literature to handle all possible spray flame structures, especially when a relative velocity exists between the liquid and the gaseous phases. In this thesis, the effect of relative velocity on homogeneous spray flame structure and propagation properties is investigated through simulations of a monodisperse drop stream crossing a one-dimensional laminar premixed flame. This study is presented in Sect. 7.1.

## 2.5 Interaction between spray, combustion and turbulence

A deep understanding of the interaction mechanisms between turbulence, spray and combustion is essential to optimize engine and burner designs. The flame structure, the mechanisms of stabilization, ignition and extinction of a two-phase turbulent flame are still not fully understood in many applications where a spray is injected in a reactive turbulent flow. Historically, experimentations of increasing complexity have been set up to better understand the physical mechanisms of the coupling between turbulence/spray/combustion and provide a reliable database for the validation of numerical models. At the same time, high-fidelity numerical simulations have been done to provide reliable numerical models. These simulations are used to validate simplified models and to better understand physical mechanisms not accessible through experiments.

### 2.5.1 Characterization of a turbulent reacting spray

To characterize an experiment of a turbulent reacting spray at a given operating point, Delabroy *et al.* [57] defined four dimensionless numbers, thanks to a dimensional analysis applied to a cloud of burning droplets. These numbers describe the turbulent burning process of a spray:

- $\Delta_1 = \frac{L_{\text{liquide}}}{L_{\text{ent}}}$ , compares the estimation of the length of the dense heart of the spray and the length of the wake generated by the spray. This number describes the global aspect of the flame.
- $\Delta_2 = \frac{\tau_{\text{mix}}}{\tau_{\text{ch}}}$ , compares a turbulent mixing time  $\tau_{\text{mix}}$  to the chemical characteristic time  $\tau_{\text{ch}}$ . This number describes the capacity of the flame to stabilize.
- $\Delta_3 = \frac{\tau_{\text{ev}}}{\tau_{\text{ch}}}$ , compares the estimation of the lifetime of the droplet  $\tau_{\text{ev}}$ , to the characteristic chemical time  $\tau_{\text{ch}}$ . This number completes the information provided by  $\Delta_2$  to take into account the delay due to evaporation.
- $\Delta_4 = \frac{d_{\text{SMD}}}{d_{\text{inj}}}$ , compares the Sauter Mean Diameter of the injected droplets, to the diameter of the injector  $d_{\text{inj}}$ . This number characterizes the efficiency of the atomization.

The relevance of these numbers has been validated in several experimental configurations. Using these numbers, the global flame structure, the stabilization mode, and the impact of the droplets on the stabilization may be anticipated.

### 2.5.2 Identification of the combustion regime

When segregated liquid fuel and oxidizer streams are injected into the combustion chamber and if  $St < 1$ , two combustion scenarios are possible (Fig. 2.18) [56].

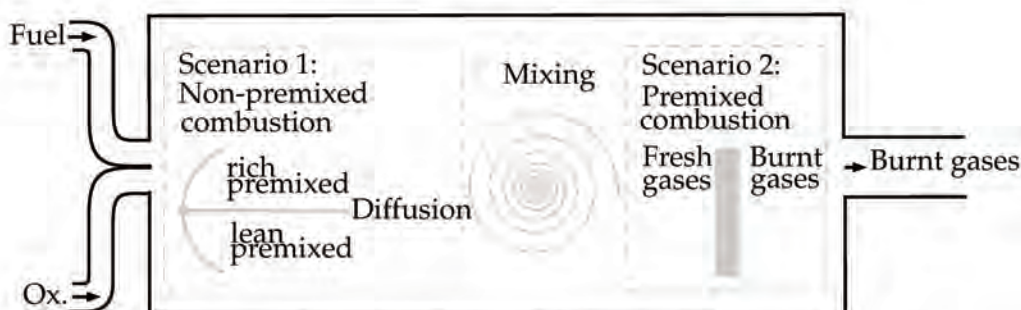


**Fig. 2.18.** Sketch representing the possible combustion regimes when liquid fuel is injected in a combustor (adapted from [56]).

For the first case, reaction takes place before any mixing between fuel and oxidizer occurs. Then a diffusion flame emerges piloted by a triple flame. Otherwise if fuel and oxidizer are mixed before ignition takes place, a premixed flame propagates in the domain. These premixed and diffusion flames have very different structures and behaviors that need to be modeled

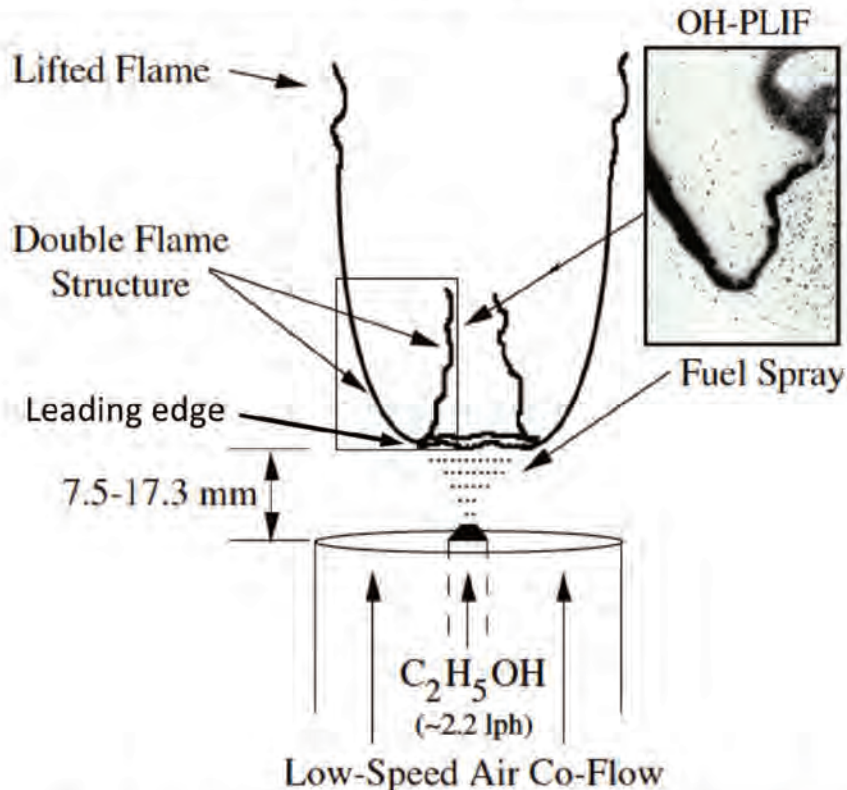


Fig. 2.19. Sketch of the experiment of Marley *et al.* (adapted from [59]).

differently. To differentiate the heat release resulting from these combustion regimes, Takeno *et al.* [58] have suggested to use a flame index based on the scalar product of the fuel and oxidizer normalized gradients:

$$I_{flame} = \frac{\nabla Y_F \nabla Y_{Ox}}{\| \nabla Y_F \nabla Y_{Ox} \|} H_R. \quad (2.16)$$

A positive flame index  $I_{flame}$  indicates a premixed combustion whereas a negative index is associated to a diffusion flame. Note that the validity of this index is relevant only in purely gaseous regions since evaporating droplets may modify the species gradients.

### 2.5.3 Turbulent spray flame stabilization process

#### Natural stabilization of a turbulent spray flame in a non-recirculating flow

Detached flames are highly sensitive to upstream conditions such as velocity and fuel concentration fluctuations. Marley *et al.* [59] and Ge *et al.* [60] have studied a turbulent detached flame stabilized downstream of a conical polydisperse spray (Fig. 2.19). This last one was injected in a low speed coaxial flow of air. The leading edge of the flame exhibits a double reaction zone structure, similar to a triple flame. The poly-disperse spray distribution facilitates the existence of this flame structure. Indeed, as a result of the spray/turbulence interactions, small droplets (small Stokes numbers) follow the gas phase flow, increasing the residence times in turbulent eddies. This process leads to enhanced vaporization and the generation of fuel vapor prior to reaching a reaction zone, increasing the likelihood of partially premixed combustion. On the other hand, the large droplet population can vaporize between the reaction zone structures to supply fuel vapor primarily to the outer diffusion flame.

Moreover, the spray cone is able to entrain some air into the flame as a result of momentum transfer to the air as observed in Fig. 2.20. The spray is continuous and therefore continuously entrains surrounding air, but the strength of entrainment is weak and only air that flows



**Fig. 2.20.** Smoke visualization photographs of the experiment of Marley *et al.* [59]. The smoke is injected upstream of the nozzle on both sides of the burner (though emanating from different radii in the co-flow) to visualize air entrainment.

immediately adjacent to the spray edge is pulled into the spray. These streams of oxidizer within the flame clearly indicate that these areas of mixing control the location (and appearance) of the inner reaction zone in conjunction with the polydisperse spray characteristics. The inner reaction zone is wrinkled and shows characteristics of partially premixed combustion due to turbulent mixing at downstream locations. The upstream combustion structure of the inner zone burns in a diffusion mode and is somewhat thinner than the outer diffusion flame, suggesting that the inner zone experiences relatively high strain rates compared to the outer zone which burns in the low speed gas flow well isolated from the flow turbulence.

This structure formed of multiple combustion modes, is typical of a turbulent reactive spray.

#### **Stabilization of a turbulent spray flame with a pilot flame**

In this configuration, the turbulent spray flame is stabilized thanks to another flame ("pilot flame") which is usually a gaseous premixed flame. The objective of the pilot flame is to continuously activate reactions in the cold injected mixture. This configuration is suitable for validating CFD codes and studying the influence of fuel volatility, entrainment flow velocity, droplets size and the turbulent dispersion. Pichard *et al.* [61] have studied a Lean Pre-vaporized Premixed (LPP) burner consisting in a conical spray injected at the center of a cylindrical duct and surrounded by a co-axial turbulent air flow (Fig. [61]). In this experiment, the rate of pre-vaporization is variable. The authors show that the degree of pre-vaporization increases when the input temperature and fuel volatility increases, and when the overall equivalence ratio and mean injection diameter decrease. The coupling effects between liquid phase and gaseous flow as well as the preferential segregation of the droplets have been observed by Karpetis *et al.* [62] in a similar configuration.

#### **Stabilization of a turbulent spray flame with burnt gases recirculation**

In this configuration, the flame is stabilized by a recirculating zone containing burnt gases. This recirculation zone is obtained through a rotating flow generated at the inlet of the domain. The recirculation zone of hot burnt gases ensures the activation of the reactions in the fresh gas mixture. This stabilization mode is usually employed in industrial configurations. Widmann

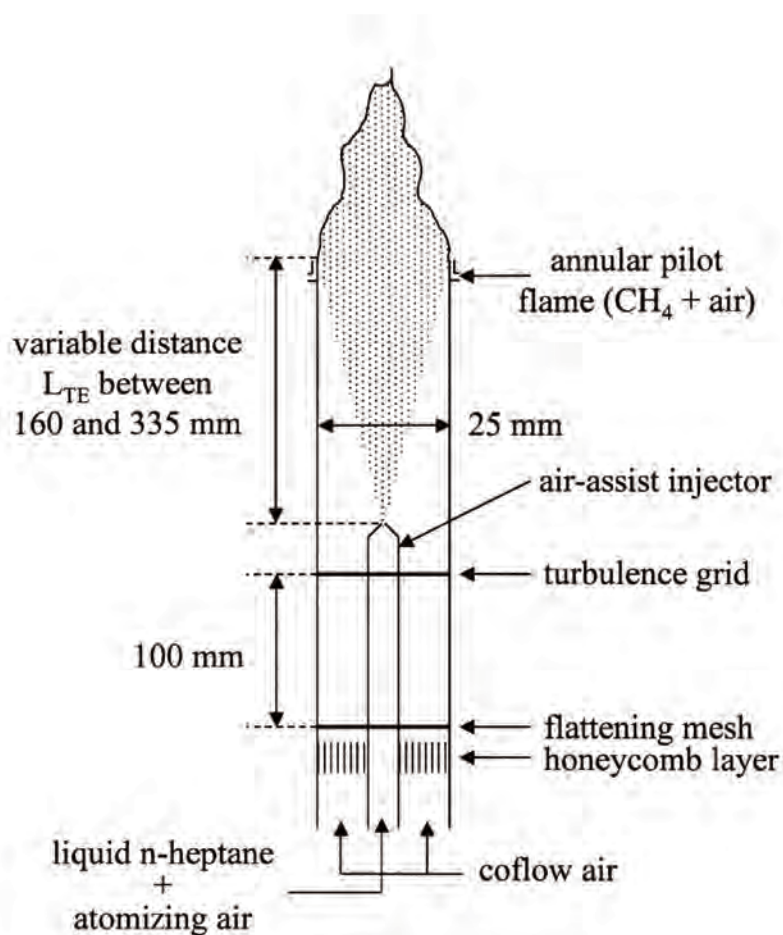


Fig. 2.21. Sketch of the experiment of Pichard *et al.* [61].

and Presser [63] study the properties of a hollow cone immersed in a turbulent air flow inside a closed combustion chamber. In their work and for a validation purpose of CFD codes, a special attention is accorded to the definition of boundary conditions. The authors provide a very comprehensive database. Sanjosé *et al.* [64] have studied a pressurized burner called "Mercato", which is close to aeronautical combustion chambers. In their work, they observed a complex flame structure: droplets evaporate while passing through the reaction zones. Therefore, a significant amount of liquid fuel crosses the flame front and evaporates within the burnt gases, resulting in strong gradients of equivalence ratio. This leads to a flame structure which cannot be found in gaseous flames: diffusion flames are formed between the air stream and the fuel evaporating in the burnt gases.

A similar configuration is studied by Cavaliere *et al.* [65] to analyze both, the different flame structures with and without spray, and the mechanisms of extinction of the flame. The different combustion regimes are analyzed with the combination of flame position, liquid phase and flow measurements. All of these experiments show the significant influence of the spray on the flame structure.

### 2.5.4 Numerical simulation of a turbulent reacting spray

Experiments involving liquid sprays are much more complex to measure. When conventional methods of non-intrusive optical measurements are used for gases, a strong attenuation of the signal, a spatial diffusion of the laser pointer, as well as interferences related to the presence of liquid drops greatly disturb the quality of measurements. Moreover, in a reactive two-phase spray experiment, a simultaneous measurement of the liquid phase and the gas phase is desirable, if possible in a non-intrusive way. Usually and because of the large size of the measuring devices related to the size of the optical accesses, the measurement techniques are unfortunately implemented one after the other. Added to this is the difficulty and cost associated to experiments operating at pressures equivalent to inlet conditions in industrial combustion chambers. Indeed, the cost of an experiment strongly increases with the internal pressure, as well as the difficulty to implement optical accesses. This mainly explains the difficulty to carry out fully representative experiments of industrial systems. For all these reasons, the numerical simulation offers an interesting complementarity to the experiments. In the following, only DNS and LES of turbulent reacting spray are presented, although a lot of works have also been done in RANS.

#### DNS approaches

In a Direct Numerical Simulation (DNS) approach, all the scales of the physical mechanisms are solved. In the framework of a turbulent reacting spray, it implies:

- The whole range of turbulent vortices.
- Each droplet composing the spray together with their internal variations and transfers at the surface.
- The chemical kinetics.

Due to their computational cost, DNS approaches capable of perfectly solving these three types of scales are only performed on small configurations and for few droplets. An alternative consists in performing DNS that only solve turbulence and chemistry, reducing droplets as point sources.

In full DNS, the fluid mechanics equations are solved separately in both phases (liquid and gaseous), the interface separating the two phases is considered as infinitely thin, and its trajectory is tracked with an appropriate numerical method.

For a non-evaporating case, Uhlmann [66] demonstrated the feasibility of Immersed Boundary Method simulating the trajectory of 1000 spherical droplets. For a non-reacting but evaporating case, Duret *et al.* [67] performed a DNS of droplets inside a Homogeneous Isotropic Turbulence (HIT). The local influence of turbulence on evaporation was analyzed and droplets

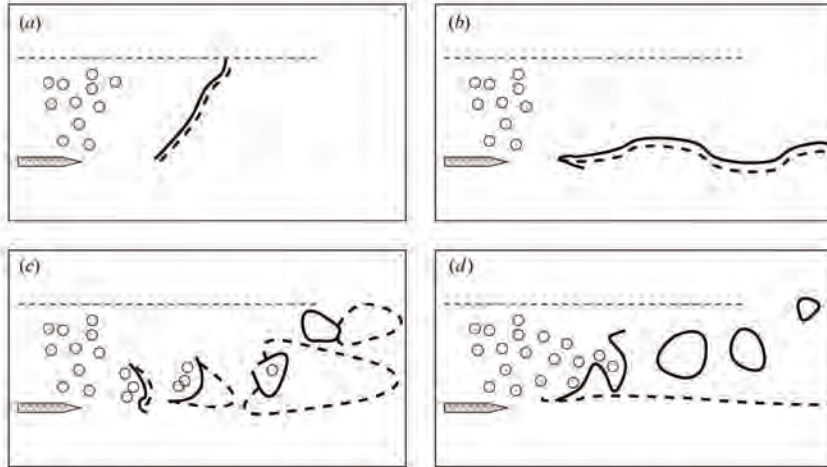


**Fig. 2.22.** Summary of weakly turbulent spray flame structures (from [29]). Continuous line: premixed combustion. Dashed line: diffusion combustion. (a) Closed external, (b) open external, (c) group, (d) hybrid.

are localized with a tracking interface method. Zoby *et al.* [68, 69] studied the evaporation and the reaction of a droplet array in a turbulent flow using a simplified chemical scheme and a Level-set/Ghost fluid method. They compared their results to the evaporation rate of droplets predicted by usual evaporation models.

Wu and Sirignano [70, 71, 72] used fully resolved 3D DNS to simulate burning droplet arrays. They studied effects of droplet spacing, relative velocity and ambient pressure on flame structure transition as well as surface temperature and burning rates of droplets, but the study was restricted to laminar convective environment.

Wang *et al.* [73] performed a 3D DNS to simulate the combustion of droplet arrays in turbulent convective flows with a four-step reduced chemical mechanism. They analyzed the characterization of the mixing process between the evaporating fuel and the surrounding gas in regions dominated by small turbulent scales.

#### DNS-DPS approaches

In this approach, the gas flow is fully resolved but the droplet surface and its vicinity affected by the boundary layer are not. Instead, droplets are represented by point sources, tracked and coupled to the Eulerian flow field with a Lagrangian approach. This Discrete Particle Simulation (DPS) approach consists in considering droplets as moving spatial points carrying source terms of mass, momentum and energy. The evolution of the trajectory, the droplet diameter and the droplet temperature are obtained using analytical and/or empirical macroscopic models. The main advantage of these models stands in their affordability. Moreover, the main mechanisms involved in turbulent spray flames may be described with this approach: Réveillon and Vervisch [29] classified turbulent spray flames the liquid equivalence ratio and the density of the injected droplets. Changing these two parameters, they observed a wide range of two-phase flame structures in a configuration where droplets are injected in a central jet surrounded by two layers of air:

- **External combustion:** the flame front is continuous and two sub-regimes are observed: a closed external regime (Fig. 2.22(a)) when a single flame front surrounds droplets and gaseous fuel vaporized upstream of the flame front, and an open external (Fig. 2.22(b)) regime when two flame fronts stabilize themselves from either sides of the jet (similarly to Marley *et al.* [59].)
- **Group combustion:** several groups of droplets are independently consumed (Fig. 2.22(c)). Premixed and non-premixed regimes are thus simultaneously observed.

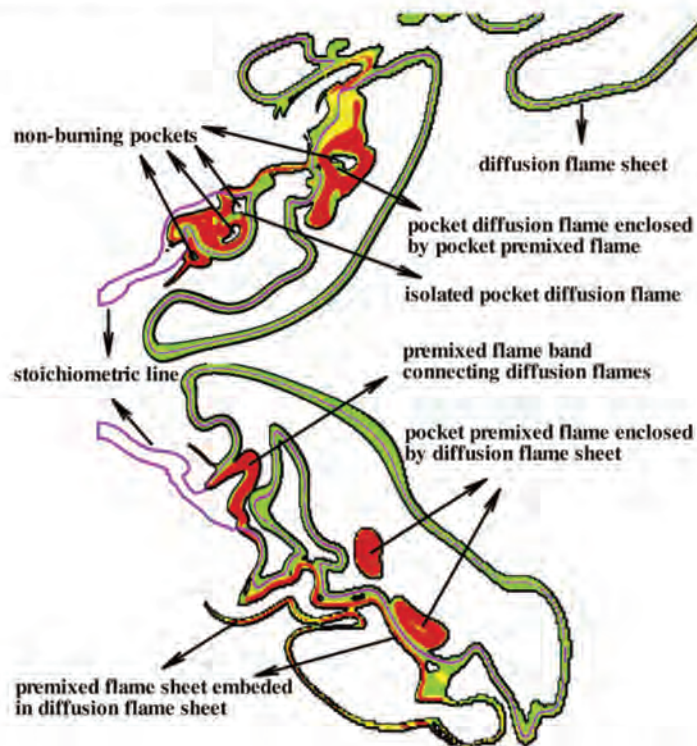


**Fig. 2.23.** Instantaneous turbulent spray flame structure (from [75]). Purple: stoichiometric mixture fraction iso-line; green: diffusion flames; red: premixed flames.

- **Hybrid combustion:** this structure is a combination of the two previous ones (Fig. 2.22(d)). Premixed flame fronts burn (in a group combustion structure) one part of the injected fuel which can not be burnt in a diffusion mode because of the too high equivalence ratios. Diffusion flames are only capable to burn remaining fuel escaping from the premixed flames with the surrounding incoming air.

The first 3D reactive DNS-DPS performed corresponds to an Isotropic Homogeneous Turbulence (IHT) in cubic domains laden with droplets. Réveillon *et al.* [74] studied the impact of preferential segregation of droplets in an IHT on an incipient flame. The preferential segregation generates dense groups of droplets that produce a high concentration of fuel resulting in a significant reduction in the evaporation process by local saturation. The flame front propagating in the domain is twice disturbed, first by turbulence and then by the highly heterogeneous mixture made of drops and vapor of fuel. For the case of drops with a small initial Stokes number, combustion is rather premixed. In contrast, for the case of large initial Stokes numbers, the combustion is partially premixed.

Since then, only few 3D DNS-DPS of reactive sprays in more complex configurations have been performed. Luo *et al.* [75] studied a turbulent reactive spray in a swirl combustor that get closer to real industrial systems. The flame structure presented in Fig. 2.23 demonstrates the complexity of such flows: premixed and diffusion flames are strongly coupled. Note that one can identify the same group combustion regime as the one in Fig. 2.22(c). In their study, the authors showed that premixed flames contribute to more than 70 % of the total heat release, although the total volume occupied by these premixed flames is smaller than the one of the diffusion flames. Moreover, the authors demonstrated that these rich premixed zones are mandatory to stabilize the flame. Their conclusion concerns the importance to correctly model two-phase premixed and partially premixed combustion in such flows.

### LES-DPS approaches

Due to its affordability, the LES approach coupled with DPS (detailed in Sect. 4.1) is nowadays widely used to simulate a turbulent reacting spray in configurations close to industrial burners. However, the LES applied to turbulent reacting flows is still in an on-going academic development stage. Many issues related to this approach are still open questions intensively discussed in the current literature.

To the complexity of the LES approach for gaseous reactive flows (subgrid scale models for the turbulence and the interaction between turbulence/combustion) are added the difficulties related to the liquid phase. On the one hand, the influence of droplets on the unresolved turbulent flow must be modeled, and on the other hand combustion models should be adapted to take into account the presence of the droplets. Indeed, these droplets lead to high heterogeneities of the reactive mixture and to a modification of the flame structure at resolved and unresolved scales.

#### Models for the interaction of the spray with turbulence.

The turbulence plays a key role in the dispersion of the spray. In a LES, only large turbulent scales are solved, whereas the impact of smaller ones on the flow is modeled with subgrid scale models. If the unresolved turbulence has an impact on the dispersion of the spray, it is mandatory to introduce a model taking into account the interaction between the subgrid turbulence and the spray. However, all droplets are not influenced the same way when facing velocity fluctuations: Fede *et al.* [76] performed a DNS-DPS of a turbulent cloud of droplets and filtered the solution at a length scale close to the usual LES ones. Results showed that the droplet dispersion was weakly dependent on the sub-grid scale velocity in this case. Indeed, droplet dispersion mainly results from large turbulent scales that are solved in LES. On the contrary, three types of interactions between droplets and local turbulence have been identified and characterized through a subgrid Stokes number  $St_\Delta$ :

- $St_\Delta > 5$ : there is no interaction between subgrid scale turbulence and the spray, the preferential segregation is not affected by the LES filtering.
- $0.5 < St_\Delta < 5$ : the subgrid scale turbulence has an influence on the spray leading to a random dispersion.
- $St_\Delta < 0.5$ : the subgrid scale turbulence generates a high preferential segregation. The model must predict the heterogeneities of the mixture resulting from the preferential segregation of the droplets.

For  $St_\Delta > 0.5$ , subgrid scale turbulence may be modeled through a Lagrangian stochastic approach. For example, Pozorski *et al.* [77] proposed to reconstruct the sub-grid scale fluctuations of the trajectory of a particle using the stochastic model of Langevin. Jones *et al.* [78, 79] introduced in their drag model a variable taking into account the inertial behaviors of the droplets. For  $St_\Delta < 0.5$ , more complex stochastic models are necessary [80].

### Two-phase turbulent combustion models

Several combustion models, initially derived in the context of purely gaseous flows, have been applied with or without modifications to LES of turbulent spray flames. The main LES-DPS formalisms taking into account the liquid phase in turbulent combustion models are described in the following.

#### Statistical PDF method

The LES filtering of the flow introduces a loss of statistical information concerning the local fluctuations of the velocity, the mixture and the temperature. However, this statistical information may be re-introduced defining a filtered density probability function (PDF)  $\hat{P}(\Phi)$  on the species mass fractions and temperature space  $\Phi = (Y_1, Y_2, \dots, Y_N, T)$  where  $N$  is the number of species [81]. Knowing this PDF, the local filtered reaction rate is estimated:

$$\tilde{\omega} = \int \dot{\omega}(\Phi) \hat{P}(\Phi) d\Phi, \quad (2.17)$$

where  $\dot{\omega}(\Phi)$  is the reaction rate obtained from any chemical kinetics. For a purely gaseous case, this PDF verifies the following transport equation:

$$\begin{aligned} \frac{\partial \bar{\rho} \hat{P}(\Phi)}{\partial t} + \frac{\partial}{\partial x_j} [\bar{\rho} \hat{u}_j \hat{P}(\Phi)] + \sum_{k=1}^N \frac{\partial}{\partial \Phi_k} \left[ \frac{1}{\rho} \dot{\omega}(\Phi) \bar{\rho} \hat{P}(\Phi) \right] \\ = - \frac{\partial}{\partial x_j} \left[ \langle u_j'' | \Phi \rangle \bar{\rho} \hat{P}(\Phi) \right] \\ + \sum_{k=1}^N \frac{\partial}{\partial \Phi_k} \left( \left\langle \frac{1}{\rho} \frac{\partial J_{i,k}}{\partial x_i} | \Phi \right\rangle \bar{\rho} \hat{P}(\Phi) \right), \end{aligned} \quad (2.18)$$

where  $J_{i,k}$  is the molecular diffusion flux. While the three left hand-side terms are closed, the right hand-side terms need to be modeled. The first term corresponds to the variation of the PDF by turbulent transport, and the second one characterizes the molecular mixture in the species mass fractions space. The application of these PDF approaches to a turbulent spray flame requires some adaptations since evaporation modifies the composition and the local temperature. The influence of the spray results in an additional source term in the transport equation of the PDF, which is closed in the same way as the reaction source term, by the droplet evaporation model.

#### Statistical CMC method

An alternative method to PDF approaches consists in filtering the species transport equations conditionally on a conservative variable, (for example the mixture fraction) taking advantage of the fact that these two variables are strongly correlated. This Conditional Moment Closure (CMC) approach has been first proposed by Klimenko and Bilger [82], then adapted to sprays by Mortensen and Bilger [83], and finally extended to LES by Navarro-Martinez *et al.* [84].

These turbulent combustion statistical models are relatively expensive to implement but provide good overall results. However, many questions remain opened about these methods, which still require further developments to be applied in an industrial context.

#### Thickened flame method

This turbulent combustion model explicitly solves the gaseous premixed flame structure on meshes much coarser than ones used in DNS [26] (the thickened flame model will be described in detail in Sect. 3.2.3). To thicken the flame, thermal and molecular diffusivities are multiplied by the thickening factor  $F$  whereas the species reaction rates  $\dot{\omega}_k$  are divided by  $F$ : the flame is  $F$  times thicker but its laminar propagation speed is preserved.

When a droplet passes through a thickened flame, its governing equations must be corrected to maintain the same physical characteristics as the ones of an unthickened flame. A correction applied to an Eulerian liquid phase was first proposed by Boileau *et al.* [85], then extended to DPS by Senoner *et al.* [86] and finally validated by Paulhiac [87].

#### Heterogeneous combustion modeling

Droplets crossing the flame front may enter in a heterogeneous burning regime. The presence of local reactive phenomena surrounding the droplet are taken into account using a macroscopic model applied to the droplet. This model takes into account the different states that an isolated burning droplet could have. Huang and Chiu [88, 89] proposed a multi-state model based on a DNS database of an isolated droplet burning in a laminar flow. They defined several criteria triggering the transition from one state to another, to recover the evaporation/consumption rate of the droplet as a function of the surrounding conditions. Three states are possible for the droplet: pure evaporation, envelop flame and wake flame. Wang *et al.* [90] developed a similar approach defining a droplet ignition criteria as a function of the local thermodynamic conditions. They applied the model to a LES-DPS of a methane spray injected in a turbulent reactive flow and they observed a better accuracy of their results compared to experimental data. However, the simplicity of their model does not make it possible to take into account

phenomena such as the extinction of the droplets. Finally, the model has been extended by De *et al.* [91] to take into account envelop flames for the droplets in LES-DPS. In addition to the ignition criteria, the authors introduced a simplified extinction criteria initially proposed by Bilger [92]. This model has finally been validated by Paulhiac [87].

## **2.6 PhD thesis objectives and manuscript outline**

### **2.6.1 Development of the AVBP code**

In partnership with IFP-Energies Nouvelles, CERFACS has been developing the AVBP code [93] for more than 30 years. This code solves the turbulent compressible Navier-Stokes equations on unstructured hybrid meshes and for massively parallel applications. Many turbulent combustion numerical studies using AVBP have already been the subject of publications, demonstrating in particular the high scalability of the code on massively parallel computers. To improve the accuracy and the fidelity of the code, AVBP is subject to a continuous development.

### **2.6.2 PhD thesis objectives**

This thesis has been funded by the French company Safran Helicopter Engines, world leader in the helicopter engine market. The main objectives of this thesis derive from the previously stated turbulent two-phase combustion modeling strategy:

- To improve the accuracy and the genericity of the combustion modeling in the framework of the thickened flame model.
- To contribute to the understanding of the mechanisms related to turbulent combustion, and to propose a LES modeling strategy to improve the fidelity of reactive simulations.
- To improve the understanding of the spray/flame interaction for the peculiar case of homogeneous spray flames where the dispersed phase has a relative velocity compared to the carrier phase.
- To participate in the understanding of the mechanisms related to turbulent spray flames using the LES-DPS approach, and to propose new LES modeling approaches to improve the fidelity of the reactive spray simulations in complex geometries.

### **2.6.3 Manuscript outline**

The manuscript is organized as follows:

- **Part II:** all the equations and models used in this thesis are detailed. Chapter 3 focuses on the turbulent reacting gaseous flow equations and models, whereas chapter 4 details the Lagrangian evaporating spray equations and models as well as the coupling between the liquid and the gaseous phases.
- **Part III** is dedicated to the modeling of turbulent combustion. In Chapter 5 an analysis of the mechanisms related to turbulent combustion in the VOLVO burner is provided. A LES modeling strategy is also discussed to improve the fidelity of such reactive simulations.
- **Part IV** presents the work done on gaseous and two-phase combustion. Chapter 6 presents a generic and self-adapting method for front detection and flame thickening whereas Chapter 7 is a numerical study about the impact of liquid relative velocity on both, the laminar spray flame speed and structure. Chapter 8 consists in a numerical study of a 3D turbulent spray flame experimentally characterized in the HERON burner.

# **II Two-phase flow turbulent combustion equations and models**

<b>3</b>	<b>Turbulent reacting gaseous flow equations and models .....</b>	<b>37</b>
3.1	Conservation equations for reacting flows	
3.2	LES filtering, equations and models	
<b>4</b>	<b>Evaporating spray equations, models .....</b>	<b>57</b>
4.1	Lagrangian deterministic approach	
4.2	Macroscopic models for an isolated droplet	



# Turbulent reacting gaseous flow equations and models

This chapter introduces the equations describing turbulent reacting gaseous flows relying on classical approaches used in the literature. Firstly, basic concepts of turbulent non-reacting and reacting flows are addressed. Then the LES equations and models are described. Finally, the LES closure models used in this work are presented. Two-phase flow equations and models are then described in Chapter 4.

## 3.1 Conservation equations for reacting flows

### 3.1.1 Basic concepts of turbulence and combustion

A flow is called turbulent when all its local properties fluctuate significantly with time and space randomly. Such flows occur when inertial forces at the origin of the movement of the fluid are intense compared to viscous ones. On the contrary, a laminar flow is stable and the trajectories of all its elementary fluid volumes are parallel. In a turbulent flow, any property  $f$  is usually split into mean ( $\bar{f}$ ) and fluctuating ( $f'$ ) contributions.

$$f = \bar{f} + f'. \quad (3.1)$$

In such a regime, velocity fluctuations may deviate by tens of percent from their mean velocity value. Turbulent fluctuations are associated to eddies with different spatial scales ranging from the largest, the integral scale  $l_i$ , to the smallest one, the Kolmogorov length scale  $\eta_k$ . Interactions between these scales come from a tri-dimensional complex process. Richardson [94], then Kolmogorov [95] observed that, for a homogeneous isotropic turbulence, the eddies sizes decay with time in a particular way. The principle of this mechanism, called the energy cascade (or Kolmogorov cascade), is that in the inertial range the energy flux from one scale to another is constant along scales and is given by the dissipation  $\varepsilon$  of the kinetic energy  $k$  (Kolmogorov [95]):

$$\varepsilon = \frac{u'^2(r)}{r/u'(r)} = \frac{u'(r)^3}{r}, \quad (3.2)$$

where  $u'(r)$  is the characteristic velocity of the vortices of size  $r$ .

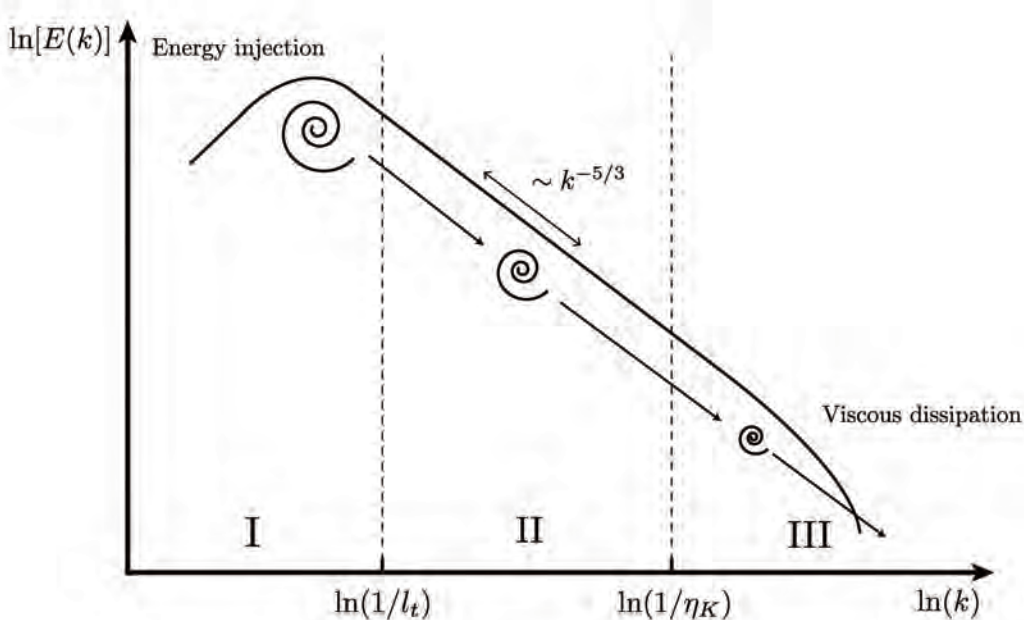


**Fig. 3.1.** Turbulent energy spectrum diagram ( $E(k)$ ). Three zones are observed in the Kolmogorov cascade (I,II,III). Zone I contains the major part of the energy, zone II is the inertial range and zone III is the dissipation range.

The Kolmogorov cascade is illustrated in Fig. 3.1: the length scale of the largest eddies ( $l_t$ ) is generally close to the characteristic length scale of the flow (for example the duct diameter for a duct flow). These eddies are subject to viscous effects making them become unstable. As a result, they progressively dislocate into smaller vortices. This phenomenon is repeated to a scale where viscous effects are predominant. When the vortices become comparable in size to the Kolmogorov scale ( $\eta_k$ ), they are no longer powerful enough and their kinetic energy is dissipated in heat. A Reynolds number  $Re(r)$  is introduced for each turbulent scale to characterize this mechanism:

$$Re(r) = \frac{u'(r)r}{\nu}, \quad (3.3)$$

where  $\nu$  is the flow kinematic viscosity. The Reynolds number represents the ratio of inertia (destabilizing) to viscous (stabilizing) forces. The largest scales in a turbulent flow are mainly controlled by inertia and are not affected by viscous dissipation. On the other hand, the Kolmogorov scale is characterized by a Reynolds number  $Re(\eta_k) \approx 1$  where kinetic energy is dissipated by viscous forces. Using Eq. 3.2 and Eq. 3.3, the Kolmogorov scale is written :

$$\eta_k = (\nu^3 / \epsilon)^{1/4}. \quad (3.4)$$

According to the Kolmogorov cascade theory, the energy density spectrum  $E(K)$  is a function of the wave number  $K$ , proportional to the inverse of a vortex characteristic diameter. For a stationary homogeneous isotropic turbulence, a zone called inertial range is characterized by a slope of  $K \sim -5/3$ . This inertial range can be observed in several turbulent configurations.

### 3.1.2 Generalities on combustion

Combustion can be split into two processes interacting together: the thermal process and the chemical process. Chemistry is highly exothermal but also highly temperature dependent and thus highly non-linear. Without thermal diffusion preheating the mixture upstream of the

### 3.1 Conservation equations for reacting flows

---

flame, chemical reactions cannot self-sustain. The chemical process is made of a succession of chemical reactions, involving chemical species: reactants and products. A chemical reaction is the exchange and/or rearrangement of atoms between colliding molecules. Reactants molecules are rearranged to become product molecules, with simultaneous release/absorption of heat. Two conditions facilitate the combustion process:

- The reactants should be mixed in optimal proportions.
- An additional energy source term should be added to ignite the mixture, i.e to make the collisions between molecules intense enough to enable the reaction process.

The Navier-Stokes equations apply for such multi-species multi-reaction gas but they require some additional terms.

#### Mixture

First, species are characterized through their mass fractions  $Y_k$  for  $k = 1$  to  $N$  where  $N$  is the total number of species in the reacting mixture [96], [18], [26]:

$$Y_k = m_k / m, \quad \sum_{k=1}^N Y_k = 1, \quad (3.5)$$

where  $m$  is the total mass of the mixture and  $m_k$  is the mass of species  $k$ .

Other usual quantities are also used to measure concentrations of species: the mole fraction  $X_k$  and the molar concentration  $[X_k]$ .

$X_k$  is defined as the ratio between the number of moles of species  $k$  in a volume  $V$ , and the total number of moles in the same volume:

$$X_k = Y_k W / W_k, \quad \sum_{k=1}^N X_k = 1, \quad (3.6)$$

where  $W_k$  is the atomic weight of species  $k$ , and  $W$  is the mean molecular weight of the mixture given by:

$$\frac{1}{W} = \sum_{k=1}^N \frac{Y_k}{W_k}. \quad (3.7)$$

$[X_k]$  is the number of moles of species  $k$  per unit volume:

$$[X_k] = \rho \frac{Y_k}{W_k} = \rho \frac{X_k}{W}, \quad (3.8)$$

where  $\rho$  is the mixture density.  $[X_k]$  is the quantity used to evaluate kinetic rates of chemical reactions (see Eq. 3.21).

The enthalpy of the mixture may be characterized through several variables:

- The sensible enthalpy  $h_{s,k}$  corresponding to the variation of enthalpy at constant pressure between two temperatures  $T$  and  $T_0$ :

$$h_{s,k} = \int_{T_0}^T C_p^k dT, \quad (3.9)$$

where  $C_p^k$  is the heat capacity of species  $k$ , and  $T_0 = 298.15K$  the reference temperature.

- The addition of the sensible and chemical enthalpies, taking into account the production/consumption of enthalpy needed to create/consume the chemical species:

$$h_k = h_{s,k} + \Delta h_{f,k}^0. \quad (3.10)$$

### Molecular transport of species and heat

Molecular and heat diffusion occur in mixtures where the concentrations of species and temperature are non-uniform. The heat diffusion is characterized by the heat diffusivity coefficient  $D_{th}$ , estimated with the thermal conductivity  $\lambda$ :

$$D_{th} = \frac{\lambda}{\rho C_p}, \quad (3.11)$$

where  $C_p$  is the heat capacity of the mixture:  $C_p = \sum_{k=1}^N C_{pk} Y_k$ . The molecular transport of species  $k$  is also characterized by a diffusion coefficient  $D_k$ , relying on binary molecular diffusion coefficients  $D_{j,k}$  between species  $k$  and each other species  $j$  [97]:

$$D_k = \frac{1 - Y_k}{\sum_{j \neq k} (X_j D_{j,k})}. \quad (3.12)$$

From these two transport coefficients, three dimensionless numbers may be defined:

- The Lewis number  $Le_k$  of species  $k$  comparing the heat diffusivity to the molecular diffusivity:

$$Le_k = \frac{\lambda}{\rho C_p D_k} = \frac{D_{th}}{D_k}. \quad (3.13)$$

- The Prandtl number  $Pr$  comparing the momentum diffusivity to the heat diffusivity:

$$Pr = \frac{\mu}{\lambda / (\rho C_p)} = \frac{\nu C_p}{\lambda}. \quad (3.14)$$

- The Schmidt number  $Sc_k$  comparing the momentum diffusivity to the heat diffusivity:

$$Sc_k = \frac{\mu}{\rho D_k} = Pr Le_k, \quad (3.15)$$

where  $\mu = \rho \nu$  is the dynamic viscosity. Assuming that the dynamic viscosity is independent of the gas composition and close to that of air,  $\mu$  is usually computed either with the Sutherland or Power law [98]:

$$\text{Sutherland law: } \mu = \mu_{0,R} \frac{T^{3/2}}{T + c_2} \frac{T_{ref} + c_2}{T_{ref}^{3/2}}, \quad (3.16)$$

$$\text{Power law: } \mu = \mu_{0,R} \left( \frac{T}{T_{ref}} \right)^b, \quad (3.17)$$

where  $T_{ref}$  and  $\mu_{0,R}$  are the reference temperature and viscosity of the mixture,  $b$  is the power law coefficient ranging between 0.5 and 1.0, and  $c_2$  is a constant equal to 110.4K. All these parameters depend on the mixture.

Note that the  $D_{j,k}$  coefficients in Eq. 3.12 are complex functions of collision integrals and thermodynamic variables. For a DNS code using complex chemistry, using Eq 3.12 makes sense. However, most CFD codes using simplified chemical schemes approximate  $D_k$  assuming that the Schmidt numbers  $Sc_k$  are constant.

### Chemical kinetics

During the combustion process, reactants are converted into products as long as the energy supplied is sufficient to activate the reaction. The conversion process follows a chemical mechanism. Usually, a chemical mechanism is a set of  $N_{reac}$  reactions involving  $N$  species  $M_k$ :

$$\sum_{k=1}^N v'_{k,j} M_k = \sum_{k=1}^N v''_{k,j} M_k, \quad \text{for } j = 1, N_{reac}, \quad (3.18)$$

### 3.1 Conservation equations for reacting flows

---

where  $M_k$  is the symbol for species  $k$ ,  $v'_{k,j}$  and  $v''_{k,j}$  are the molar stoichiometric coefficients of species  $k$  in reaction  $j$  such that the mass is conserved:

$$\sum_{k=1}^N v'_{k,j} W_k = \sum_{k=1}^N v''_{k,j} W_k \quad \text{or} \quad \sum_{k=1}^N v_{kj} W_k = 0, \quad (3.19)$$

where  $v_{kj} = v''_{kj} - v'_{kj}$ .

For species  $k$ , the mass reaction rate  $\dot{\omega}_k$  is the sum of rates  $\dot{\omega}_{kj}$  produced by the  $N_{reac}$  reactions:

$$\dot{\omega}_k = \sum_{j=1}^{N_{reac}} \dot{\omega}_{kj} = W_k \sum_{j=1}^{N_{reac}} v_{kj} Q_j, \quad \text{with } \frac{\dot{\omega}_{kj}}{W_k v_{kj}} = Q_j, \quad (3.20)$$

where  $Q_j$  is the progress rate of reaction  $j$ :

$$Q_j = K_{fj} \prod_{k=1}^N [X_k]^{n'_{kj}} - K_{rj} \prod_{k=1}^N [X_k]^{n''_{kj}}, \quad (3.21)$$

where  $n'_{kj}$  and  $n''_{kj}$  are the forward and reverse orders of species  $k$  for the reaction  $j$ , and  $K_{fj}$  and  $K_{rj}$  are the forward and reverse rates of reaction  $j$ . Note that the progress rate  $Q_j$  is proportional to the molecular density of each of the reactant.

The reaction rates are usually modeled with the Arrhenius empirical law, describing the rate at which reactions occur as a function of the temperature and the mixture:

$$K_{fj} = A_{fj} T^{\beta_j} \exp\left(-\frac{E_j}{RT}\right) = A_{fj} T^{\beta_j} \exp\left(-\frac{T_{aj}}{T}\right), \quad (3.22)$$

where  $A_{fj}$  is the pre-exponential constant,  $\beta_j$  is the temperature exponent, and  $T_{aj}$  is the activation temperature (or equivalently the activation energy  $E_j = RT_{aj}$ ) at which the chemical reactions start to self-sustain. The reverse reaction rate is linked to the forward one by the equilibrium constant  $K_{eq,j}$ :

$$K_{rj} = \frac{K_{fj}}{K_{eq,j}}. \quad (3.23)$$

The equilibrium constant  $K_{eq,j}$  is defined [96] by:

$$K_{eq,j} = \left(\frac{p_0}{RT}\right)^{\sum_{k=1}^N v_{kj}} \exp\left(\frac{\Delta S_j^0}{R} - \frac{\Delta H_j^0}{RT}\right), \quad (3.24)$$

where  $p_0 = 1$  bar.  $\Delta H_j^0$  and  $\Delta S_j^0$  are respectively the variations of enthalpy (sensible + chemical) and entropy occurring when passing from reactants to products in the  $j^{th}$  reaction:

$$\Delta H_j^0 = h(T) - h(0) = \sum_{k=1}^N v_{kj} W_k (h_{s,k}(T) + \Delta h_{f,k}^0), \quad (3.25)$$

$$\Delta S_j^0 = \sum_{k=1}^N v_{kj} W_k s_k(T), \quad (3.26)$$

where  $s_k$  is the entropy of species  $k$ . Note that  $\Delta H_j^0$  and  $\Delta S_j^0$  are obtained from tabulations. Note also that for a single-step global reaction the forward and reverse orders  $n'_{kj}$  and  $n''_{kj}$  in Eq. 3.21 are different from the stoichiometric coefficients  $v'_{kj}$ ,  $v''_{kj}$ . These orders are set so as to recover the correct laminar flame speed over the whole range of equivalence ratios in between the flammability limits [99].

In a simplified form, combustion can be represented by a single irreversible reaction involving a fuel and an oxidizer. Indeed the knowledge of a detailed chemical mechanism is not essential to estimate only the global impact of a flame. The global effects of the combustion on the gas flow will be taken into account if the reaction rate resulting from the simplified scheme captures the basic properties of the real flames [56]:

- The heat released by combustion. An accurate prediction of the heat release is important to take into account the gas dilatation in the flow motion and to determine the correct burnt gas temperature.
- The flame velocity. A correct flame velocity prediction is essential to capture the burning rate corresponding to the local equivalence ratio.
- The flame thickness. The flame thickness allows to estimate the scale of the vortices able to cross the flame front and thus responsible for the flame wrinkling.
- The flame response to stretch. An accurate prediction of the flame response to stretch is important to establish local extinction because of the local dissipation rate.
- The ignition delay. The ignition delay controls for instance the lift-off height between the injector and the flame.

Note that the burnt gas temperature is controlled by thermochemistry (i.e formation enthalpies  $\Delta h_{f,k}^0$ , heat capacities  $C_{p,k}$  and reactants species mass fractions) whereas the speed of combustion is controlled by chemical parameters (pre-exponential constant  $A_{fj}$ , activation energy  $T_{aj}$  and exponent  $\beta_j$ ).

### 3.1.3 Conservation equations for reacting flows

The Navier-Stokes equations for a multi-species reacting flow are derived from mass, momentum and energy balances [100].

**Conservation of mass:**

$$\frac{\partial \rho}{\partial t} + \frac{\partial \rho u_j}{\partial x_j} = 0, \quad (3.27)$$

Note that a repeated subscript  $j$  corresponds to a sum on this index (Einstein summation rule).

**Conservation of mass and species:**

Note that for a multi-species reacting flow, the mixture is composed by several chemical species which temporal evolutions are controlled by three physical phenomena : convection, diffusion and chemical kinetics. In order to describe the reacting mixture, each species must be transported individually. The number of transport equations that needs to be solved is multiplied by the number  $N$  of chemical species in the numerical simulation.

$$\frac{\partial \rho Y_k}{\partial t} + \frac{\partial}{\partial x_j} \rho (u_j + V_j^c) Y_k = \frac{\partial}{\partial x_j} (\rho D_k \frac{W_k}{W} \frac{\partial X_k}{\partial x_j}) + \dot{\omega}_k, \quad (3.28)$$

where:

-  $V_j^c = \sum_{k=1}^N D_k \frac{W_k}{W} \frac{\partial X_k}{\partial x_j}$  is the correction diffusion velocity ensuring the conservation of

global mass when all the species mass fraction transport equations Eq. 3.28 are summed. Indeed to ensure mass conservation, the equation  $\sum_{k=1}^N Y_k = 1$  is added to the  $N$  species transport equations. As a result, the system made of  $N$  independent equations is over determined. Any one of the  $N$  species equations or the mass conservation equation may be eliminated: this issue is not a difficulty when exact expressions for diffusion velocities are used. However, this is no longer the case when Hirschfelder's law is used:

the non-zero term  $\frac{\partial}{\partial x_i} \left( \rho \sum_{k=1}^N D_k \frac{W_k}{W} \frac{\partial X_k}{\partial x_i} \right)$  appears in the RHS of Eq. 3.28. To satisfy global mass conservation the correction velocity  $V^c$  is introduced.

### 3.1 Conservation equations for reacting flows

- $\dot{\omega}_k \propto Y_k \exp\left(\frac{-T_a}{T}\right)$  are the reaction rates of species  $k$ , following an Arrhenius Law.  $T_a$  is the activation temperature. As  $T_a$  is usually high, reaction rates are extremely sensitive to the temperature.

**Conservation of momentum:**

$$\frac{\partial \rho u_i}{\partial t} + \frac{\partial}{\partial x_j} (\rho u_i u_j) = - \frac{\partial}{\partial x_j} \left[ P \delta_{ij} - 2\mu \left( S_{ij} - \frac{1}{3} S_{kk} \delta_{ij} \right) \right] \quad (3.29)$$

where :

- $P$  is the static pressure.
- $\delta_{ij}$  is the Kronecker symbol:  $\delta_{ij} = 1$  if  $i = j$  and 0 otherwise.
- $S_{ij} = \frac{1}{2} \left( \frac{\partial u_i}{\partial x_j} + \frac{\partial u_j}{\partial x_i} \right)$  is the viscous strain rate tensor.
- $S_{kk} = \frac{\partial u_k}{\partial x_k}$  is the trace of the viscous strain rate tensor.

**Conservation of energy:**

$$\begin{aligned} \frac{\partial \rho E}{\partial t} + \frac{\partial}{\partial x_j} (\rho u_j E) &= - \frac{\partial}{\partial x_j} \left[ u_i P \delta_{ij} - 2u_i \mu \left( S_{ij} - \frac{1}{3} S_{kk} \delta_{ij} \right) \right] \\ &\quad + \frac{\partial}{\partial x_j} \left[ C_p \frac{\mu}{P_r} \frac{\partial T}{\partial x_j} \right] \\ &\quad + \frac{\partial}{\partial x_j} \left[ \sum_{k=1}^N \left( \frac{\mu}{S_{c,k}} \frac{W_k}{W} \frac{\partial X_k}{\partial x_j} - \rho Y_k V_j^c \right) h_{s,k} \right] \\ &\quad + \dot{Q} \\ &\quad + \dot{\omega}_T (Y_k, T), \end{aligned} \quad (3.30)$$

where:

- $E = \int_{T_0}^T C_v dT + \frac{1}{2} u_i u_i$  is the total energy corresponding to the addition of the internal and kinetic energies.
- $C_p \frac{\mu}{P_r} \frac{\partial T}{\partial x_i} = \lambda \frac{\partial T}{\partial x_i}$  is the heat diffusion flux expressed by Fourier's Law.
- $\dot{Q}$  is an external heat source term.  $\dot{Q}$  could be for example the energy provided to the system during a spark ignition scenario.
- $\dot{\omega}_T = - \sum_{k=1}^N \Delta h_{f,k}^0 \dot{\omega}_k$  is the heat release rate.

To close this set of equations, an equation of state is mandatory:

$$p = \sum_{k=1}^N p_k = \sum_{k=1}^N \rho_k R T / W_k, \quad (3.31)$$

where  $R = 8.314 \text{ J/(mole K)}$  is the perfect gas constant, and  $\rho_k = \rho Y_k$  is the density of species  $k$ . As the mixture density is defined through  $\rho = \sum_{k=1}^N \rho_k$ , the mixture equation of state is written :

$$p = \frac{\rho}{W} RT. \quad (3.32)$$

Assuming a calorically perfect gas the following relations are valid:

$$\gamma = \frac{C_p}{C_v}, \quad e = C_v T, \quad C_p - C_v = R. \quad (3.33)$$

To sum up, numerically solving the Navier-Stokes equations for reacting flows involves to compute many complex equations at high computational cost. This cost is all the more important that chemical species react together with a highly non-linear reacting rates.

Minimizing this computational cost while maintaining the accuracy of the numerical simulation is a real challenge that is at the origin of scientific innovations, such as the development of an intermediate approach to RANS and DNS: the Large Eddy Simulation (LES).

## 3.2 LES filtering, equations and models

### 3.2.1 LES filtering

The Large Eddy Simulation (LES) approach [6, 101] consists in computing the large turbulent scales of the flow whereas the effects of the smaller ones (typically structures that are smaller than the computational mesh size) are modeled using sub-grid closure terms. This method is based on Kolmogorov assumptions: the information coming from large vortices generated by geometrical singularities is progressively lost during the Kolmogorov cascade. Therefore, small vortices are not affected by geometry effects anymore: small structures have an isotropic behaviour, and could be isolated from the large anisotropic ones. The LES predictions of complex turbulent flows are henceforth closer to the physics since large scale phenomena are embedded in the set of governing equations [26]. The distinction between the resolved and modeled structures is done using a convolution product between an unfiltered scalar quantity  $f$  and a filter  $G_\Delta$  of characteristic size  $\Delta$ . The filtered quantity  $\bar{f}$  is defined as:

$$\bar{f}(x_i, t) = \int f(x'_i, t) G_\Delta(x_i - x'_i) dx'_i. \quad (3.34)$$

For variable density flows, a mass-weighted Favre filtering is introduced to avoid additional terms during the filtering process of the Navier-Stokes equations:

$$\tilde{f} = \frac{\bar{\rho} \bar{f}}{\bar{\rho}}. \quad (3.35)$$

The Favre filtering is done according to:

$$\bar{\rho} \tilde{f}(x_i, t) = \int \rho f(x'_i, t) G_{\bar{\Delta}}(x_i - x'_i) dx'_i. \quad (3.36)$$

While the filtered quantity  $\bar{f}$  is resolved in the numerical simulation, the unresolved quantity  $f' = f - \bar{f}$  (i.e the subgrid scale part due to the unresolved flow motions) is modeled. Finally, the large eddy simulation balance equations are obtained by filtering the instantaneous balance equations Eq. 3.27 to Eq. 3.30:

**Mass:**

$$\frac{\partial \bar{\rho}}{\partial t} + \frac{\partial \bar{\rho} \tilde{u}_j}{\partial x_j} = 0. \quad (3.37)$$

**Species:**

$$\frac{\partial \bar{\rho} \tilde{Y}_k}{\partial t} + \frac{\partial}{\partial x_j} \left( \bar{\rho} \tilde{Y}_k \tilde{u}_j \right) + \frac{\partial}{\partial x_j} \bar{\rho} \left( \tilde{u}_j \tilde{Y}_k - \tilde{u}_j \tilde{Y}_k \right) = - \frac{\partial}{\partial x_j} \left[ \bar{J}_{j,k} \right] + \bar{\omega}_k, \quad (3.38)$$

where  $\bar{J}_{j,k}$  is the diffusive species flux:

$$\bar{J}_{j,k} = - \left( \frac{\mu}{S_{c,k}} \frac{W_k}{W} \frac{\partial X_k}{\partial x_j} - Y_k V_j^c \right) \approx - \left( \frac{\bar{\mu}}{S_{c,k}} \frac{W_k}{W} \frac{\partial \tilde{X}_k}{\partial x_j} - \tilde{Y}_k \tilde{V}_j^c \right), \quad (3.39)$$

with  $\tilde{V}_j^c = \sum_{k=1}^N \frac{\bar{\mu}}{S_{c,k}} \frac{W_k}{W} \frac{\partial \tilde{X}_k}{\partial x_j}$ .

**Momentum:**

$$\frac{\partial \bar{\rho} \tilde{u}_i}{\partial t} + \frac{\partial}{\partial x_j} (\bar{\rho} \tilde{u}_i \tilde{u}_j) + \frac{\partial}{\partial x_j} \bar{\rho} (\tilde{u}_i \tilde{u}_j - \tilde{u}_i \tilde{u}_j) = - \frac{\partial \bar{P} \delta_{ij}}{\partial x_j} + \frac{\partial \bar{\tau}_{ij}}{\partial x_j}, \quad (3.40)$$

where  $\bar{\tau}_{ij}$  is the laminar filtered stress tensor:

$$\bar{\tau}_{ij} = \overline{2\mu \left( S_{ij} - \frac{1}{3} S_{kk} \delta_{ij} \right)} \approx 2\bar{\mu} \left( \tilde{S}_{ij} - \frac{1}{3} \tilde{S}_{kk} \delta_{ij} \right), \quad (3.41)$$

with  $\bar{\mu} \approx \mu(\tilde{T})$  and the strain rate of the resolved structures  $\tilde{S}_{ij} = \frac{1}{2} \left( \frac{\partial \tilde{u}_j}{\partial x_i} + \frac{\partial \tilde{u}_i}{\partial x_j} \right)$ .

**Energy:**

$$\frac{\partial \bar{\rho} \tilde{E}}{\partial t} + \frac{\partial}{\partial x_j} (\bar{\rho} \tilde{u}_j \tilde{E}) + \frac{\partial}{\partial x_j} \bar{\rho} (\tilde{u}_j \tilde{E} - \tilde{u}_j \tilde{E}) = - \frac{\partial}{\partial x_j} \left[ \bar{u}_i (P \delta_{ij} - \bar{\tau}_{ij}) + \bar{q}_j \right] + \bar{\omega}_T, \quad (3.42)$$

where  $\bar{q}_j$  is the heat flux:

$$\bar{q}_j = - \frac{\bar{C}_p \bar{\mu}}{P_r} \frac{\partial \bar{T}}{\partial x_j} + \sum_{k=1}^N \bar{J}_{j,k} \bar{h}_{s,k} \approx - \bar{C}_p \frac{\bar{\mu}}{P_r} \frac{\partial \bar{T}}{\partial x_j} + \sum_{k=1}^N \bar{J}_{j,k} \bar{h}_{s,k}. \quad (3.43)$$

These equations present sub-grid scale turbulent terms that need to be modeled:

- **Unresolved Reynolds stress tensor:**  $\bar{\tau}_{ij}^t = \bar{\rho} (\tilde{u}_i \tilde{u}_j - \bar{u}_i \bar{u}_j)$ . The sub-grid scale terms in the filtered Navier-Stokes equations describe the influence of unresolved small scales on the resolved motion of the flow. According to the Boussinesq [102] hypothesis, this influence is taken into account by sub-grid scale models based on the introduction of a turbulent viscosity  $\nu^t$ . In other words, the effect of the sub-grid scale field on the resolved field is assumed to be purely dissipative. Note that this assumption is mainly valid within the Kolmogorov [103] turbulent cascade. The unresolved Reynolds stress tensor is thus written as:

$$\bar{\tau}_{ij}^t = -2\bar{\rho}\nu^t \left( \tilde{S}_{ij} - \frac{1}{3} \tilde{S}_{kk} \delta_{ij} \right). \quad (3.44)$$

To close this equation, a turbulent viscosity must be specified. Three eddy viscosity models (among a large variety of models available in the literature [104]) are presented in the following.

#### Smagorinsky model

The Smagorinsky turbulent viscosity is written as:

$$\nu^t = (C_S \Delta)^2 \sqrt{2\tilde{S}_{ij}\tilde{S}_{ij}}, \quad (3.45)$$

where  $C_S$  is a constant of the model. Usually  $C_S = 0.18$ , but it can vary between 0.1 and 0.18 depending on the configuration of the flow. Despite an accurate prediction of dissipation for a homogeneous isotropic turbulence case, this model over-predicts the turbulent viscosity as soon as the flow becomes anisotropic (i.e. close to solid boundaries and mixing layers).

#### Sigma model

The Sigma turbulent viscosity [105] is written as:

$$\nu^t = (C_\sigma \Delta)^2 \frac{\sigma_3 (\sigma_1 - \sigma_2) (\sigma_2 - \sigma_3)}{\sigma_1^2}, \quad (3.46)$$

where  $C_\sigma = 1.5$  is the constant of the model.  $\sigma_1 \geq \sigma_2 \geq \sigma_3 \geq 0$  are the singular values of the resolved velocity gradient tensor. The  $\sigma$ -model was developed to overcome some drawbacks observed on most of the static models without using additional test filter. Indeed, it presents the interesting properties to vanish in various laminar flow configurations (i.e. pure shear, pure rotation, pure dilatation/contraction,...) for which no sub-grid scale activity is expected. It also shares with the WALE model [106] the property to vanish with the proper asymptotic behaviour near solid boundaries.

**WALE model**

The WALE (Wall Adapting Linear Eddy) [106] turbulent viscosity is written as:

$$\nu_t = (C_W \Delta)^2 \frac{(S_{ij}^d S_{ij}^d)^{3/2}}{(\tilde{S}_{ij} \tilde{S}_{ij})^{5/2} + (S_{ij}^d S_{ij}^d)^{5/4}}, \quad (3.47)$$

where  $C_W = 0.4929$  is a constant of the model.  $S_{ij}^d$  is the traceless symmetric part of the square of the gradient velocity tensor:

$$S_{ij}^d = \frac{1}{2} \left[ \left( \frac{\partial \tilde{u}_i}{\partial x_j} \right)^2 + \left( \frac{\partial \tilde{u}_j}{\partial x_i} \right)^2 \right] - \frac{1}{3} \left( \frac{\partial \tilde{u}_k}{\partial x_k} \right)^2 \delta_{ij}. \quad (3.48)$$

The WALE model [106] was developed for wall bounded flows in an attempt to recover the scaling laws of the wall. As for the Sigma model, it presents the interesting properties to vanish in flow configurations such as pure shear.

The WALE eddy viscosity model is chosen to treat the turbulent configurations presented in this manuscript.

- **Unresolved Species fluxes:**  $\bar{J}_{j,k}^t = \bar{\rho} (\widetilde{u_i Y_k} - \widetilde{u_i} \widetilde{Y_k})$ . The turbulent species transport is modeled using a turbulent Schmidt  $S_c^t$  number such as:

$$D_k^t = \frac{\nu_t}{S_c^t}, \quad (3.49)$$

$$\bar{J}_{j,k}^t = \bar{\rho} (\widetilde{u_i Y_k} - \widetilde{u_i} \widetilde{Y_k}) \approx - \left( \frac{\nu_t}{S_c^t} \frac{W_k}{W} \frac{\partial \widetilde{X}_k}{\partial x_i} - \widetilde{Y_k} \widetilde{V}_j^{c,t} \right). \quad (3.50)$$

The correction diffusion velocities are written as:

$$\widetilde{V}_j^c + \widetilde{V}_j^{c,t} = \sum_{k=1}^N \left( \frac{\bar{\mu}}{\bar{\rho} S_{c,k}} + \frac{\mu_t}{\bar{\rho} S_{c,k}^t} \right) \frac{W_k}{W} \frac{\partial \widetilde{X}_k}{\partial x_j}. \quad (3.51)$$

The typical turbulent Schmidt value is  $S_c^t = 0.6$ .

- **Unresolved energy fluxes:**  $\bar{q}_{j,k}^t \bar{\rho} (\widetilde{u_i E} - \widetilde{u_i} \widetilde{E})$ . The turbulent heat transport is modeled with a turbulent Prandtl  $P_r^t$  number such that:

$$\lambda_t = \frac{\mu^t \bar{C}_p}{P_r^t}, \quad (3.52)$$

$$\bar{q}_{j,k}^t \bar{\rho} (\widetilde{u_i E} - \widetilde{u_i} \widetilde{E}) \approx - \frac{\bar{C}_p \mu_t}{P_r^t} \frac{\partial \widetilde{T}}{\partial x_j} + \sum_{k=1}^N \bar{J}_{j,k}^t \widetilde{h}_{s,k}. \quad (3.53)$$

The typical turbulent Prandtl value is  $P_r^t = 0.6$ .

Finally, the filtered instantaneous balance equations are written as:

**Mass**

$$\frac{\partial \bar{\rho}}{\partial t} + \frac{\partial \bar{\rho} \widetilde{u}_j}{\partial x_j} = 0, \quad (3.54)$$

**Momentum**

$$\frac{\partial \bar{\rho} \widetilde{u}_i}{\partial t} + \frac{\partial}{\partial x_j} (\bar{\rho} \widetilde{u}_i \widetilde{u}_j) = - \frac{\partial}{\partial x_j} \left[ \bar{P} \delta_{ij} - 2 (\bar{\mu} + \mu_t) \left( \bar{s}_{ij} - \frac{1}{3} \bar{s}_{kk} \delta_{ij} \right) \right], \quad (3.55)$$

**Species**

$$\frac{\partial \bar{\rho} \tilde{Y}_k}{\partial t} + \frac{\partial}{\partial x_j} (\bar{\rho} \tilde{u}_j \tilde{Y}_k) = \frac{\partial}{\partial x_j} \left[ \left( \frac{\bar{\mu}}{S_{c,k}} + \frac{\mu_t}{S_{c,k}^t} \right) \frac{W_k \partial \tilde{X}_k}{W \partial x_j} - \bar{\rho} \tilde{Y}_k (\tilde{V}_j^c + \tilde{V}_j^{c,t}) \right] + \dot{\omega}_k (\tilde{Y}_k, \tilde{T}), \quad (3.56)$$

**Energy**

$$\begin{aligned} \frac{\partial \bar{\rho} \tilde{E}}{\partial t} + \frac{\partial}{\partial x_j} (\bar{\rho} \tilde{u}_j \tilde{E}) &= - \frac{\partial}{\partial x_j} \left[ \tilde{u}_i \bar{P} \delta_{ij} - 2 \tilde{u}_i \bar{\mu} \left( \tilde{S}_{ij} - \frac{1}{3} \tilde{S}_{kk} \delta_{ij} \right) \right] \\ &\quad + \frac{\partial}{\partial x_j} \left[ \bar{C}_p \left( \frac{\bar{\mu}}{P_r} + \frac{\mu_t}{P_r^t} \right) \frac{\partial \tilde{T}}{\partial x_j} \right] \\ &\quad + \frac{\partial}{\partial x_j} \left[ \sum_{k=1}^N \left( \left[ \frac{\bar{\mu}}{S_{c,k}} + \frac{\mu_t}{S_{c,k}^t} \right] \frac{W_k \partial \tilde{X}_k}{W \partial x_j} - \bar{\rho} \tilde{Y}_k (\tilde{V}_j^c + \tilde{V}_j^{c,t}) \right) \tilde{h}_{s,k} \right] \\ &\quad + \dot{\omega}_T (\tilde{Y}_k, \tilde{T}) \\ &\quad + \bar{Q}. \end{aligned} \quad (3.57)$$

### 3.2.2 Chemistry modeling in LES

Several modeling strategies, mainly differentiable by their CPU costs, are available for LES. Detailed chemical kinetics involve numerous intermediate species and reactions to accurately describe the chemical reaction paths. For large hydrocarbons chains, the number of species and reactions is such that the detailed chemistry can only be used in simple canonic configurations such as auto-ignition, premixed and diffusion planar flames. For instance, the detailed mechanism for kerosene/air proposed by Dagaut and Cathonnet [107] is composed of 209 species and 1673 reactions. The cost of such mechanisms is not only linked to the number of transport equations that need to be solved, but also to the high space and temporal discretization required to capture the stiff profiles of intermediate species and radicals.

With a lower but still high CPU costs skeletal schemes are derived from detailed mechanisms by removing species and corresponding reactions which have a weak influence on the phenomena of interest. For example from the Dagaut and Cathonnet detailed mechanism, Luche *et al.* [108] have proposed a skeletal scheme comprising 91 species and 680 reactions to compute kerosene/air flames.

Another type of mechanisms exists to keep the accuracy of the chemical description without using skeletal or detailed schemes which are too expensive in the context of LES: Analytically Reduced Chemistry (ARC) [109, 110, 111]. Based on skeletal schemes, analytical mechanisms use the quasi-steady state approximation (QSS) for some species and a partial equilibrium assumption for some reactions. When the creation rate of a given species  $k$  is slow compared to its destruction rate, the concentration produced is quasi-instantaneously consumed. This species can then be assumed in a quasi-steady state and its net rate may be considered as equal to zero:  $\dot{\omega}_k \approx 0$ . Using Eq. 3.20, this leads to a relation between the involved species concentrations:

$$\dot{\omega}_k = W_k \sum_{j=1}^{N_{\text{reac}}} v_{kj} \left[ K_{fj} \prod_{k=1}^N [X_k]^{n'_{k,j}} - K_{rj} \prod_{k=1}^N [X_k]^{n''_{k,j}} \right] = 0. \quad (3.58)$$

The concentration of species  $k$  is then computed from Eq. 3.58 and no longer from its conservation equation, reducing the size of the system of equations. This system may be further simplified using the partial equilibrium hypothesis for a given reaction  $j$ . This simplification can be assumed whenever both the forward and the backward components of reaction  $j$  are fast compared to all other reactions. The reaction  $j$  is then in a partial equilibrium condition:

$$Q_j = K_{fj} \prod_{k=1}^N [X_k]^{n'_{k,j}} - K_{rj} \prod_{k=1}^N [X_k]^{n''_{k,j}} = 0. \quad (3.59)$$

In a more simplified form, combustion can also be described with global chemical schemes including a limited number of species (around 6) and reactions (usually 2 to 4) [112, 113]. The global reactions are calibrated at a given operating conditions to reproduce the main properties of the flame such as the laminar flame speed and the burnt gas state. Their affordable costs have made the global chemical schemes the most widely used schemes in LES of industrial configurations.

Recently, the Virtual Optimized Mechanism has been introduced by Cailler *et al.* [114]. Unlike the previous methods, the idea of the optimization procedure is to build a chemical mechanism from scratch by evaluating a set of virtual species properties and reaction rate parameters to reproduce the temperature profile and laminar flame speed of reference premixed flames. The development of this method is still an on-going work.

An alternative method to lower CPU costs while taking into account detailed chemistry effects in LES is the tabulated chemistry. The chemical flame structure can be described in a reduced phase subspace from canonic configurations: the chemical subspace of a turbulent premixed flame is approximated from a collection of one-dimensional laminar flames. This collection of flames and the related thermo-chemical quantities are tabulated as a function of a single progress variable  $c$  which evolves monotonically between fresh and burnt gases. Since only the controlling variables are solved, the efficiency of the method depends on the number of variables defined as inputs of the table. Note that on massively parallel machines the table is duplicated on each core: a too high number of table inputs may lead to memory issues. Moreover for some cases, knowing *a priori* the combustion regime to construct the table with the adapted flame prototype may be a complicated task.

Both reduced and analytically reduced chemical schemes are chosen to treat the different configurations presented in this manuscript.

### 3.2.3 LES premixed turbulent combustion models

#### G-equation approach

In the G-equation formalism, the flame front is assimilated to a thin interface, convected by the unsteady flow field. This interface propagates toward the unburned region at a velocity  $S_T$  which depends on the local curvature and strain rate. To track the flame front, a field variable  $\tilde{G}$  is used, the flame surface being identified by a given iso-level  $\tilde{G} = G^*$ . The G-equation is written [115] as:

$$\frac{\partial \tilde{G}}{\partial t} + \frac{\partial \tilde{\rho} \tilde{u}_i \tilde{G}}{\partial x_i} = \rho_{fg} S_T \left| \frac{\partial \tilde{G}}{\partial x_i} \right|. \quad (3.60)$$

A model for the sub-grid scale turbulent flame speed  $S_T$  is needed. This closure is generally based on:

$$\frac{S_T}{S_L^0} = 1 + \alpha \left( \frac{u'_\Delta}{S_L^0} \right)^p, \quad (3.61)$$

where  $\rho_{fg}$  and  $S_L^0$  are respectively the fresh gas density and the laminar flame speed.  $\alpha$  and  $p$  are user-defined constants and  $u'_\Delta$  is the sub-grid scale turbulence level which may be estimated as:

$$u'_\Delta \approx \sqrt{|2\tilde{S}_{ij}\tilde{S}_{ij}|}. \quad (3.62)$$

#### F-TACLES approach

A commonly used approach to address fluid/chemistry interactions at a reduced computational cost consists in tabulating the chemistry as a function of a reduced set of variables [116]. Two classical methods have been developed for premixed flames: the Flamelet Generated Manifold (FGM) [117] and the Flame Prolongation of ILDM (FPI) [118]. Both techniques assume that the chemical flame structure can be described in a reduced phase subspace from canonic

### 3.2 LES filtering, equations and models

---

configurations: the chemical subspace of a turbulent premixed flame is approximated from a collection of one-dimensional laminar flames. This collection of flames and the related thermochemical quantities are tabulated as a function of a single progress variable  $c$  which evolves monotonically between fresh and burnt gases.  $c$  is transported according to the following filtered balance equation:

$$\frac{\partial \bar{p}\tilde{c}}{\partial t} + \frac{\partial \bar{p}\tilde{u}_i\tilde{c}}{\partial x_i} + \frac{\partial}{\partial x_i}(\bar{p}\tilde{u}_i\tilde{c} - \bar{p}\tilde{u}_i\tilde{c}) = \frac{\partial}{\partial x_i}\left(\bar{\rho}D\frac{\partial c}{\partial x_i}\right) + \bar{\omega}_c. \quad (3.63)$$

Equation 3.63 comprises resolved and unresolved terms. Indeed, the sub-grid scale transport term  $\nabla \cdot (\bar{p}\tilde{u}\tilde{c} - \bar{p}\tilde{u}\tilde{c})$ , the filtered laminar diffusion term  $\nabla \cdot (\bar{\rho}D\nabla c)$  and the filtered source term  $\bar{\omega}_c$  have to be modeled. The principle of the Filtered Tabulated Chemistry model is to tabulate the unresolved terms by filtering the one-dimensional laminar flames. These terms are tabulated as a function of  $\tilde{c}$  and  $\Delta$  in a filtered chemical database:

$$\bar{\omega}_c = \Xi_\Delta \bar{\omega}_c^{tab} [\tilde{c}, \Delta], \quad (3.64)$$

$$\nabla \cdot (\bar{\rho}D\nabla c) = \nabla \cdot \left( \alpha_c^{tab} [\tilde{c}, \Delta] \bar{\rho}D\nabla \tilde{c} \right), \quad (3.65)$$

$$-\nabla \cdot (\bar{p}\tilde{u}\tilde{c} - \bar{p}\tilde{u}\tilde{c}) = (\Xi_\Delta - 1) \nabla \cdot \left( \alpha_c^{tab} [\tilde{c}, \Delta] \bar{\rho}D\nabla \tilde{c} \right) + \Xi_\Delta \Omega_c^{tab} [\tilde{c}, \Delta], \quad (3.66)$$

where the superscript  $.^{tab}$  denotes tabulated quantities.  $\Omega_c^{tab}$  corresponds to the transport of the unresolved progress variable due to thermal expansion and  $\alpha_c^{tab} [\tilde{c}, \Delta]$  is a correction parameter.  $\Xi_\Delta$  is the sub-grid scale flame wrinkling factor that must be modeled. It corresponds to the sub-grid flame surface divided by the projected surface in the propagating direction.

#### Flame surface density approach

As the flame front and the gradient of progress variable  $c$  are generally too thin to be resolved on the LES computational mesh, Boger *et al.* [119] and more recently Duwig *et al.* [120] have introduced a physical space Gaussian filter with a filter size larger than the mesh size, to resolve the filtered flame structure:

$$\frac{\partial \bar{p}\tilde{c}}{\partial t} + \frac{\partial \bar{p}\tilde{u}_i\tilde{c}}{\partial x_i} + \frac{\partial}{\partial x_i}(\bar{p}\tilde{u}_i\tilde{c} - \bar{p}\tilde{u}_i\tilde{c}) = \bar{\rho}S_d |\nabla c|, \quad (3.67)$$

where  $S_d$  is the local displacement speed and  $\bar{\rho}S_d |\nabla c|$  corresponds to the flame front displacement which may be modeled as [119]:

$$\bar{\rho}S_d |\nabla c| \approx \rho_{fg} S_L \Sigma = \rho_{fg} S_L \Xi_\Delta |\nabla \tilde{c}|, \quad (3.68)$$

where  $\Sigma$  is the sub-grid scale flame surface density. Algebraic expressions or balance equations may be proposed to model either  $\Sigma$  or  $\Xi_\Delta$ .

Based on a DNS database of a laminar premixed flame interacting with a homogeneous and isotropic flow [121], Boger *et al.* [119] have proposed an algebraic model for  $\Sigma$ :

$$\Sigma = 4\Xi_\Delta \sqrt{\frac{6}{\pi}} \frac{\tilde{c}(1-\tilde{c})}{\Delta}. \quad (3.69)$$

Note that Eq. 3.69 may also be used as a F-TACLES model in the framework of infinitely thin flame fronts.

Moreover, to close the unresolved progress variable transport term  $\nabla \cdot (\bar{p}\tilde{u}_i\tilde{c} - \bar{p}\tilde{u}_i\tilde{c})$ , Boger and Veynante [122] have proposed the following model:

$$\frac{\partial \bar{p}\tilde{c}}{\partial t} + \frac{\partial \bar{p}\tilde{u}_i\tilde{c}}{\partial x_i} = \frac{\partial}{\partial x_i} \left( \rho_{fg} \frac{S_L \Xi_\Delta}{16\sqrt{6/\pi}} \frac{\partial \tilde{c}}{\partial x_i} \right) + 4\rho_{fg} S_L \Xi_\Delta \sqrt{\frac{6}{\pi}} \frac{\tilde{c}(1-\tilde{c})}{\Delta}. \quad (3.70)$$

**Principle of the LES Thickened flame model (TFLES)**

Originally proposed by Butler and O'Rourke [123], and O'Rourke and Bracco [124], the principle of the LES Thickened Flame model is to thicken the spatial structure of the flame to allow its resolution on the numerical grid while keeping the laminar flame speed unchanged.

On the basis of the usual premixed laminar flame theory [26, 125], they demonstrated that by multiplying species and heat diffusion coefficients by a factor  $F$  and dividing the chemical source terms by the same factor  $F$ , the flame thickness is increased while the flame structure and the flame speed are unchanged.

Indeed, for a single-step reaction, the premixed flame theory [18, 26] shows that both the laminar flame speed  $S_L^0$  and the laminar flame thickness  $\delta_L^0$  are controlled by the diffusive and source terms as:

$$S_L^0 \propto \sqrt{D_{th}A} \xrightarrow{\text{Thickening}} \sqrt{FD_{th}\frac{A}{F}} = \sqrt{D_{th}A}, \quad (3.71)$$

$$\delta_L^0 \propto \frac{D_{th}}{S_L^0} = \sqrt{\frac{D_{th}}{A}} \xrightarrow{\text{Thickening}} \sqrt{FD_{th}\frac{F}{A}} = F\sqrt{\frac{D_{th}}{A}}, \quad (3.72)$$

where  $A$  is the pre-exponential factor of the single-step reaction. To thicken the flame, thermal and molecular diffusivities are multiplied by the thickening factor  $F$  whereas the reaction rates  $\omega_k$  are divided by  $F$ : the flame is  $F$  times thicker but its laminar propagation speed is preserved. Sufficiently large values of  $F$  then allow the resolution of the thickened flame structure on the LES grid.

For the simplest version of the TFLES model,  $F$  is constant in space and time. This formalism is well suited to simple academic uniform-grid cases where species and temperature gradients only occur in the flame. When using non-uniform meshes,  $F$  must be locally estimated to ensure that the flame structure is sufficiently resolved everywhere. To avoid a modification of the diffusion processes in non-zero species and temperature gradients, the local thickening factor is applied only in the vicinity of the flame front [126]:

$$F = 1 + (F_{max} - 1)S, \quad (3.73)$$

where  $F_{max}$  is the maximum thickening factor and  $S$  is a flame sensor.  $F_{max}$  is estimated as a function of the local cell size  $\Delta_x$ :

$$F_{max} = \frac{N_c \Delta_x}{\delta_L^0}, \quad (3.74)$$

where  $N_c$  is the number of points requested in the front.

Other flame markers may be used to compute  $S$ , for example the progress variable  $c$ , leading to  $S = 16[c(1 - c)]^2$  [127, 128]. To avoid unnecessary thickening out of the flame, Proch *et al.* [129] used gradients of  $c$  compared to those obtained in a one-dimensional freely propagating premixed flame. Strakey and Eggenspieler [130] used a combination of heat release rate and  $Y_{H_2O}$  gradient also compared to maximum values in one-dimensional reference flames. In AVBP, the standard flame sensor  $S$  is a reaction rate based sensor:

$$S = \tanh \left( C_1 \frac{\Omega}{\Omega_0} \right), \quad (3.75)$$

$\Omega$  is a sensor function detecting the presence of a reaction zone using the kinetic parameters of the chemical scheme.  $\Omega_0$  corresponds to the maximum value of  $\Omega$  computed for a one-dimensional premixed non-thickened flame.  $C_1$  is a parameter which controls the stiffness with which the flame sensor  $S$  goes from 0 to 1. For multi-step chemical mechanisms, the reaction

### 3.2 LES filtering, equations and models

---

on which the sensor is based must be chosen by the user. If the fuel breakdown reaction is chosen,  $\Omega$  writes:

$$\Omega = Y_F^{n_F} Y_O^{n_O} \exp\left(-C_2 \frac{E_a}{RT}\right), \quad (3.76)$$

where  $n_F$  and  $n_O$  are the forward Arrhenius coefficients and  $E_a$  is the activation energy.  $C_2$  is a constant parameter used to start the thickening process before reaching the maximum reaction intensity (usually  $C_2 = 0.5$ ).

Finally, the transport equations for the filtered species mass fractions Eq. 3.56 and the total energy Eq. 3.57 become:

$$\begin{aligned} \frac{\partial \bar{\rho} \tilde{Y}_k}{\partial t} + \frac{\partial}{\partial x_j} (\bar{\rho} \tilde{u}_j \tilde{Y}_k) &= \frac{\partial}{\partial x_j} \left[ \left( F \frac{\mu}{S_{c,k}} + (1-S) \frac{\mu_t}{S_{c,k}^t} \right) \frac{W_k \partial \tilde{X}_k}{W \partial x_j} - \bar{\rho} \tilde{Y}_k (\tilde{V}_j^c + \tilde{V}_j^{c,t}) \right] \\ &\quad + \frac{1}{F} \dot{\omega}_k (\tilde{Y}_k, \tilde{T}), \end{aligned} \quad (3.77)$$

$$\begin{aligned} \frac{\partial \bar{\rho} \tilde{E}}{\partial t} + \frac{\partial}{\partial x_j} (\bar{\rho} \tilde{u}_j \tilde{E}) &= - \frac{\partial}{\partial x_j} [\tilde{u}_j \bar{P} \delta_{ij} - \tilde{u}_i \bar{\tau}_{ij}] \\ &\quad + \frac{\partial}{\partial x_j} \left[ C_p \left( F \frac{\mu}{P_r} + (1-S) \frac{\mu_t}{P_r^t} \right) \frac{\partial \tilde{T}}{\partial x_j} \right] \\ &\quad + \frac{\partial}{\partial x_j} \left[ \sum_{k=1}^N \left( \left[ F \frac{\mu}{S_{c,k}} + (1-S) \frac{\mu_t}{S_{c,k}^t} \right] \frac{W_k \partial \tilde{X}_k}{W \partial x_j} - \bar{\rho} \tilde{Y}_k (\tilde{V}_j^c + \tilde{V}_j^{c,t}) \right) \tilde{h}_{s,k} \right] \\ &\quad + \frac{\dot{\omega}_T (\tilde{Y}_k, \tilde{T})}{F}. \end{aligned} \quad (3.78)$$

The following relation for the correction diffusion velocities is used:

$$\tilde{V}_j^c + \tilde{V}_j^{c,t} = \sum_{k=1}^N \left( F \frac{\mu}{\bar{\rho} S_{c,k}} + (1-S) \frac{\mu_t}{\bar{\rho} S_{c,k}^t} \right) \frac{W_k \partial \tilde{X}_k}{W \partial x_j}. \quad (3.79)$$

However, as observed in Fig. 3.2(right) representing a thickened flame in a turbulent flow, the thickening process alters the interaction between turbulence and chemistry [131]:

- Scales smaller than a cut-off length scale  $\delta_L^{c,1}$  of the order of the thick flame thickness  $\delta_L^1$  are unable to wrinkle the front.
- For scales larger than  $\approx 5\delta_L^1$ , the stretch induced by the vortex, which is the combination of strain and curvature effects is dominated by the strain term (curvature, viscous and thermo-diffusive effects become secondary) and the flame is thin compared to the vortex size.
- In intermediate range ( $\delta_L^{c,1} \leq r \leq 5\delta_L^1$ ), the vortex efficiency is reduced. In this regime, the flame is thick compared to the vortex size.

The Damköhler dimensional number  $Da$  allows to characterize the interactions between turbulence and chemistry:

$$Da = \frac{\tau_t}{\tau_c} = \tau_t \frac{s_l^0}{\delta_l^0}, \quad (3.80)$$

$$\tau_t = \frac{l_t}{u'}, \quad (3.81)$$

where  $\tau_t$  and  $\tau_c$  are respectively turbulent and chemical characteristic times, and  $u'$  a turbulent fluctuation velocity.

From the Damköhler number, two situations can be distinguished:

- $Da \ll 1$  : chemical reactions are slow compared to the turbulent characteristic time. The flame thickness is large. Vortices have time to cross the flame front and mix the inner structure of the flame before the beginning of chemical reactions. The combustion regime is close to the perfectly stirred reactor.
- $Da \gg 1$  : chemical reactions are infinitely fast compared to the turbulent characteristic time. The flame thickness is thin. Eddies do not have time to cross the flame front nor to mix the inner structure of the flame. However, the flame front is wrinkled by these vortices, the flame surface increases and the flame burns in the flamelet regime.

When a flame is thickened, the Damköhler number is divided by  $F$ :

$$Da = \frac{\tau_t}{\tau_c} = \tau_t \frac{s_l^0}{F \delta_l^0}. \quad (3.82)$$

As a result, the thickening of the flame reduces the ability of the vortices to wrinkle the flame front. As the flame surface is reduced, the reaction rate is underestimated.

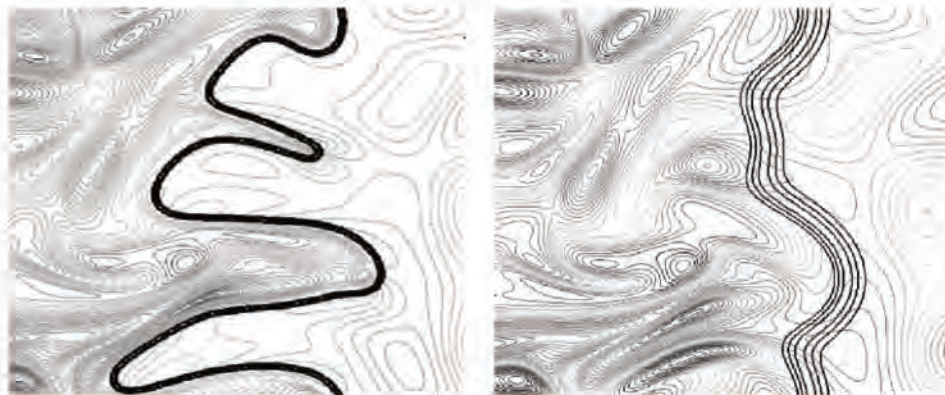


**Fig. 3.2.** Direct Numerical Simulation of flame/turbulence interactions [26, 132]). Left: unthickened flame, right: thickened flame ( $F = 5$ ).

An efficiency function  $\varepsilon$  has been introduced [131, 133] from DNS results to correct this effect. The correction consists in multiplying the diffusion coefficient and the reaction rates with  $\varepsilon$ . Using this efficiency function, Eqs. 3.77 and 3.78 propagate a flame front of thickness  $F \delta_L^0$  with the velocity  $S_t = \varepsilon S_L$ . The filtered species mass fractions Eq. 3.77 and the total energy Eq. 3.78 are finally written as:

$$\begin{aligned} \frac{\partial \bar{\rho} \tilde{Y}_k}{\partial t} + \frac{\partial}{\partial x_j} (\bar{\rho} \tilde{u}_j \tilde{Y}_k) &= \frac{\partial}{\partial x_j} \left[ \left( \varepsilon F \frac{\mu}{S_{c,k}} + (1 - S) \frac{\mu_t}{S_{c,k}^t} \right) \frac{W_k \partial \tilde{X}_k}{W \partial x_j} - \bar{\rho} \tilde{Y}_k (\tilde{V}_i^c + \tilde{V}_j^{c,t}) \right] \\ &+ \frac{\varepsilon}{F} \dot{\omega}_k (\tilde{Y}_k, \tilde{T}), \end{aligned} \quad (3.83)$$

$$\begin{aligned}
 \frac{\partial \bar{\rho} \tilde{E}}{\partial t} + \frac{\partial}{\partial x_j} (\bar{\rho} \tilde{u}_j \tilde{E}) &= - \frac{\partial}{\partial x_j} [\tilde{u}_i \bar{P} \delta_{ij} - \tilde{u}_i \bar{\tau}_{ij}] \\
 &\quad + \frac{\partial}{\partial x_j} \left[ C_p \left( \varepsilon F \frac{\mu}{P_r} + (1-S) \frac{\mu_t}{P_r^t} \right) \frac{\partial \tilde{T}}{\partial x_j} \right] \\
 &\quad + \frac{\partial}{\partial x_j} \left[ \sum_{k=1}^N \left( \left[ \varepsilon F \frac{\mu}{S_{c,k}} + (1-S) \frac{\mu_t}{S_{c,k}^t} \right] \frac{W_k \partial \tilde{X}_k}{W \partial x_j} - \bar{\rho} \tilde{Y}_k (\tilde{V}_j^c + \tilde{V}_j^{c,t}) \right) \tilde{h}_{s,k} \right] \\
 &\quad + \frac{\varepsilon \dot{\omega}_T (\tilde{Y}_k, \tilde{T})}{F}.
 \end{aligned} \tag{3.84}$$

The correction diffusion velocities are also recasted:

$$\tilde{V}_j^c + \tilde{V}_j^{c,t} = \sum_{k=1}^N \left( \varepsilon F \frac{\mu}{\bar{\rho} S_{c,k}} + (1-S) \frac{\mu_t}{\bar{\rho} S_{c,k}^t} \right) \frac{W_k \partial \tilde{X}_k}{W \partial x_j}. \tag{3.85}$$

#### Static TFLES model - Colin efficiency function

Multiple expressions can be found in the literature for the efficiency function  $\varepsilon$ . In the following, only the efficiency functions in AVBP are described. The Colin efficiency function [131] is an algebraic equation derived from the filtered flame surface density balance equation [119]:

$$\frac{\partial \bar{\Sigma}}{\partial t} + \nabla \cdot [\langle \vec{u} \rangle_s \bar{\Sigma}] + \nabla \cdot [\langle w \vec{n} \rangle_s \bar{\Sigma}] = \langle \nabla \cdot \vec{u} - \vec{n} \vec{n} : \nabla \vec{u} \rangle_s \bar{\Sigma} + \langle w \nabla \cdot \vec{n} \rangle_s \bar{\Sigma} = \langle \kappa \rangle_s \bar{\Sigma}, \tag{3.86}$$

where  $\vec{n} = -\nabla c / |\nabla c|$  is the unit vector normal to the iso- $c$  surface pointing toward the fresh gases.  $\nabla \cdot \vec{n}$  corresponds to the curvature of the iso-surface, whereas  $\nabla \cdot \vec{u} - \vec{n} \vec{n} : \nabla \vec{u} = \alpha_T$  is the strain rate acting on the iso- $c$  surfaces and to the normal front displacement. Colin *et al.* [131] proposed to estimate the sub-grid scale surface averaged curvature  $\langle \nabla \cdot \vec{n} \rangle_s$  as:

$$|\langle \nabla \cdot \vec{n} \rangle_s| \approx \frac{1}{\alpha} \frac{\Xi_\Delta - 1}{\Delta}, \tag{3.87}$$

where  $\alpha$  is a constant of the model, and  $\Delta$  a filter size. Then, assuming an equilibrium at the sub-grid scale level between flame surface and turbulence (i.e.  $\langle \kappa \rangle_s \approx 0$ ), the wrinkling factor  $\Xi_\Delta$  is estimated:

$$\Xi_\Delta \approx 1 + \alpha \frac{\Delta}{S_L^0} \langle \alpha_T \rangle_s. \tag{3.88}$$

To close the model, an estimation of the sub-grid scale strain rate  $\langle \alpha_T \rangle_s$  is required:

$$\langle \alpha_T \rangle_s = \Gamma \left( \frac{\Delta}{\delta_L^0}, \frac{u'_\Delta}{S_L^0} \right) \frac{u'_\Delta}{\Delta}, \tag{3.89}$$

where  $\Gamma$  is a DNS-based correction function introduced to take into account the inability of small vortices (relatively to the flame thickness) to wrinkle the flame front. Note that  $u'_\Delta$  is calculated using an operator based on the rotational of the velocity field to remove the dilatational part of the velocity [131]. Using Eqs. 3.89 and 3.88, the following expression for the wrinkling factor is obtained:

$$\Xi_\Delta \approx 1 + \alpha \Gamma \left( \frac{\Delta}{\delta_L^0}, \frac{u'_\Delta}{S_L^0} \right) \frac{\Delta}{S_L^0}. \tag{3.90}$$

Finally,  $\varepsilon$  is expressed as the wrinkling ratio between the un-thickened reference flame, and the thickened flame:

$$\varepsilon = \frac{\Xi_\Delta(\delta_L^0)}{\Xi_\Delta(\delta_L^1)} = \frac{1 + \alpha \Gamma\left(\frac{\Delta}{\delta_L^0}, \frac{u'_\Delta}{S_L^0}\right)}{1 + \alpha \Gamma\left(\frac{\Delta}{\delta_L^1}, \frac{u'_\Delta}{S_L^0}\right)}, \quad (3.91)$$

The main issue related to the Colin efficiency function is that the efficiency function does not tend toward a saturated value when turbulence intensity increases. Indeed, a flame front can not infinitely create flame area when facing intense turbulent motions. For large turbulent intensities the flame reaches a saturated regime. Charlette *et al.* [133] have proposed another efficiency function to take into account this regime.

#### Static TFLES model - Charlette efficiency function

The usual Charlette model also estimates  $\Xi_\Delta$  from an algebraic expression [133, 134]. The model is based on writing the unresolved flame surface density equation Eq. 3.86 in terms of a general power-law expression that involves an inner  $\eta_c$  and outer  $\Delta$  cutoff scales:

$$\Xi_\Delta = \left(1 + \frac{\Delta}{\eta_c}\right)^{\beta_{Ch}} = (1 + \Delta |\langle \nabla \cdot n \rangle_s|)^{\beta_{Ch}}, \quad (3.92)$$

where  $\beta_{Ch}$  is a user-defined parameter which is of the order of 0.5.  $\eta_c$  limits wrinkling at the smallest length-scales of the flame and is defined as:

$$\eta_c = |\langle \nabla \cdot n \rangle_s|^{-1}. \quad (3.93)$$

Then, assuming an equilibrium between the sub-grid scale turbulent motions and the flame front:

$$S_L^0 \langle \nabla \cdot \vec{n} \rangle_s = \langle \nabla \cdot \vec{u} - \vec{n} \vec{n} : \nabla \vec{u} \rangle_s \approx \frac{u'_\Delta}{\Delta} \Gamma_{Ch} \left( \frac{\Delta}{\delta_L^0}, \frac{u'_\Delta}{S_L^0}, Re_\Delta \right), \quad (3.94)$$

where  $\Gamma_{Ch}$  is also a correction function that measures the ability of vortices to effectively wrinkle the flame front and create flame area.  $u'_\Delta$  and  $Re_\Delta = u'_\Delta \Delta / \nu$  are the sub-grid scale turbulent velocity and Reynolds number, respectively,  $\nu$  being the fresh gas kinematic viscosity. Note that  $u'_\Delta$  is calculated using the same operator as previously [131].

Finally, using Eqs. 3.94 and 3.92, the Charlette efficiency function writes:

$$\Xi_\Delta^{Ch} \left( \frac{\Delta}{\delta_L^0}, \frac{u'_\Delta}{S_L^0}, Re_\Delta \right) = \left( 1 + \min \left[ \frac{\Delta}{\delta_L^0}, \Gamma_{Ch} \left( \frac{\Delta}{\delta_L^0}, \frac{u'_\Delta}{S_L^0}, Re_\Delta \right) \frac{u'_\Delta}{S_L^0} \right] \right)^{\beta_{Ch}}. \quad (3.95)$$

Note that Eq. 3.95 is clipped with a minimum operator to avoid the prediction of unphysical cutoff scales smaller than the laminar flame thickness  $\delta_L^0$  (i.e.  $\eta_c \geq \delta_L^0$ ). In other words, the clipping operator is introduced to take into account the saturated regime and limit the production of flame surface for too large turbulent intensities. Note that Wang *et al.* [134] replaced the  $\Delta/\delta_L^0$  term in Eq. 3.95 by  $\Delta/\delta_L^0 - 1$  to maximise the wrinkling factor by the fractal model:  $\Xi_\Delta^{max} = (\Delta/\delta_L^0)^\beta$  which is the expression of total area in fractal surfaces of dimension  $D = \beta + 2$  [15, 135]. In practice, it is shown that the wrinkling factor  $\Xi_\Delta$  is often saturated [136]: the minimum term in Eq. 3.95 is related to  $\Delta/\eta_c$  and is independent of  $u'_\Delta$ . Eq. 3.95 is thus recasted in a more convenient way called the "Charlette saturated efficiency function":

$$\Xi_\Delta = \left( \frac{\Delta}{\delta_L^0} \right)^\beta. \quad (3.96)$$

Equation 3.96 simply states that the SGS surface has a fractal dimension  $\beta + 2$ , an inner cutoff set to the laminar flame thickness  $\delta_L^0$  [133] and an outer cutoff  $\Delta$ . However, note that Eq. 3.96

relies on a coefficient  $\beta$  specified by the user. This raises two difficulties: (1)  $\beta$  is often unknown and (2)  $\beta$  may change with location and time. Tests in LES of explosions [137] or flames in internal combustion engines [138, 139] for example show that  $\beta$  should be a function of space and time, and that different  $\beta$  values have to be used when the Reynolds number varies over a wide range. An intuitive way to circumvent this limitation is to make the turbulent combustion model for  $\Xi_\Delta$  dynamic [136, 140, 141] as done for dynamic models for the SGS transport terms [142, 143, 144, 145].

#### Dynamic TFLES formulation - Dynamic Charlette saturated efficiency function

With the dynamic wrinkling formulation, the exponent  $\beta$  of Eq. 3.96 is automatically adjusted from the known resolved flow field. This is done by equating the flame surface densities computed at filtered and test-filtered level (Germano-like identity [143]):

$$\langle \widehat{\Xi_\Delta} |\nabla \tilde{c}| \rangle = \langle \Xi_{\gamma\Delta} |\nabla \tilde{c}| \rangle, \quad (3.97)$$

where  $c$  is the progress variable, estimated here from the temperature. The  $\widehat{\cdot}$  symbol denotes the test-filtering operation, and  $\langle \cdot \rangle$  denotes an averaging operator [146] that can be the overall computational domain (dynamic global formulation) or a small local volume (dynamic local formulation). In this latter case, the averaging operation can be replaced by a Gaussian filtering of size  $\Delta_{avg}$  [136, 147]. For Gaussian filters, the ratio  $\gamma$  between the effective filtered scale (i.e the scale of the filter that should be applied to the instantaneous field to have the same result as the one computed using the successive combination of both LES and test filters) and the LES filtered scale is given by:

$$\gamma = \sqrt{1 + \left(\frac{\widehat{\Delta}}{\Delta}\right)^2}. \quad (3.98)$$

Combining Eqs. 3.96 and 3.97, and assuming that  $\beta$  is constant over the averaging domain  $\langle \cdot \rangle$  provides the value of  $\beta$ :

$$\beta = \frac{\log \left( \langle |\nabla \tilde{c}| \rangle / \langle |\nabla \tilde{c}| \rangle \right)}{\log (\gamma)}. \quad (3.99)$$

Two turbulent reacting configurations are simulated in the current work: the VOLVO and the HERON burners. Both exhibit high turbulent intensity vortices strongly interacting with the flame fronts: the saturated regime may be reached and the Charlette efficiency functions should be more adapted. However in such configurations, choosing a value for  $\beta_{Ch}$  is not an easy task, all the more that  $\beta$  may change with location and time. For these reasons, two efficiency functions have been tested in this thesis: the static Charlette efficiency function, and the dynamic Charlette saturated efficiency function.



# Evaporating spray equations and models

This chapter first introduces the Lagrangian DPS deterministic approach and the equations used to model a two-phase flow spray. Then, the usual closure models characterizing an isolated droplet are presented.

## 4.1 Lagrangian deterministic approach

### 4.1.1 Lagrangian set of equations

In a Lagrangian Discrete Particle Simulation (DPS) approach, the dispersed phase consists of particles which are assumed to be rigid spheres with diameters comparable or smaller than the Kolmogorov length scale. This assumption is valid (1) for diluted sprays (interactions between particles are neglected) and (2) for small enough droplets which remain spherical due to the high surface tension force. Under these assumptions, the isolated droplet is thus considered as a spatial point facing the surroundings gaseous conditions. The evolution of the position, velocity and temperature of this droplet are calculated at the corresponding spatial location. The coupling gas → liquid and liquid → gas is called "two-way coupling".

The influence of the particles on the gas-phase is taken into account introducing mass, momentum and energy source terms into the Eulerian conservation equations. Each droplet is considered as a source point to which is associated a trajectory, a mass and a liquid temperature. These associated quantities are transported according to the following set of equations:

$$\frac{dx_{p,j}}{dt} = u_{p,j}, \quad (4.1)$$

$$\frac{dm_p}{dt} = \dot{m}_p, \quad (4.2)$$

$$\frac{dm_p u_{p,j}}{dt} = F_{p,j}^{ext}, \quad (4.3)$$

$$\frac{dm_p h_{s,p}}{dt} = \dot{\Phi}_p, \quad (4.4)$$

where  $j$  is the spatial coordinates. Subscript  $p$ ,  $x_{p,j}$  and  $m_p$  are respectively the index, the position and the mass of the particle.  $F_{p,j}^{ext}$  corresponds to the external forces acting on the droplet, whereas  $\dot{m}_p$  and  $\dot{\Phi}_p$  are the variation of mass and energy of the droplet, obtained from the macroscopic models detailed in Sect. 4.2.

### 4.1.2 Coupling with the Eulerian gaseous phase

The coupling with the Eulerian gaseous phase is done with a conservative transfer of the mass, momentum and energy fluxes through the source terms  $S_*^{l \rightarrow g}$  which are added to Eqs. 3.54-3.57:

$$S_m^{l \rightarrow g} = \frac{1}{\Delta V} \sum_{n=1}^{N_p} \psi_n(x_{p,n}) \dot{m}_{p,n}, \quad (4.5)$$

$$S_{qdm,j}^{l \rightarrow g} = \frac{1}{\Delta V} \sum_{n=1}^{N_p} \psi_n(x_{p,n}) \left( -m_{p,n} F_{p,n,j}^{ext} + \dot{m}_{p,n} u_{p,n,j} \right), \quad (4.6)$$

$$S_F^{l \rightarrow g} = \frac{1}{\Delta V} \sum_{n=1}^{N_p} \psi_n(x_{p,n}) \dot{m}_{p,n}, \quad (4.7)$$

$$S_E^{l \rightarrow g} = \frac{1}{\Delta V} \sum_{n=1}^{N_p} \psi_n(x_{p,n}) \left( -m_{p,n} F_{p,n,j}^{ext} \cdot \vec{u}_{p,n} + \frac{1}{2} \dot{m}_{p,n} \|\vec{u}_{p,n}\|^2 - \Phi_{p,n} \right), \quad (4.8)$$

where  $\Delta V$  is the transfer control volume,  $N_p$  is the number of droplets inside this volume and  $\psi_n(x_p)$  is the interpolation function.

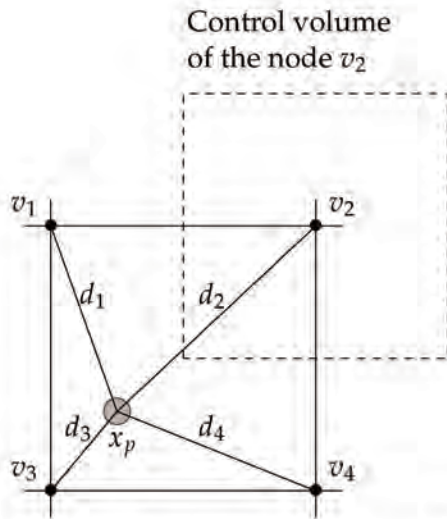


**Fig. 4.1.** Projection of the source terms of a droplet located at  $x_p$ , on the vertices ( $v_1, v_2, v_3$  and  $v_4$ ) of a square element.

The interpolation is performed between the droplet location and the vertices of the mesh element containing the droplet. The weights used for the interpolation are inversely proportional to the distance  $d_k$  between the droplet and the vertices  $v_k$  (Fig. 4.1):

$$\psi_{n,v_k} = \frac{1/d_k}{\sum_{k'=1}^{N_v} 1/d_{k'}}, \quad (4.9)$$

where  $k$  is the index of the vertex, and  $N_v$  is the number of vertices. Herein, the control volume is equal to the nodal volume.

## 4.2 Macroscopic models for an isolated droplet

Considering a deterministic Lagrangian DPS approach, the evolution of the spray corresponds to the one of isolated droplets. In this section, the usual isolated droplet macroscopic models closing the set of Lagrangian equations Eqs. 4.2-4.4 are presented. First, a description of the dynamic of an isolated droplet is detailed. Then, a simplified evaporation model is described, as well as several approaches to improve its accuracy. In the following and for a matter of readability, subscript "g" is added to gaseous variables.

### 4.2.1 Dynamic of an isolated droplet

To study the dynamic of an evaporating isolated droplet, a common assumption consists in considering that this droplet acts like a non-evaporating rigid sphere. Even if the evaporation

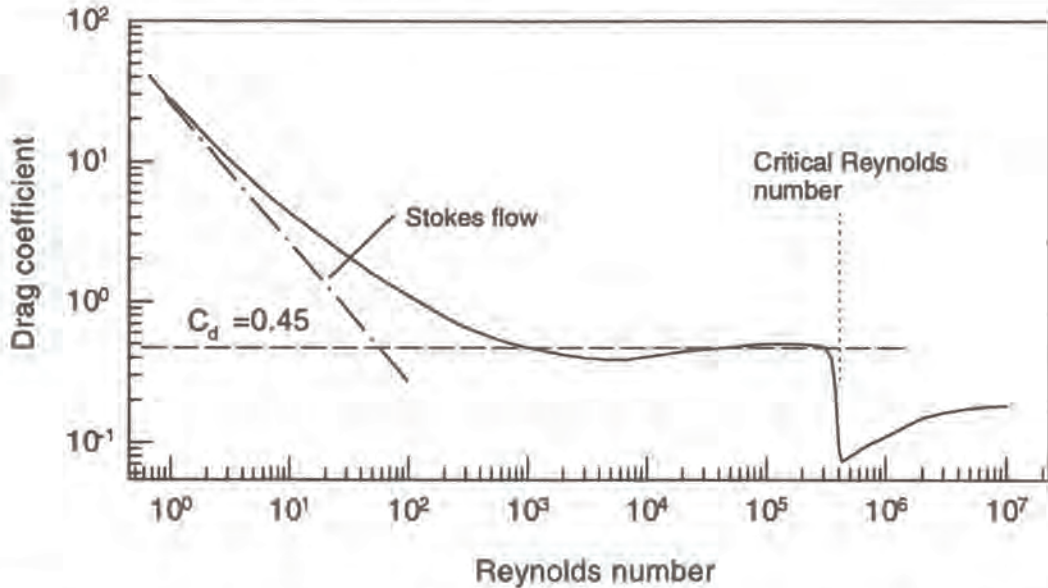


**Fig. 4.2.** Variation of the drag coefficient  $C_D$  as a function of the particle Reynolds number  $Re_p$  [148].

of a droplet could be heterogeneous along its surface and generate a global lift, neglecting the influence of evaporation on drag is a reasonable assumption. Indeed, due to the weak surface variations, this global lift is usually small compared to other forces, and thus not sufficient to modify the trajectory of the droplet. The external forces acting on the droplet are obtained integrating the Navier-Stokes equations around the surface of the sphere. Two types of forces are identified: steady and unsteady.

#### Steady forces

##### Steady drag force

The steady drag force  $\vec{F}_D$  is the force acting on the sphere in a uniform pressure environment, and without relative acceleration of the sphere compared to the flow. This force is expressed using a drag coefficient  $C_D$ :

$$\vec{F}_D = \frac{1}{2} \rho_g C_D A \| \vec{u}_g - \vec{u}_p \| (\vec{u}_g - \vec{u}_p), \quad (4.10)$$

where  $\rho_g$  is the surrounding gaseous phase density,  $\vec{u}_g$  and  $\vec{u}_p$  are respectively the gaseous and liquid velocities, and  $A = \frac{\pi d_p^2}{4}$  is the projected area of the sphere. The drag coefficient  $C_D$  is difficult to estimate since it highly depends on the relative velocity between the flow and the particle, as illustrated in Fig. 4.2. The local drag coefficient  $C_D$  may be expressed in terms of the particle Reynolds number  $Re_p$  (characterizing the intensity of the flow) following [149]:

$$C_D = \frac{24}{Re_p} \left[ 1 + 0.15 Re_p^{0.687} \right], \quad (4.11)$$

$$Re_p = \frac{\rho_g d_p \| \vec{u}_g - \vec{u}_p \|}{\mu_g}, \quad (4.12)$$

where  $d_p$  is the diameter of the sphere and  $\mu_g$  is the viscosity of the gas.

##### Steady pressure force

A local pressure gradient at the location of the droplet generates a force toward the same direction. For the peculiar case of hydrostatic pressure, the associated pressure force is the

Archimede force:

$$\vec{F}_P = -\rho_g V_p \vec{g}, \quad (4.13)$$

where  $\vec{g}$  is the gravity vector and  $V_p$  is the volume of the droplet. Adding the gravity force  $-m_p \vec{g}$  acting on the droplet to Eq. 4.13 leads to the following expression of the steady pressure force:

$$\vec{F}_P^{tot} = \rho_l V_p \vec{g} \left( 1 - \frac{\rho_g}{\rho_l} \right), \quad (4.14)$$

When droplets of fuel are immersed in a gas, the density ratio  $\rho_l / \rho_g \gg 1$ . The Archimede force is in this case negligible compared to the weight of the droplet.

### Stokes number and characteristic time

Finally, the Lagrangian momentum equation Eq. 4.3 reads:

$$\frac{du_{p,j}}{dt} = F_{p,j}^{ext} = F_{D,j} + F_{P,j} = \frac{1}{\tau_p} (u_{g,j} - u_{p,j}) + g_j, \quad (4.15)$$

where  $\tau_p$  is the characteristic relaxation time:

$$\tau_p = \frac{\rho_l d_p^2}{18 \mu_g (1 + 0.15 Re_p^{0.687})}, \quad (4.16)$$

The inertial behavior of a particle is characterized comparing  $\tau_p$  to a characteristic time of the gaseous phase  $\tau_g$ :

$$S_t = \frac{\tau_p}{\tau_g}, \quad (4.17)$$

where  $\tau_g = L / |u_g|$  with  $L$  a characteristic length scale of the gaseous flow.

#### 4.2.2 Evaporation of an isolated droplet

Let's consider a droplet evaporating in a flow where the gaseous temperature  $T_g$  is higher than the liquid one. Thermal and mass exchanges start at the surface of the droplet, leading to four main phenomena taking place during the evaporation process:

- The surrounding heat in the gas phase diffuses to the droplet surface.
- The heat arriving to the surface of the droplet is diffused by conduction inside this last one, resulting in an increase of its temperature and therefore its internal energy.
- The molecules of fuel detach from the droplet surface due to their increasing internal energy (vaporization process), leading to an increase of the amount of fuel vapor at this surface.
- The gaseous fuel diffuses from the droplet surface to the surrounding gas.

The development of an analytical evaporation model requires to assume that the interface between the liquid and the gas is at thermodynamic equilibrium: at the surface of the droplet, the flow of molecules moving from the liquid state to the gaseous state is equal to the flow of molecules moving from the gaseous to the liquid state. It is thus possible to obtain the quantity of fuel vapor at the surface of the droplet, for a given surrounding condition.

In the following, the Spalding evaporation model [150] is presented as well as the modifications proposed by Abramzon and Sirignano [151].

#### Spalding evaporation model

The set of equations describing the evaporation can be analytically solved assuming that:

- The droplet is considered spherical and isolated: the interaction with other droplets is neglected.

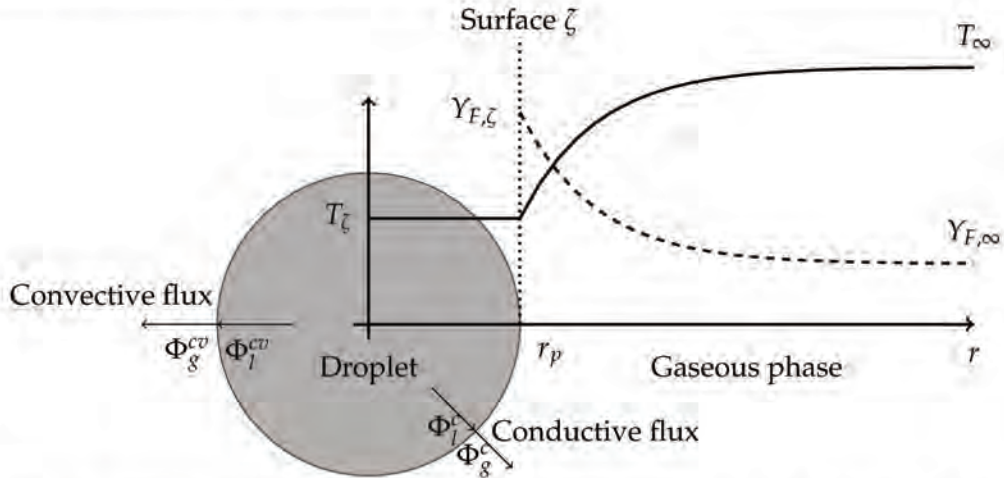


**Fig. 4.3.** Sketch representing the profiles of radial temperature  $T$  and mass fraction of fuel  $Y_F$  for a spherical droplet at a uniform temperature  $T_p = T_\zeta$ .

- Inside the droplet, the thermal conductivity is considered infinite and the temperature is uniform. This hypothesis is justified by the fact that the thermal conductivity of a liquid is usually an order of magnitude higher than the thermal conductivity of the gas. As a result, the typical homogenization time of the liquid is faster than the gaseous thermal adaptation.
- The gas is considered quasi-stationary, so the thermal and mass transfers in the gaseous phase depend only on the distance to the surface of the droplet. Furthermore, the particle density being higher than the fluid density ( $\rho_p \gg \rho_g$ ), the velocity of regression of the droplet surface is much smaller than that of the gaseous fuel leaving the surface, so that the position of the liquid surface may be considered constant.

Thanks to these assumptions and due to the spherical symmetry of the configuration (Fig. 4.3), the equations of the gaseous phase are quasi-static and expressed in spherical coordinates. Therefore, only variations in radial coordinates are considered.

The following conservation equations of momentum, species and energy of the gaseous flow field for  $r > r_\zeta$  are obtained:

$$\rho_g u r^2 = \text{constant} = \frac{\dot{m}_F}{4\pi}, \quad (4.18)$$

$$\rho_g u r^2 \frac{dY_F}{dr} = \frac{d}{dr} \left( r^2 \rho_g D_F \frac{dY_F}{dr} \right), \quad (4.19)$$

$$\rho_g u r^2 \frac{dC_P T}{dr} = \frac{d}{dr} \left( r^2 \frac{\lambda}{C_P} \frac{dC_P T}{dr} \right), \quad (4.20)$$

where  $r$  is the radial coordinate,  $\dot{m}_F$  is the fuel vapor flux at the surface, and  $Y_F$  is the fuel mass fraction.  $D_F$  is the diffusion coefficient of the species representing the fuel. It can be expressed as a function of both the gas viscosity  $\mu$  and the Schmidt number  $S_{C_F}$ .

The integration of the evaporation model is done in two steps. First, the temporal evolution of the droplet mass is determined. Then, the temporal evolution of the temperature of the droplet is obtained through an energy balance.

#### Temporal evolution of the droplet mass

The mass exchange through the droplet surface may be represented by the fuel mass flux leaving the surface ( $\zeta$  and  $u_r$  respectively represent the droplet surface and regression velocity):

$$\dot{m}_F = \left( 4\pi \rho_g u_r r_p^2 \right)_\zeta. \quad (4.21)$$

Another definition for the mass exchange through the droplet surface is obtained using the temporal evolution of the droplet total mass  $\dot{m}_p$ :

$$\dot{m}_p = \frac{dm_p}{dt}. \quad (4.22)$$

As the droplet mass loss due to evaporation is totally converted into gaseous fuel,  $\dot{m}_F = -\dot{m}_p$ . Integrating twice Eq. 4.19 between the far field and the surface of the droplet, Spalding [150] proposed the following expression to estimate the variation of droplet mass:

$$\dot{m}_p = -\pi d_p S h \rho_g D_F \ln(1 + B_M), \quad (4.23)$$

where  $Sh$  is the Sherwood dimensionless number corresponding to the ratio of convective and diffusive mass transport. For evaporation in quiescent atmosphere, the Sherwood number is equal to 2.  $B_M$  is the Spalding mass number given by:

$$B_M = \frac{Y_{F,\zeta} - Y_{F,\infty}}{1 - Y_{F,\zeta}}, \quad (4.24)$$

where  $Y_{F,\zeta}$  and  $Y_{F,\infty}$  are respectively the evaporated fuel mass fractions located at both the film surrounding the surface of the droplet, and the far field.  $Y_{F,\zeta}$  is expressed at the surface following:

$$Y_{F,\zeta} = \frac{X_{F,\zeta} W_F}{X_{F,\zeta} W_F + (1 - X_{F,\zeta}) \bar{W}_{F,\zeta}}, \quad (4.25)$$

where  $W_F$  is the molar weight of the fuel,  $\bar{W}_{F,\zeta}$  is the molar weight of the mixture of all species other than the fuel:

$$\bar{W}_{F,\zeta} = \bar{W}_{F,\infty} = \frac{1 - Y_{F,\infty}}{1 - Y_{F,\infty} \frac{W_F}{\bar{W}}}. \quad (4.26)$$

$X_{F,\zeta}$  is the molar fraction of the fuel vapor at the surface, written using the partial pressure of the fuel species  $P_{F,\zeta}$ :

$$X_{F,\zeta} = \frac{P_{F,\zeta}}{P}, \quad (4.27)$$

where  $P_{F,\zeta}$  is calculated by the Clausius-Clapeyron law:

$$P_{F,\zeta} = P_{cc} \exp \left( \frac{W_F L_v(T_{ref})}{R} \left( \frac{1}{T_{cc}} - \frac{1}{T_\zeta} \right) \right), \quad (4.28)$$

where  $T_{cc}$  and  $p_{cc}$  correspond to an arbitrary reference point on the saturation curve,  $R$  is the universal gas constant and  $L_v(T_{ref})$  is the latent heat at  $T_{ref}$ . The latent heat  $L_v$  at a given temperature  $T$  is defined as:

$$L_v(T) = h_{s,F}(T) - h_{s,p}(T). \quad (4.29)$$

Note that  $T_\zeta = T_p$  since the droplet temperature is uniform and its surface does not store energy. Also note that the mass variation proposed by Spalding in Eq. 4.23 depends on both the temperature  $T_p$  and the diameter  $d_p$  of the droplet. The derivation of the temporal evolution of  $T_p$  is described in the following paragraph, whereas the temporal evolution of the droplet diameter is simply obtained using the definition of  $\dot{m}_p$ :

$$\dot{m}_p = \frac{d}{dt} \left[ \frac{4}{3} \pi \rho_l r_p^3 \right]. \quad (4.30)$$

By temporally integrating Eq. 4.30 and using Eq. 4.23, the variation of the droplet diameter squared is:

$$d_p^2 = d_{p,0}^2 - \frac{8 \rho_g D_F}{\rho_l} \ln(B_M + 1) t, \quad (4.31)$$

where  $d_{p,0}$  is the initial diameter of the droplet. A constant droplet temperature  $T_p$  results in a constant factor  $\frac{8\rho_g D_F}{\rho_l} \ln(B_M + 1)$ , leading to a linear decrease of  $d_p^2$ . The characteristic evaporation time  $\tau_{ev}$  is thus obtained:

$$\tau_{ev} = \frac{\rho_l d_{p,0}^2}{8\rho_g D_F \ln(B_M + 1)}. \quad (4.32)$$

### Temporal evolution of the droplet temperature

In order to completely characterize the evaporation process, an equation for the evolution of the droplet temperature needs to be provided. The derivation of a law for the temporal evolution of this temperature involves the enthalpy conservation (Eq. 4.20) with boundary conditions at the far-field ( $\infty$ ) and the droplet surface ( $\zeta$ ). Furthermore, since the interface does not store energy, a conservation law for the enthalpy fluxes at the liquid/gas interface can be stated. Figure 4.3 gives an overview of the four contributions:

$$\Phi_l^{cv} + \Phi_l^c + \Phi_g^{cv} + \Phi_g^c = 0 \quad (4.33)$$

On the gaseous side, there is a convective part  $\Phi_g^{cv}$  representing the sensible enthalpy of the fuel species  $h_{s,F}$  that is transported by the Stefan flux  $\dot{m}_F$ , i.e., the evaporated mass moving away from the surface at the velocity  $u_\zeta$ :

$$\Phi_g^{cv} = \dot{m}_F h_{s,F}(T_\zeta), \quad (4.34)$$

The other contribution on the gaseous side is the conductive heat transfer  $\Phi_g^c$  which is proportional to the temperature gradient at the surface:

$$\Phi_g^c = \left( -4\pi r_p^2 \lambda \frac{dT}{dr} \right)_\zeta \quad (4.35)$$

Similarly, there is also a convective and a conductive contribution on the liquid side. Mass conservation at the interface states that the mass flux in the liquid is the same as the one in the gaseous phase. On the liquid side however, this mass flux transports the sensible enthalpy of the liquid  $h_{s,p}(T_\zeta)$ . The liquid convective flux  $\Phi_l^{cv}$  is thus defined as:

$$\Phi_l^{cv} = -\dot{m}_F h_{s,p}(T_\zeta). \quad (4.36)$$

The liquid conductive flux  $\Phi_l^c$  depends on the temperature gradient at the surface inside the droplet:

$$\Phi_l^c = \left( -4\pi r_p^2 \lambda \frac{dT_p}{dr} \right)_\zeta. \quad (4.37)$$

However, as the droplet temperature is assumed constant, this expression can not be evaluated directly. Replacing the convective contributions in Eq. 4.33 leads to:

$$-\dot{m}_F h_{s,p}(T_\zeta) + \Phi_l^c + \dot{m}_F h_{s,F}(T_\zeta) + \Phi_g^c = 0. \quad (4.38)$$

Using the definition of the latent heat  $L_v$  yields the following form:

$$\Phi_l^c = -\Phi_g^c - \dot{m}_F L_v(T_\zeta). \quad (4.39)$$

The total heat flux out of the liquid phase  $\Phi_l^{cv} + \Phi_l^c$  is directly linked to the temporal evolution of the liquid enthalpy:

$$\frac{d}{dt} [m_p h_{s,p}(T_p)] = \Phi_l^{cv} + \Phi_l^c \quad (4.40)$$

Splitting up the temporal derivative on the left hand side and substituting  $\Phi_l^{cv}$  according to Eq. 4.36 gives:

$$\frac{dm_p}{dt} h_{s,p}(T_p) + m_p \frac{dh_{s,p}(T_p)}{dt} = -\dot{m}_F h_{s,p}(T_\zeta) + \Phi_l^c. \quad (4.41)$$

The droplet temperature is constant over  $r$ , so  $T_\zeta$  equals  $T_p$ . Furthermore, the gaseous fuel mass flux  $\dot{m}_F$  can be substituted by the variation of the droplet mass  $\dot{m}_p$ , leading to:

$$\frac{dm_p}{dt} h_{s,p}(T_p) = \dot{m}_p h_{s,p}(T_\zeta). \quad (4.42)$$

Moreover, the variation of the liquid sensible enthalpy,  $d(h_{s,p}(T_p))$ , can be expressed as:

$$d(h_{s,p}(T_p)) = C_{p,l} dT_p. \quad (4.43)$$

Injecting Eqs. 4.43 and 4.42 into Eq. 4.41 finally yields a law for the Lagrangian temporal derivative of the droplet temperature:

$$\frac{dT_p}{dt} = \frac{1}{m_p C_{p,l}} \Phi_l^c \quad (4.44)$$

$\Phi_l^c$  can be substituted using Eqs. 4.39-4.21:

$$\frac{dT_p}{dt} = \frac{1}{m_p C_{p,l}} \left( -\Phi_g^c + \dot{m}_p L_v(T_\zeta) \right) \quad (4.45)$$

Note that the evolution of the droplet temperature given by Eq. 4.44 depends on the liquid conductive heat exchange  $\Phi_l^c$  which, in most cases, only plays a role during the droplet heat-up phase at the onset of evaporation. At later phases in the evaporation process, the terms  $-\Phi_g^c$  and  $\dot{m}_p L_v(T_\zeta)$  will balance each other so that  $\Phi_l^c$  goes to zero. The droplet then trends towards an equilibrium temperature called the "wet bulb temperature" ( $T_{wb}$ ). Simpler evaporation laws like the d2-law are based on the assumption that this equilibrium conditions is always satisfied. Similarly to the saturation pressure, the latent heat of vaporization  $L_v$  is tabulated as a function of the temperature in AVBP. The conductive heat flux in the gas  $\Phi_g^c$  is obtained integrating Eq. 4.20 twice. Assuming a constant thermal conductivity  $\lambda$  yields:

$$\Phi_g^c = \pi d_p \lambda N u (T_\zeta - T_\infty) \frac{\ln(B_T + 1)}{B_T}, \quad (4.46)$$

where  $B_T$  is the Spalding thermal number that may be estimated as a function of the Spalding mass number:

$$B_T = (1 + B_M)^\beta - 1, \quad (4.47)$$

with:

$$\beta = \frac{ShPr}{NuSc_F}, \quad (4.48)$$

where  $Nu$  is the Nusselt number, representing the ratio between the convective and the conductive heat transfer (normal to the droplet boundary). It is also equal to 2 in a quiescent atmosphere.

#### Abramzon-Sirignano evaporation model

The Spalding evaporation model does not take into account the existence of a relative flow around the droplet. The presence of this relative flow leads to two main issues:

- When the particle Reynolds number  $Re_p$  is different from zero, a boundary layer is generated around the droplet. This boundary layer depends on  $Re_p$  and leads to an increase of the mass and heat transfers.

## 4.2 Macroscopic models for an isolated droplet

---

- The relative flow introduces a shear stress at the surface of the droplet, causing circulation movements within droplet. These movements tend to homogenize the droplet temperature.

The evaporation rate increases with the relative velocity of the flow, and thus with the particle Reynolds number. To take into account this change, the most common approach consists in correcting the evaporation and heat transfers obtained for a quiescent flow through modified Sherwood and Nusselt numbers. The most common modification is the one proposed by Ranz and Marshall [152]:

$$Sh = 2 + 0.55Re_p^{1/2}S_{cf}^{1/3}, \quad (4.49)$$

$$Nu = 2 + 0.55Re_p^{1/2}P_r^{1/3}. \quad (4.50)$$

Abramzon and Sirignano [153] have proposed another approach to modify the Sherwood and Nusselt numbers taking into account the convective boundary layer in the derivation of their model. Using the film theory that defines the mass and thermal thickness of the boundary layer, two correction factors  $F_M$  and  $F_T$  are proposed:

$$F_x = (1 + B_x)^{0.7} \frac{\ln(1 + B_x)}{B_x}, \quad (4.51)$$

where  $x = M$  or  $T$ . The modified Sherwood and Nusselt numbers are thus expressed as:

$$Sh^* = 2 + \frac{(Sh - 2)}{F_M}, \quad (4.52)$$

$$Nu^* = 2 + \frac{(Nu - 2)}{F_T}, \quad (4.53)$$

where  $Sh$  and  $Nu$  are obtained with Eqs. 4.49-4.50.



# **III Application of the turbulent gaseous combustion models**

<b>5</b>	<b>Influence of chemical schemes, numerical method and dynamic turbulent combustion modeling on LES of premixed turbulent flames .....</b>	<b>69</b>
5.1	Introduction	
5.2	Chemistry description	
5.3	The TFLES model for flame/turbulence SGS interactions	
5.4	Second and third-order LES convection schemes	
5.5	The VOLVO experiment	
5.6	Results	
5.7	Conclusion	



# Influence of chemical schemes, numerical method and dynamic turbulent combustion modeling on LES of premixed turbulent flames

The objective of this Chapter is to contribute to the understanding of the mechanisms related to turbulent combustion, and to propose a LES modeling strategy in the framework of the thickened flame model to improve the fidelity of such reactive simulations. This Chapter is based on a paper published in Combustion and Flame (2018) [154].

## 5.1 Introduction

The quest for a universal turbulent combustion model has been going on for a long time [18, 26, 155, 156] but it has become more challenging in the last years. Today, turbulent combustion models are not only expected to provide reasonable estimates of mean heat release or temperature fields but also additional targets such as (1) pollutant emissions (NO<sub>x</sub> and CO for example) as well as soot, (2) possible combustion instabilities and noise level, (3) ignition and quenching phenomena. All these objectives must be satisfied for (4) liquid fuels, and (5) the detailed chemistry characteristics of real fuels must be included.

To satisfy these five objectives, the introduction of Large Eddy Simulation (LES) has offered a powerful approach [26, 157, 158, 159] not because the subgrid LES models are better than their classical Reynolds Averaged (RANS) counterparts but because they are applied to a more limited part of the turbulence spectrum, while the rest of the unsteady activity is directly captured by the simulation. LES applied to combustion permits a better identification, at resolved scales, of the intermittency between fresh and burnt gases regions (where properties of turbulence, pollutant emissions, etc., are different) than RANS. However, what the last ten years have shown is that LES was only part of the solution. Many other ingredients remain necessary both on the physical and the numerical aspects to make LES predictive.

There are a few usual test cases for LES of reacting flows. For turbulent swirling flames, the PRECCINSTA chamber of DLR [160] has been computed many times [141, 161, 162, 163, 164, 165]. Since PRECCINSTA is a swirled flame, many authors have started validations with an unswirled configuration and the so-called 'VOLVO' turbulent flame [166, 167, 168] has been used as a benchmark for turbulent combustion codes for a long time [169, 170, 171] for steady flames as well as for combustion instabilities [170]. Multiple solvers were applied for the VOLVO flames, leading to results which were all different [169] showing the lack of maturity of LES for turbulent flames. Considering that the VOLVO flames are fully premixed, gaseous flames, this indicates that major efforts are still required to address real flames such as those found in gas turbines for example.

## **Chapter 5. Influence of chemical schemes, numerical method and dynamic turbulent combustion modeling on LES of premixed turbulent flames**

The reasons why large discrepancies are observed for the VOLVO flames are not clear yet. Most solvers provide consistent, similar results for the cold flow in this setup, matching experimental data and demonstrating that the difficulties begin with combustion. Understanding which parts of the numerical strategy control the quality of the solution with combustion is a first but difficult step. Multiple potential sources of differences may be listed: (A) chemistry description, (B) flame / turbulence interaction model, (C) quality of the numerical solver, (D) boundary conditions, especially impedances at inlet and outlet which control the intensity of thermoacoustic modes, (E) wall numerical treatments, (F) wall temperatures and heat losses. The present work focuses on the first three sources (A) chemistry, (B) flame turbulence SGS models and (C) numerics.

Even if turbulent premixed flames can often be treated as thin interfaces, knowing whether the dynamics of these interfaces (response to small scale turbulence, to strain, to curvature) is really captured correctly for a given chemical scheme remains a daunting question for the LES community. Moreover, since objective (1) in real flames is to correctly capture all important species, LES chemical models must include more and more chemistry details. Knowing how the LES solution changes when a reasonably complex chemical scheme is used instead of a heuristic one or two-step scheme is the first objective of the present work. This objective is similar to the recent work of Zettervall *et al.* [171]. Note that it depends not only on the chemical scheme but also on the flame/turbulence interaction model (B) used in the LES. Here the TFLES (Thickened Flame model) is retained with either an usual non-dynamic (called static in the following) or a dynamic subgrid scale formulation. The third source (C) influencing the quality of LES results is the quality of the discretization scheme itself. This question is rarely discussed in the combustion community but is central in the aerodynamics community where the search for high-order methods has driven research for a long time. In the present study, a second and a third/fourth order method (space accuracy<sup>1</sup>) are compared: results show that turbulent structures and therefore the whole flame structure are indeed sensitive to the spatial accuracy of the discretization scheme, thereby explaining why different LES solvers often lead to different results even when all physical models are the same.

Of course, the three modeling sources affecting LES studied here (A-chemistry, B-SGS turbulent combustion model and C-numerics) are not the only ones controlling the quality of LES results. The present work aims only at demonstrating that these three are important and that the quality of LES solutions cannot be investigated if these aspects are not properly considered.

### **5.2 Chemistry description**

In most turbulent flames, chemistry description can rapidly become an issue. The Volvo experiment is a usual benchmark for codes which ultimately will have to handle kerosene flames. Even if simplified chemical schemes (one or two steps) can be used for the premixed propane/air flames of the Volvo rig, going to more precise chemical schemes has become a necessity: today such options are readily maturing and for example, Analytically Reduced Chemistry (ARC) tools can produce chemical schemes that LES can fully resolve [110, 111]. Here, two chemical schemes have been used to describe propane-air flames.

#### **5.2.1 A two-step scheme for propane-air flames**

The first scheme is a two-step scheme based on a fast oxidation reaction followed by a CO-CO<sub>2</sub> equilibrium. Six species are taken into account ( $C_3H_8$ ,  $O_2$ ,  $CO_2$ ,  $CO$ ,  $H_2O$  and  $N_2$ ) and two

<sup>1</sup>The TTGC scheme used here [181] is fourth order accurate on regular unstructured grids and third order on arbitrary grids.

## 5.2 Chemistry description

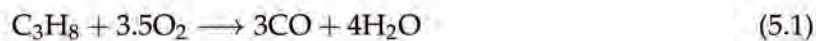
	$A_j[\text{cgs}]$	$E_j[\text{cgs}]$
Reaction 1	$2.0 \times 10^{12}$	$3.3 \times 10^4$
Reaction 2	$4.51 \times 10^{10}$	$1.2 \times 10^4$

**Tab. 5.1.** Two-step reduced chemical mechanism for  $C_3H_8 - Air$ . Pre-exponential factor  $A_j$  and activation energies  $E_j$  are both in cgs units [170].

Transported species (22)	QSS species (12)
$N_2, O, O_2, H, OH$	$CH_2GSG-CH_2, CH_3O, C_2H_5, HCO, HCCO$
$H_2, H_2O, H_2O_2, HO_2, CO$	$C_2H_3, CH_2CHO, C_3H_5-A-C_3H_5, I-C_3H_7, N-C_3H_7$
$CH_2O, CH_3, C_2H_6, CH_4, C_2H_4$	$I-C_3H_7O_2, N-C_3H_7O_2$
$CO_2, CH_3O_2, CH_3O_2H, C_2H_2, C_3H_6$	
$C_3H_5O, C_3H_8$	

**Tab. 5.2.** Summary of ARC – 22 – 12QSS: transported (left) and Quasi Steady State (QSS) (right) species.

reactions [170]:



The reaction rates  $q_j$  follow an Arrhenius law:

$$q_1 = A_1 \left( \frac{\rho Y_{C_3H_8}}{W_{C_3H_8}} \right)^{0.9028} \left( \frac{\rho Y_{O_2}}{W_{O_2}} \right)^{0.6855} \exp \left( \frac{-E_{a,1}}{RT} \right) \quad (5.3)$$

$$q_2 = A_2 \left[ \left( \frac{\rho Y_{CO}}{W_{CO}} \right)^{1.0} \left( \frac{\rho Y_{O_2}}{W_{O_2}} \right)^{0.5} - \frac{1}{K} \left( \frac{\rho Y_{CO_2}}{W_{CO_2}} \right)^{1.0} \right] \exp \left( \frac{-E_{a,2}}{RT} \right) \quad (5.4)$$

The pre-exponential constants  $A_j$  and the activation energies  $E_j$  are given in Table 8.2, and  $K$  is the equilibrium constant [96].

### 5.2.2 An analytically reduced scheme (22 species) for propane-air flames

The second method is based on the ARC approach. Using YARC reduction tools [109], the ARC chemical scheme is constructed from a skeletal mechanism proposed by Jerzembeck [172] using 99 transported species and 669 reactions. This skeletal scheme was derived from the LLNL detailed mechanisms for n-heptane [173] and iso-octane [174]. Laminar flames with an equivalence ratio in the range  $\phi = 0.5 - 1.6$  are chosen as the sampled reference cases for the reduction process. The first step of the methodology is to discriminate unimportant species and reactions using the directed relation graph method with error propagation [109]. Then, suitable species for Quasi-Steady State Approximation (QSSA) are selected using the Level Of Importance criterion [175]. The resulting ARC chemical scheme (named ARC-22-12QSS in the following) treats 22 transported species and 12 QSS species (Table 5.2).

### 5.2.3 Comparison of two-step and ARC schemes on premixed laminar flames

Since the VOLVO experiment is fully premixed, a good method to compare chemical schemes is to apply them for premixed laminar flames. This is done here in terms of flame speeds and response to strain at atmospheric pressure. Adiabatic flame temperatures are not presented because they match very well for both schemes. The two-step and ARC schemes are validated

## Chapter 5. Influence of chemical schemes, numerical method and dynamic turbulent combustion modeling on LES of premixed turbulent flames

against the Jerzembeck skeletal mechanism [172] in Fig. 7.1. Flame speeds are computed using Cantera for a 1D resolved planar flame, at the operating conditions used for the LES simulations ( $T_0 = 288K$  and  $P_0 = 101325Pa$ ): results show a good agreement for the ARC scheme and a slight overestimation of the flame speed for the two-step reduced chemistry.

Flame response to stretch was also studied using 1D premixed counter-flow flames computed with Cantera. Premixed fresh gases are injected on one side and burnt gases at the adiabatic flame temperature on the other. For consistency with the counter-flow configuration where the flame is stabilized on a stagnation plane, the consumption speed  $S_c$  based on the spatial integral of the fuel consumption rate, is retained to study the flame response to stretch. Fig. 5.2 shows that the ARC mechanism captures stretch effects as well as the full scheme while the two-step mechanism overestimates them.

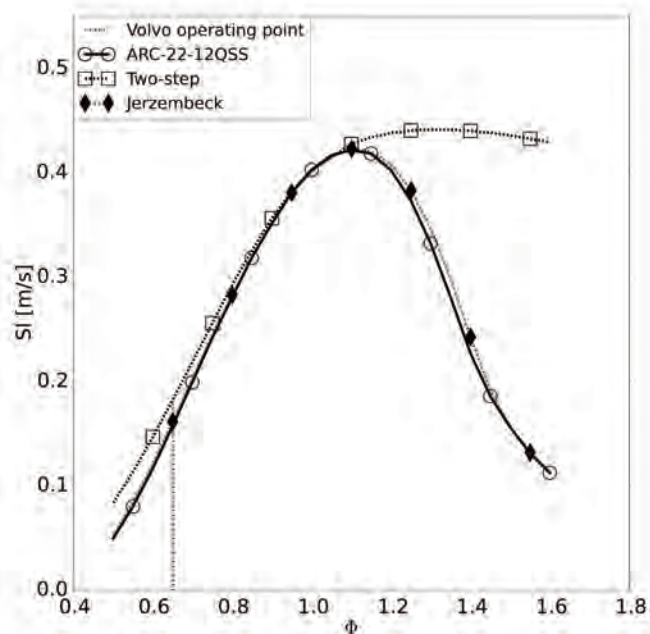


**Fig. 5.1.** Comparison of Jerzembeck skeletal mechanism [172], two-step and ARC chemistry for laminar flame speed,  $T_0 = 288K$ ,  $P = 101325Pa$ .

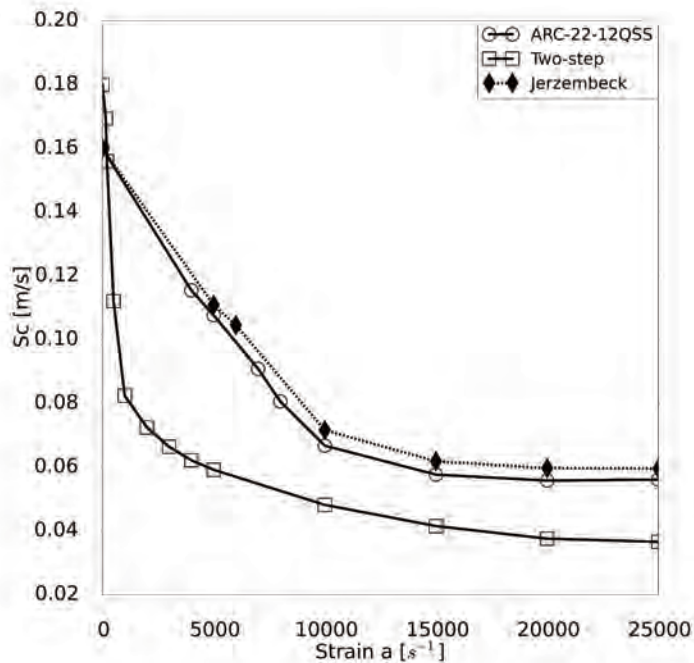


**Fig. 5.2.** Comparison of Jerzembeck skeletal mechanism [172], two-step and ARC flame consumption speed response to stretch,  $\Phi = 0.65$ ,  $T_0 = 288K$  and  $P = 101325Pa$ .

### 5.3 The TFLES model for flame/turbulence SGS interactions

Using a precise chemical scheme is only part of the solution in a LES solver. Handling the subgrid scale interaction model between turbulence and flames is a second critical part. This question has been central in the RANS community for decades [176, 177, 178] and it would be a mistake to believe that it can simply be ignored in LES codes: the interaction between turbulence and flames must be modeled. The first reason for this is that flame fronts are usually too thin to be resolved even on LES grids and a model is required to handle this difficulty. Discussing all possible models for SGS in combustion is beyond the objectives of this study. However, it is worth mentioning that the constraint of using complex chemical schemes with multiple independent species strongly limits possible choices for turbulent combustion models. Tabulation techniques for example, which assume frozen flamelet structures and have been very successful in the past [118, 179], probably reach their limits here because they constrain the chemical state to a manifold of limited dimension (2 or 3). Similarly, using pdf methods [180] becomes difficult: with ARC chemistry for the present  $C_3H_8$ -air flames, 22 independent species are used leading to a pdf space of dimension 23 (with temperature). In the present study, the TFLES (Thickened Flame) model has been used with the static Charlette efficiency function, and the dynamic Charlette saturated efficiency function. This TFLES model explicitly estimates conservation equations for all species considered in the chemical scheme, thickening their spatial structure to allow its resolution on the numerical grid and accounting for sub-grid scale thickening effects through an efficiency function based on DNS. Therefore, it is compatible with complex schemes such as ARC as described in the previous section.

A second characteristic of turbulent combustion models is that they all rely on a few constants which are often adjusted by the user to match the overall flame structure. This is true also for the standard static Charlette efficiency function where a  $\beta$  constant is user specified in the expression of the sub-grid efficiency. In the present work, we propose to move to a fully dynamic model [134, 136, 138, 140, 141, 181] where this  $\beta$  coefficient is automatically determined and therefore, not user-adjustable anymore.

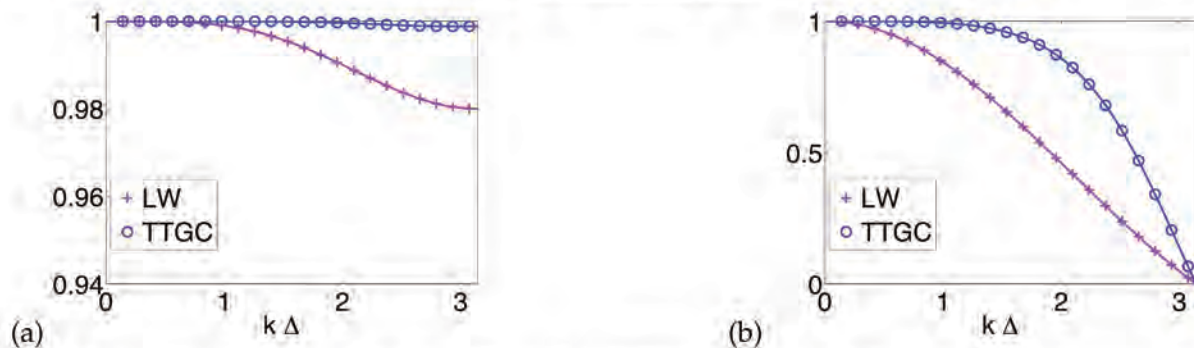


**Fig. 5.3.** Amplification function of the Lax-Wendroff and TTGC schemes for a CFL number of 0.1: (a) modulus of the amplification function and (b) relative phase velocity as a function of the non-dimensional wave number  $k\Delta_x$ .

#### 5.4 Second and third-order LES convection schemes

An additional component of LES lies in the numerical schemes adopted by the CFD solver. Different numerical strategies are possible to solve the set of modeled LES equations. These numerical schemes can be either explicit or implicit, the effective difference being the size of the time-step accessible to the numerical integrator without leading to numerical instabilities or affecting the actual flow reference time scales targeted by the simulation. Implicit solvers are often advocated although this choice may induce difficulties in the parallelization of the algorithms and their efficiency with increasing numbers of processors. Furthermore, arbitrarily imposing a time step several orders of magnitudes higher than the smallest cell size to flow speed ratio naturally raises precision issues and comes with undesirable dispersive/dissipative properties of the solver which can overshadow the modeling. In the following, only fully compressible explicit schemes are tested: (a) the Lax-Wendroff scheme [182] (LW) which is second order in time and space and (b) the TTGC scheme [183] which offers third order accuracy in time and space on arbitrary unstructured meshes.

LW is a finite-volume based scheme where increased accuracy is obtained by use of the flux Jacobian instead of the second order derivative [184] present in the original temporal Taylor expansion of the problem. TTGC relies on a Finite Element approach used in the context of a two-step temporal scheme [185]. This approach provides a family of schemes with adjustable temporal coefficients providing third order accuracy in space and time [183]. TTGC schemes also use a mass matrix which improves the spectral properties compared to the more conventional finite volume scheme that is LW.

For a typical CFL condition of 0.1 (based on the local mesh characteristic size and acoustic wave speed which involves the flow speed and sound velocity), these schemes have very distinct spectral features as evidenced by Fig. 5.3 which shows the amplification factor ((a) its norm and (b) its phase) of each scheme for a 1D convection problem. For high wavelengths that can be captured by a reasonable number of points ( $0 < k\Delta_x < 1$  where  $k$  stands for the wave number), the signal can be transported without too much numerical dissipation, Fig. 5.3(a), and at the correct speed, Fig. 5.3(b). Differences start however appearing for both properties around  $k\Delta_x \approx 1$ . For shorter wavelengths or equivalently larger non-dimensional wave numbers, two distinct behaviors are clearly shown. Beyond  $k\Delta_x \approx 1$ , TTGC is clearly superior both in terms of dissipation and dispersion. This implies that the TTGC scheme can preserve the small-scale structures generated in high shear regions better than LW for the same grid resolution. Note that these structures may be of potential importance at the flame front because they are the source of flame wrinkling. This can be even more critical with complex chemical schemes where multiple chemical scales are present and the response of the flame to the flow structures can be of importance. For the same reason, the generation of flow

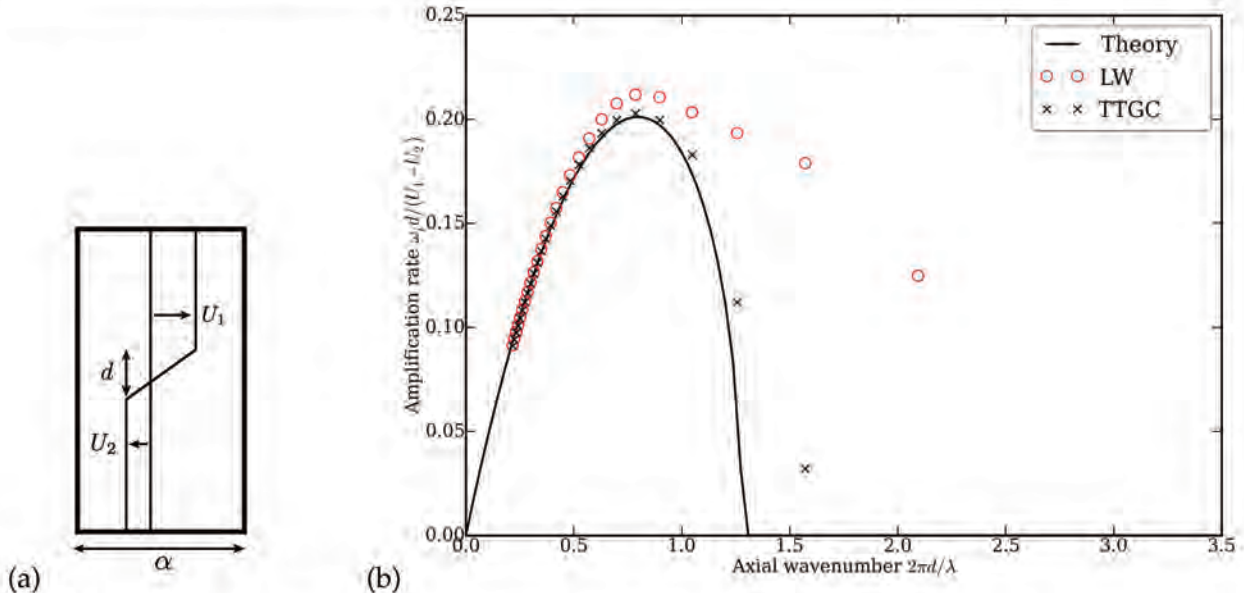


**Fig. 5.4.** (a): Schematic of the numerical case to study the growth of a perturbation super-imposed onto an inviscid piecewise linear velocity field of thickness  $d$ . (b): Non-dimensional growth rate,  $\omega_i d / (\Delta U)$ , of a perturbation using TTGC or LW for a CFL condition of 0.7.

instabilities will be impacted by the numerical scheme as linearly unstable modes may grow or be damped depending on the grid resolution and equivalently the scheme properties. This specific difficulty is illustrated in Fig. 5.4 for the growth of a spatial perturbation of wavelength  $\lambda$  by a piecewise continuous velocity deficit noted  $\Delta U$ . Solved analytically by Rayleigh [186], this problem can be resolved numerically for numerical scheme assessment. Fig. 5.4(b) presents the comparison between theory, TTGC and LW. For all simulations, the grid is 2D, uniform, made of square cells of size  $\Delta_x = 8$  mm.  $d$  corresponds to the length of the velocity ramp between  $U_1$  and  $U_2$  (here  $d = 0.1$  m). Only the axial length  $\alpha$  (Fig. 5.4(a)) of the computational domain is changed and matches the initial perturbation wavelength  $\lambda$ . This results in a fixed axial spacing to wavelength ratio, the problem being resolved for thirty different values of the wavelength  $\lambda$  covering the range [0.3 – 2.5 m].

For large wavelength perturbations (low values of  $d / \lambda$ ) both schemes perform well. Beyond  $\frac{2\pi d}{\lambda} = 0.8$ , however, the LW scheme greatly overestimates the linear growth rate of the perturbation while TTGC is much closer to the analytical solution. Again, this suggests that high order schemes are better suited to LES of reacting shear flows.

## 5.5 The VOLVO experiment

### 5.5.1 Experimental configuration

The VOLVO combustor [166, 167, 168] (Fig. 5.5) is a straight rectangular cross-section channel ( $0.12$  m  $\times$   $0.24$  m), divided into an inlet section, and a combustor section ending into a round exhaust. The total length of the configuration (without exhaust) is 1.55 m. Gaseous propane is injected and premixed with air in the inlet section, upstream of a honeycomb used to generate a turbulence level equal to 3% of the inlet bulk velocity [166]. Three bluff-body flameholders were used during the experimental tests, but only the equilateral triangular-shaped one of height  $h = 0.04$  m is studied in the current work. The top and bottom walls of the combustor are water-cooled and the side walls are air-cooled in order to accommodate the quartz windows for optical access. The cooling temperature is not provided in the experiments [166]. Experimental data, including high-speed and Schlieren imaging, gas analysis, Laser Doppler

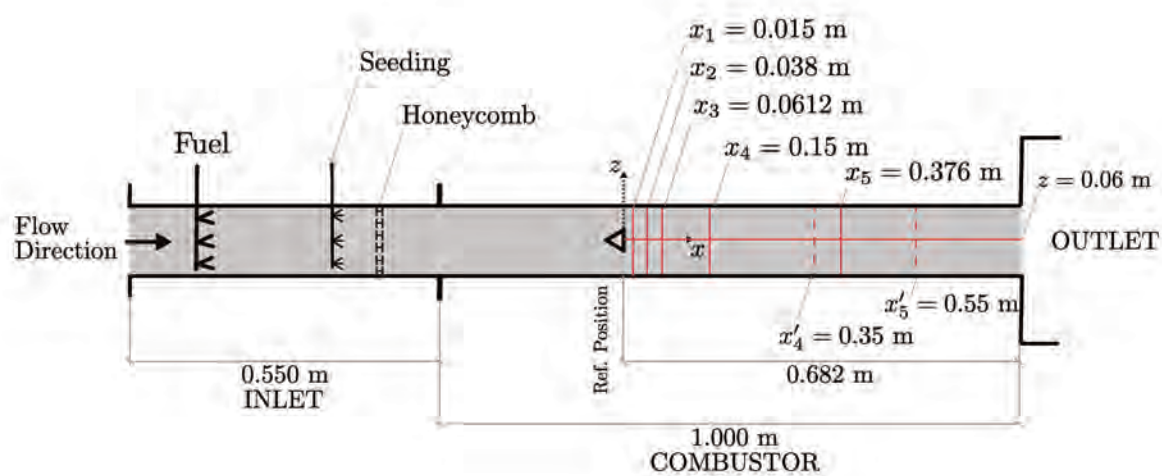


**Fig. 5.5.** The VOLVO rig combustor. The computational domain is identified by the shaded area. Note that some of the geometrical complexities of the experimental rig (fuel injection, seeding and honeycomb) are omitted in LES the representation.

## 5.5 The VOLVO experiment

---

Publications	$\phi$	$U_0$ (m/s)	$T_0$ (K)	Re	Comment
Sjunnesson et al. [168]	0.65	16.6	288	48000	Measurements: $T$ and $Y_{CO}$
Sjunnesson et al. [166]	0.65	17.3	288	47000	Measurements: $U$ , $U_{rms}$ , $V$ and $V_{rms}$
Sjunnesson et al. [167]	0.61	17.3	288	47000	Measurements: $T$ and $T_{rms}$
Zettervall et al. [171]	0.62	17.6	288	46592	LES: $U$ , $V$ , $V_{rms}$ , $T$ , $T_{rms}$ , $Y_{CO}$
Present work	0.65	17.3	288	47000	LES: $U$ , $V$ , $U_{rms}$ , $V_{rms}$ , $T$ and $T_{rms}$

**Tab. 5.3.** Comparison between the operating point used in the present work and available literature measurements and operating points.

Velocimetry (LDV), and Coherent Anti-Stokes Raman Scattering (CARS), are used to investigate a baseline case described in Table 5.3. For the operating point used in the present work, only velocity and turbulence data are available [166]. We will also compare mean [168] and RMS [167] temperature profiles, but note that these data were obtained experimentally at slightly different operating points (Table 5.3). Measurements were made on seven longitudinal ( $x_1, x_2, x_3, x_4, x'_4, x'_5$  and  $x_5$ ) and one ( $z$ ) transverse locations (Fig. 5.5).

Additional cases experiencing different types of combustion instabilities also exist [170] but here, only the stable case is studied to quantify the influence of chemical schemes, turbulent combustion models and numerical schemes.

### 5.5.2 Numerical setup

LES is performed using the AVBP solver co-developed by CERFACS and IFPEN [93]. It solves the fully compressible multispecies Navier-Stokes equations on unstructured grids. The computational domain is shown in Figs. 5.5 and 5.6. In the longitudinal direction, it includes the entire burner (the inlet and combustor sections). In the transverse direction, the mesh includes exactly the chamber transverse dimension (0.24 m) and not only a slice of it, as done in previous papers [187, 188, 189], to capture all large scale effects as well as transverse acoustic modes. Two elements which were not fully characterized in the experiments (fuel feeding line and honeycomb) are not considered in the simulations since their impacts on the results are marginal [170]: fully premixed gases are injected at the inlet of the LES and replace the fuel feeding line. Turbulence is injected at  $x = 0$  m in the inlet plane.

The unstructured mesh comprises 68 million tetrahedral elements and is refined in shear and combustion regions (Fig. 5.6). The mesh size in the flame zone just downstream of the flameholder is  $\Delta_x = 500\mu m$ , whereas the laminar flame thickness is  $\delta_L^0 = 650\mu m$ , leading to a minimum thickening factor  $F \approx 5$  when choosing 7 points to resolve the flame structure. The integral scale is estimated as the distance between the top (or bottom) wall of the burner and the bluffbody upper (or lower) edge:  $l_t = 0.04m$ . Using a turbulent RMS velocity  $u' \approx 0.26$ , the Karlovitz number is estimated as:  $Ka \approx 0.2$  for both two-step and ARC schemes. As  $Ka < 1$  and  $u' > S_L^0$ , combustion occurs in the turbulent flamelet regime, the flame front is wrinkled and thinner than all turbulent scales [17]. The near wall region of the flame holder features dimensionless wall distances of  $y^+ = 25$ , versus  $y^+ = 80$  near the combustor walls.

Inlet and outlet boundary conditions are treated with Navier-Stokes Characteristic Boundary Conditions (NSCBC) [190]. To avoid exciting a particular acoustic mode, these two boundary conditions are modeled as non-reflecting sections. Turbulence is injected at the inlet using the method of Guezenne and Poinsot [191]. The turbulence intensity of the inlet section is equal to 8 % of the bulk velocity  $U_0$  and decreases at the honeycomb position to 3 %, which corresponds to measurements obtained at this position [166]. To avoid choosing a particular

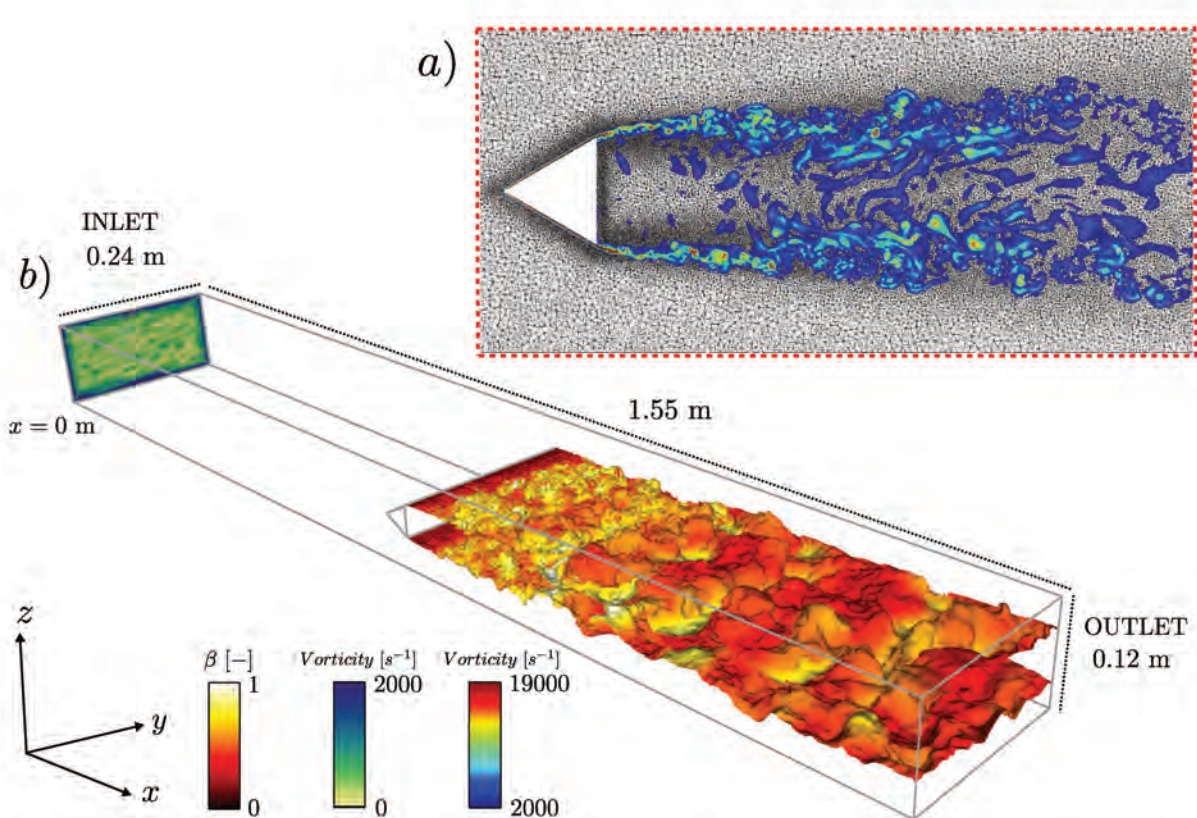


**Fig. 5.6.** Overview of the computational domain, with a focus on the unstructured mesh refinement downstream of the flame holder, at  $y = 0.12$  m (a). The flame is represented through an iso-surface of progress variable  $c = 0.5$ , colored by  $\beta$  of run 2s – ttgc – dyn (red colormap, b). The vorticity field ranging from  $0 s^{-1}$  to  $2000 s^{-1}$  is represented by the green colormap (inlet, b) whereas the vorticity field ranging from  $2000 s^{-1}$  to  $19000 s^{-1}$  is represented by the rainbow colormap (a).

## 5.6 Results

Simulations	Turbulent combustion model	Chemical scheme	Numerical scheme	Normalized CPU cost	Normalized averaging time
2s-lw	non-dynamic	two-step	LW	1	4.2
2s-ttgc-dyn	dynamic	two-step	TTGC	2.5	2.4
2s-lw-dyn	dynamic	two-step	LW	1.6	3.3
arc-lw-dyn	dynamic	ARC-22-12QSS	LW	3.2	2.92
arc-ttgc-dyn	dynamic	ARC-22-12QSS	TTGC	5.5	3.6

**Tab. 5.4.** Summary of simulated cases, CPU costs (normalized by the fastest computation:  $2s - lw$ ) and averaging time (normalized by the flow through time  $\tau$  computed with the distance from the backward wall of the bluff-body to the end of the combustion chamber:  $\tau = 39ms$ ). Note that statistical convergence is achieved for a normalized averaging time  $\approx 1.3$ .

cooling temperature (not provided in experiments [166]), the walls are modeled as adiabatic no-slip walls. The unique closure coefficient  $\beta_{Ch}$  of the Charlette static formulation model is set to the standard value:  $\beta_{Ch} = 0.5$ . For the dynamic formulation of Eq. 3.99, filter ratio between effective filtered and filtered scales, and averaging filter widths are set to  $\Delta = 1.4F\delta_L^0$ ,  $\gamma = 2.2$  and  $\Delta_{avg} = 2.5\Delta$  respectively. The value 1.4 is a calibration factor introduced by Wang et al. [134] in order to recover  $\beta = 0$  and  $\Xi_\Delta = 1$  for planar laminar flames. Results are very weakly dependent on these parameters [140].

## 5.6 Results

Table 5.4 summarizes the VOLVO cases simulated. All dimensions, velocities and velocity fluctuations are made dimensionless with the flameholder height,  $h = 0.04$  m, and the inlet bulk velocity  $U_0 = 17.3$  m/s respectively. Only reacting results are presented. Cold flow results match the experimental data of Sjunnesson [166] very well in terms of mean and RMS values.

### 5.6.1 Influence of the turbulent combustion model

The effects of the turbulent combustion static and dynamic formulations are investigated first. Figure 5.7 compares the mean axial velocity profiles computed with the non-dynamic and the dynamic formulations. The dynamic approach does not have a major impact on these results. The spatial evolution of the  $\beta$  parameter along the flame front computed with the dynamic formulation is illustrated on Fig. 5.8. On the major part of the flame,  $\beta$  is close to  $\beta_{Ch} = 0.5$ , except downstream of the bluff-body and at the end of the flame, where  $\beta < \beta_{Ch}$ . This explains why the dynamic formulation has a limited impact on the burnt gas velocity for this case. Note that this comparison can be misleading: the dynamic model procedure determined the values of  $\beta$  on its own while the  $\beta_{Ch} = 0.5$  value is specified by the user and can be adjusted to fit the experimental data. Going to a dynamic formulation removes one user-specified constant and significantly increases the prediction capacities of the model. Figure 5.9 top provides a scatter plot view for all points in the flame of thickening factor  $F$  as a function of the local temperature-based progress variable  $c$  for two cases:  $2s - lw - dyn$  (triangles), and a 1D resolved laminar premixed flame computation (black line). Points are considered to be in the flame when their heat release rates are different from zero. The maximum  $F$  values are obtained either in highly reacting points or in places where the mesh is not very fine.  $F$  never exceeds 30 and most points have  $F$  values of the order of 5 to 10. Figure 5.9 bottom displays a scatter plot of the fuel reaction rate as a function of the progress variable. As expected, compared to the laminar flame (solid line), the reaction rate is reduced by a factor  $F$  due to the thickening procedure. The PDF of  $\beta$  over the whole domain is given in Fig. 5.10. The value  $\beta = 0.5$  used

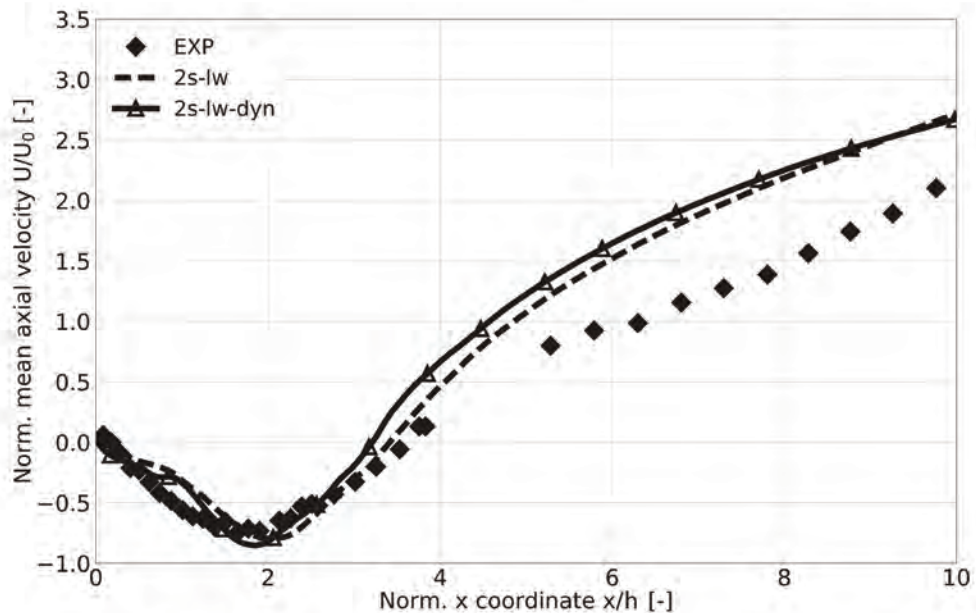


**Fig. 5.7.** Mean axial velocity evolution along the central axis of the Volvo burner measured experimentally and obtained by LES with the Charlette static model ( $\beta_{Ch} = 0.5$ ) and the Charlette dynamic model. The axis measures the downstream location from the backward wall of the bluff-body (cf. axis  $x$  at  $z = 0.06$  m in Fig. 5.5).

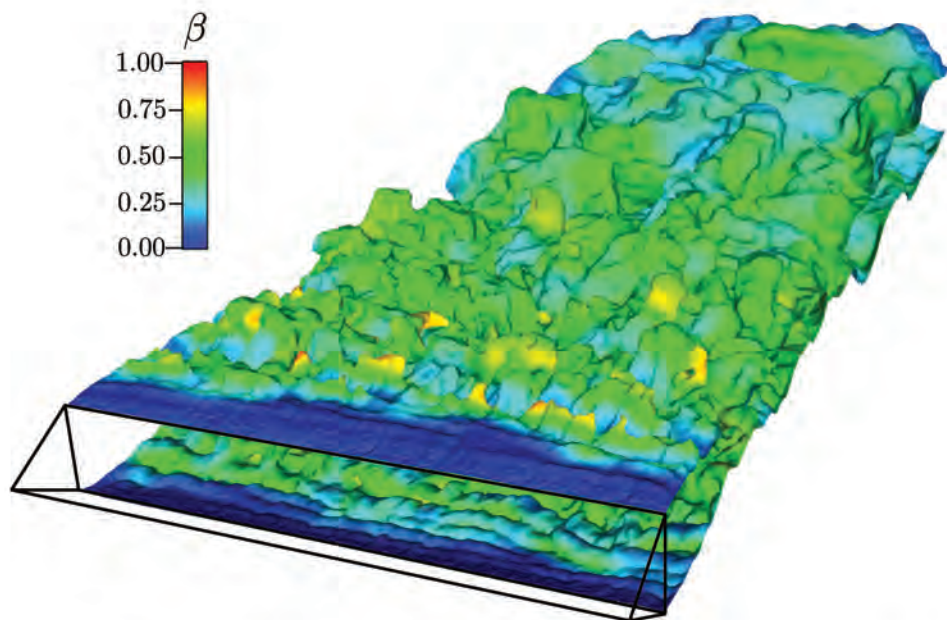


**Fig. 5.8.** Iso-surface of the progress variable  $c = 0.5$ , colored by the  $\beta$  parameter computed with the dynamic formulation (case 2s – lw – dyn).

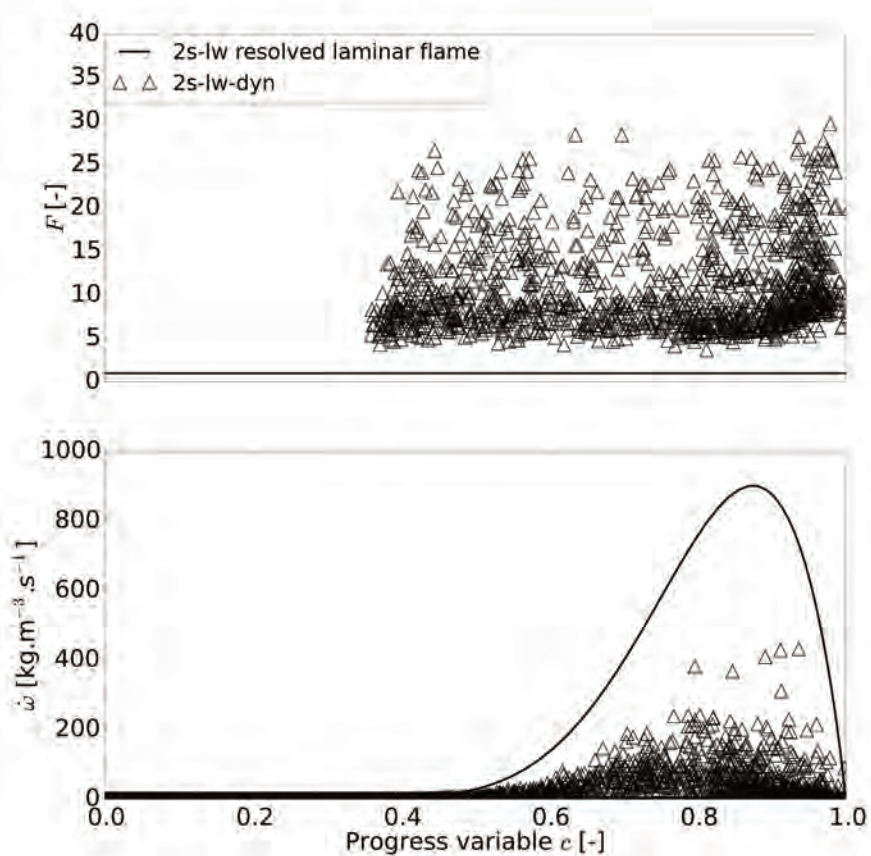


**Fig. 5.9.** Scatter plot of the thickening factor  $F$  where heat release rate is different from zero (top) and the fuel reaction rate (bottom) as a function of the temperature-based progress variable  $c$ . The black line corresponds to a 1D resolved unthickened laminar premixed flame computed at  $\phi = 0.65$ ,  $T_0 = 288\text{K}$  and  $P_0 = 101325\text{Pa}$  (case 2s - lw - dyn).

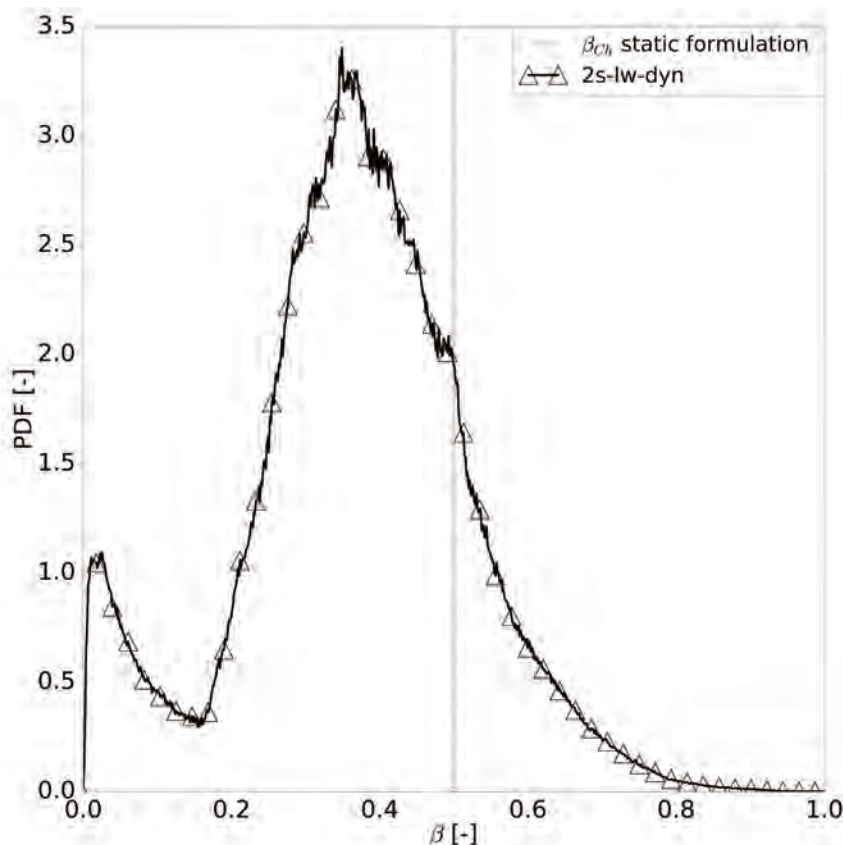


**Fig. 5.10.** PDF of the wrinkling exponent  $\beta$  (3.99) computed along the flame front, for a progress variable ranging between  $0.4 \leq \bar{c} \leq 0.99$  (in practice for  $\bar{c} \leq 0.4$ ,  $\dot{\omega} \approx 0$ , cf. Fig. 5.9).

for the static model belongs to the range predicted by the dynamic model but is not the most probable value, nor the average value:  $\beta$  fluctuates significantly but the major advantage of the dynamic formulation is that this is done automatically with no possible parameter adjustment. Note that low values of  $\beta$  correspond to zones which are almost two-dimensional (flat).

### 5.6.2 Influence of chemistry description and numerical scheme

The influence of chemistry description and numerical scheme on LES predictions are investigated together in this section. The two chemical schemes (two-step and ARC-22-12QSS) and the two numerical schemes (LW and TTGC) are tested, all with the dynamic turbulent combustion model.

Figure 5.11 compares the axial profiles of the mean axial velocity component. Except for case  $2s - ttgc - dyn$  where a slight overestimation is observed, the mean recirculation zone amplitude is correctly predicted for all cases. However, its length increases with TTGC. This growth may be due to a longitudinal low-frequency oscillation that would require a tuning of the inlet and outlet impedances in the LES. The best results are obtained with the combination of ARC chemistry and TTGC numerical scheme, which is not surprising since the chemical description is closer to the real mechanism and the numerical scheme accuracy is higher in time and space. Moreover, the flame response to stretch is better reproduced with ARC, as shown in Fig. 5.2. Note that for some quantities (for example the mean axial velocity) the simplest models are almost as precise as the more sophisticated approaches. Figure 5.12 compares PDFs

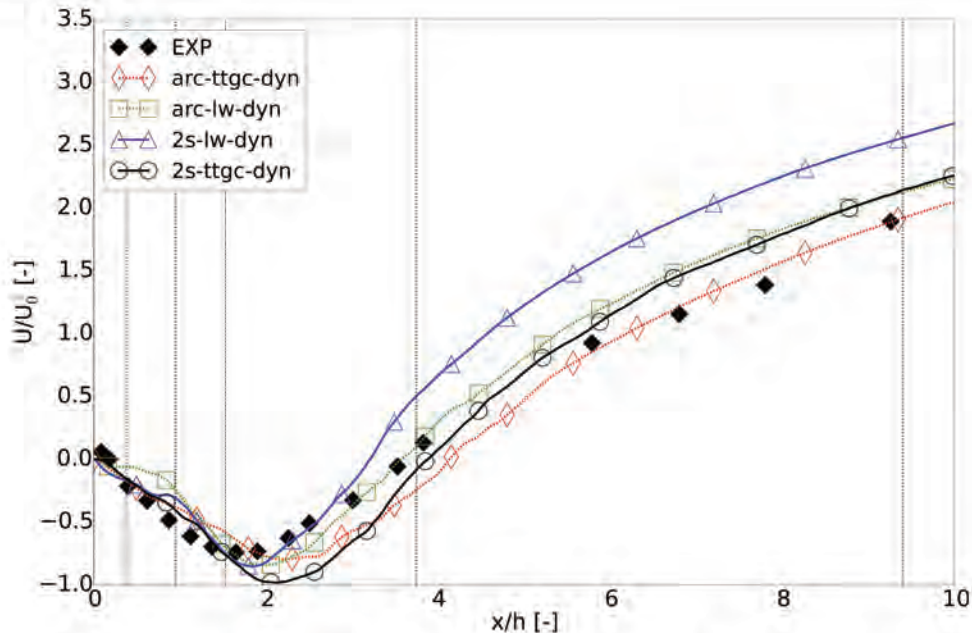


**Fig. 5.11.** Mean axial velocity evolution along the central axis of the Volvo burner measured experimentally and obtained with LES for arc – *lw* – dyn, arc – *ttgc* – dyn, 2s – *lw* – dyn and 2s – *ttgc* – dyn (see Table 5.4 for runs description). All cases are computed with the Charlette dynamic model. The axis measures the downstream location from the backward wall of the bluff-body (cf. axis  $x$  at  $z = 0.06$  m in Fig. 5.5 ).

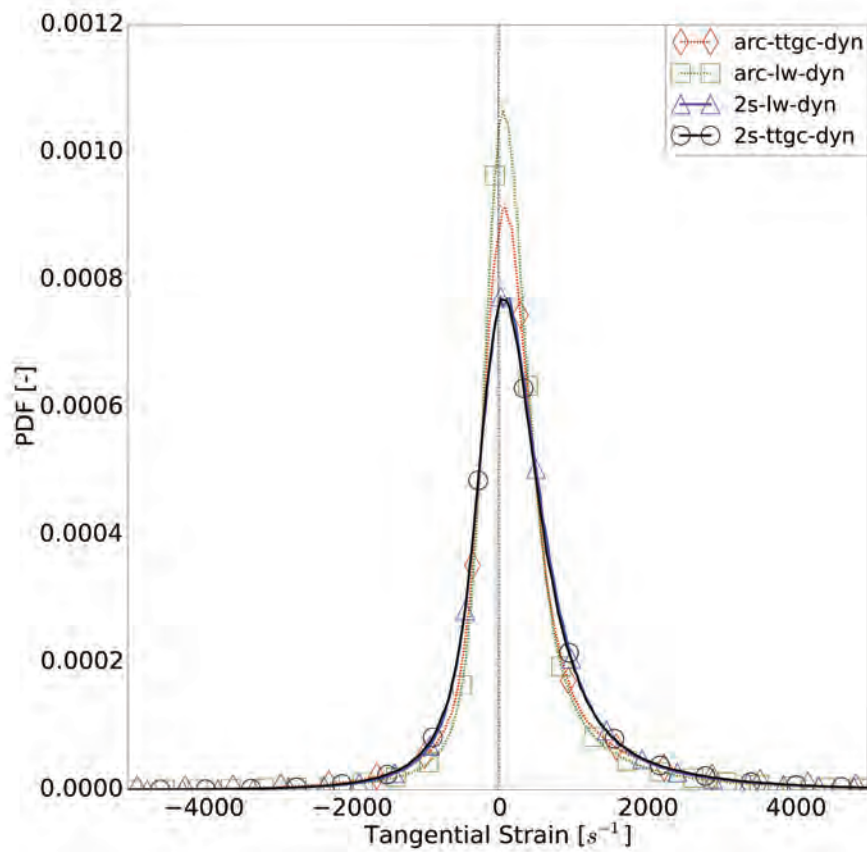
of the tangential strain calculated along the flame front, for a filtered progress variable ranging between  $0.4 \leq \bar{c} \leq 0.99$ . Note that, to be consistent with results in Fig. 5.2, the contribution of flame front curvature effects on stretch is not taken into account in the tangential strain evaluation. All flame fronts are subject to a tangential strain smaller than  $2000\text{s}^{-1}$ , which corresponds to the range where a significant difference exists between ARC and two-step laminar consumption speed (Fig. 5.2). This could influence the width of mean transverse temperature profiles.

Figure 5.13 presents transverse profiles of the mean normalized axial velocity component. For all cases the first three profiles ( $x_1$  to  $x_3$ ) located in the recirculation zone are well predicted. Differences are observed on  $x_4$  and  $x_5$  profiles in the burnt gas acceleration zone ( $2 < x/h < 9$  in Fig. 5.11). Except for *arc – ttgc – dyn* which provides again the best results, the mean axial velocity at planes  $x_4$  and  $x_5$  is also overestimated for all other simulations, indicating that combustion is too fast with these models.

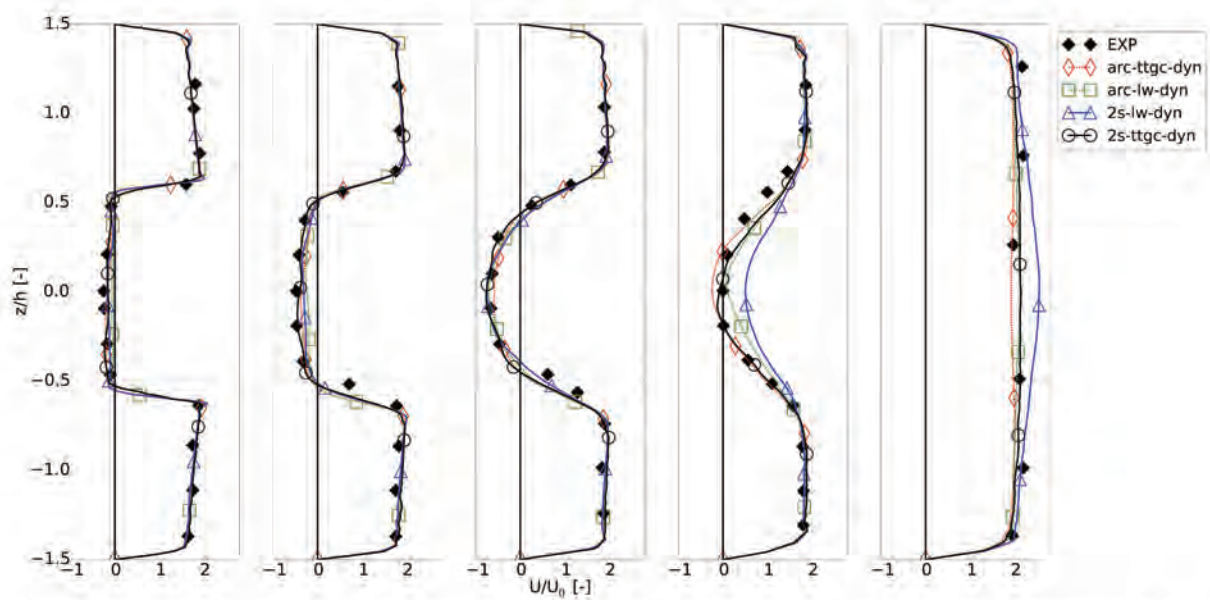
Figure 5.14 compares transverse profiles of the normalized RMS axial velocity fluctuations  $U_{rms}$  from  $x_1$  to  $x_5$ :  $U_{rms}$  is reasonably well captured by all LES (note that only RMS fluctuations of the resolved field are considered). Figure 5.15 shows that the primary factor controlling RMS transverse velocity profiles is the chemical scheme: indeed,  $V_{rms}$  profiles computed using the ARC chemical scheme are in good agreement with experimental data, which is not the case with the two-step mechanism.

Figure 5.16 shows the transverse profiles of the normalized mean temperature. The broadening of the experimental profiles is slightly more pronounced than in the LES. This could result from a lack of turbulent mixing between low and high temperature regions or from a difference in the flame front location. This latter one is more probable since experimental temperature measurements were made with a bulk velocity  $U_0 = 16.6$  m/s, which is slightly lower than the one used in all LES runs (Table 5.3).

Figure 5.17 compares transverse profiles of the normalized RMS temperature with experimental measurements. RMS maximum values are well captured by all runs but not the minimum values at  $x_2$  and  $x_5$ , indicating that the level of turbulent fluctuation may be too low



**Fig. 5.12.** PDF of tangential strain computed along the flame front, for a filtered progress variable ranging between  $0.4 \leq \bar{c} \leq 0.99$ .



**Fig. 5.13.** Transverse profiles of mean normalized axial velocity at measurement planes  $x_1 - x_5$  of Fig. 5.5.

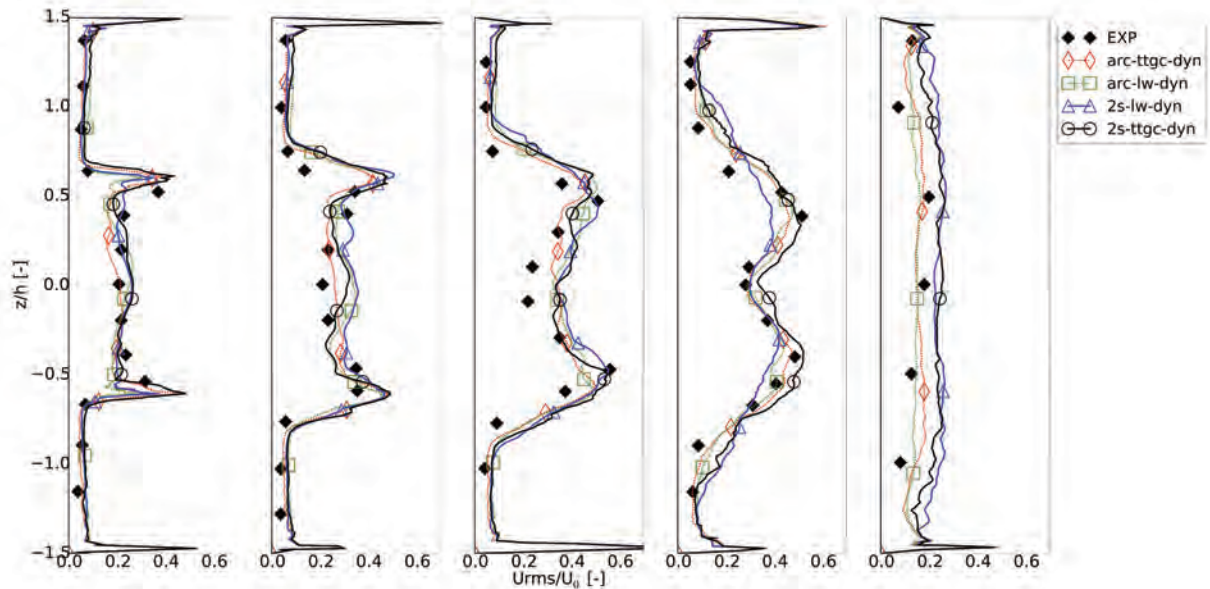


**Fig. 5.14.** Transverse profiles of the normalized RMS axial velocity component at measurement planes  $x_1 - x_5$  on Fig. 5.5.

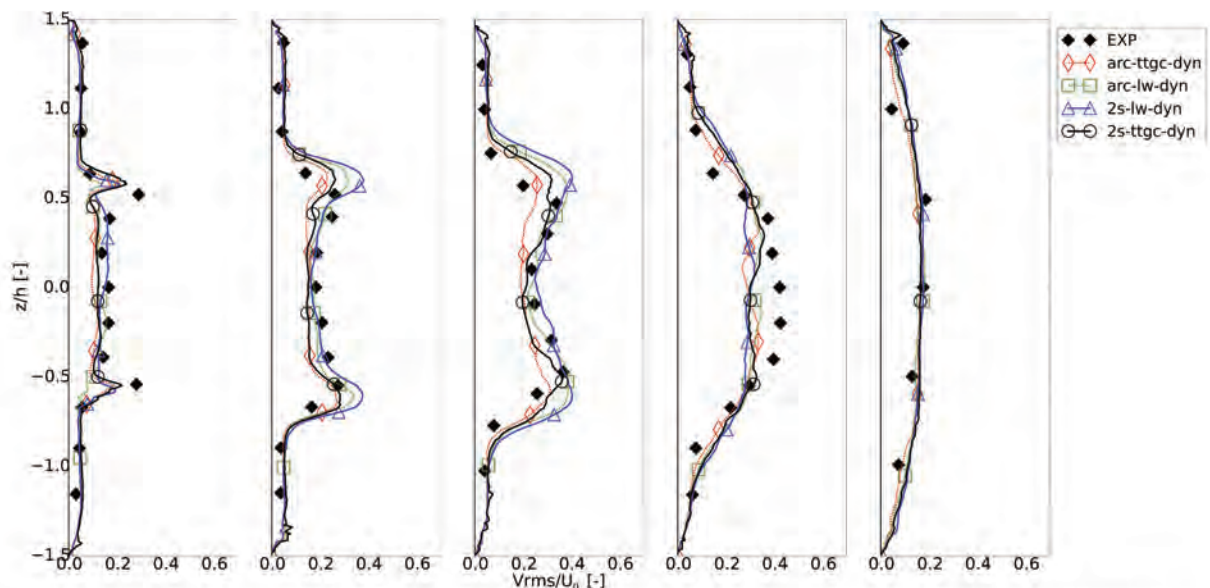


**Fig. 5.15.** Mean transverse profiles of the normalized RMS transverse velocity component at measurement planes  $x_1 - x_5$  on Fig. 5.5.

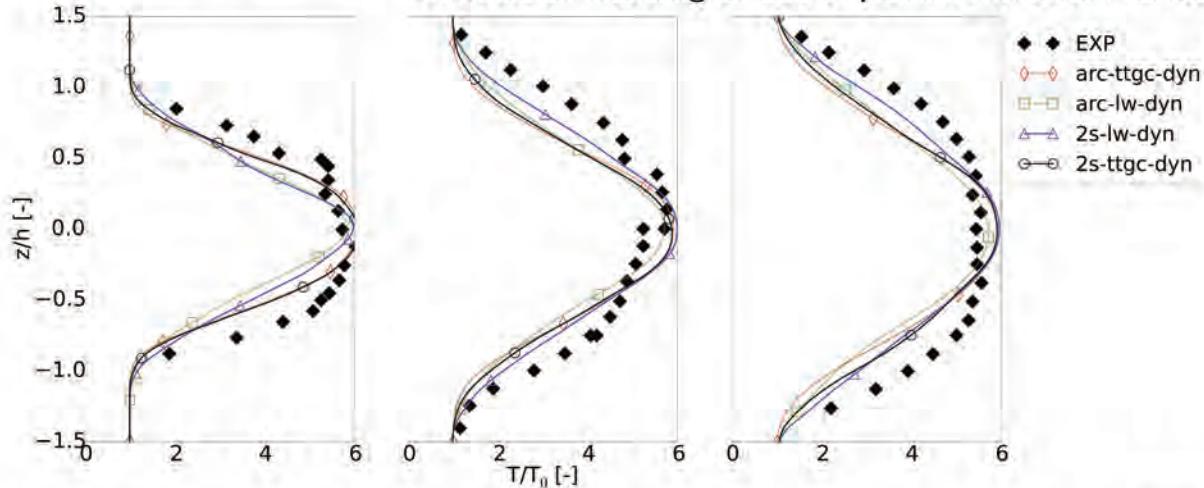


**Fig. 5.16.** Transverse profiles of the normalized mean temperature at measurement planes  $x_4$ ,  $x'_4$  and  $x'_5$  on Fig. 5.5.

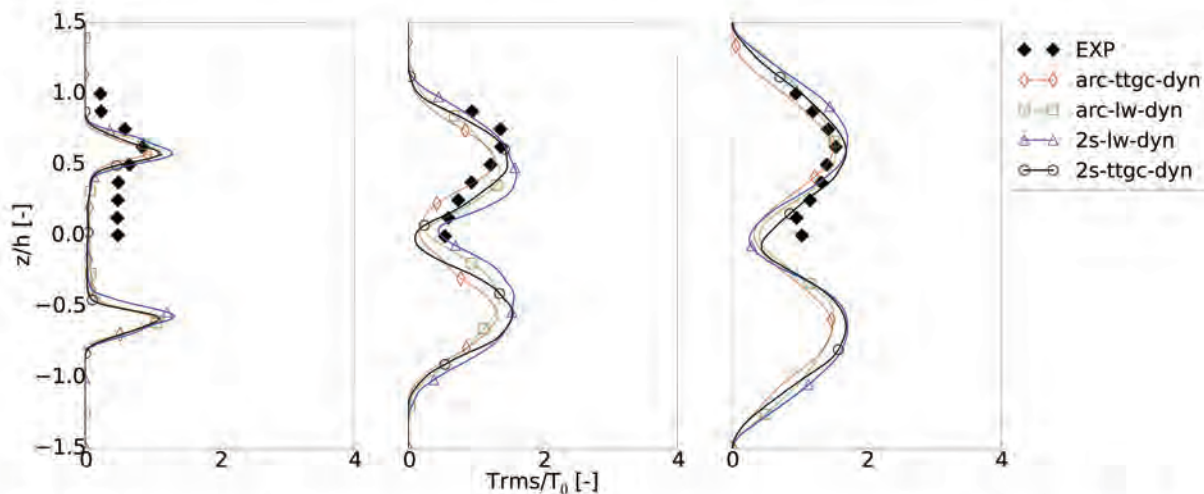


**Fig. 5.17.** Transverse profiles of the normalized RMS temperature at measurement planes  $x_2$ ,  $x_4$  and  $x_5$  on Fig. 5.5.

in the LES near the flame holder (where  $y^+ \approx 25$ ).

Figures 5.18-5.21 show averaged axial velocity and temperature iso-contours for all runs using the dynamic model. The shaded area corresponds to a zone where the mean heat release is higher than  $60 \text{ MW/m}^3$ . Using the LW numerical scheme (Fig. 5.18 vs Fig. 5.19 for two-step chemistry or Fig. 5.20 vs Fig. 5.21 for ARC), leads to a larger reaction zone closer to the central line  $z = 0.06 \text{ m}$ , for both chemical schemes. This closer reaction zone to the central line may lead to flame front interactions. When using complex chemistry ( $\text{arc} - \text{ttgc} - \text{dyn}$ , Fig. 5.21), and compared to the two-step mechanism ( $2s - \text{ttgc} - \text{dyn}$ , Fig. 5.19), the flame brush is thinner and attached to the bluff-body.

Figures 5.22 and 5.23 are focuses of Figs. 5.19 and 5.21, showing the mean tangential resolved strain field just downstream of the flameholder. Note that the two mean tangential strain fields are almost the same but the flame stabilization region of case  $2s - \text{ttgc} - \text{dyn}$  is further from the flameholder than the one of case  $\text{arc} - \text{ttgc} - \text{dyn}$ . Figure 5.22 points out the clear weakness of the two-step chemical scheme: the flame consumption speed is highly under-predicted at tangential strain rates up to at least  $2000 \text{ s}^{-1}$  (cf. Fig. 5.2). As a consequence and compared to the ARC mechanism, the two-step flame front will not be able to stabilize itself in regions of high strain (Fig. 5.22).

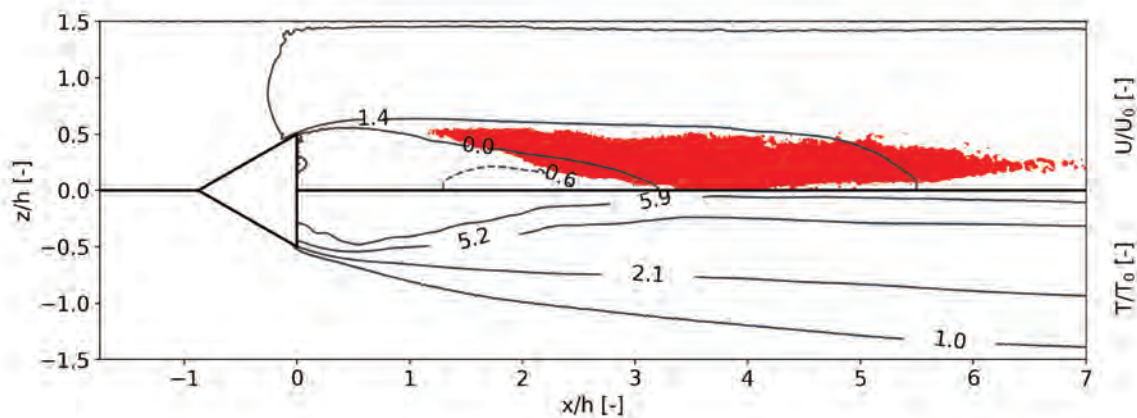


**Fig. 5.18.** Mean iso-contours of axial velocity (top) and temperature (bottom) of case 2s - lw - dyn, (side view). The red shaded area corresponds to a zone where heat release:  $hr \geq 60 \text{ MW/m}^3$ .

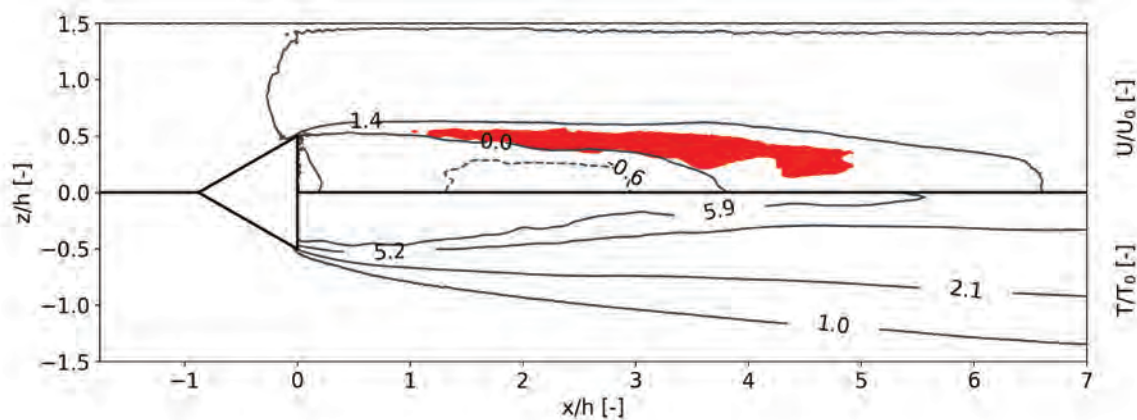


**Fig. 5.19.** Mean iso-contours of axial velocity (top) and temperature (bottom) of case 2s - ttgc - dyn, (side view). The red shaded area corresponds to a zone where heat release:  $hr \geq 60 \text{ MW/m}^3$ .

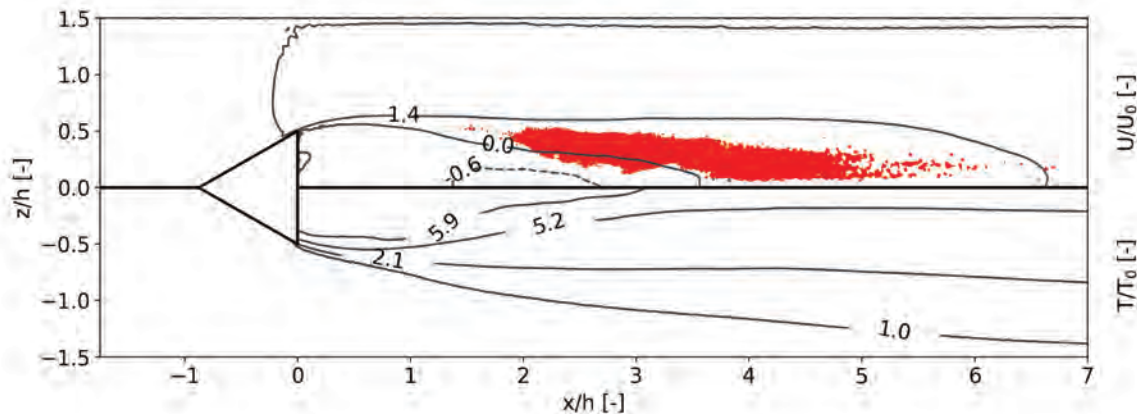


**Fig. 5.20.** Mean iso-contours of axial velocity (top) and temperature (bottom) of case arc – lw – dyn, (side view). The red shaded area corresponds to a zone where heat release:  $hr \geq 60 \text{ MW/m}^3$ .

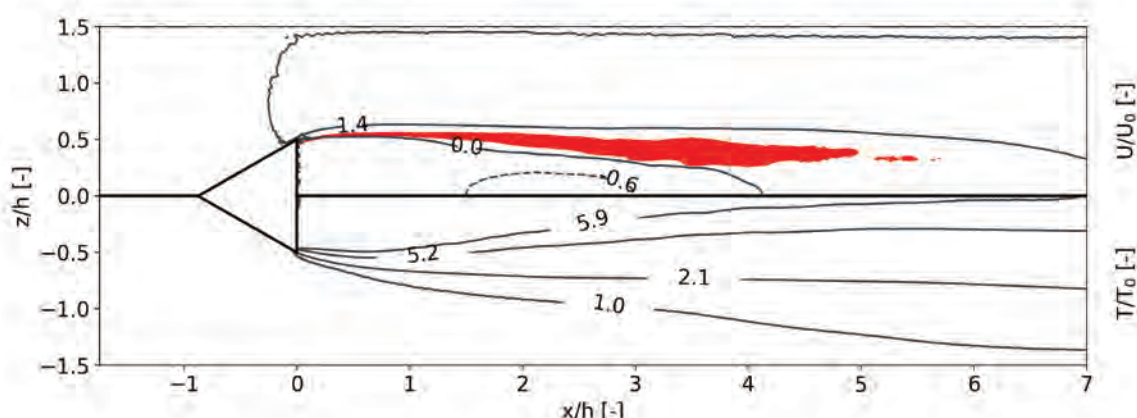


**Fig. 5.21.** Mean iso-contours of axial velocity (top) and temperature (bottom) of case arc – ttgc – dyn, (side view). The red shaded area corresponds to a zone where heat release:  $hr \geq 60 \text{ MW/m}^3$ .

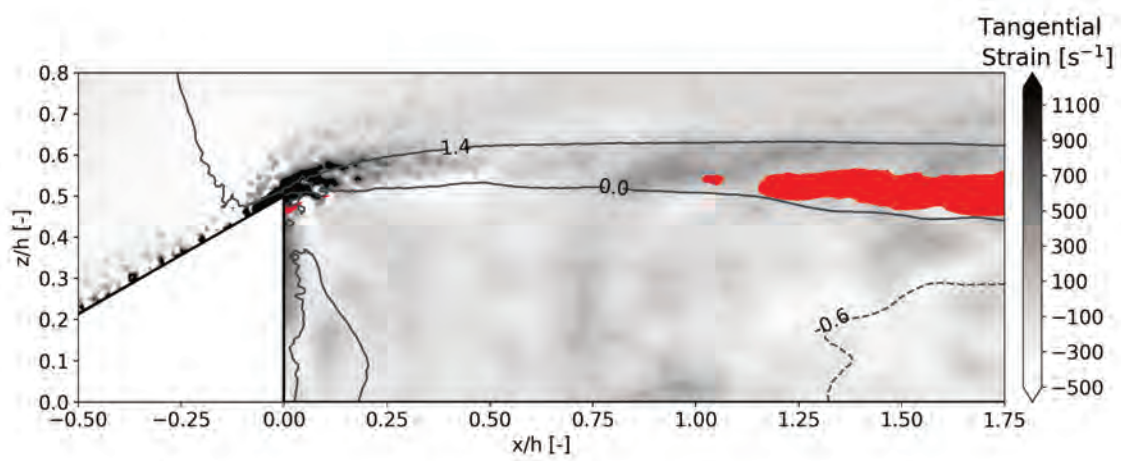


**Fig. 5.22.** Mean tangential strain field (grey colormap) and mean iso-contours of axial velocity of case 2s – ttgc – dyn, (side view). The red shaded area corresponds to a zone where heat release:  $hr \geq 60 \text{ MW/m}^3$ .

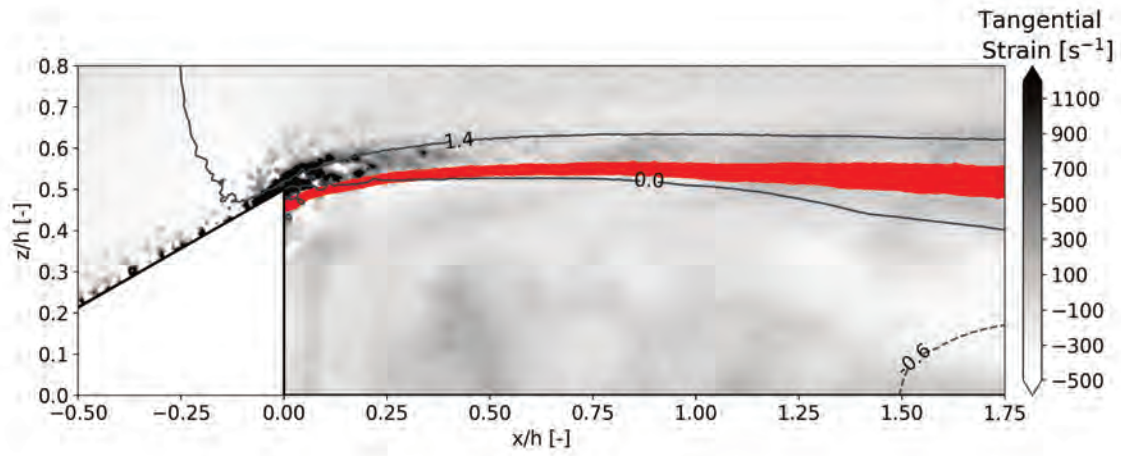


**Fig. 5.23.** Mean tangential strain field (grey colormap) and mean iso-contours of axial velocity of case arc – ttgc – dyn, (side view). The red shaded area corresponds to a zone where heat release:  $hr \geq 60 \text{ MW/m}^3$ .

Simulations	$\eta$
2s - <i>lw</i> - <i>dyn</i>	0.418
2s - <i>ttgc</i> - <i>dyn</i>	0.401
<i>arc</i> - <i>lw</i> - <i>dyn</i>	0.419
<i>arc</i> - <i>ttgc</i> - <i>dyn</i>	0.399

**Tab. 5.5.** Volvo simulated cases efficiencies  $\eta$

Figures 5.18-5.21 suggest that combustion is far from complete for this operating point. This was checked by computing the efficiency  $\eta$ :

$$\eta = 1 - \frac{\int_{outlet} \rho Y_{Fuel} u \cdot dy \cdot dz}{\int_{inlet} \rho Y_{Fuel} u \cdot dy \cdot dz} \quad (5.5)$$

For all cases,  $\eta$  does not exceed  $\eta \approx 0.42$ : more than half of the injected fuel has not burnt and exits the burner. This is very different from gas turbine chambers where values of  $\eta$  of the order of 0.99 are expected. A higher fuel conversion efficiency implies a higher fuel consumption rate and therefore an increase of the mean temperature (averaged on the entire volume) and the burnt gas expansion. As the consumption rate depends on the flame surface, the turbulent flame speed increases and the flame front stabilizes itself in a different region. Table 5.5 also shows that efficiencies are higher when using LW numerical scheme, pointing out again that the spatial accuracy of the code affects overall results. No experimental data is available for  $\eta$ .

### 5.6.3 Discussions

The VOLVO flame is an unswirled fully premixed gaseous flame anchored to a simple shaped bluff-body. Multiple solvers were applied for the VOLVO flames, each leading to different results with the same goal: match experimental data (from the early 1990s). Without knowing nor the inlet/outlet experimental acoustic impedances, neither the wall cooling temperature, matching experimental results should not be a priority but a guideline in the numerical combustion understanding process: which physical phenomena drive the most the VOLVO flame ? According to the capabilities of the LES solver, what is the most efficient way to better characterize such flames ?

The primary factor of change pointed out in the current work is the chemical scheme accuracy and more particularly the correct flame response to stretch: the flame faces vortex shedding generated by the bluff-body, and high velocity gradients from the recirculation zone. The overcost linked to a more detailed chemical scheme is not negligible (Tab. 5.4): the cost of the ARC chemical scheme is twice the one of the two-step reduced mechanism. This increased cost may be worth paying if the flame response to stretch is improved. If the flame is stretched, is the "low-order" chemical scheme capable to reproduce the flame response to stretch ? If not, using a more detailed chemical scheme is preferred.

Results also depend on how the flow and turbulence are discretized. The more accurate the numerical scheme is, the better. In the current work, the third order TTGC cases cost between 1.5 – 1.7 more than the second order LW ones which is less than the overcost linked to the chemical scheme, but required to accurately capture the flame response to stretch.

Once chemistry and turbulence are well described, the last element having an impact on the results is the flame/turbulence interaction model. In the current work, the Charlette static and local dynamic formalisms were used. Compared to the static formulation, the computational overcost linked to the dynamic model is 1.6, which is again not negligible but it has a huge

## 5.7 Conclusion

---

advantage: it finds the model constant on its own, eliminating one source of parametrization and tuning.

### 5.7 Conclusion

This Chapter has described the effects of three simulation elements: (1) chemistry description, (2) subgrid scale flame / turbulence interaction and (3) spatial accuracy of the numerical method, on Large Eddy Simulation of the turbulent premixed flame of the VOLVO rig [166, 167, 168]. Results show that going from global two-step chemistry to an analytically reduced chemistry (ARC) using 22 independent species improves the simulation accuracy. The use of a dynamic procedure for SGS flame-turbulence interaction model, as proposed by Charlette et al. [146], avoids the need for the user to specify the fractal dimension of the model, going from a static to fully dynamic model with no user adjustable model constant. Finally, the order of accuracy of the numerical method plays a significant role, probably because it captures the growth rates of hydrodynamic instabilities along the flame front with more accuracy: results obtained with the 3rd order TTGC scheme [131] are also better than those obtained with the second order Lax-Wendroff scheme. In conclusion, this Chapter confirms that high-order spatial numerical methods combined with dynamic SGS models and analytically reduced chemistry can be used to simulate turbulent flames and that these ingredients should now be applied to more complex flames.



# **IV Turbulent two-phase combustion modeling and simulations**

<b>6</b>	<b>A generic and self-adapting method for flame detection and thickening in the TFLES model . . .</b>	<b>95</b>
6.1	Introduction	
6.2	The generic thickening approach	
6.3	Validation	
6.4	Conclusions	
<b>7</b>	<b>Effect of relative velocity on the flame speed and structure of laminar spray flames .....</b>	<b>113</b>
7.1	Introduction	
7.2	Chemistry description	
7.3	Numerical setup	
7.4	Results	
7.5	Conclusions	
<b>8</b>	<b>Turbulent two-phase combustion simulations .</b>	<b>129</b>
8.1	The HERON experiment	
8.2	Numerical setup	
8.3	Numerical results	
8.4	Application of the new generic thickening approach	
8.5	Conclusion	



# A generic and self-adapting method for flame detection and thickening in the TFLES model

In the previous Chapter, the TFLES model has been applied to a gaseous premixed turbulent flame. For such cases where the mixture is fully premixed and the local conditions do not vary, the calibration of the flame sensor is simple, but still require the computation of a reference 1D-premixed flame. This calibration is a much more difficult task for varying local conditions, complex chemistry or liquid fuel.

In this Chapter, a generic and self-adapting method for flame front detection and thickening is presented. This approach relies solely on geometric considerations and unlike previous thickening methods does not need any parameterization nor preliminary calibration. The detection process is based on the analysis of the curvature of a test function, associating a bell-curve shape to a flame front. Once the front is located, the front thickness is also evaluated from the test function, allowing (1) a thickening restricted to under-resolved flame regions, (2) a self-adapting thickening of the front. The thickening process is finally applied to the detected front, over a normal-to-the-flame distance, using a Lagrangian point-localization algorithm. The method was developed and implemented in an unstructured and massively parallel environment and is therefore directly usable for the computation of complex configurations. Three test cases are presented to validate the methodology. Note that this Chapter is based on a paper which is going to be submitted to Combustion and Flame.

## 6.1 Introduction

The first TFLES attempt proposed by Colin *et al.* [131] was to apply a constant and uniform user-defined thickening factor  $F$ . However this modifies the species and thermal diffusion and mixing in the entire domain, even in non-reacting but segregated regions (e.g., at injection or close to isothermal walls). To overcome this issue, Legier *et al.* [126] developed a dynamic and local estimation of  $F$  using a flame sensor: with the so-called DTFLES model, thickening is applied only in the vicinity of the flame and deactivated elsewhere. This is done by comparing the local LES chemical activity, based on one reaction or heat release, to the one of a one-dimensional resolved flame in same conditions. In this approach, the same flame sensor is used for both detection and thickening. Ideally these two processes should be decoupled to better adjust the shape and size of the flame thickening zone.

The DTFLES formalism has been widely used during the past decades and proved to be robust and accurate for flame localization [126, 129, 130, 192]. It however suffers from two main weaknesses. First the flame sensor is based on a reference flame which must be defined and pre-tabulated. Moreover, turbulent flames may significantly differ from 1D flames. Similarly, defining a reference flame for two-phase combustion is not obvious. The identification of reference 1D flames can be particularly tricky in situations where the operating point is not clearly defined or changes in space and time due to variations in equivalence ratio or pressure. These situations require to know beforehand the range of variation of these physical quantities and to perform preliminary calculations of large series of reference flames. A second weakness of the DTFLES model is that all detected flames are thickened, whatever their actual thickness

is. This may lead for example to thickening in the post-flame zone where it is however not needed.

One way to avoid all these dependencies is to use geometrical flame features rather than physical ones. Differential geometry is standard for surface detection in other applications such as X-ray scanner images analysis [193], or carbon fibers localization [194, 195], which have inspired the present work.

In the following, a new and generic method based on differential geometry for flame detection and thickening is presented. The description of the generic method is first detailed in Section 6.2. Then the numerical setup and the validation test cases are described in Section 6.3.

## 6.2 The generic thickening approach

In the generic method, detection and thickening are two different processes. The detection is ensured by a geometrical shape analysis which is independent of the operating point and the chemical scheme, and does not require any reference flame. Once the front is localized, the thickening process is applied with a thickening factor also determined from the flame shape. Thanks to a Lagrangian algorithm, this method is applicable to all types of meshes, structured or unstructured, and to all types of elements in a massively parallel environment.

### 6.2.1 Front detection

Let  $\vec{x}$  be a vector made up of cell centers coordinates and let  $f(\vec{x})$  be a continuously twice differentiable function of  $\vec{x}$ . The gradient vector is noted  $\vec{g}(\vec{x}) = \nabla f(\vec{x})$ , and the Hessian matrix  $H(\vec{x}) = [f_{ij}(\vec{x})]$ , where  $f_{ij} = \frac{\partial^2 f}{\partial x_i \partial x_j}$ .

According to the Schwarz theorem  $H(\vec{x})$  is symmetric and real, so that it is diagonalizable (spectral theorem) with  $\lambda_i(\vec{x})$  eigenvalues. The eigenvalues of  $H(\vec{x})$  describe the curvature of the function  $f$ . Depending on the sign of these eigenvalues, an identification of the local shape of  $f$  is possible:

- If  $\lambda_i(\vec{x}) > 0, \forall i$  (i.e.  $H$  is positive definite at  $\vec{x}$ ), then  $f$  is strictly convex and has a local minimum at  $\vec{x}$ .
- If  $\lambda_i(\vec{x}) < 0, \forall i$  (i.e.  $H$  is negative definite at  $\vec{x}$ ), then  $f$  is strictly concave and has a local maximum at  $\vec{x}$ .
- If  $H$  has both positive and negative eigenvalues then  $\vec{x}$  is a saddle point for  $f$ , with concave and convex directions.

Geometrically, a front is characterized by a ridge line. Along this ridge, one of the eigenvectors of the Hessian is parallel to the gradient. The eigenvalue associated to this eigenvector is negative and much larger than the eigenvalues of all remaining eigenvectors. Therefore,  $f$  is mainly concave along the gradient and in the vicinity of the ridge line. For flame front detection,  $f$  is chosen such that the flame front location coincides with concave regions (saddle points and local maxima) of  $f$  as shown in Fig. 6.1. The front detection process then simply consists in identifying regions where the largest eigenvalue of the Hessian is negative.

As an illustration, Fig. 6.2 shows the concave regions (red crosses) obtained with the negative eigenvalues of the Hessian for a Gaussian function.

This geometrical detection makes it possible to locally and simply identify the flame front (even already thickened), without any user-defined parameter or chemistry characteristics. The next step consists in computing the thickening field.

### 6.2.2 Front thickening

Obviously the thickening factor has to be maximum in the detected elements, and applied over a distance at least equal to the flame thickness. However the detected points are mainly located in the vicinity of the ridge line, in a region thinner than the flame thickness. The question now is how to extend the zone of thickening from the ridge line throughout the flame thickness, i.e.,

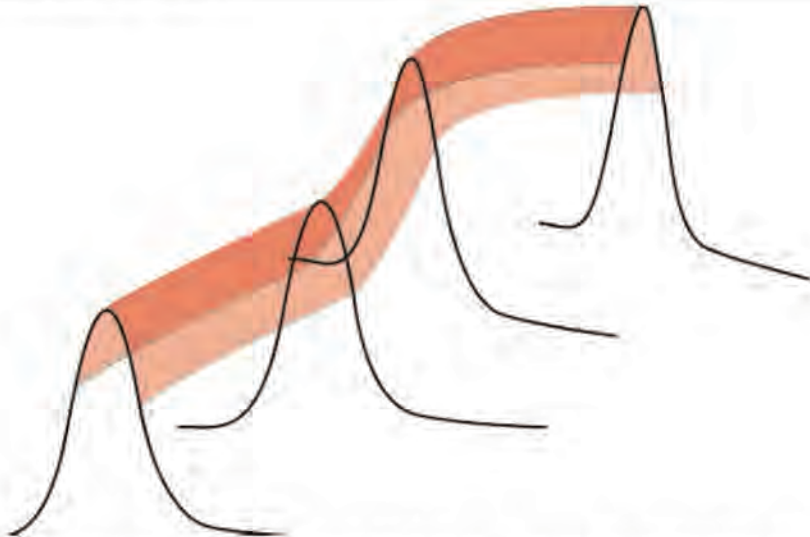


**Fig. 6.1.** Sketch representing a function  $f$  chosen such that the flame front coincides with the concave region of  $f$ .

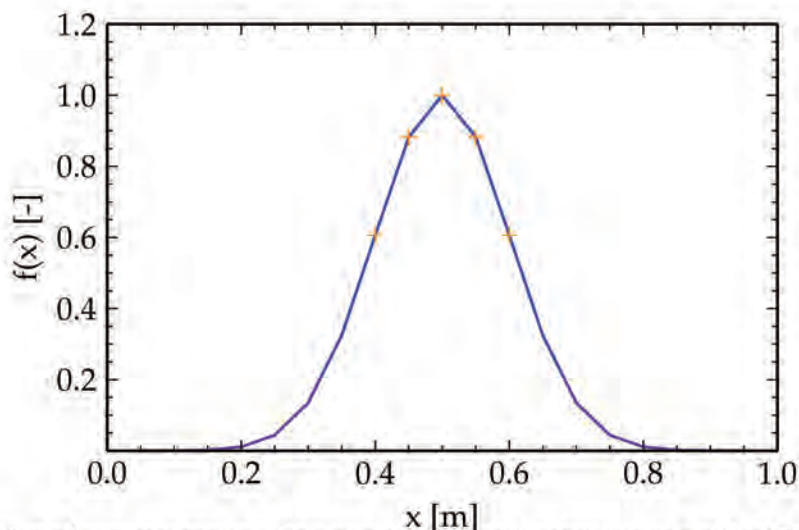


**Fig. 6.2.** Detection of concave regions for a one-dimensional spatial profile of the Gaussian function  $f(x)$ . Crosses correspond to the detected points.

to the neighboring points of the ridge line region. If the solution is relatively simple when using structured meshes, it is much more complex for unstructured meshes on massively parallel computers, where neighbors are not easy to find and may be located in other processors. The originality of the present approach is to cover the extended thickening zone with a Lagrangian algorithm originally developed for particle-localization [196]. This algorithm, widely used in Lagrangian simulations [197, 198, 199, 200], tracks particle trajectories by computing their intersections with cell faces. Here particles correspond to fluid particles placed at the center of the grid elements. Starting from each detected point in the vicinity of the ridge line, a trajectory in the direction normal to the flame front is determined. The fluid particles are moved along this trajectory and are used to apply the thickening factor in each cell they cross, until they reach a maximum distance  $dist$  from the ridge line, representing the limit of the thickening zone. A thickening function may be defined, maximum along the ridge line, and decreasing along the normal trajectories over the distance  $dist$ . This function replaces the sensor  $S$  in Eq. 3.73 and ranges between 0 and 1.

An illustration of the method is shown in Fig. 6.3. Let  $c_1$  be a point detected during the detection procedure described in Section 6.2.1. From the element center  $\vec{x}_{c1}$ , a trajectory is calculated in the direction  $\vec{n}$ , the normal to the flame front computed as:

$$\vec{n}(\vec{x}) = \frac{\vec{g}(\vec{x})}{\|\vec{g}(\vec{x})\|}, \quad (6.1)$$

where  $g$  is the gradient of the sensor function  $f$ .

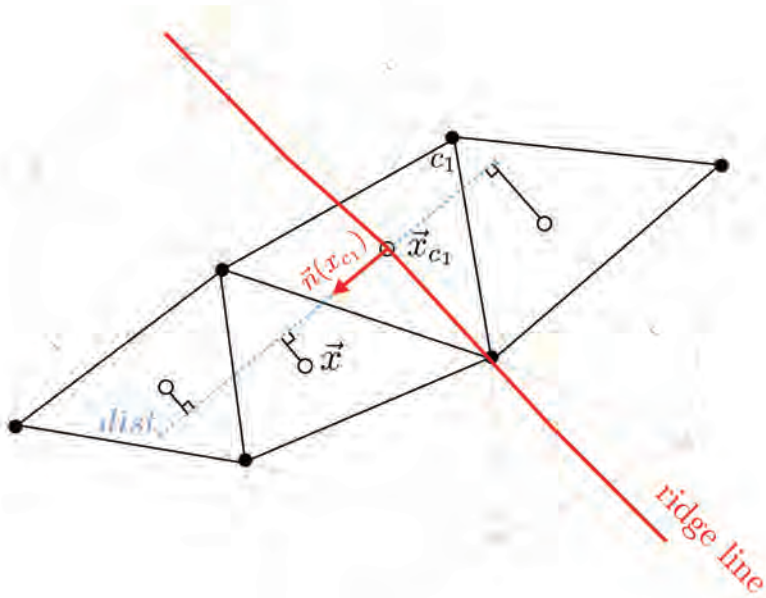


**Fig. 6.3.** Illustration of the fluid particle-localization principle applied to the new thickening process. Starting from the detected point  $c_1$ , the fluid particle is located at the cell center of coordinates  $\vec{x}_{c_1}$ ,  $\vec{n}(\vec{x}_{c_1})$  corresponds to the normal to the front, and the direction along which the fluid particle is transported.  $dist$  is the maximum distance over which the fluid particle is transported.

Along this trajectory, the thickening function  $tf$  has an analytic form and reads:

$$tf(\vec{x}) = 1 - \tanh\left(\frac{((\vec{x} - \vec{x}_{c_1}) \cdot \vec{n}_{c_1})^2}{\sigma}\right)^2, \quad (6.2)$$

where  $\sigma$  is a parameter controlling the width of the thickening zone. To ensure a sufficiently large thickening zone,  $\sigma$  is estimated as  $\sigma = N_c \Delta_x$ , where  $\Delta_x$  is the size of the detected element on the ridge line and  $N_c$  is the number of points required in the flame front.

Note that in a parallel computing environment, the Haselbacher algorithm [196] is used to move fluid particles from a partition to another. This operation may induce a slight over-cost, increasing with the number of partitions crossed. In practice partition crossing is a rare event, limiting the number of additional MPI communications.

### 6.2.3 Asymmetric thickening

The thickening may differ on both sides of the flame. In particular, thickening must extend farther on the fresh gas (FG) side compared to the burnt gas (BG) side, to include the density

## 6.2 The generic thickening approach

---

gradient: high density gradients located in fresh gas may cause numerical issues that can be significantly reduced by the thickening procedure. This is simply obtained in the present approach by introducing different values for  $\sigma$  on both sides of the flame,  $\sigma_{FG} = \alpha N_c \Delta_x$  and  $\sigma_{BG} = (1 - \alpha) N_c \Delta_x$  in the function  $t f$  of Eq. 6.2. Typically  $\alpha = 2/3$ .

### 6.2.4 Flame thickness estimation

Once the thickening region has been determined, the thickening factor  $F_0$  (Eq. 3.73) must be estimated. Indeed, all detected fronts may not necessarily need to be thickened. Another originality of the present approach is to use a geometrical evaluation of the flame thickness. A resolution criterion  $R_c$  is introduced, which compares the thickened flame thickness  $\delta$  to the local cell size  $\Delta_x$ :  $R_c = \delta / \Delta_x$ . If  $R_c \leq N_c$ , the thickening factor may be kept or increased. If  $R_c \geq N_c$ , it may be decreased. To evaluate  $\delta$ , the test function  $f$  is analyzed in the direction  $\vec{n}$  normal to the front, using the new coordinate:

$$\xi_\perp = \vec{n}(\vec{x}_{c_1}) \cdot (\vec{x} - \vec{x}_{c_1}), \quad (6.3)$$

The first and second  $\xi_\perp$  derivatives of  $f(\vec{x}_{c_1})$  write:

$$\frac{\partial f}{\partial \xi_\perp} = g_\perp(x_{c_1}) = g(\vec{x}_{c_1}) \cdot \vec{n}(\vec{x}_{c_1}), \quad (6.4)$$

$$\frac{\partial^2 f}{\partial \xi_\perp^2} = H_\perp(x_{c_1}) = \vec{n}(\vec{x}_{c_1})^T H(\vec{x}_{c_1}) \vec{n}(\vec{x}_{c_1}), \quad (6.5)$$

allowing to approximate  $f$  around  $\vec{x}_{c_1}$  as:

$$f(\xi_\perp) = f(\vec{x}_{c_1}) + g_\perp(\vec{x}_{c_1}) * \xi_\perp + \frac{H_\perp(\vec{x}_{c_1})}{2} * \xi_\perp^2. \quad (6.6)$$

The 2 values  $\xi_+$  and  $\xi_-$  where the approximation of  $f$  nullifies are:

$$\xi_\pm = \frac{-g_\perp(\vec{x}_{c_1}) \pm \sqrt{g_\perp(\vec{x}_{c_1})^2 - 2H_\perp(\vec{x}_{c_1})f(\vec{x}_{c_1})}}{H_\perp(\vec{x}_{c_1})}, \quad (6.7)$$

The front thickness estimation is then simply:

$$\delta = \xi_+ - \xi_-. \quad (6.8)$$

Figure 6.4 illustrates the method on a 1D Gaussian function. The local approximation  $f(\xi_\perp)$  (dashed line) of  $f$  (continuous line) is zero at  $\xi_+$  and  $\xi_-$ , whose difference gives an estimation of  $\delta$ . Note that this definition is quite arbitrary. However there is no strict definition of flame thickness and choosing one or the other only has an impact on  $N_c$ .

Once  $\delta$  is known, the non-thickened flame thickness can be calculated with  $\delta_L^0 = \delta / F$ , where  $F$  is the known thickening factor of the analyzed solution. It is then possible to estimate the thickening factor from the current solution with Eq. 3.74. In a time-discretized integration, this translates in:

$$F^n = \frac{N_c \Delta_x}{\delta^{n-1} / F^{n-1}} = \frac{N_c F^{n-1}}{R_c}, \quad (6.9)$$

where  $n$  is the iteration number. The target being  $R_c = N_c$ , Eq. 6.9 increases  $F$  if  $N_c > R_c$  (under-resolution), or decreases  $F$  if  $N_c < R_c$  (over-resolution).

Equation 6.9 guarantees to reach the targeted number of points  $N_c$  in the flame front, whatever the initial resolution of the flame is. Obviously, higher flame resolution leads to better estimation of  $\delta$ . However, Eq. 6.9 is also capable to handle severe under-resolved conditions: even if the first estimation of  $\delta$  is not accurate, it will lead to a progressive thickening of the flame front and an increase of its discretization, therefore progressively increasing the accuracy of the estimation of  $\delta$ . The self-adapting method is therefore very robust.

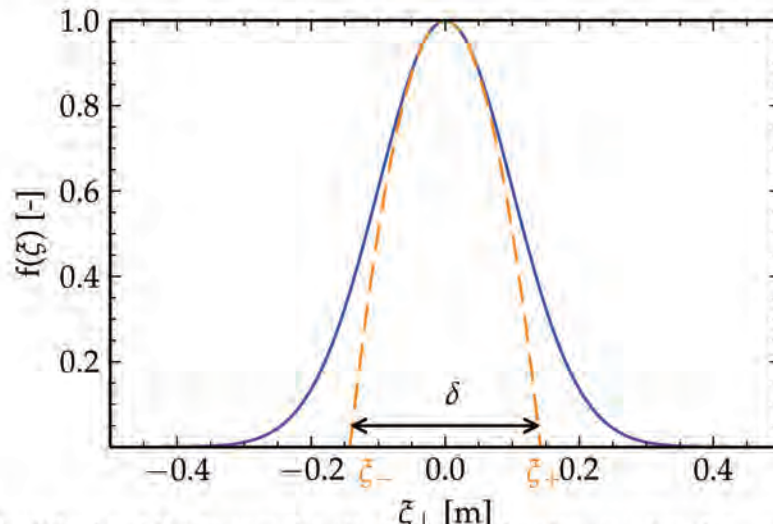


Fig. 6.4. Sketch of the front thickness estimation method. Continuous line: Gaussian function  $f$ . Dashed line: Approximation  $f(\xi_{\perp})$  Eq. 6.6.

### 6.3 Validation

Various canonical test cases of increasing complexity are used to assess the robustness and the generic nature of the method described in Section 6.2. First, a one-dimensional flame is shown to illustrate the approach. Then a two-dimensional flame propagating on a non-uniform mesh is used to demonstrate the self-adapting capacity and robustness of the algorithm. Finally, the approach is applied to a turbulent flame.

All simulations were performed with the AVBP solver co-developed by CERFACS and IFPEN [93], which solves the fully compressible multi-species Navier-Stokes equations on unstructured grids.

#### 6.3.1 Laminar cases

Premixed laminar n-heptane/air flames are considered here. Chemistry is described with a global two-step mechanism based on a fast oxidation reaction, followed by a CO-CO<sub>2</sub> equilibrium, and involving six species ( $C_7H_{16}$ ,  $O_2$ , CO, H<sub>2</sub>O, CO<sub>2</sub> and N<sub>2</sub>) [87]:



Reaction rates for reactions  $R_1$  and  $R_2$  follow an Arrhenius law:

$$q_1 = A_1 f_1(\phi) \left( \frac{\rho Y_{C_7H_{16}}}{W_{C_7H_{16}}} \right)^{0.6} \left( \frac{\rho Y_{O_2}}{W_{O_2}} \right)^{0.9} \exp \left( \frac{-E_{a,1}}{RT} \right) \quad (6.12)$$

$$q_2 = A_2 f_2(\phi) \left[ \left( \frac{\rho Y_{CO}}{W_{CO}} \right)^{1.0} \left( \frac{\rho Y_{O_2}}{W_{O_2}} \right)^{0.5} - \frac{1}{K_2} \left( \frac{\rho Y_{CO_2}}{W_{CO_2}} \right)^{1.0} \right] \exp \left( \frac{-E_{a,2}}{RT} \right) \quad (6.13)$$

The pre-exponential constants  $A_i$  and the activation energies  $E_i$  are given in Tab. 8.2, and  $K_2$  is the equilibrium constant of reaction  $R_2$ . The correction function  $f_1(\phi)$  and  $f_2(\phi)$  allow to recover the correct flame speed  $S_L(\phi)$  and may be found in [87].

Simulations were run with the Lax-Wendroff [182] convective scheme without artificial viscosity. Each case is computed twice, with the standard and the generic thickening methods. For the sake of comparison, both methods use the same quantity  $q_1$  (Eq. 6.12) for the calculation of the sensor.

	$A_j[\text{cgs}]$	$E_j[\text{cgs}]$
Reaction 1	$1.4 \times 10^{11}$	$2.9 \times 10^4$
Reaction 2	$5.0 \times 10^9$	$2.1 \times 10^4$

**Tab. 6.1.** Reaction constants of the two-step chemical mechanism for n-heptane/air. Pre-exponential factors  $A_j$  and activation energies  $E_j$  are both in cgs units.

#### Test case 1: steady 1D premixed laminar flame on a uniform mesh

The first test case consists in a stoichiometric one-dimensional thickened laminar flame, computed on a uniform mesh ( $\Delta_x = 5 * 10^{-4} \text{ m}$ ). Fresh gas conditions are  $T = 300 \text{ K}$  and  $P = 101325 \text{ Pa}$ . To keep the flame steady, the inlet velocity is equal to the laminar flame speed  $S_L^0$ , here of  $0.409 \text{ m/s}$ . The thermal laminar flame thickness is  $\delta_L^0 = 3.417 * 10^{-4} \text{ m}$  i.e lower than  $\Delta_x$ . The simulation is initialized with a strong under-resolved flame front, in order to verify that (1) the thickening factor is correctly computed and applied according to the analytic function  $tf$ , (2) the front thickness estimation  $\delta$  is accurately estimated, (3) the flame front resolution reaches the target value of  $N_c$  grid points, and finally . The initial solution is a thickened flame obtained with  $N_c = 2$ , whereas the target resolution is  $N_c = 5$ . Note that the efficiency function  $\varepsilon$  is set to one in this laminar case.

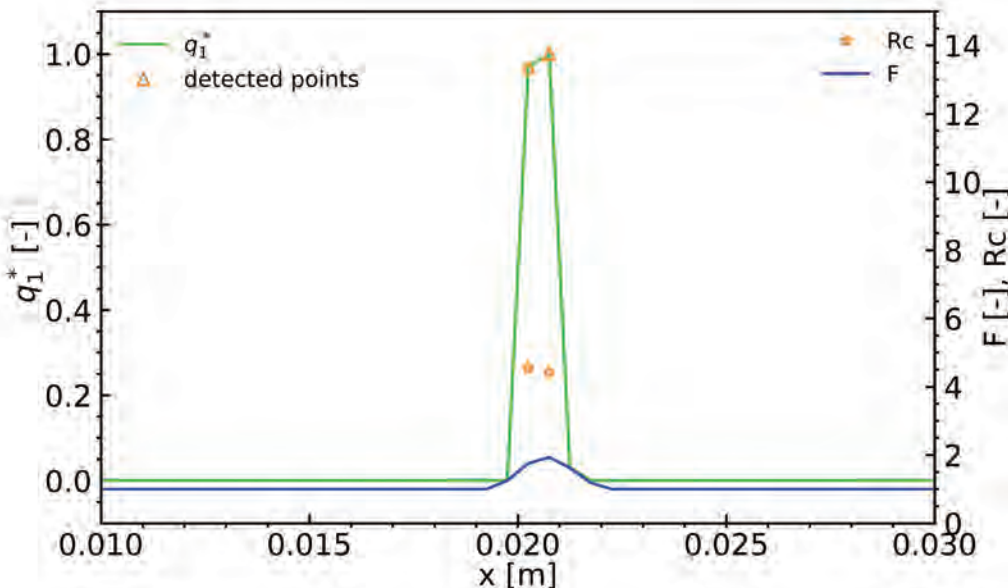


**Fig. 6.5.** Spatial profiles of normalized reaction rate  $q_1^* = q_1/q_{1,max}$ , and thickening factor  $F$  of the initial solution for case 1 with the generic thickening approach. Vertical lines correspond to the cells. Triangles indicate detected points for which the flame front resolution  $R_c$  is also shown.

Figure. 6.5 shows the spatial profiles of the normalized reaction rate  $q_1^* = q_1/q_{1,max}$  and of thickening factor  $F$  of the initial solution for case 1, obtained with the generic thickening approach. One can notice that the initial solution is highly under-resolved, the flame front being discretized on only three points. With  $N_c = 2$ , the initial maximum thickening factor  $F \approx 2$ . Despite the initial under-resolution, the generic method detects two points in the concave region of  $q_1^*$  (triangles in Fig. 6.5). The two corresponding flame front resolution values  $R_c$  (stars in Fig 6.5) range from 4 to 5, which is larger than the true value  $\delta_L^0/\Delta_x = 0.68$ , due to a rough estimation of  $\delta$ . Indeed, the local second order Taylor approximation is not adapted to

sharp-functions. However as  $F$  is estimated from the smaller  $R_c$ , this is sufficient to increase the thickening factor and the flame front discretization. This will first decrease  $R_c$ , as the better estimated  $\delta$  will decrease, until the correct  $\delta/F = \delta_L^0$  values is found and  $R_c$  increases again with  $F$ , until the limit  $R_c = N_c$  is reached.

Figure 6.6 shows the spatial profiles of the normalized reaction rate  $q_1^*$  and of the thickening factor  $F$  of the updated solution for case 1 after  $14.3\text{ms}$ , still with the generic thickening method. Compared to the initial solution (Fig. 6.5), the concave region of  $q_1^*$  is now discretized with about 5 points, which corresponds to the target number of points  $N_c = 5$ , and  $F$  has increased to  $\approx 12$ . The number of detected points has increased to 4, and  $R_c$  ranges now between 5 and 10, i.e., above  $N_c = 5$ . Note that as the flame front is more discretized, the accuracy of the flame front thickness estimation is improved, especially around the maximum of  $q_1^*$ .

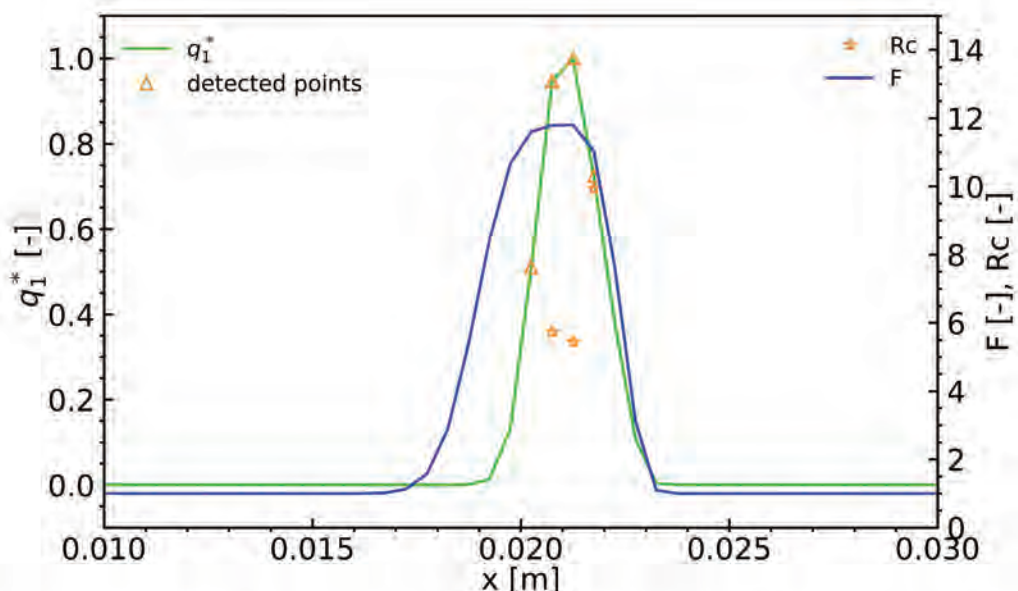


**Fig. 6.6.** Spatial profiles of normalized reaction rate  $q_1^* = q_1/q_{1,\max}$  and the thickening factor  $F$  of the steady thickened flame solution for case 1 at  $t = 14.3\text{ms}$ , with the generic thickening approach. Vertical lines corresponds to the cells. Triangles indicate detected points, for which  $R_c$  is also shown.

To give a better idea on how the algorithm works, Fig. 6.7 shows the temporal evolution of the maximum thickening factor  $F_0$  compared to  $F_0$  of the standard thickening method for the same target  $N_c = 5$ . With this method,  $F_0$  (Eq. 3.74) is constant since it is determined from flame parameters provided by the user. For the generic method, as the flame front of the initial solution is highly under-resolved,  $F_0$  increases gradually as the estimation of  $\delta$  becomes more accurate until stabilizing to a value corresponding to  $\delta/F = \delta_L^0$ , i.e., a correct estimation of the flame thickness. The converged value of  $F_0$  is therefore equal to the one obtained with the standard method,  $F_0 = 12.5$ .

Note that it takes  $\approx 4\text{ms}$  to reach the final value of  $F_0$ , as the initial value was very far from the target. Figure 6.8 presents a comparison between thickening factor and density profiles obtained with both the standard and generic methods. The standard thickening factor profile does not encompass the density gradient in the fresh gas side, resulting in high oscillations of density. Thanks to the function  $tf$  (Eq. 6.2, black dashed line in Fig. 6.8), applied with  $\sigma_{FG} = 2/3N_c\Delta_x$  and  $\sigma_{BG} = 1/3N_c\Delta_x$ , the generic thickening profile has a shaper better adapted to the flame structure, avoiding spurious oscillations.

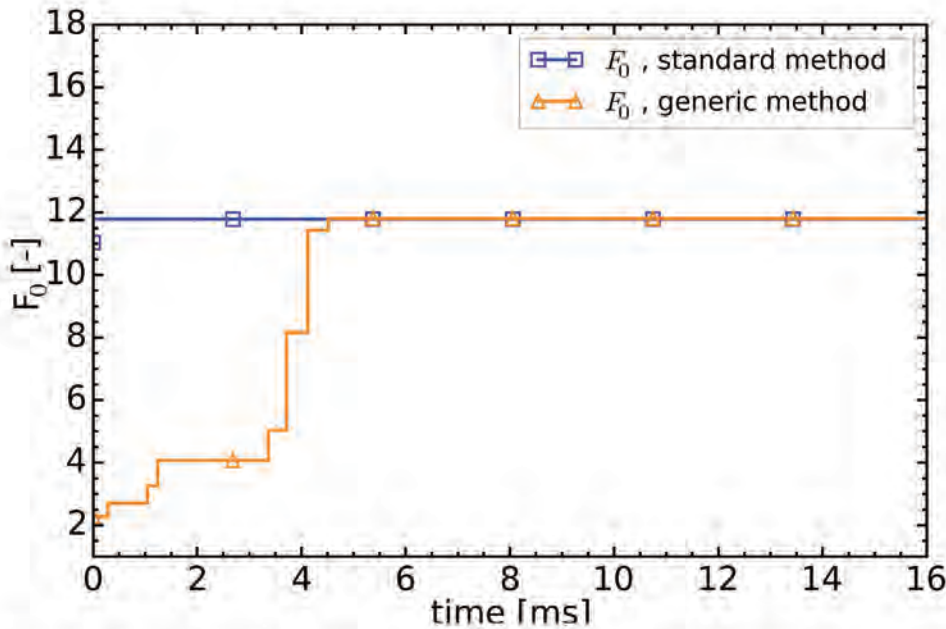


**Fig. 6.7.** Temporal evolution of the maximum thickening factor  $F_0$  estimated with the standard (blue squares) and generic (orange triangles) methods for case 1.

#### Test case 2: 2D premixed laminar flame propagating on an unstructured and non-uniform mesh

The same laminar flame of case 1 is now propagated on an unstructured non-uniform triangular 2D-mesh: the cell size is multiplied by two ( $\Delta_x = 1\text{mm}$ ) in the 2/3 left part of the domain. The initial solution and numerical setup are the same as in case 1. The objective of this case is to demonstrate the capacity of the generic methodology to handle unstructured grids and sudden mesh resolution changes.

Figure 6.9 shows the temporal evolution of the maximum thickening factor  $F_0$  for case 2 obtained with both standard and generic methods. While the flame travels from the refined to the coarse mesh areas, the value of  $F_0$  increases. The two vertical lines correspond to the times when the flame crosses the limits of the mesh resolution transition region. With the standard method,  $F_0$  starts to increase before the flame reaches the mesh resolution change since it is computed in all reacting cells, whereas for the generic method,  $F_0$  is only computed in the concave regions of  $q_1^*$ , which are thinner. After the start of mesh change,  $F_0$  is larger with the standard method before reducing at the end of mesh change. On the contrary, the generic method leads to a monotonous increase of  $F_0$ . Finally, both methods converge to approximately the same  $F_0$  in the coarse mesh zone.

Figure 6.10 bottom is a snapshot at  $t = 70\text{ms}$  (i.e., after the flame has crossed the transition of mesh resolution) showing the thickening factor field obtained with the standard method with an overview of the mesh, whereas Fig. 6.10 top shows the corresponding thickening and normalized reaction rate  $q_1^*$  spatial profiles plotted along the center line. The standard flame sensor localizes regions where the chemical activity is higher than the pre-calibrated threshold. Below this chemical threshold,  $F_0$  suddenly drops to unity. This on-off behavior introduces a geometrical dependency of the reaction rates on mesh elements, resulting in a non-parallel iso-line of  $q_1^*$  in Fig. 6.10 bottom. Also note that  $F_0$  is lower at the top and bottom boundary conditions since the cells on these boundaries are slightly smaller than the others.

The same fields and profiles obtained with the generic method are shown in Fig. 6.11. Note that, compared to the standard method (Fig. 6.10), the thickening field obtained with the generic sensor is smoother and does not drop in two cells. As the same smooth analytic profile of  $F$  is applied to all detected elements, the iso-lines of  $q_1^*$  stay parallel. As in case 1, the

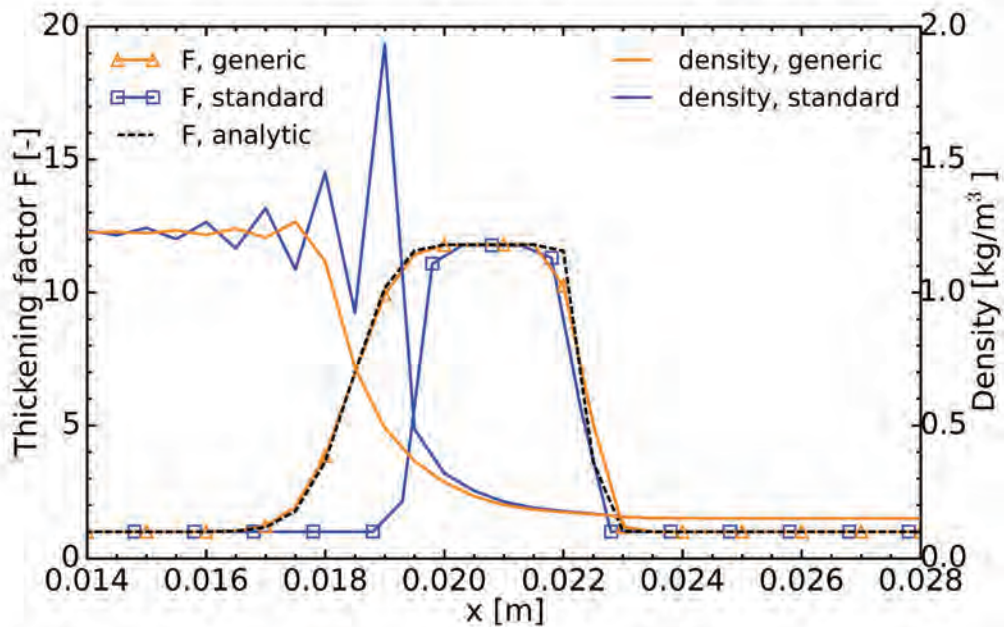


**Fig. 6.8.** Spatial profiles of instantaneous thickening factor and density for case 1, computed with the standard (blue crosses) and generic (orange triangles) thickening methods and plotted at  $t = 16.0\text{ms}$ . The dashed line corresponds to the thickening function  $tf$  (Eq. 6.2).

thickening function extends farther in the fresh gases. This is better shown in Fig. 6.12 where density and thickening factor profiles show a wider thickening zone with the generic method, allowing to smooth the density gradient.

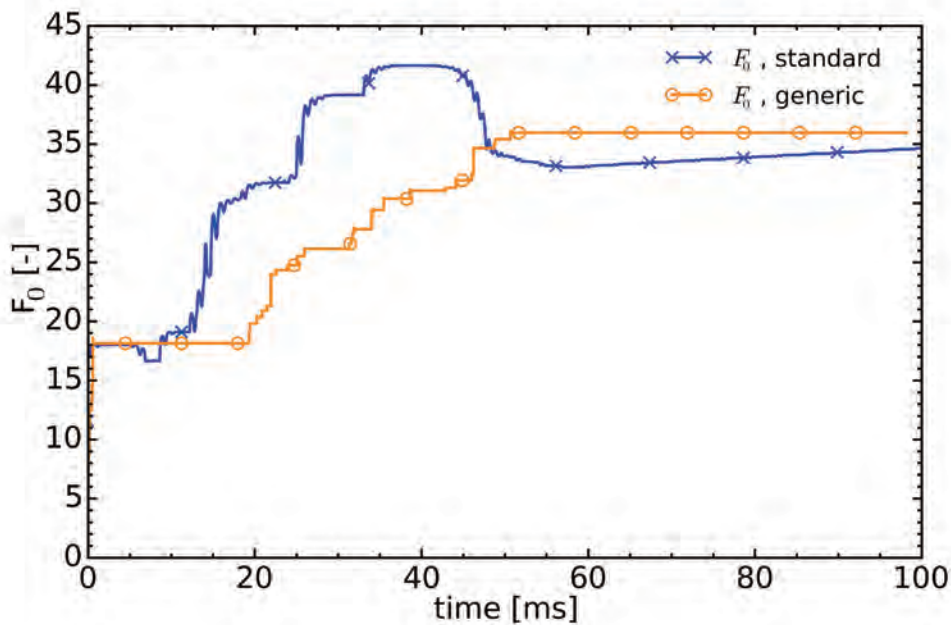


**Fig. 6.9.** Temporal evolution of the maximum thickening factor  $F_0$  obtained with the standard and generic methods. The two vertical lines correspond to the times when the flame crosses the limits of the region of mesh resolution transition.

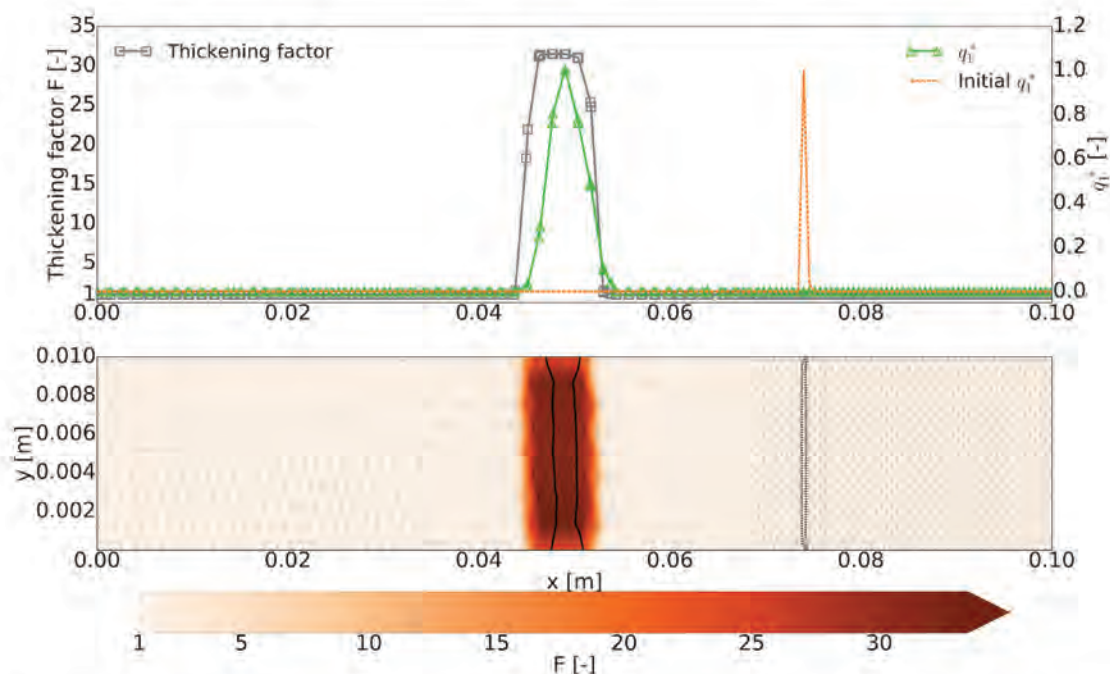


**Fig. 6.10.** Top: spatial profiles of thickening factor and normalized reaction rate obtained with the standard method and plotted along the center line at  $t = 70\text{ms}$ . The dashed line corresponds to the initial reaction rate. Bottom: thickening factor field with an overview of the mesh and an iso-line of normalized reaction rate  $q_1^* = 0.6$ . The dashed line is an iso-line of the initial normalized reaction rate  $q_1^* = 0.6$ .

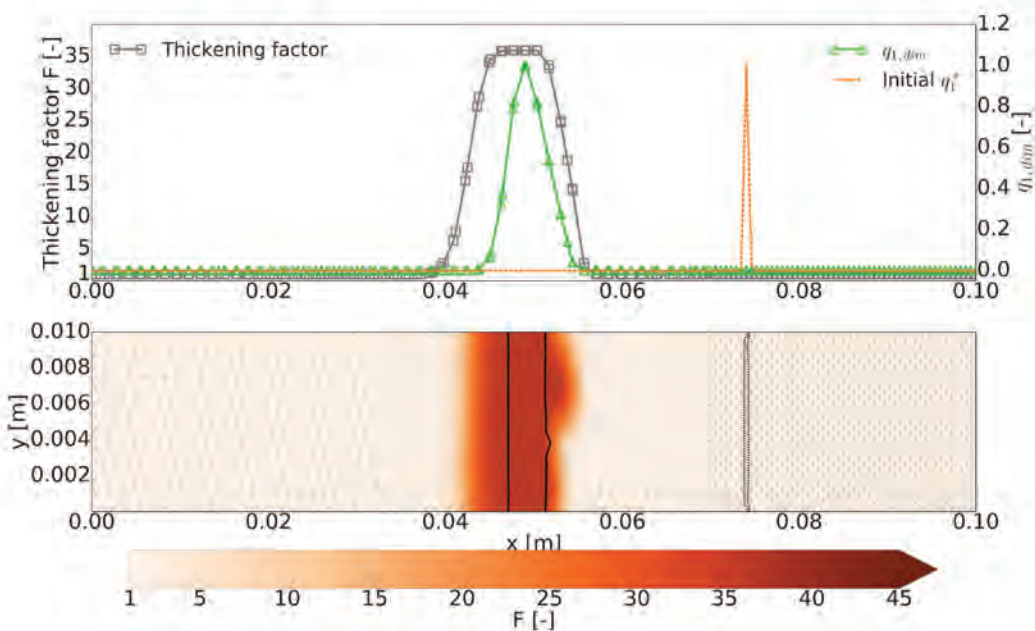


**Fig. 6.11.** Top: spatial profiles of thickening factor and normalized reaction rate obtained with the generic method and plotted along the center line at  $t = 70ms$ . The dashed line corresponds to the initial reaction rate. Bottom: thickening factor field with an overview of the mesh and an iso-line of the normalized reaction rate  $q_1^* = 0.6$ . The dashed line is an iso-line of the initial normalized reaction rate  $q_1^* = 0.6$ .

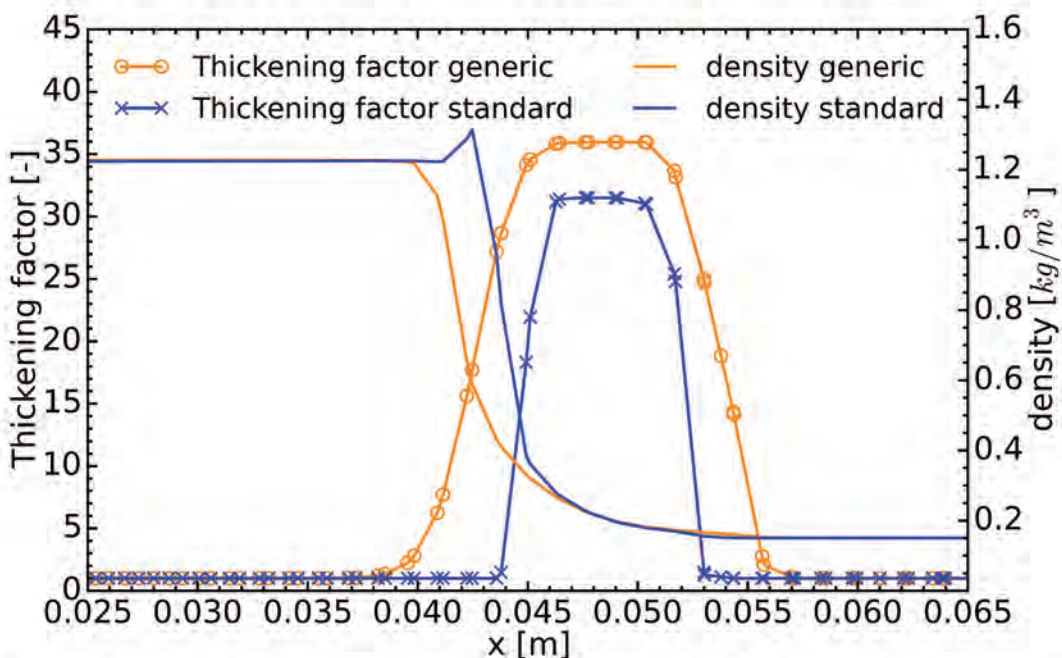


**Fig. 6.12.** Spatial longitudinal profiles of instantaneous longitudinal thickening factor and density for the standard and generic methods, plotted along the center line at  $t = 70ms$ .

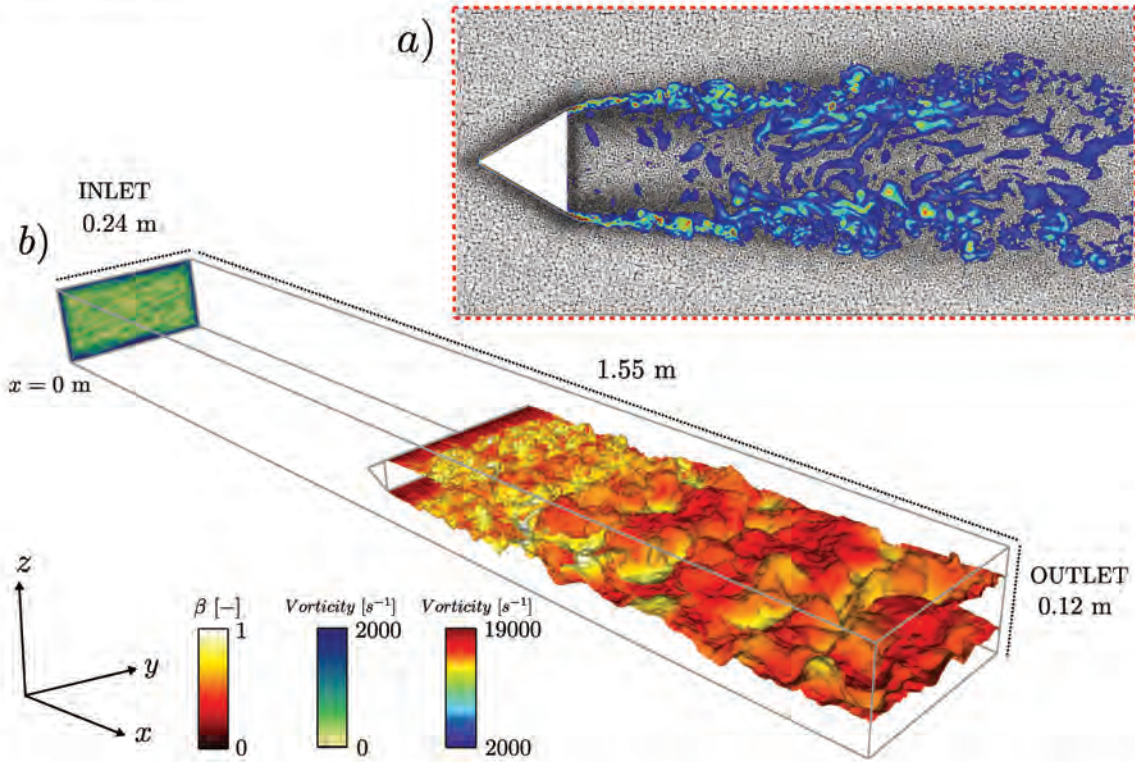


**Fig. 6.13.** Overview of the computational domain (adapted from [154]), with (a) a focus on the unstructured mesh refinement downstream of the flame holder, at  $y = 0.12$  m with the vorticity field ranging from  $2000\text{ s}^{-1}$  to  $19000\text{ s}^{-1}$  is represented by the rainbow colormap. The flame is represented through an iso-surface of progress variable  $c = 0.5$  (b), colored by the dynamic efficiency factor  $\beta$  [136, 140, 141, 146] of run 2s – ttgc – dyn (red colormap) detailed in [154]. The vorticity field ranging from  $0\text{ s}^{-1}$  to  $2000\text{ s}^{-1}$  is represented by the green colormap (inlet).

### 6.3.2 Turbulent case

#### Test case 3: 3D turbulent premixed flame on an unstructured mesh

The third and final test case consists in a 3D propane-air turbulent premixed flame. The VOLVO combustor [166, 167, 168] (Fig. 6.13) is a straight rectangular cross-section channel ( $0.12\text{ m} \times 0.24\text{ m}$ ) inside which bluff-body flame-holders are used to stabilize the flame. It has been numerically studied by several groups [169, 170, 171] as a benchmark.

The computational domain is shown in Fig. 6.13. In the longitudinal direction, it includes the entire burner (the inlet and combustor sections). In the transverse direction, domain has the exact chamber transverse dimension ( $0.24\text{ m}$ ). The unstructured mesh comprises 68 million tetrahedral elements and is refined in shear and combustion regions (Fig. 6.13).

The operating conditions and numerical setup are both detailed in Rochette *et al.* [154] (case 2s –  $lw$  – dyn, i.e., Lax-Wendroff scheme, dynamic DTFLES, two-step chemistry) as well as in Chapter 5. Fresh gas conditions are  $T = 288K$  and  $P = 101325Pa$ . At the inlet, gaseous propane is premixed with air at an equivalence ratio equal to 0.65 and injected at an inlet bulk velocity  $U_0 = 17.3m/s$ . Turbulence is injected at the inlet using the method of [191] to recover the turbulence intensity measurements [166]. The same solution from case 2s –  $lw$  – dyn is used to initialize the simulations with both the standard and generic thickening methods.

In this case, the target resolution is kept as the initial one with  $N_c = 7$ . The objective of this case is to demonstrate the capacity of the generic method to automatically locate and thicken a 3D turbulent flame. To compare both methods, instantaneous results are plotted after a simulation period corresponding to a hundred of iterations.

Figures 6.14 and 6.15 are snapshots of the thickening field respectively obtained with the

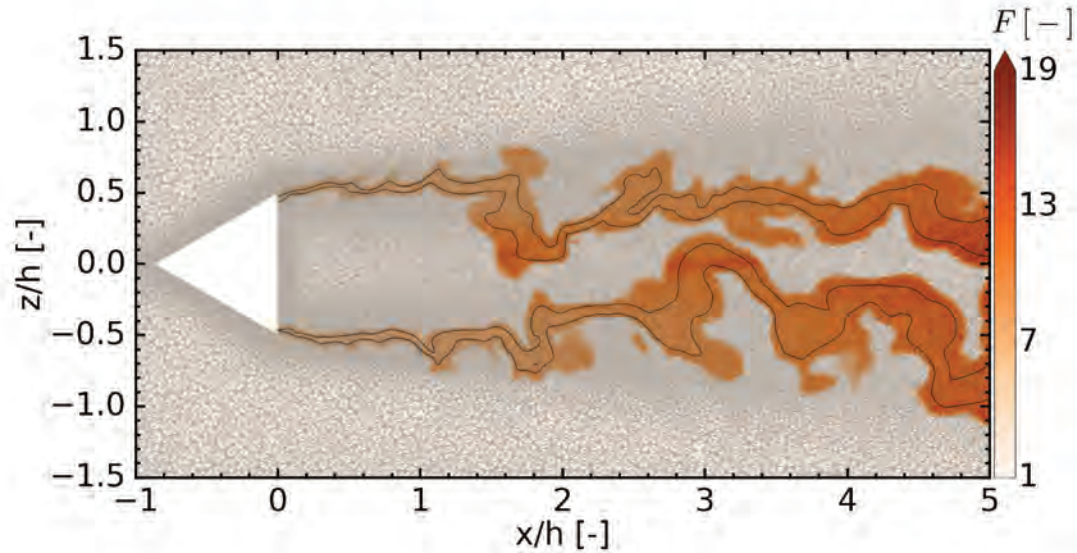


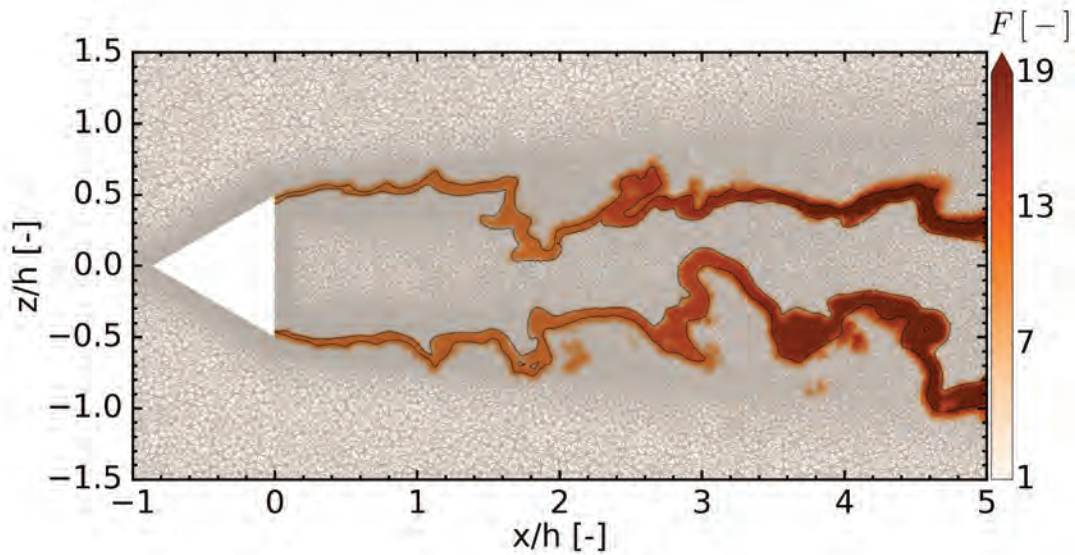
**Fig. 6.14.** Instantaneous thickening field with an overview of the mesh and an iso-line of forward reaction rate  $q_1 = 60 \text{ m}^{-3} \text{s}^{-1}$  for a thickened flame computed with the standard method for case 2s - lw - dyn [154].

standard and the generic methods. The continuous lines correspond to iso-lines of forward reaction rate:  $q^1 = 60 \text{ m}^{-3} \text{s}^{-1}$ .

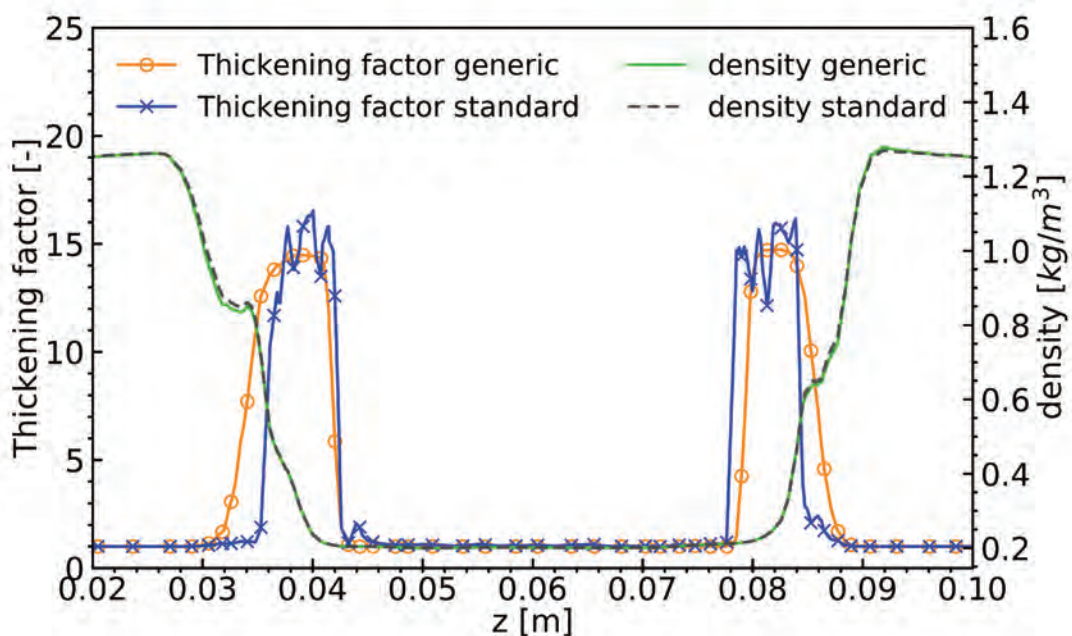
With both methods, the flame front is correctly located and the same flame front shape and thickness are found, as shown by the  $q_1$  iso-lines. However it seems that the standard method leads to a thicker thickening zone with a slightly smaller  $F_0$ . This is the direct result of the fixed value of  $\delta_L^0$  used in this approach. Note that thickening is correctly applied with the generic method in all directions, whatever the orientation of both, the tetrahedral element and the local curvature of the flame front, demonstrating the capacity of the generic method to thicken complex flame fronts.

Figure 6.16 shows instantaneous spatial profiles of thickening factor and density, obtained with both methods and plotted at  $x/h = 0.6$  (see Fig. 6.15). Maximum thickening factors obtained with both methods are almost identical. The standard maximum thickening factor fluctuates because of the local estimation of  $\Delta_x$  within the thickened flame thickness, whereas the generic method only uses the value of  $\Delta_x$  estimated at the ridge line location. With the generic method the thickening factor goes farther in the fresh gas side (as expected), and is smoother thanks to the use of the thickening function  $tf$ . Note that the intermediate peak in the density profiles is not a numerical oscillation but the result of  $F$  going to unity, which changes the spatial scale.

Figure 6.17 is a snapshot of the flame front resolution  $R_c$  field estimated with the generic method. The continuous line is an iso-line of forward reaction rate:  $q^1 = 60 \text{ m}^{-3} \text{s}^{-1}$ . The estimation of the flame front resolution ranges between 3 and 4, which is coherent with the number of cells delimited by the iso-line but lower than  $N_c$ . Note that a lower  $R_c$  is computed at the location where the flame front is thinner, demonstrating the robustness of the flame front thickness estimation.



**Fig. 6.15.** Instantaneous thickening field with an overview of the mesh and an iso-line of forward reaction rate  $q_1 = 60 \text{ m}^{-3} \text{s}^{-1}$  for a thickened flame computed with the generic method for case 2S – *lw – dyn* [154].



**Fig. 6.16.** Instantaneous spatial profiles of thickening factor (left axis) and density (right axis) obtained with the standard and the generic methods plotted at  $x/h = 0.6$  for case 2s – *lw – dyn* [154].

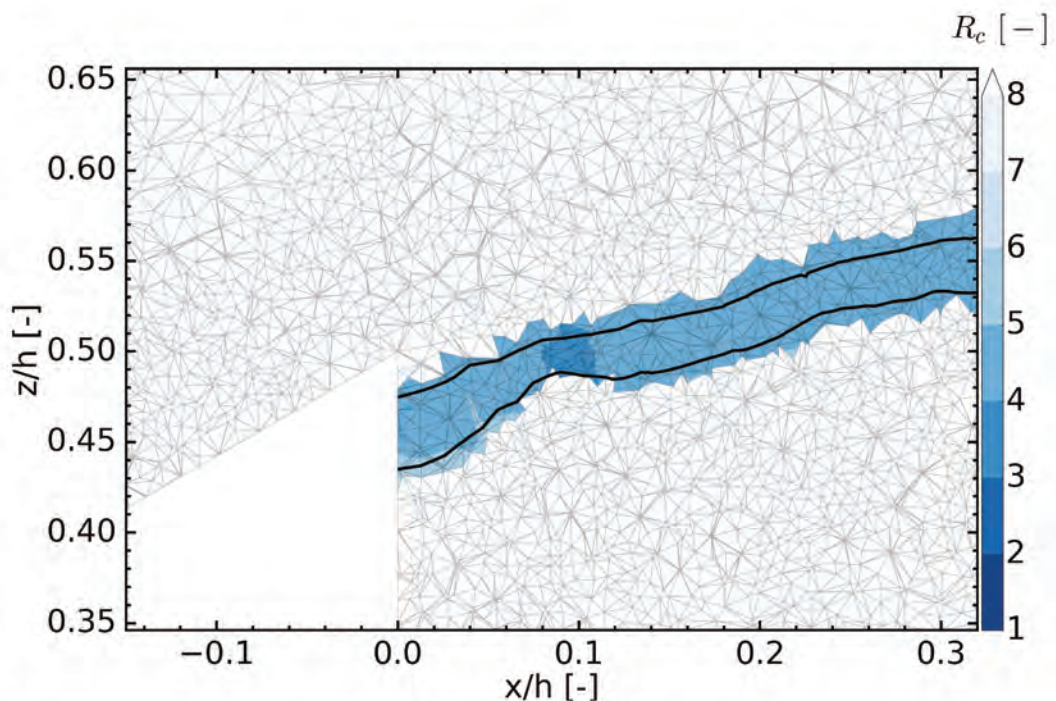


**Fig. 6.17.** Instantaneous flame front resolution field  $R_c$  obtained with the generic method and an iso-line of forward reaction rate  $q_1 = 60 \text{ m}^{-3} \text{ s}^{-1}$  for case 2s - lw - dyn.

CPU cost [ $\mu\text{s}/\text{ite} \cdot \text{node}^{-1}$ ]	Case 1	Case 2	Case 3
Generic method	6.22	8.45	50.0
Standard method	6.1	5.133	33.5

**Tab. 6.2.** Comparison of the CPU costs for the generic and the standard methods

CPU cost [ $\mu\text{s}/\text{ite} \cdot \text{node}^{-1}$ ]	Case 1	Case 2	Case 3
TFLES routine: TF [s]	6.28	27.53	66.8
Front detection [% TF]	2.48	3.04	5.45
Haselbacher algorithm [% TF]	6.01	0.481	16.0
MPI communication [% TF]	0	25.0	20.2

**Tab. 6.3.** Detailed CPU costs for the generic method

### 6.3.3 CPU costs

Table 6.2 presents the CPU costs for both thickening methods and all cases. For case 1, where the flame was computed on a single processor, the CPU cost of the generic method is almost the same as the standard one. Only a slight over-cost is observed due to the second derivative computation. For case 3, representing a more challenging case, the generic method costs approximately 1.5 times more than the standard method.

Table 6.3 shows more detailed CPU costs for several parts of the combustion routine for the generic method and all cases. One can observe that the front detection part is very efficient for all cases. However, for cases 2 and 3, the MPI communication part represents 20-25 % of the TFLES routine. This over-cost is due to a non-efficient dispatching of the tasks between processors. In other words, with a more efficient partitioning, this over-cost can be reduced. Note that the Haselbacher algorithm represents a higher part of the TFLES routine for the third case since the flame is much longer than for other cases, leading to a higher number of associated Lagrangian particles. Moreover, as the flame is established almost over the half of the computational domain, the tasks are better dispatched between processors, leading to a lower MPI communication cost than for case 2.

#### **6.4 Conclusions**

In this Chapter a generic and self-adapting method for flame detection and thickening has been presented. This generic approach relies on local geometric considerations and, unlike previous thickening methods, does not need any parameterization nor preliminary calibration. First, the flame is located by analyzing the curvature of the flame front. Then, an estimation of the flame front thickness is obtained, allowing a thickening restricted to under-resolved flame regions, and a self-adapting thickening of the front. One originality of the present paper is to propagate the thickening factor with fluid particles, using an algorithm originally developed for particle-tracking.

Three test cases were performed to validate the methodology. The first one consists in a highly under-resolved one-dimensional flame computed on a structured mesh. The generic method has demonstrated its capacity to temporally self-adapt the maximum thickening factor so that the flame resolution corresponds to the target one. The second case is a two-dimensional planar laminar flame discretized on an unstructured triangular mesh. In this case the flame moves from a fine to a coarse mesh. The new method correctly catches the mesh resolution transition and self-adapts the maximum thickening factor to keep the flame resolution constant. Finally, the last test case consists in a three-dimensional turbulent flame and once again, the generic sensor proves to be very efficient to locate and thicken complex flame fronts.

Apart from an easier use, and the reduction of user input only to one parameter ( $N_c$ ), this approach is critical to apply TFLES to complex cases with varying local conditions, complex chemistry or liquid fuel. Indeed in all these cases, the a priori knowledge of the flame thickness is difficult or even not possible, and the standard thickening could lead to large over- or under-thickening, decreasing the accuracy of the simulation.

# Effect of relative velocity on the flame speed and structure of laminar spray flames

The objective of this Chapter is to contribute to the understanding of the spray/flame interaction in laminar spray flame, where the dispersed phase has a relative velocity compared to the carrier phase. This chapter is based on a paper published in Proceedings of the Combustion Institute (2019) [201].

## 7.1 Introduction

Spray combustion occurs in a variety of combustion systems, including internal combustion engines or aviation gas turbines. The presence of a spray in a combustion chamber leads to complex spray/combustion interactions. The liquid phase may significantly change the propagation properties of a premixed flame [39, 40, 41, 42, 43]. Ballal and Lefebvre [41] experimentally pointed out the effect of droplet size on the laminar spray flame speed for lean and stoichiometric mixtures, showing that increasing droplet diameter reduces the laminar flame speed. They also proposed a correlation to evaluate the laminar spray flame speed according to inlet liquid injection properties. However, this expression was shown inappropriate either for rich mixtures, or for a full range of droplet diameters [52]. For rich mixtures, Hayashi et al. [53] observed the existence of an optimum droplet size that results in an enhanced laminar flame speed compared to gaseous premixed flame. This phenomenon was explained by defining an effective fuel-air ratio which accounts for the unvaporized and incompletely mixed fuel. The resulting reacting mixture burns close to stoichiometry, leading to high flame propagation speed. The increase of the flame speed for overall rich flames has also been numerically observed in one-dimensional laminar premixed spray flame simulations [52, 54, 55]. However no clear theoretical framework has been proposed in the literature to handle all possible spray flame structures.

In combustion chambers, the relative velocity between the gas and the droplets can be high as the air and spray injections are separated and large Stokes droplets do not immediately take the gas flow velocity. Moreover, the gas flow is often subjected to high shear, particularly in dilution area. These strong velocity gradients increase the relative velocity with the droplets. Finally, turbulent velocity fluctuations may also contribute to a velocity difference with the droplets. To the authors knowledge, the impact of the relative velocity between the spray and the gas on the flame structure and velocity has never been studied.

For a better understanding of the parameters controlling spray flame propagation, combustion in one-dimensional mono-disperse mists of moving droplets is numerically studied in this work. The objective is to characterize the effect of overall equivalence ratio, droplet size, liquid loading and relative velocity on the flame structure and propagation. In Section 7.3, the numerical solver and physical models are presented, together with the computed configuration and the various test cases. Section 7.4 presents the results, evidencing the influence of relative velocity on the spray flame properties. Two expressions of the laminar spray flame speed that cover all the cases are finally proposed.

	$A_j[\text{cgs}]$	$E_j[\text{cgs}]$
Reaction 1	$1.4 \times 10^{11}$	$2.9 \times 10^4$
Reaction 2	$-5.0 \times 10^9$	$2.1 \times 10^4$

Tab. 7.1. Two-steps reduced chemical mechanism for n-heptane/air. Pre-exponential factor  $A_j$  and activation energies  $E_j$  are both in  $\text{cgs}$  units.

## 7.2 Chemistry description

A simplified global mechanism is used for premixed n-heptane/air flames with the Pre-Exponential Adjustement (PEA) method to recover the correct flame speed for rich mixtures [202]. This two-step mechanism is based on a fast oxydation reaction, followed by a CO-CO<sub>2</sub> equilibrium. Six species ( $C_7H_{16}$ ,  $O_2$ , CO, H<sub>2</sub>O, CO<sub>2</sub> and N<sub>2</sub>) and two reactions are taken into account, with rate constants of [87]:



Reaction rates  $q_j$  follow an Arrhenius law:

$$q_1 = A_1 f_1(\Phi_{loc}) \left( \frac{\rho Y_{C_7H_{16}}}{W_{C_7H_{16}}} \right)^{0.6} \left( \frac{\rho Y_{O_2}}{W_{O_2}} \right)^{0.9} \exp \left( \frac{-E_{a,1}}{RT} \right) \quad (7.3)$$

$$q_2 = A_2 f_2(\Phi_{loc}) \left[ \left( \frac{\rho Y_{CO}}{W_{CO}} \right)^{1.0} \left( \frac{\rho Y_{O_2}}{W_{O_2}} \right)^{0.5} - \frac{1}{K} \left( \frac{\rho Y_{CO_2}}{W_{CO_2}} \right)^{1.0} \right] \exp \left( \frac{-E_{a,2}}{RT} \right) \quad (7.4)$$

The pre-exponential constants  $A_j$  and the activation energies  $E_j$  are given in Tab. 7.1, and  $K$  is the equilibrium constant. This method accounts for both the fuel oxidation reaction and the CO-CO<sub>2</sub> equilibrium. This last reaction is difficult to handle numerically since it shows a sudden change in behavior from lean to rich combustion. Therefore, the pre-exponential factor of the second reaction varies with local equivalence ratio  $\Phi_{loc}$  using a correction function  $f_2(\Phi_{loc})$  to reproduce this specific behavior. Then, the pre-exponential factor of the fuel oxidation reaction is also corrected to correctly predict the laminar flame speed. The local equivalence ratio is based on a passive scalar  $Z \in [0, 1]$  [26].  $Z$  is calculated on the principle of atoms conservation in the gas phase. To avoid  $Z$  variations due to differential diffusion, the construction of  $Z$  requires that all species laminar Schmidt numbers are equal, which is the case for the two-step chemical scheme.

$$\Phi_{loc} = \frac{1 - Z_{st}}{Z_{st}} \frac{Z}{1 - Z'} \quad (7.5)$$

$$Z = \frac{n - n_O}{n_F - n_O} \text{ with } n = \sum_{k=1}^N \alpha_{kp} \frac{W_p Y_k}{W_k}, \quad (7.6)$$

where  $n_O$  and  $n_F$  stand for the values of  $n$  in the oxidizer and fuel streams respectively,  $\alpha_{kp}$  is the number of atoms of type  $p$  in species  $k$ . The two-step scheme is validated against the experimental laminar flame speed measurements provided by Kumar et al. [203] in Fig. 7.1. The Cantera software is used to compute flame speeds for a 1D resolved planar flame at the same operating conditions as the simulations ( $T = 300\text{K}$  and  $P = 101325\text{ Pa}$ ): results show a good agreement for the two-step reduced chemistry for equivalence ratios ranging from  $\phi_g = 0.8$  to  $\phi_g = 1.4$ .

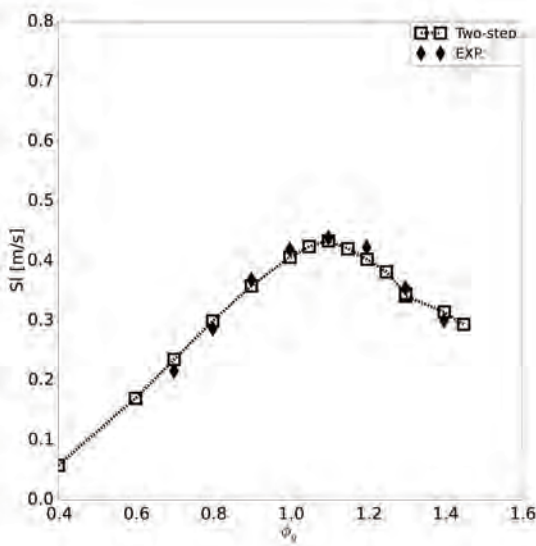


**Fig. 7.1.** Comparison of experimental measurements [203] and two-step chemistry for laminar flame speed computed at  $T = 300\text{K}$ ,  $P = 101325\text{Pa}$ .

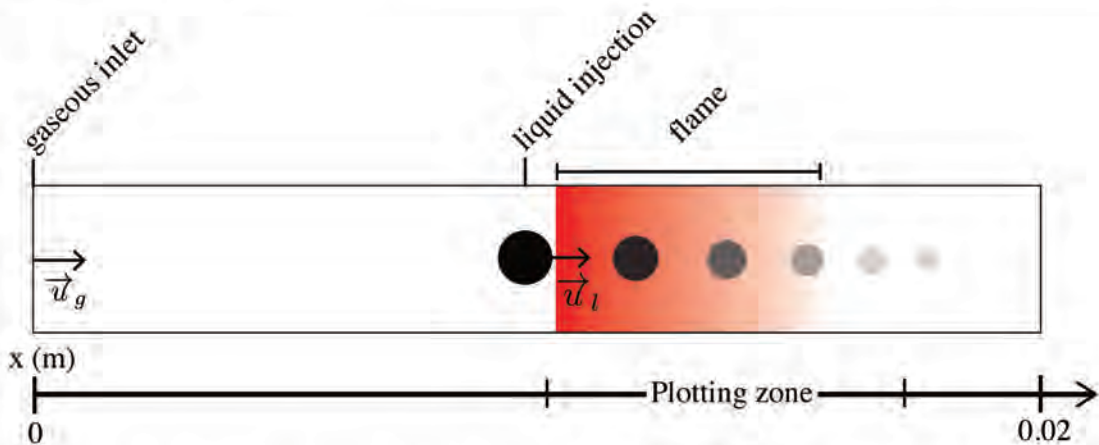


**Fig. 7.2.** Sketch of the configuration. Results presented in Section 7.4.1 are limited to the "plotting zone".

### 7.3 Numerical setup

The AVBP solver [93] is used with the Lagrangian formalism to treat the liquid phase [204]. Droplets are considered as isolated points in space, influenced by the surrounding Eulerian gaseous flow conditions. In the two-way coupling approach, the liquid phase transfers mass, momentum and energy to the gas via source terms locally estimated from the number of droplets inside a nodal control volume [204].

The modified Sherwood  $Sh^*$  and Nusselt  $Nu^*$  numbers are used to take into account the change in film thickness due to Stefan's law.

A common approximation used in Section 7.4.2 for the analytical spray flame expressions consists in evaluating the mass Spalding number  $B_M$  at a liquid temperature  $T_l = (T_{wb} + T_{inj})/2$ , where  $T_{wb}$  is the wet bulb temperature of the liquid fuel and  $T_{inj}$  the liquid injection temperature.

Case	$\phi_{tot}$	Gaseous and liquid fuel equivalence ratios	$u^*$	$d_p$ ( $\mu\text{m}$ )
A	0.9	$\phi_g = 0.8, \phi_l = 0.1$	1, 30	5-80
B	0.9	$\phi_g = 0.0, \phi_l = 0.9$	1, 30	5-80
C	1.3	$\phi_g = 0.8, \phi_l = 0.5$	1, 30	5-80
D	1.3	$\phi_g = 0.0, \phi_l = 1.3$	1, 30	5-80

Tab. 7.2. Summary of simulated cases

### 7.3.1 Configuration

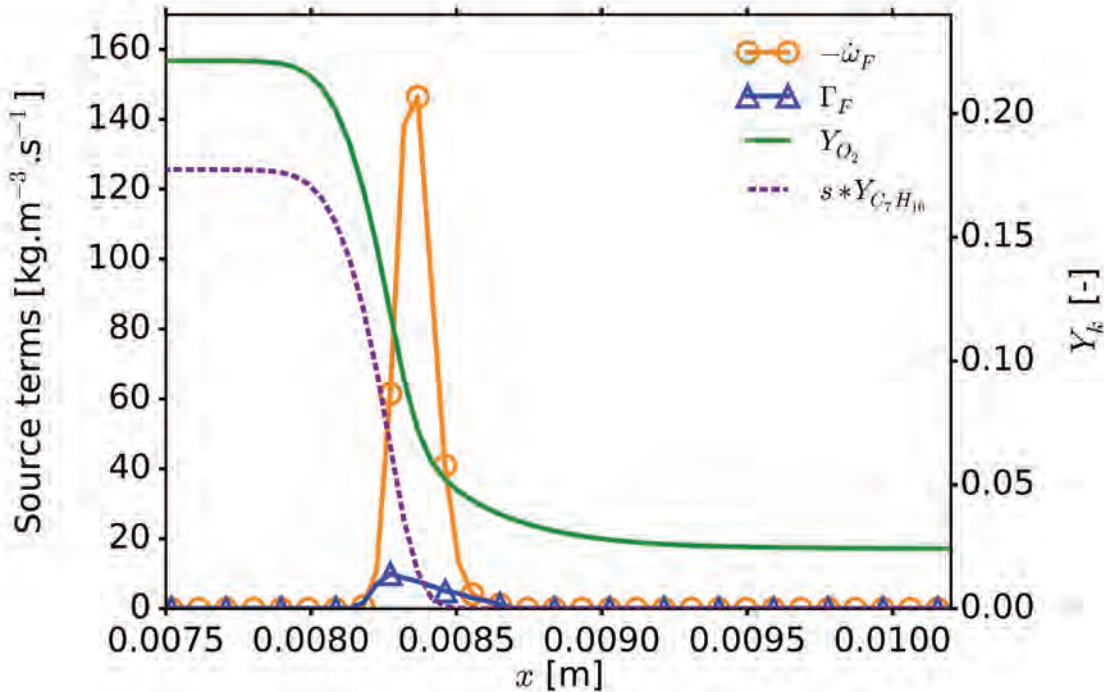
The computational domain is illustrated in Fig. 7.2. It consists in a 0.02 m long cartesian one-dimensional grid composed of 826 elements. The domain is sufficiently long to allow the liquid droplets to completely evaporate before reaching the outlet, and the grid is fine enough to solve the inner flame structure. A steady solution is obtained by setting the inflow velocity at the flame speed. In such configuration, and as in purely gaseous flames, the flame can stabilize anywhere in the domain. This has a direct impact on the two-phase flame structure, as droplets may evaporate and interact with the gas flow during their travel from injection to the flame. In other words, the solution of the two-phase flame depends on an additional parameter compared to gaseous flames, which is the distance from injection. This parameter is not considered in the current work as it is arbitrary for the target configuration. The two-phase flame is here characterized by the droplet properties just in front of the flame, i.e., at the location where they start to interact with the flame. To easily control these properties, droplets are injected just in front of the flame (see Fig. 7.2).

Table 7.2 summarizes the simulated cases. As the evolution of the laminar spray flame speed as a function of droplet diameter is different if the mixture is lean or rich, two overall equivalence ratios are investigated,  $\phi_{tot} = 0.9$  (cases A and B) and  $\phi_{tot} = 1.3$  (cases C and D). Note that the overall equivalence ratio is defined as:  $\phi_{tot} = s * Y_{F,tot} / Y_{O_2}$ , where the total fuel mass fraction  $Y_{F,tot}$  is the sum of gaseous and liquid fuel mass fractions. For cases B and D, only liquid fuel is provided to the flame ( $\phi_{tot} = \phi_l$ ) whereas for cases A and C fuel vapor is also injected so that  $\phi_{tot} = \phi_l + \phi_g$ . The velocity ratio between liquid and gaseous phases is expressed as  $u^* = u_l / u_g$ . For each case, two velocity ratios are tested ( $u^* = 1$  and  $30$ ), with droplets of diameter ranging from  $d_p = 5 \mu\text{m}$  to  $80 \mu\text{m}$ . Droplets are injected at the same temperature as the gas,  $T_l = T_g = 300\text{K}$ . For a given droplet diameter, the number of droplets is adjusted to the targeted equivalence ratio, and ensures a continuous feeding of the flame, making the isolated burning droplet regime unreachable. Finally, Stokes numbers (defined as  $S_t = \tau_p / \tau_g$  with  $\tau_p$  the droplets relaxation time proposed by Schiller and Nauman [149], and  $\tau_g = \delta_L^0 / u_g$  with  $\delta_L^0$  the laminar flame thickness and  $u_g$  the gaseous velocity) range from  $S_t = 0.011$  for case D,  $u^* = 30$  and  $d_p = 5 \mu\text{m}$  to  $S_t = 2.9$  for case A,  $u^* = 1$  and  $d_p = 80 \mu\text{m}$ : the droplets velocity quickly relaxes toward the gaseous one downstream the flame.

## 7.4 Results

### 7.4.1 Spray flame structures

To analyze in detail spray flame structures, focus is made here on the flames with initial diameter  $d_p = 20 \mu\text{m}$  and the two velocity ratios for each case in Table 7.2. Figures 7.3 and 7.4 show the fuel consumption  $\dot{\omega}_F$  and evaporation  $\Gamma_F$  rates as well as the mass fraction profiles of  $O_2$  and  $C_7H_{16}$  for case A,  $u^* = 1$  and  $u^* = 30$ . Note that  $\Gamma_F$  being the total mass of gaseous fuel provided by liquid droplets per unit volume and time, can be directly compared to the reaction source term. For a better readability, the fuel mass fraction profile  $Y_{C_7H_{16}}$  is multiplied by the



**Fig. 7.3.** Comparison of source terms and mass fraction profiles for case A, droplets diameter  $d_p = 20\mu\text{m}$  and velocity ratio  $u^* = 1$ .

stoichiometric ratio  $s$  (dotted line Figs. 7.3 and 7.4).

For  $u^* = 1$  (Fig. 7.3), the spray flame structure is similar to a gaseous flame: small droplets with low injection speed rapidly evaporate inside the flame front. The evaporation rate ( $\Gamma_F$ ) is much lower than the chemical source term ( $-\dot{\omega}_F$ ) and does not play a critical role.

For  $u^* = 30$  (Fig. 7.4), droplets move too fast to completely evaporate within the gaseous flame thickness, showing non-zero  $\dot{\omega}_F$  and  $\Gamma_F$  behind the main reaction zone. Two zones may be distinguished depending on whether  $\dot{\omega}_F$  and  $\Gamma_F$  superpose or not. In the front part of the flame, which controls the flame speed  $\dot{\omega}_F$  and  $\Gamma_F$  do not superpose:  $\Gamma_F$  is much smaller than  $\dot{\omega}_F$ , and as in the previous case it does not have a big impact on the flame structure. However, the quantity of fuel burning in this first zone is lower than the total fuel as droplets cross the flame too fast. The resulting effective equivalence ratio seen by the flame is lower than the total  $\phi_{tot}$ , which modifies the propagation speed: it is found that  $S_L^{tp} = 0.309\text{m/s}$ . The second part of the flame consumes only evaporated fuel and does not contribute to the main flame propagation. In this zone  $\Gamma_F = \dot{\omega}_F$  and the combustion is controlled by evaporation.

Figure 7.5 reports  $S_L^{tp}$  and the link with the effective equivalence ratio. As  $\phi_{eff}$  is always lower than  $\phi_{tot}$ , the laminar spray flame velocity  $S_L^{tp}$  is also always lower than the gaseous flame speed at the same total equivalence ratio in lean cases.

On the other hand,  $\phi_{eff}$  cannot be lower than  $\phi_g$ . This leads in the present case to  $S_{L,\phi_g=0.8}^0 \leq S_L^{tp} \leq S_{L,\phi_g=0.9}^0$ . It is finally found that  $S_L^{tp}(u^* = 1) = S_{(L,\phi_{tot})}^0$  and  $S_L^{tp}(u^* = 30) = S_{(L,\phi_g)}^0$ . In terms of gaseous temperature profile (Fig. 7.6), case A shows little difference with the corresponding gaseous flame (dashed line), whatever the relative velocity. The flame thickness is a bit larger and the equilibrium temperature is the same as the one of the gaseous flame: as the mixture is lean all the injected fuel is finally burnt thanks to sufficient amount of oxidizer. Note that for case A, the same trends are also observed for the other injected droplets diameters.

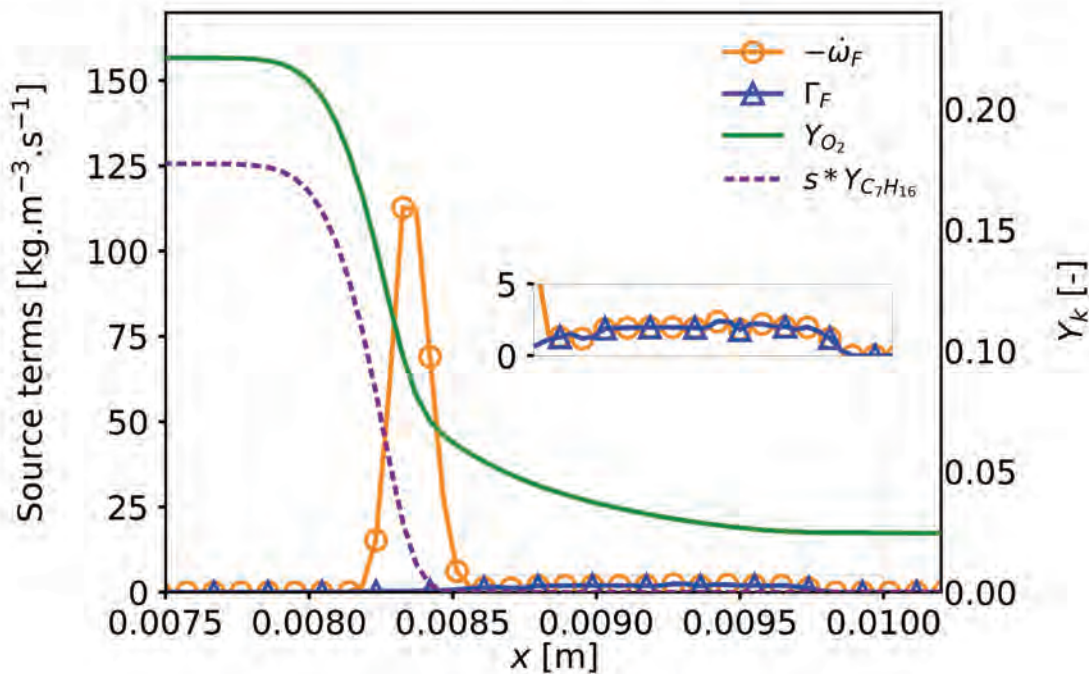


Fig. 7.4. Comparison of source terms and mass fraction profiles for case A, droplets diameter  $d_p = 20\mu\text{m}$  and velocity ratio  $u^* = 30$ .

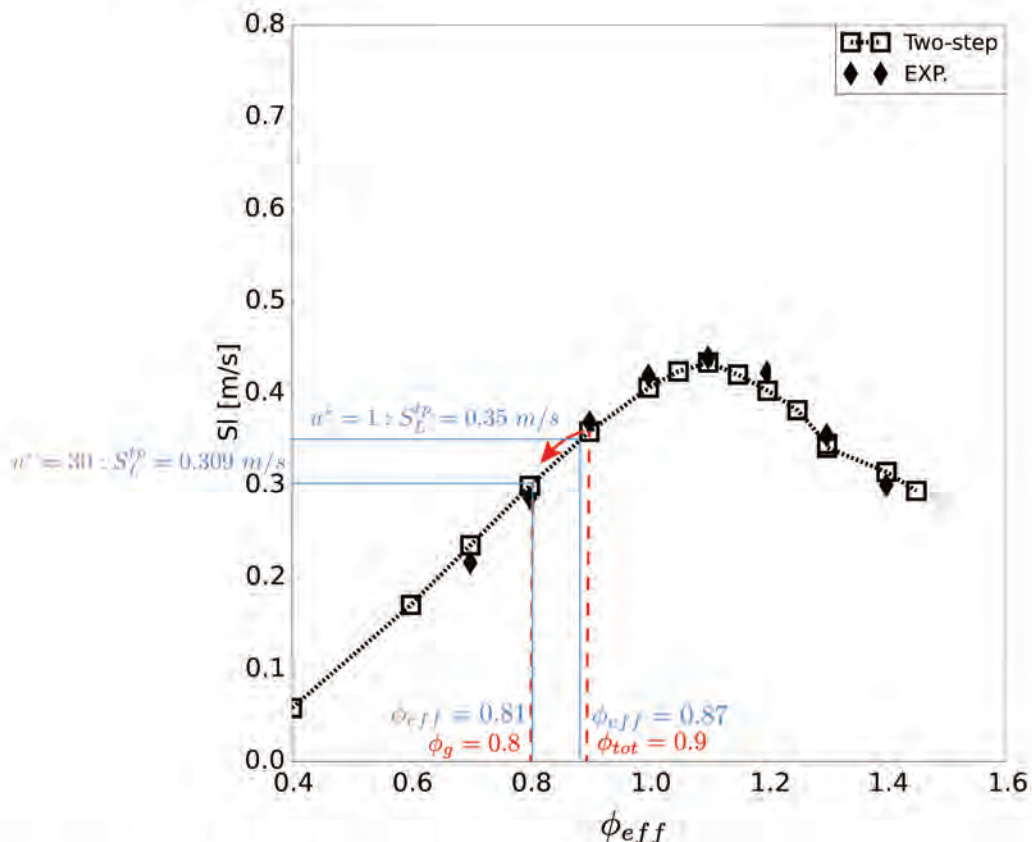
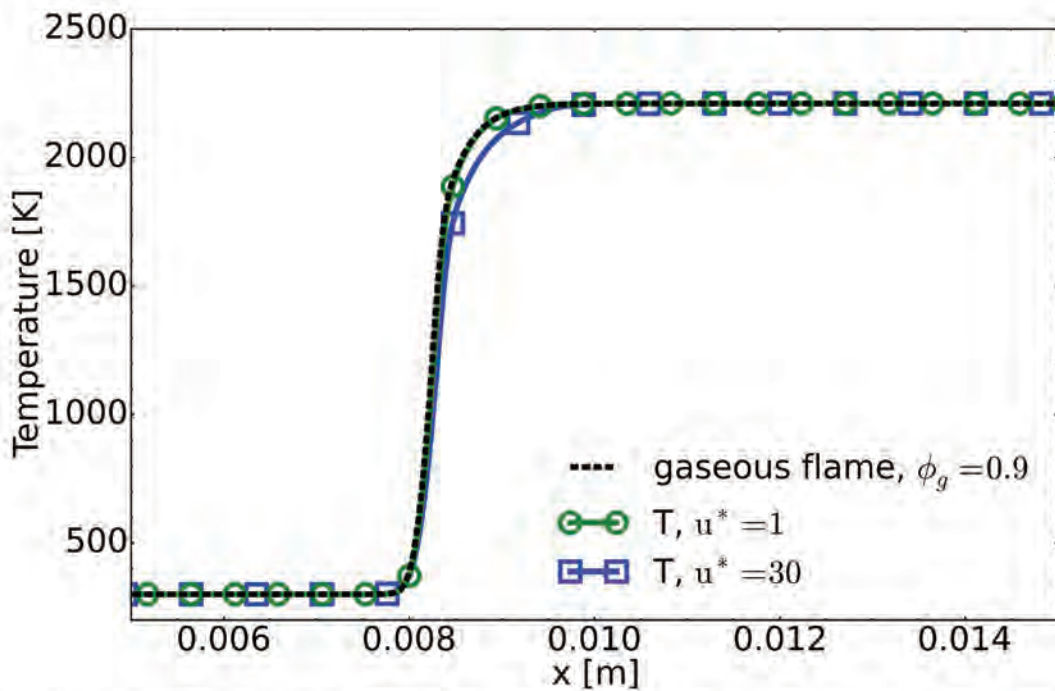


Fig. 7.5. Link between the effective equivalence ratio and  $S_L^{tp}$  for case A, droplets diameter  $d_p = 20\mu\text{m}$  and both velocity ratios  $u^* = 1$  and  $u^* = 30$ .



**Fig. 7.6.** Comparison of temperature profiles for gaseous and spray flames for case A. The droplet diameter is  $d_p = 20\mu\text{m}$  and velocity ratios are  $u^* = 1$  and  $u^* = 30$ .

Figures 7.7 and 7.8 show the same quantities for case B, where only liquid fuel is injected with the same total equivalence ratio as case A. For  $u^* = 1$  the fuel consumption rate  $\dot{\omega}_F$  and the evaporation rate  $\Gamma_F$  now have the same order of magnitude, and even superpose at the end of the reaction zone. Therefore a large amount of evaporating fuel is located in the back side of the flame and does not contribute to the flame propagation. As less fuel vapor is available in the first zone, a lower  $\phi_{eff}$  is expected, leading to  $0 < S_L^{tp} \leq S_{L,\phi_g=0.9}^0$ . It is found that  $S_L^{tp}(u^* = 1) = 0.29\text{m/s}$ . Note that weak pre-evaporation occurs in front of the flame, introducing some deviation from a purely liquid-fed flame. For  $u^* = 30$ ,  $\Gamma_F = \dot{\omega}_F$  everywhere so that the flame structure is fully controlled by evaporation. The resulting fuel vapor mass fraction is close to zero as it is consumed as soon as produced by evaporation. In this case, calculating an effective equivalence ratio is more difficult and not relevant as the flame is too far from an equivalent gaseous flame.

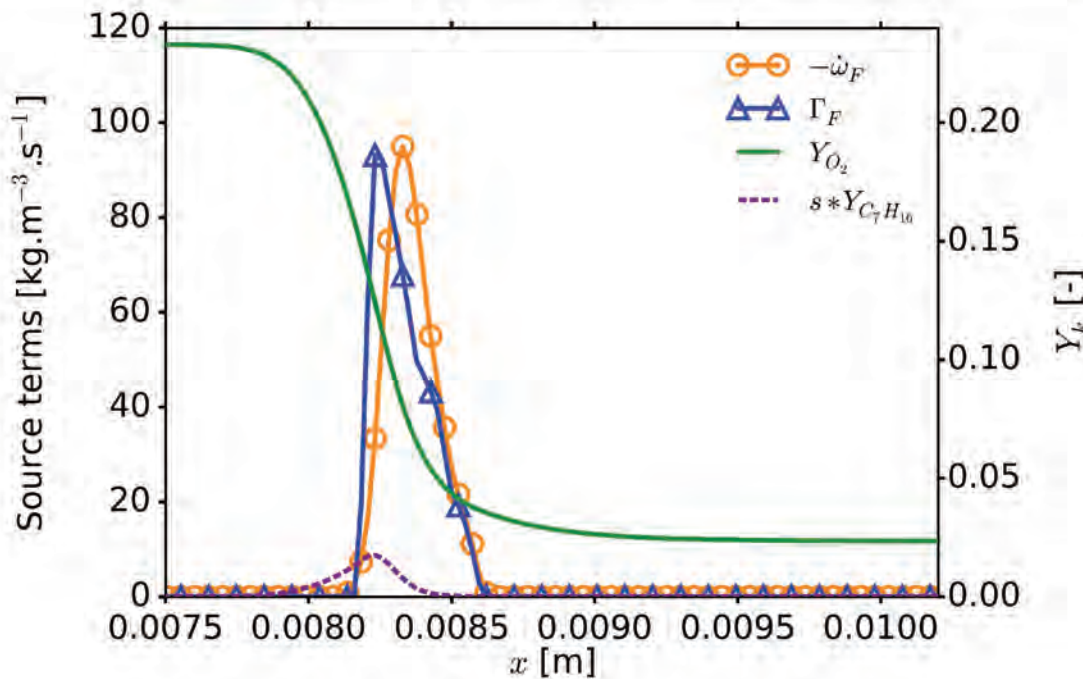


Fig. 7.7. Comparison of source terms and mass fraction profiles for case B, droplets diameter  $d_p = 20\mu\text{m}$  and velocity ratio  $u^* = 1$ .

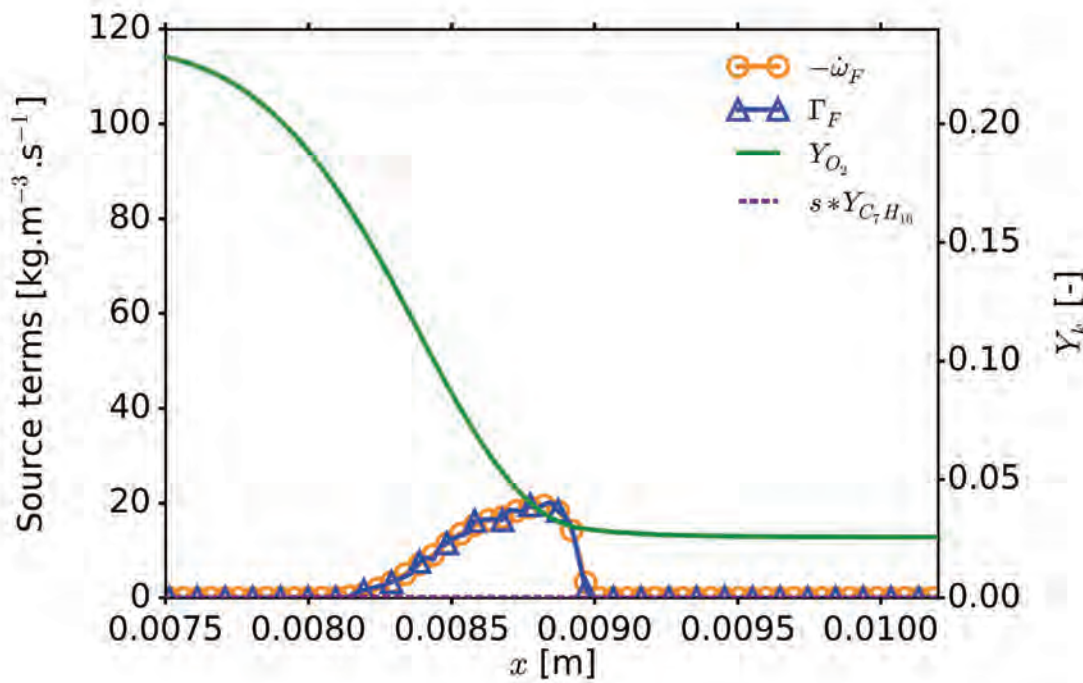
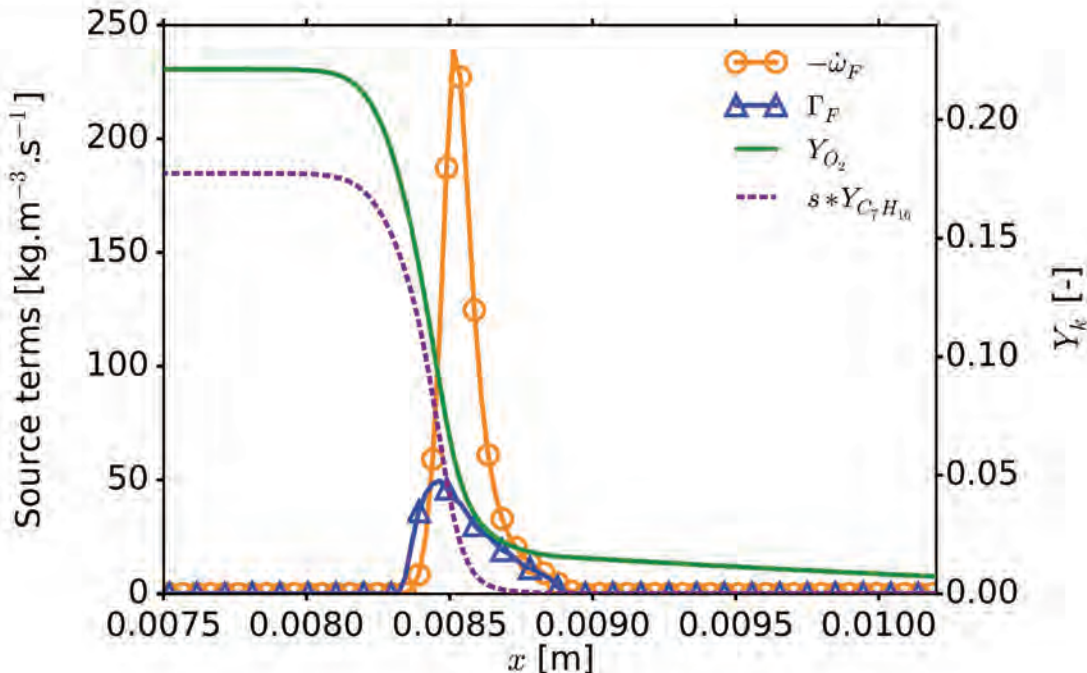


Fig. 7.8. Comparison of source terms and mass fraction profiles for case B, droplets diameter  $d_p = 20\mu\text{m}$  and velocity ratio  $u^* = 30$ .

Figures 7.9 and 7.10 show the results for the rich case C. For  $u^* = 1$ , the situation is similar to case A with  $u^* = 1$ , leading to an effective equivalence ratio smaller than  $\phi_{tot} = 1.3$ . As the mixture is rich, two situations are considered: if  $1 \leq \phi_{eff} \leq \phi_{tot}$  or if  $1 - (\phi_{tot} - 1) \leq \phi_{eff} \leq 1$ ,



**Fig. 7.9.** Comparison of source terms and mass fraction profiles for case C, droplets diameter  $d_p = 20\mu\text{m}$  and velocity ratio  $u^* = 1$ .

a higher spray flame speed is found, but if  $\phi_{eff} \leq 1 - (\phi_{tot} - 1)$ , the spray flame speed is found lower. This is sketched in Fig. 7.11. In the present case,  $S_L^{tp}(u^* = 1) = 0.365\text{m/s}$ , corresponding to  $\phi_{eff} = 0.9$ .

For  $u^* = 30$  the rich mixture leads to a very different flame structure, where all oxidizer is consumed before the evaporation is completed. As a consequence combustion stops, and the continuing evaporation re-introduces gaseous fuel in the burnt gases. Note that presence of a diffusion flame in the burnt gas side, burning on one side the  $O_2$  coming from the premixed fresh gas and on the other side the vaporized fuel diffusing from the burnt gases. In this case,  $S_L^{tp}(u^* = 30) = 0.337\text{m/s}$ , corresponding to  $\phi_{eff} = 0.81$ .

The gaseous temperature profiles shown in Fig. 7.12 are different for the two velocity ratios. The temperature is almost similar to the gaseous one for  $u^* = 1$  except for a slight decrease of the equilibrium temperature due to the latent heat of evaporation. On the contrary for  $u^* = 30$ , the temperature profile reaches a maximum value above the final burnt gas temperature. Note that in this case the temperature is not yet at the final burnt gas temperature at the end of the computational domain. It has been verified that the temperature eventually reaches the correct final value in a sufficiently long domain (not shown). This higher maximum temperature is due to a local equivalence ratio closer to stoichiometry since part of the injected fuel evaporates without burning. The hot gases are then cooled down by a dilution effect from the evaporating droplets which release vapor at a lower temperature.

Finally case D is presented in Figs. 7.13 and 7.14. Here for  $u^* = 1$  the flame structure is similar to the case B with  $u^* = 1$  and a lower  $\phi_{eff}$  is found. However as the mixture is rich the spray flame speed may be higher or lower than the gaseous flame, similarly to case C. For  $u^* = 30$ , the fuel consumption rate  $\dot{\omega}_F$  and the evaporation rate  $\Gamma_F$ , superpose in the front part of the flame. The flame structure is complex, with a first evaporation-controlled premixed flame and a second diffusion flame. As for case B, the definition of a  $\phi_{eff}$  is difficult here. In this case,  $S_L^{tp}(u^* = 1) = 0.348\text{m/s}$  and  $S_L^{tp}(u^* = 30) = 0.183\text{m/s}$ .

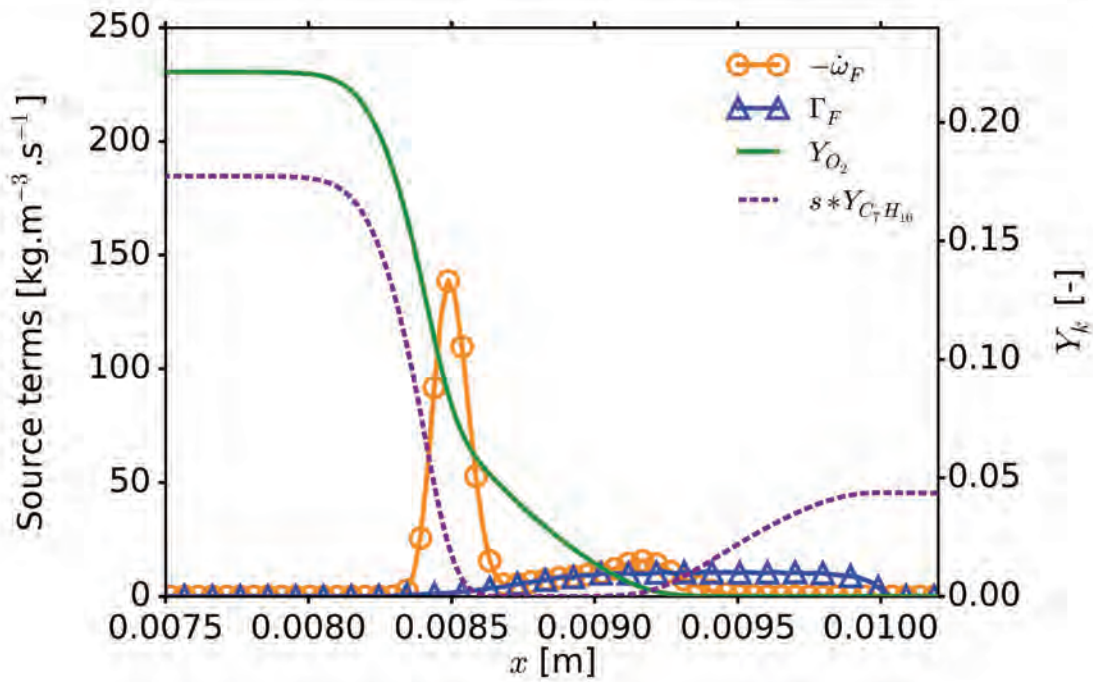


Fig. 7.10. Comparison of source terms and mass fraction profiles for case C, droplets diameter  $d_p = 20\mu\text{m}$  and velocity ratio  $u^* = 30$ .

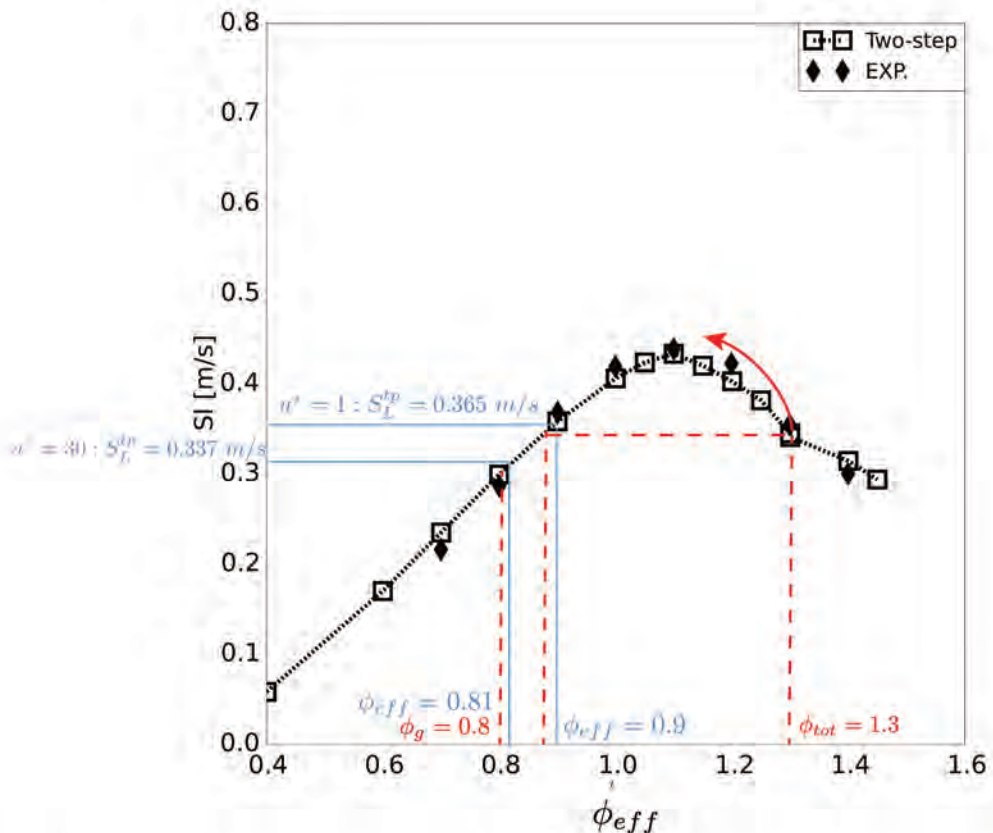


Fig. 7.11. Link between the effective equivalence ratio and  $S_L^{tp}$  for case C, droplets diameter  $d_p = 20\mu\text{m}$  and both velocity ratios  $u^* = 1$  and  $u^* = 30$ .

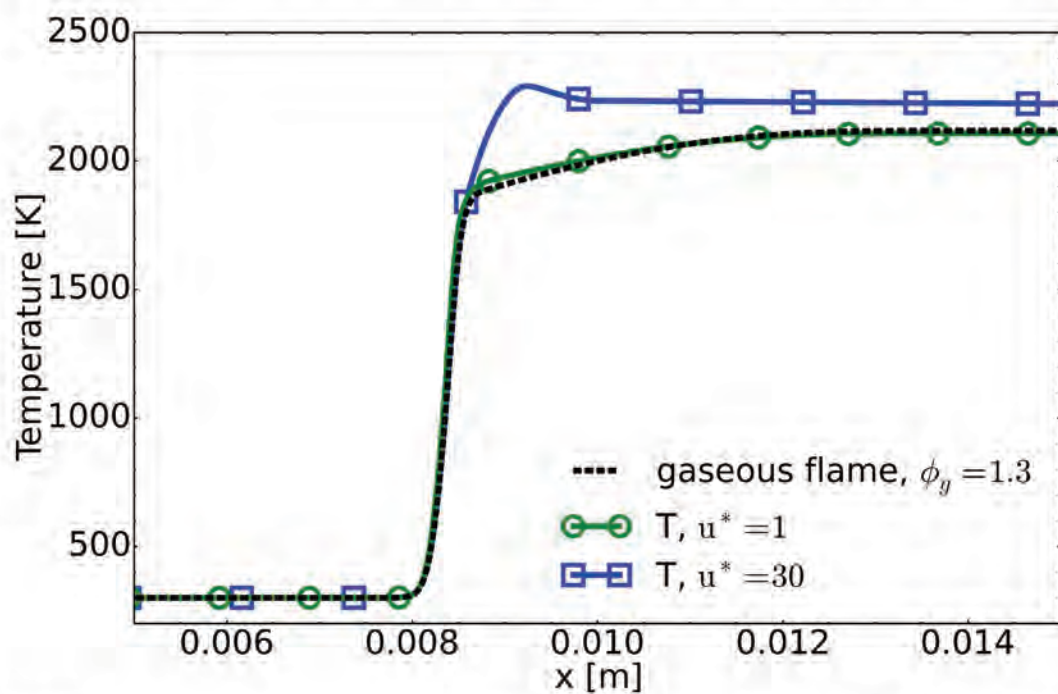


Fig. 7.12. Comparison of temperature profiles for gaseous and spray flames for case C. The droplet diameter is  $d_p = 20\mu\text{m}$  and velocity ratios are  $u^* = 1$  and  $u^* = 30$ .

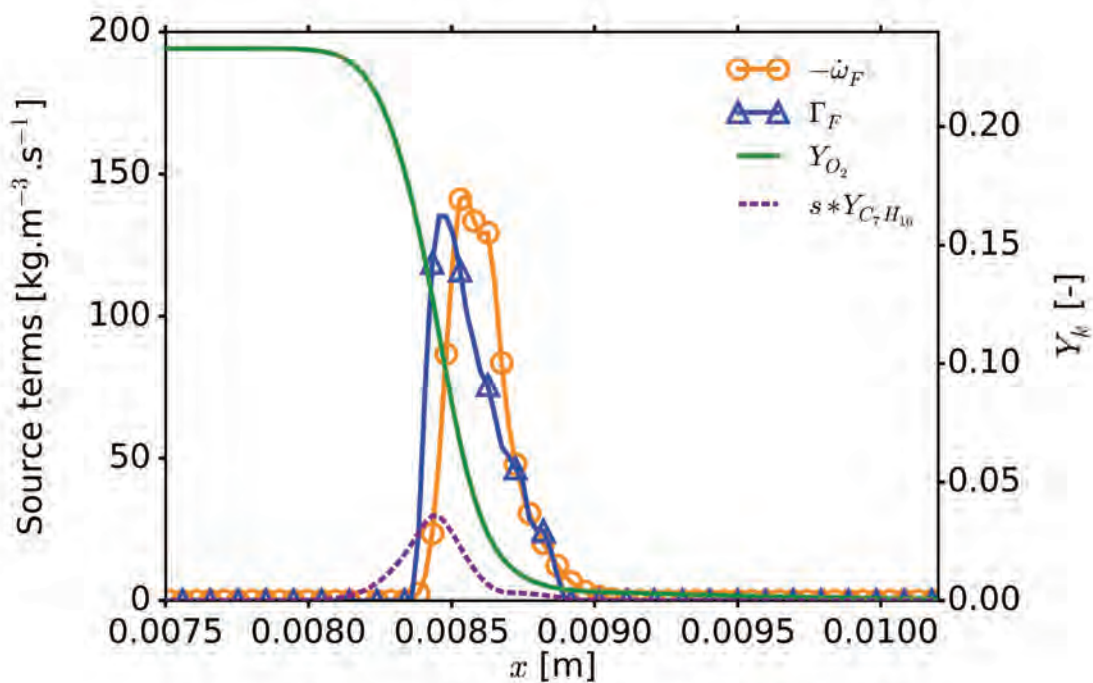
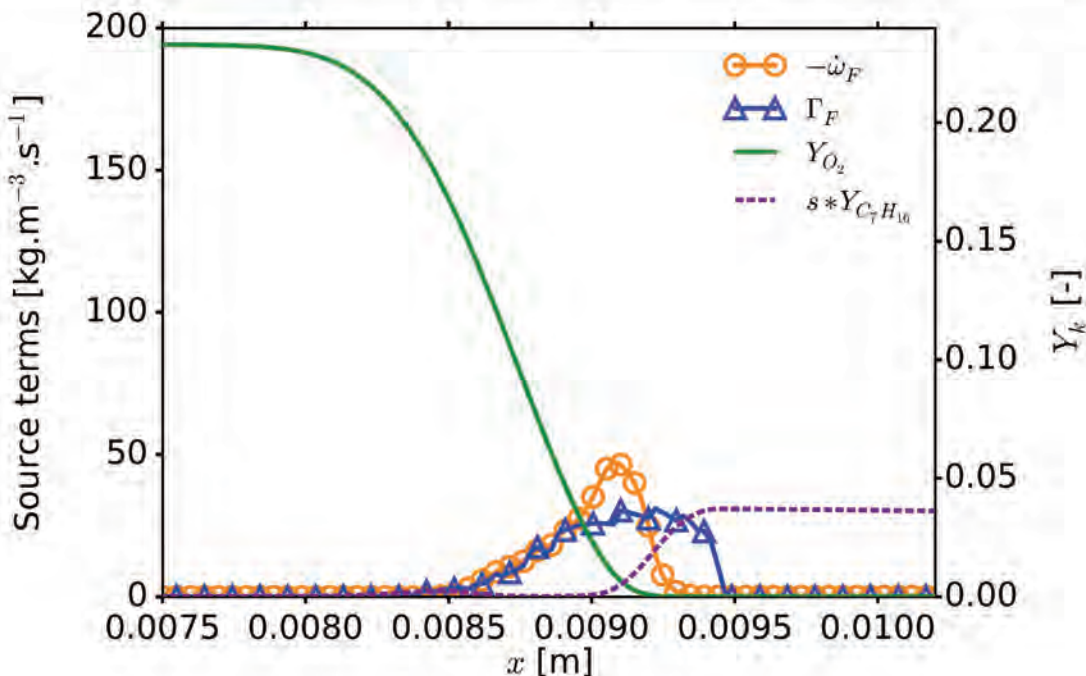


Fig. 7.13. Comparison of source terms and mass fraction profiles for case D, droplets diameter  $d_p = 20\mu\text{m}$  and velocity ratio  $u^* = 1$ .



**Fig. 7.14.** Comparison of source terms and mass fraction profiles for case D, droplets diameter  $d_p = 20\mu\text{m}$  and velocity ratio  $u^* = 30$ .

#### 7.4.2 Determination of the laminar two-phase flame speed

To determine the laminar two-phase flame speed, two situations are considered, depending on either the combustion is fully controlled by evaporation or not. This depends on how  $\phi_g$  compares to  $\phi_{lim}$  where  $\phi_{lim}$  is the equivalence ratio corresponding to the lean flammability limit. If  $\phi_g > \phi_{lim}$ , the spray flame is mainly controlled by gaseous combustion ("weakly evaporation controlled regime"). On the contrary, if  $\phi_g < \phi_{lim}$  the flame is mainly controlled by evaporation ("fully evaporation controlled regime"), except if  $u^* \tau_{ev} / \tau_c < 1$ , where  $\tau_{ev}$  is the evaporation characteristic time (Eq. 7.9) and  $\tau_c$  is the combustion characteristic time: in that case, evaporation is fast and can not be the limiting phenomenon.

##### Weakly evaporation-controlled flames

For weakly evaporation-controlled flames,  $S_L^{tp}$  is determined from the effective equivalence ratio at which the combustion occurs as  $S_L^{tp} = S_{L,\phi_{eff}}^0$ . The laminar two-phase flame speed  $S_L^{tp}$  depends therefore on the total quantity of fuel (gaseous + evaporating) consumed within a consumption zone of length  $\delta_L^0$  (herein the front part of the flame thickness is assumed to be equal to the gaseous laminar flame thickness). The effective equivalence ratio  $\phi_{eff}$  characterizing the laminar spray flame speed is then determined by estimating the total quantity of fuel vapor released and burning in this consumption zone. To evaluate this quantity, the mass of fuel vapor released and burning over a distance  $\delta$  is calculated using the  $d^2$ -law:  $d_p^2(t) \propto t \rightarrow d_p^3(t) \propto t^{3/2}$ . Replacing  $t$  with  $x/u_l$  gives the scaling  $d_p^3(x) \propto x^{3/2}$ . In other words, the amount of vapor released after a distance  $\delta$  scales as  $\delta^{2/3}$ . This allows to calculate the effective equivalence ratio as:

$$\phi_{eff} = \left( \frac{\delta_L^0}{\max(\delta_{ev}, \delta_L^0)} \right)^{2/3} \phi_l + \phi_g \quad (7.7)$$

with:

$$\delta_{ev} = u_l \tau_{ev}, \quad (7.8)$$

$$\tau_{ev} = \frac{\rho_l d_{p_0}^2}{8\rho_g D_F \ln(1 + B_M)}, \quad (7.9)$$

where  $B_M$  is evaluated at a constant liquid temperature  $T_l = (T_{wb} + T_{inj})/2$ . If droplets are small and move slowly, they rapidly evaporate inside the consumption zone:  $\delta_{ev} \leq \delta_L^0$  and Eq. 7.7 recovers  $\phi_{eff} = \phi_{tot}$ . On the contrary, when large droplets are injected with a high velocity ratio, only a part of the liquid fuel evaporates in the consumption zone:  $\delta_{ev} > \delta_L^0$  and Eq. 7.7 leads to  $\phi_{eff} < \phi_{tot}$ . Note that the effect of relative velocity is taken into account in the expression of  $\delta_{ev}$ . The resulting flame speed  $S_L^{tp} = S_L(\phi_{eff})$  is lower than  $S_L(\phi_{tot})$  in lean cases and decreases with  $d_p$ , whereas it may increase or decrease in rich cases, as explained in Fig. 7.11.

#### Fully evaporation-controlled flames

If combustion is fully controlled by evaporation, i.e.,  $\phi_g < \phi_{lim}$  and  $u^* \tau_{ev} / \tau_c > 1$  (or equivalently  $\delta_{ev} > \delta_L^0$ ), the combustion chemistry is not the limiting mechanism, and the laminar two-phase flame speed is determined by the evaporation time, replacing  $\tau_c$  by  $\tau_{ev}$  in the definition of the flame speed:

$$S_L^{tp} = \frac{\delta_L^0 (\min(\phi_{tot}, 1))}{\tau_{ev}}. \quad (7.10)$$

Note that the function  $\min(\phi_{tot}, 1)$  is introduced in Eq. 7.10 to evaluate  $\delta_L^0$  at stoichiometry for rich cases where the equivalence ratio seen by the premixed flame is closer to stoichiometry.

#### 7.4.3 Spray flame speed of the test cases

The spray flame speed  $S_L^{tp}$  is measured in the test cases the inlet fresh gas velocity required to stabilize and keep the spray flame steady. To guarantee that flames are effectively in steady state, the obtained flame speed  $S_L^{tp}$  has been compared to the consumption speed  $S_{c,Ox}^{tp}$  of the oxidizer.

##### Overall lean mixture cases

Figure 7.15 shows the evolution of the laminar spray flame speed  $S_L^{tp}$  versus droplet initial diameter for the two relative velocities ( $u^* = 1, 30$ ) in case A. For an overall lean mixture,  $S_L^{tp}$  never exceeds the gaseous laminar flame speed at the same equivalence ratio and the trend of decreasing  $S_L^{tp}$  with increasing  $d_p$  is well retrieved.

Note that for droplets of diameter  $d_p \geq 30\mu m$  and  $u^* = 30$ ,  $S_L^{tp}$  reaches a minimum value corresponding to the laminar flame speed  $S_L^0$  of a gaseous flame at an equivalence ratio of 0.8: the liquid evaporation is so weak that  $\phi_{eff} = \phi_g$ . Figure 7.16 shows the evolution of the laminar spray flame speed versus droplet initial diameter for the two relative velocities ( $u^* = 1, 30$ ) in case B. The higher liquid loading accentuates the decrease of  $S_L^{tp}$  with the increase of  $d_p$  and  $u^*$ . Compared to Fig. 7.15, as  $\phi_g = 0$  the laminar spray flame speed does not reach a minimum value and goes to zero. Note that the spray flame still holds at consumption rates much lower than the minimum values obtained at the flammability limits of a gaseous premixed flame.

##### Overall rich mixture cases

Figure 7.17 shows the laminar spray flame speed as a function of both droplet diameter and relative velocity in case C. As already observed,  $S_L^{tp}$  is higher than the gaseous premixed laminar flame speed at the same equivalence ratio for fast evaporation.

Figure 7.18 finally shows the laminar spray flame speed as a function of both droplet diameter and relative velocity in case D. Once again the higher liquid loading accentuates the

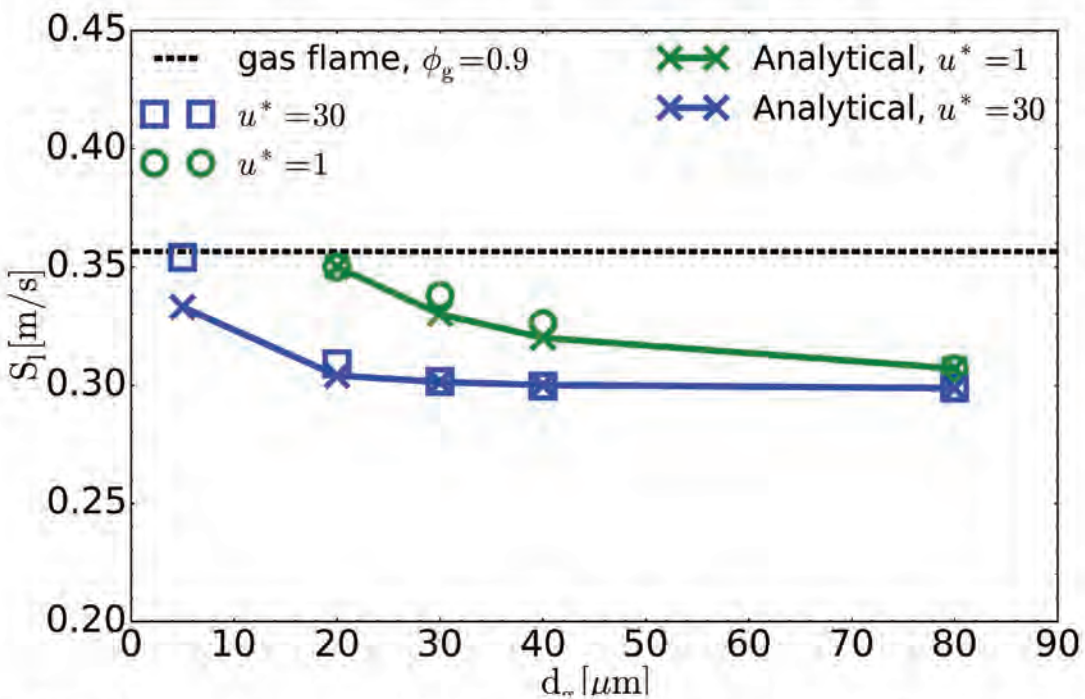


Fig. 7.15. N-heptane spray flame speed as a function of the initial droplet diameter for case A. The analytical laminar spray flame speeds are obtained with Eq. 7.7.

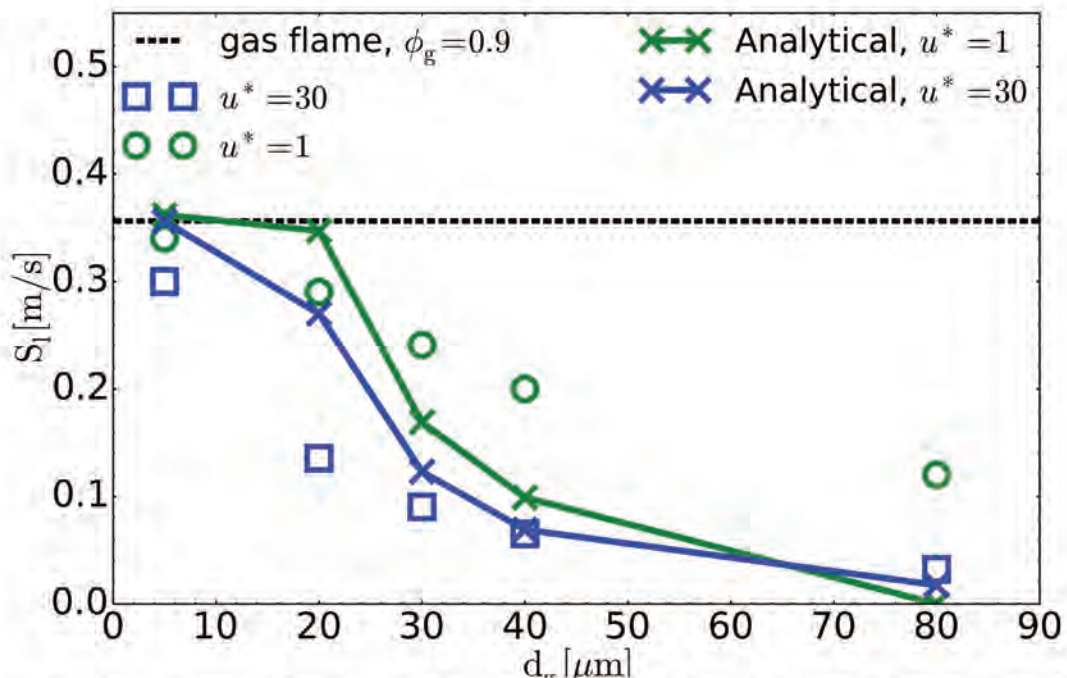


Fig. 7.16. N-heptane spray flame speed as a function of the initial droplet diameter for case B. For  $u^* = 1$  the analytical laminar spray flame speeds are obtained with Eq. 7.7, whereas Eq. 7.10 is applied for  $u^* = 30$ .

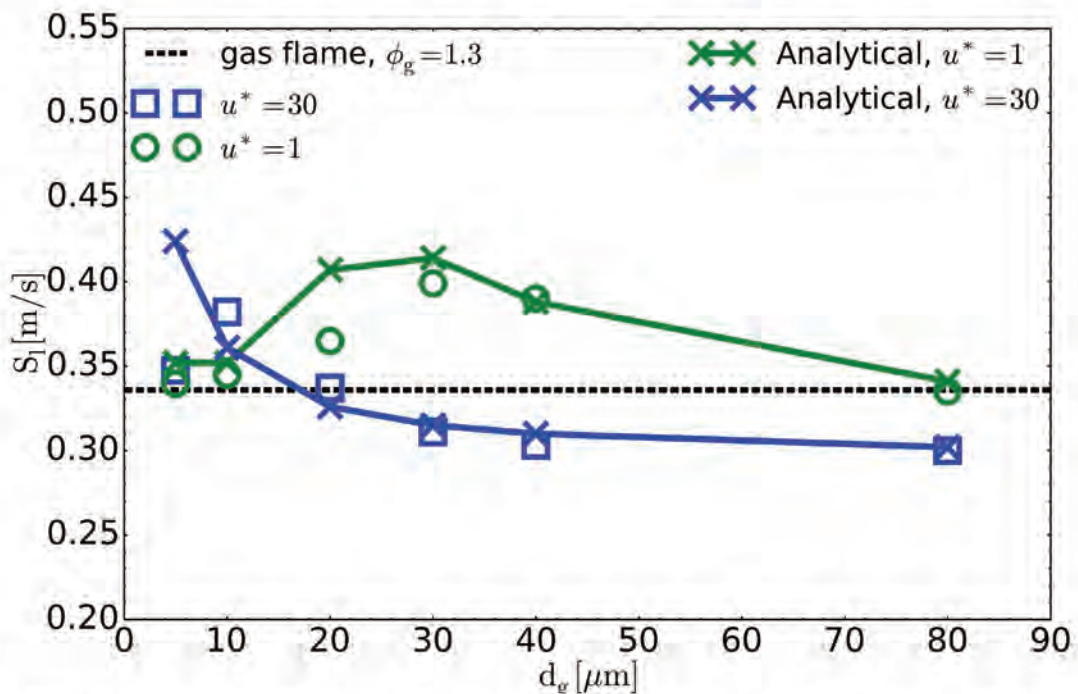


Fig. 7.17. N-heptane spray flame speed as a function of the initial droplet diameter for case C. The analytical laminar spray flame speeds are obtained with Eq. 7.7.

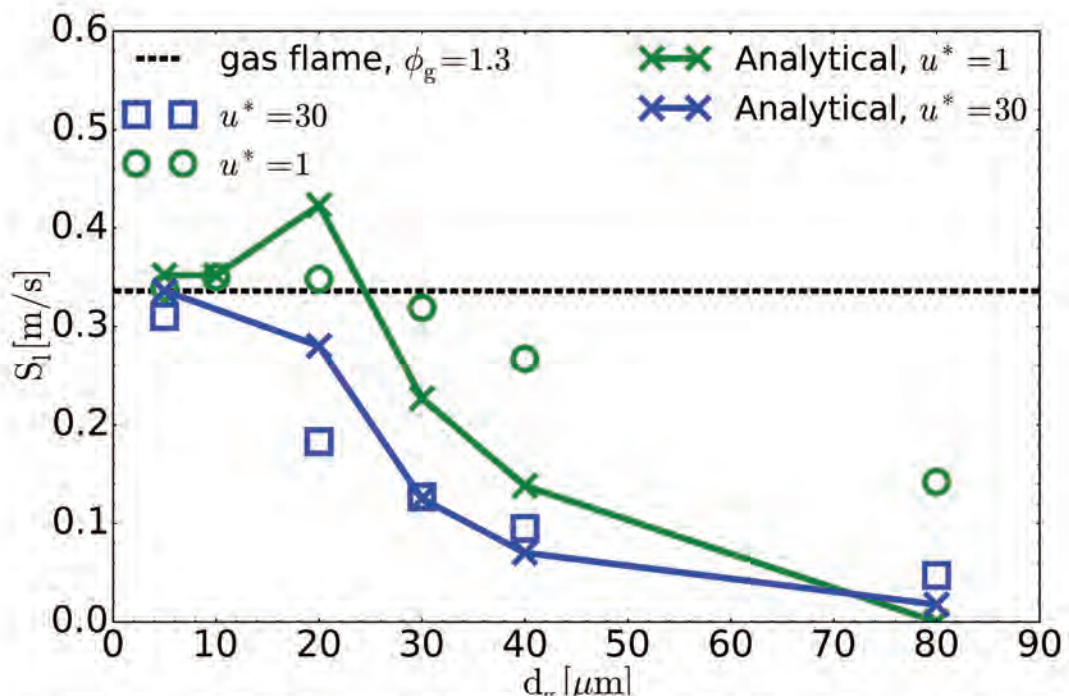


Fig. 7.18. N-heptane spray flame speed as a function of the initial droplet diameter for case D. For  $u^* = 1$  the analytical laminar spray flame speeds are obtained with Eq. 7.7, whereas Eq. 7.10 is applied for  $u^* = 30$ .

## **Chapter 7. Effect of relative velocity on the flame speed and structure of laminar spray flames**

decrease of  $S_L^{tp}$  with the increase of  $d_p$  and  $u^*$  and as  $\phi_g = 0$ , there is no minimum value of  $S_L^{tp}$ . As for case C, the spray flame speed exceeds the equivalent gaseous flame speed for sufficiently small droplets. For  $u^* = 30$ , evaporation is so much delayed that  $\phi_{eff}$  reaches lean values for droplet diameter as small as  $d_p = 5\mu m$ .

In all cases, the expressions for the spray flame speed derived in Sections 7.4.2 and 7.4.2 have been applied, according to the spray flame regime. Results are reported with solid lines in Figs. 7.15, 7.16 and Figs. 7.17, 7.18. The analytical model recovers very well all trends and curves shapes. It is less accurate when droplets evaporate fast due to inaccuracy in the evaluation of the Spalding number (see case C,  $d_p = 5\mu m$ ,  $u^* = 30$  and cases D/B,  $d_p = 20\mu m$ ,  $u^* = 1$ ). For other conditions the agreement is very good. These result demonstrate the validity of the analysis which provides useful estimations of spray flame speeds.

### **7.5 Conclusions**

In this Chapter the effect of relative velocity between liquid and gaseous flows in one-dimensional two-phase laminar flames has been described. Results evidence two regimes of two-phase flames. The first one, identified for lean mixtures, is similar to a corresponding gaseous premixed flame in terms of burnt gas temperature profiles. In this case the relative velocity increases the flame thickness and decreases the laminar flame speed. The second one, identified for rich mixtures, is more complex. The flame burns at a lower equivalence ratio that can be closer to stoichiometry, leading to higher local gas temperature and higher flame speed than the gaseous premixed flame at the same total equivalence ratio. However if the relative velocity is too high or droplets are too large, the local equivalence ratio at which the flame burns may be very low and the two-phase flame is slower than the gaseous flame. From the detailed analysis of the flames, two analytical formulations for the spray flame propagation speed have been proposed and validated, providing useful estimates for turbulent spray combustion analysis and modeling. The agreement between the overall trend of both the measured/estimated spray flame speeds demonstrates that the model and its parameters correctly take into account the main physical mechanisms controlling laminar spray flames.

# Turbulent two-phase combustion simulations

The HERON test rig (High pressure facility for aero-engine combustion) is an optically accessible combustor built at CORIA laboratory [205, 206] to study lean combustion concepts under high pressure and temperature conditions. The various shapes of the flame for different operating conditions has made the HERON burner a challenging configuration for LES. The objective of this chapter is to simulate and analyze the HERON turbulent spray flame under realistic operating conditions (pressure, temperature, type of fuel and injection device). The spray flame structure is investigated, as well as the impact of the new generic flame sensor described developed in this thesis.

## 8.1 The HERON experiment

### 8.1.1 Experimental configuration

The HERON burner comprises three main parts (Fig. 8.2):

- The first part consists in a plenum (located upstream of the combustion chamber), routing pre-heated air and fuel supplies into the LP injector. The fuel supply line enters into the plenum, reaches the LP injector at its centerline, and is encapsulated in a water-cooled jacket to maintain the temperature of liquid kerosene constant during experiments. The fuel is injected inside the injection nozzle by a multi-point injector as illustrated in Fig. 8.1. The injector is composed of 8 surrounding holes oriented toward the walls separating the first and second stages, and one central hole oriented toward the combustion chamber. Note that it is a new generation injector which has not yet been characterized in pressurized conditions.
- The second part of the test rig is the combustion chamber. Optical access to the flame is possible from three sides over the full width of the visualizing sector. A 40% fixed proportion of the main air flow rate is used to cool the optical windows with an air film.
- Finally, the exit of the combustor is equipped with a sonic throttle which can be partly obstructed by a needle in order to control the pressure inside the combustion chamber. To mechanically protect the nozzle, a secondary air supply at ambient temperature is placed at the end of the combustion chamber to significantly quench the burned gases. During the experiments, this secondary air mass flow rate is kept constant and is equal to 20g/s.

Pressure [MPa]	Global Air Flow Rate [g/s]	Pre-heated air temperature [K]
0.41	53	670
0.83	108	500-670
1.38	179	670

**Tab. 8.1.** Summary of operating conditions during the measurement campaign at CORIA. Note that some data are omitted for confidentiality purpose.

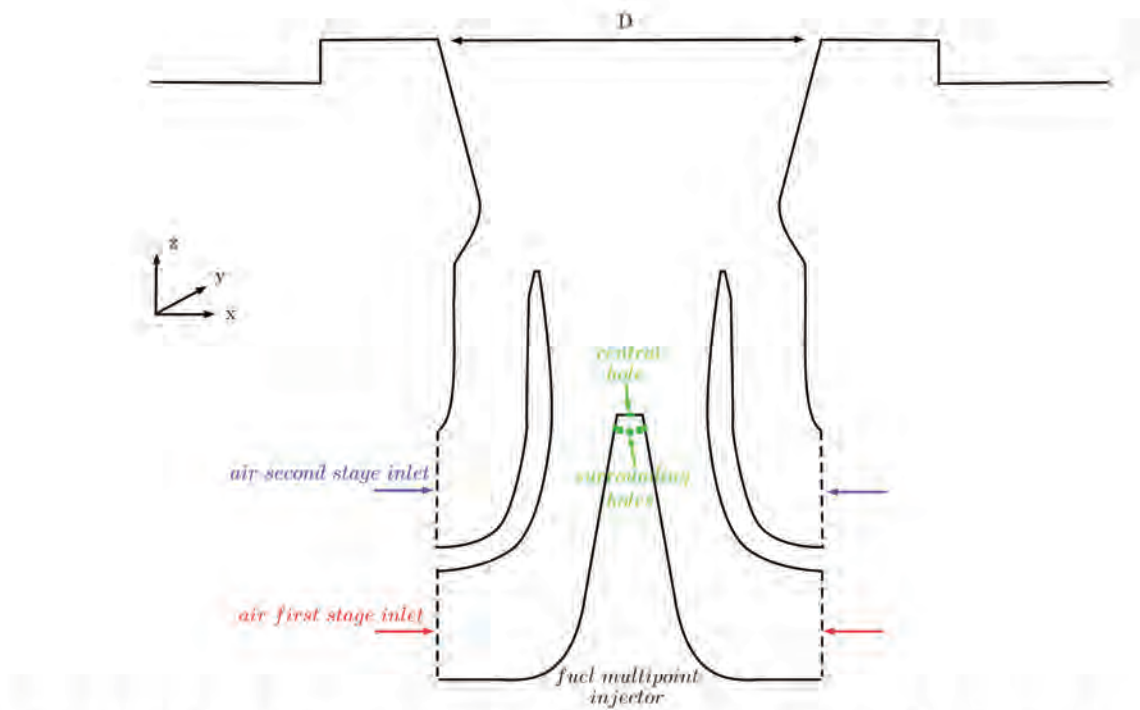


**Fig. 8.1.** Sketch of the HERON injector composed of two pre-heated air stages and one multi-point injector. The fuel injection holes are represented in green whereas the discontinuous lines indicate the patches where the inlet conditions are imposed numerically for the gas phase.

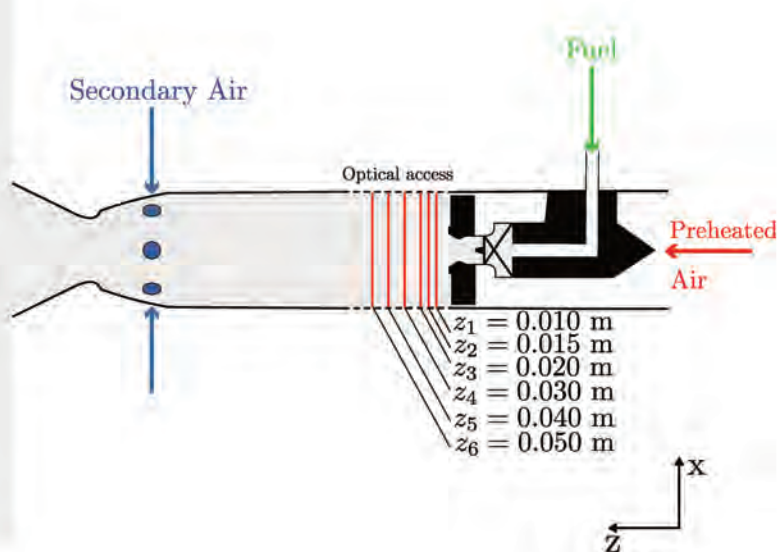


**Fig. 8.2.** Sketch of the HERON combustor. The computational domain is identified by the shaded area, the plenum, needle and fuel supply line being omitted in the LES.

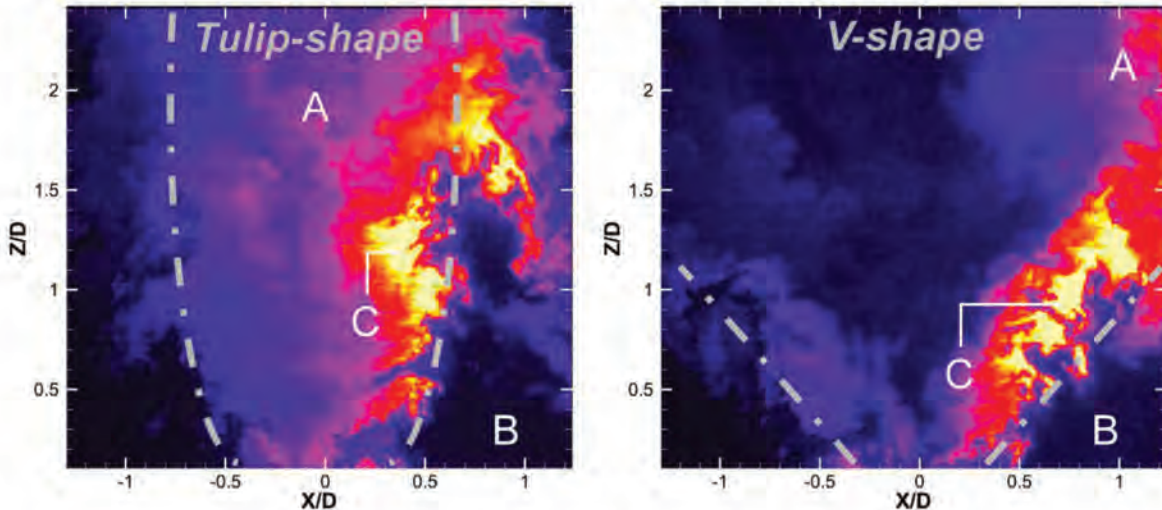


**Fig. 8.3.** Instantaneous OH-PLIF images at  $P = 0.41 \text{ MPa}$ , (left) "tulip-shape" flame, (right) "V-shape" flame colored by OH fluorescence intensity. Flow goes from the bottom to the top. Laser sheet enters from the right and is absorbed by hot burned gases [205].

The operating conditions experimentally tested at CORIA are summarized in Tab. 8.1: the burner has been designed for a maximum combustor pressure of  $2.0 \text{ MPa}$ , a maximum air preheating temperature of  $900 \text{ K}$  and a combustion temperature up to  $2400 \text{ K}$ . Depending on the pressure, the flame has shown two different topologies. For pressure higher than  $0.4 \text{ MPa}$ , the flame exhibits a "tulip-shape" (Fig. 8.3, left), the flame being straight and confined around the axis of the combustion chamber. For pressure below  $0.40 \text{ MPa}$ , the flame shows a flared "V-shape" (Fig. 8.3, right), resulting in a wider opening of the flame and forming a large inner recirculation zone.

For the operating point studied in the current work ( $P = 0.83 \text{ MPa}$ , and  $T = 670 \text{ K}$ ), the tulip-shape is expected.

To analyze the flame, measurements at the location of the optical accesses (cf. Fig 8.2) are used, including PIV, PDA and OH-PLIF measurements. Velocity and turbulence data are available at six axial locations ( $z_1, z_2, z_3, z_4, z_5$  and  $z_6$  in Fig. 8.2) for both reacting and non-reacting cases, whereas mean droplet diameter profiles are only measured for the reacting case at two axial positions:  $z = 0.001 \text{ m}$  and  $z = 0.015 \text{ m}$ . Instantaneous and mean OH fields are also available.

For all experimental cases the flame stabilizes within the nozzle of the injection system (not optically accessible) where no measurements are possible. As a result, an important part of the experimental flame is missing for the analysis and the validation of the current work. As the liquid is injected together with the highly turbulent pre-heated air, it may be assumed that the flame is premixed (this assumption will be investigated in Sect. 8.3.3). Unfortunately measurements for non-reactive two-phase flows were not performed due to issues related to the injection of un-burning liquid fuel inside the combustion chamber, and the injected droplet size distribution is therefore unknown. Finally for two-phase reactive flows and due to either obscuration of the detection volume by window frames on the detector side or clipping laser beams on the transmitter side, droplet diameter and velocity measurements were made through the flame over a restricted part of the injection nozzle exit planes ( $z = 0.001 \text{ m}$  and  $z = 0.015 \text{ m}$ ).

## 8.2 Numerical setup

LES was performed using AVBP. Time and space discretization are achieved with the fully explicit TTGC scheme [183] (third order accuracy in time and space on unstructured meshes). The Lagrangian formalism is used to handle the liquid phase [204], in a two-way coupling approach: the liquid phase transfers mass, momentum and energy to the gas via source terms locally estimated from the number of droplets inside a control volume [204]. The Abramzon & Sirignano evaporation model [153] and the Schiller & Nauman drag model [149] are applied with complex thermodynamic and transport properties ( $Pr^{evap} = 0.71$  and  $Sc^{evap} = 2.27$ ) to capture the temporal evolution of the droplet. As the flame is assumed to be premixed, the TFLES model is used. Both thickening sensors, the standard (calibrated as a function of the local equivalence ratio) and the new generic one are compared. For the efficiency function, the saturated dynamic formulation of the Charlette model is employed with the usual filter, ratio between effective filtered and filtered scales, and averaging filter widths.

In the framework of the TFLES model, the TP-TFLES model is used: droplets source terms are scaled by the thickening factor [87]. Moreover, neither the re-atomization, nor the isolated burning regime of the liquid phase are modeled.

The computational domain is shown in Fig. 8.2 (shaded area) and Fig. 8.5. While the combustion chamber and the dilution holes (colored in green in Fig. 8.5) are the same as in the experiments, the outlet and the injection system have been simplified. First, the needle and the fuel supply line have been omitted. Liquid fuel is directly injected at the 9 holes of the multipoint injection system. Second, to ensure the same mass flow split as experiments between the air injected along the windows and the air injected through the two swirlers (colored in blue in Fig. 8.5), as well as the air split between these two swirling stages, air mass flow rates are directly injected at the four inlet boundary patches according to the experimental measurements. Therefore, even if the plenum has been removed, the 40 % fixed proportion of the main air flow rate used to cool the optical windows is still injected inside the combustion chamber through an inlet located at the intersection between the walls and the bottom plate of the combustion chamber (cooling films are colored in orange in Fig. 8.5). Also note that a numerical half spherical atmosphere has been added downstream of the outlet of the original geometry (Fig. 8.2) to guide the exhaust gases through the outlet boundary condition and prevent numerical issues.

As the liquid multipoint injector has not yet been experimentally characterized, a distribution provided by SAFRAN Helicopter Engines was used. This distribution has been extrapolated from a similar injector experimentally characterized at DLR at a pressure equal to  $1\text{ MPa}$ . As displayed in Fig. 8.4, it consists in a Rosin-Rammler distribution with a Sauter Mean Diameter (SMD) equal to  $15\mu\text{m}$  and the distribution spread  $q$  equal to 3.1. The Stokes numbers estimated with a droplet diameter equal to  $15\mu\text{m}$  at the location of the surrounding and the central holes are respectively  $S_{t_{surrounding}} = 0.47$  and  $S_{t_{central}} = 0.34$ . Note that the gaseous characteristic time  $\tau_g$  is estimated using local integral length scales and turbulent intensities. As these Stokes numbers are lower than unity, droplets are going to be dispersed by turbulence. Still for a droplet diameter equal to  $15\mu\text{m}$ , the evaporation characteristic time  $\tau_{ev}$  is equal to:

- $3.015\text{ms}$  for droplets evaporating in the fresh gases temperature.
- $1.28\text{ms}$  for droplets evaporating in an averaged temperature between the burnt and the fresh gas temperatures.
- $0.72\text{ms}$  for droplets evaporating in the burnt gases temperature.

Assuming the flame being premixed and taking into account the low global equivalence ratio ( $\phi = s * FAR \approx 0.3$ ), the combustion characteristic time is  $\tau_c = 4.3\text{ms}$ .

Slip boundary conditions are applied when droplets reach the walls of the injection nozzle, whereas Navier-Stokes Characteristic Boundary Conditions (NSCBC) [190] are employed to impose non-reflecting boundary conditions at both inlet and outlet of the domain. The walls are modeled as adiabatic no-slip walls.

## 8.2 Numerical setup

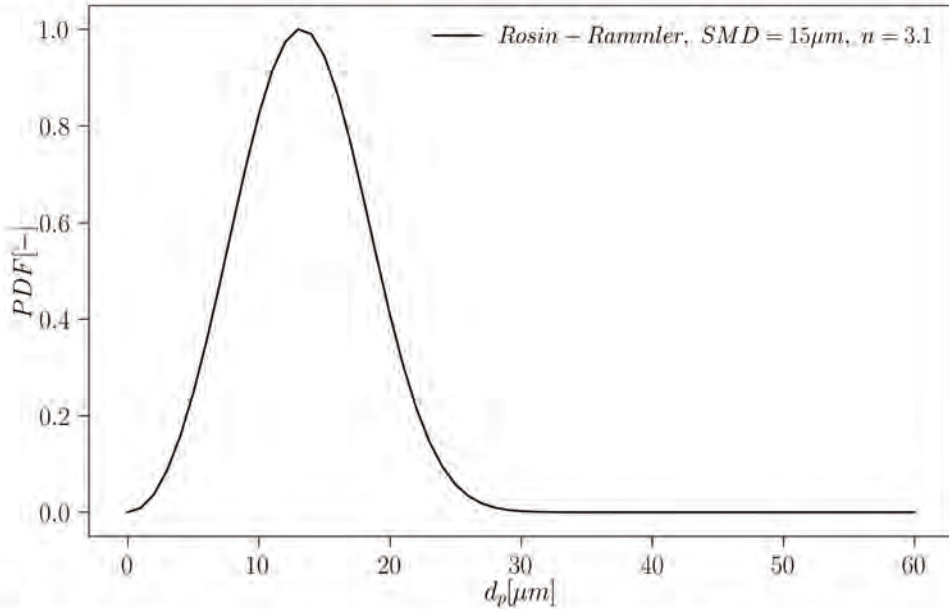


**Fig. 8.4.** Droplet size distribution imposed at the 9 injection holes of the HERON multipoint injector: Rosin-Rammler distribution with a Sauter Mean Diameter (SMD) equal to  $15\mu m$  and the distribution spread  $q$  is equal to 3.1.

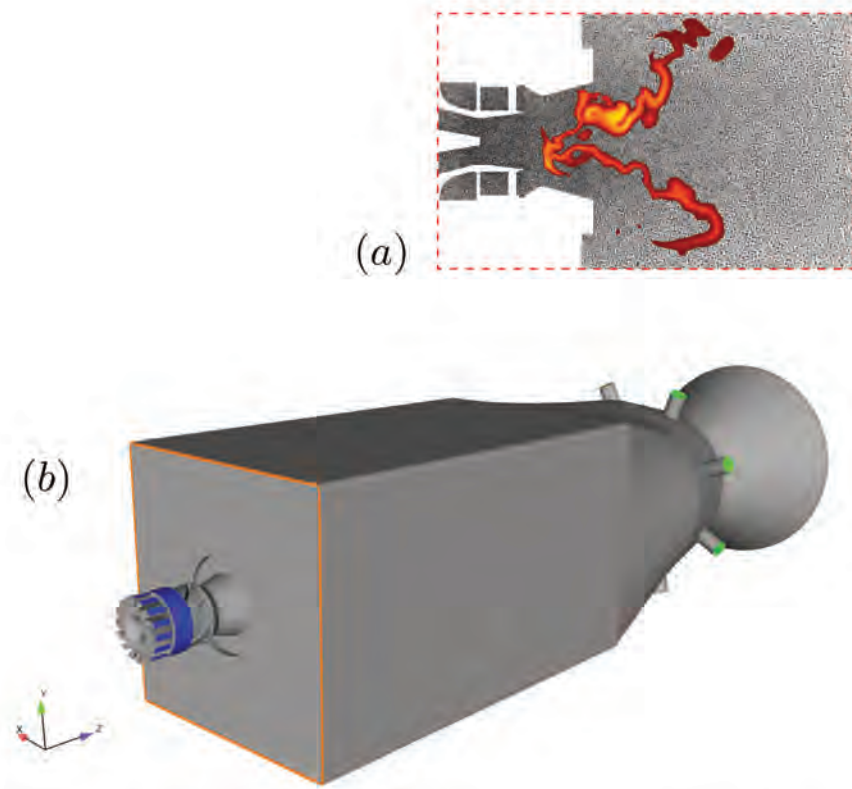


**Fig. 8.5.** Overview of the computational domain (b) where the inlet patches are colored. A focus is made on the unstructured mesh refinement in the injection nozzle and the combustion regions, at  $x = 0.05 m$  (a).

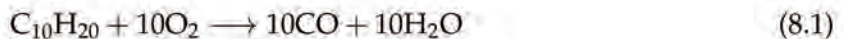
The unstructured mesh comprises 41 million tetrahedral elements and is refined in the injection nozzle, the combustion regions (Fig. 8.5), the air cooling inlet films and the secondary air dilution holes. The mesh size in the injector nozzle and nearby flame zones is  $\Delta_x = 200\mu m$ .

	$A_j[\text{cgs}]$	$E_j[\text{cgs}]$
Reaction 1	$0.8 \times 10^{12}$	$4.15 \times 10^4$
Reaction 2	$4.5 \times 10^{10}$	$2.0 \times 10^4$

**Tab. 8.2.** Pre-exponential factors  $A_j$  and activation energies  $E_j$  for the 2S\_KERO\_BFER scheme (cgs units).

### 8.2.1 Chemistry description

The chemical scheme is the global two-step 2S\_KERO.BFER mechanism based on a kerosene oxidation reaction followed by a fast CO-CO<sub>2</sub> equilibrium. Six species are taken into account ( $C_{10}H_{20}$ ,  $O_2$ ,  $CO_2$ ,  $CO$ ,  $H_2O$  and  $N_2$ ) and two reactions [202]:



The reaction rates  $q_j$  follow an Arrhenius law:

$$q_1 = A_1 \left( \frac{\rho Y_{C_{10}H_{20}}}{W_{C_{10}H_{20}}} \right)^{0.55} \left( \frac{\rho Y_{O_2}}{W_{O_2}} \right)^{0.9} \exp \left( \frac{-E_{a,1}}{RT} \right) f_1(\phi) \quad (8.3)$$

$$q_2 = A_2 \left[ \left( \frac{\rho Y_{CO}}{W_{CO}} \right)^{1.0} \left( \frac{\rho Y_{O_2}}{W_{O_2}} \right)^{0.5} - \frac{1}{K_2} \left( \frac{\rho Y_{CO_2}}{W_{CO_2}} \right)^{1.0} \right] \exp \left( \frac{-E_{a,2}}{RT} \right) f_2(\phi) \quad (8.4)$$

The pre-exponential constants  $A_j$  and the activation energies  $E_j$  are given in Table 8.2, and  $K_2$  is the equilibrium constant [96]. To recover the correct flame speed for rich mixtures, the Pre-Exponential Adjustement (PEA) method is used [202]. This method accounts for both the fuel oxidation reaction and the CO-CO<sub>2</sub> equilibrium. The pre-exponential factor of the fuel oxidation reaction is corrected with  $f_1(\Phi_{loc})$  to correctly predict the laminar flame speed with local equivalence ratio  $\Phi_{loc}$ . To reproduce the sudden change in behaviour from lean to rich combustion due to the CO-CO<sub>2</sub> equilibrium, the pre-exponential factor of the second reaction also varies using a correction function  $f_2(\Phi_{loc})$ . For the function  $f_1$  and  $f_2$ , the reader can refer to Franzelli *et al.* [112].

Note that the 2S\_KERO\_BFER scheme has been fitted over a wide range of pressure ([1,12] bars) and temperature ([300;700]K) and is herein validated for the studied operating conditions against the Luche skeletal mechanism [108] (91 species and 694 reactions) in Fig. 8.6. Laminar flame speeds are computed using Cantera. The 1D premixed flames are computed for the whole range of equivalence ratios and at the operating point considered in this study ( $T_0 = 670K$  and  $P_0 = 0.83MPa$ ). Results show a slight under-prediction of the laminar flame speed ( $\approx 15\%$ ) for the 2S\_KERO\_BFER scheme near stoichiometric equivalence ratios. However, as a LP injector is used in the combustion chamber, the range of equivalence ratios should be closer to the lean flammability limit (where a lower error on the flame speed is observed) than stoichiometry.

In the following, results obtained for non-reacting gaseous simulation are first presented to validate the numerical setup and analyze the overall structure of the flow. Then, reacting two-phase simulations performed with the standard flame sensor are analyzed. Finally, the generic flame sensor is tested and validated against the results obtained with the standard sensor.

## 8.3 Numerical results

### 8.3.1 Flow characteristics

Before presenting the results of numerical simulations, the main flow characteristics are introduced:

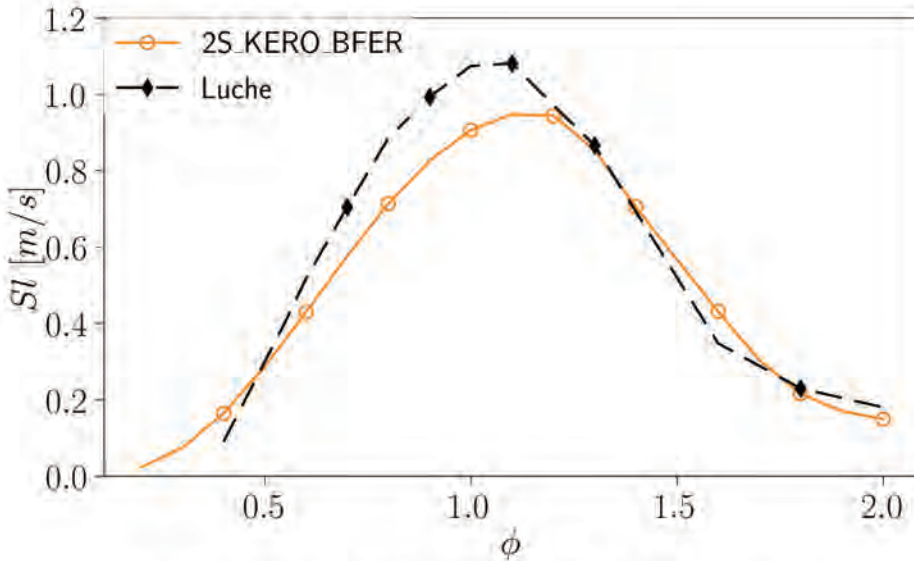


**Fig. 8.6.** Laminar flame speed versus the equivalence ratio at  $T_0 = 670\text{K}$  and  $P_0 = 0.83\text{MPa}$ . Comparison between the Luche skeletal mechanism [108] and the 2S\_KERO\_BFER scheme.

- The convective time scale is evaluated from the volume of the combustion chamber  $V_c$  and the inlet mass flow rate  $\dot{m}$ :

$$\tau_{conv} = \frac{\rho V_c}{\dot{m}} = 72\text{ms}. \quad (8.5)$$

- The rotation time scale is evaluated at the combustion chamber inlet:

$$\tau_{rot} = \frac{\pi R_i}{u_{\theta,i}} = 0.5\text{ms}, \quad (8.6)$$

where  $R_i$  is the mean radius of the convergent inlet and  $u_{\theta,i}$  is the mean azimuthal velocity component of the inlet plane.

- The Reynolds number is evaluated at the combustion chamber inlet:

$$Re = \frac{|\vec{u}|_i D_i}{\nu} = 200500, \quad (8.7)$$

where  $|\vec{u}|_i$  is the norm of the velocity vector in the inlet plane of the combustion chamber,  $D_i$  is the mean diameter of the convergent inlet and  $\nu$  is the kinematic viscosity.

### 8.3.2 Non-reacting case

A non-reacting gaseous simulation is first performed to validate the numerical setup and the aerodynamic field. Figure 8.7 shows time-averaged streamlines in a x-normal plane. The swirled jet (SJ) generates two types of recirculation zones pointed out by negative axial velocities (blue regions in Fig. 8.7), which is typical of highly swirled configurations. The Inner Recirculation Zone (IRZ) corresponds to the reverse flow along the axial direction of the burner, whereas the Outer Recirculation Zones (ORZ) are located in between the swirled jet and the combustion chamber walls. Also note that the cooling films supposed to cool down the combustion chamber walls are caught by the ORZ, leading to a detachment of the films from the walls.

Figure 8.7 enhances the presence of a vortex breakdown characterized by the oscillation of the IRZ along the axis of the burner (due to the swirl): the IRZ starts with a vortex aligned with

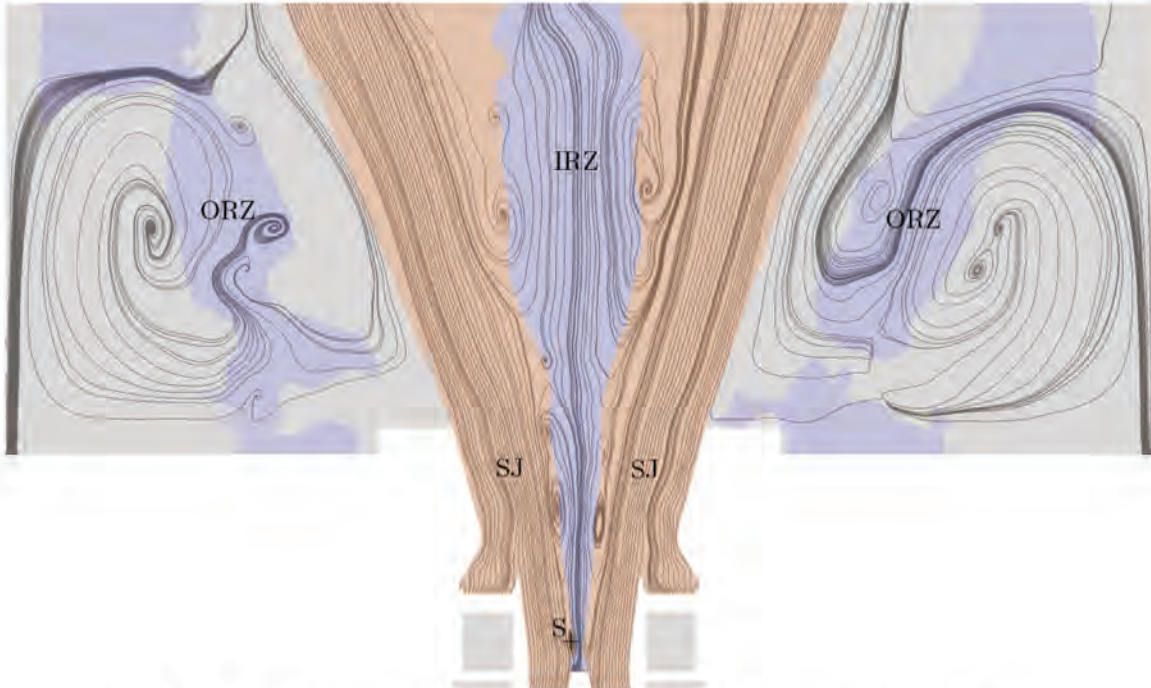


**Fig. 8.7.** Time-averaged streamlines in a  $x$ -normal plane for the non-reacting case.

the axis of the burner and then breaks down at the stagnation point ( $S$ ) (herein located close to the tip of the injector). The onset of vortex breakdown is generally related to the Swirl number  $S_w$  [207, 208]. Based on the assumption that the incoming flow velocity profile is that of a Rankine vortex, Billant et al. [208] derived a critical theoretical value  $S_{w,c} = 0.707$  above which vortex breakdown occurs. To define  $S_w$ , it is convenient to introduce a cylindrical referential  $(r, \theta, z)$  whose  $z$ -axis is aligned with the  $z$ -axis of the cartesian referential presented in Fig. 8.2. Following the definition of Ivanic et al. [209],  $S_w$  writes:

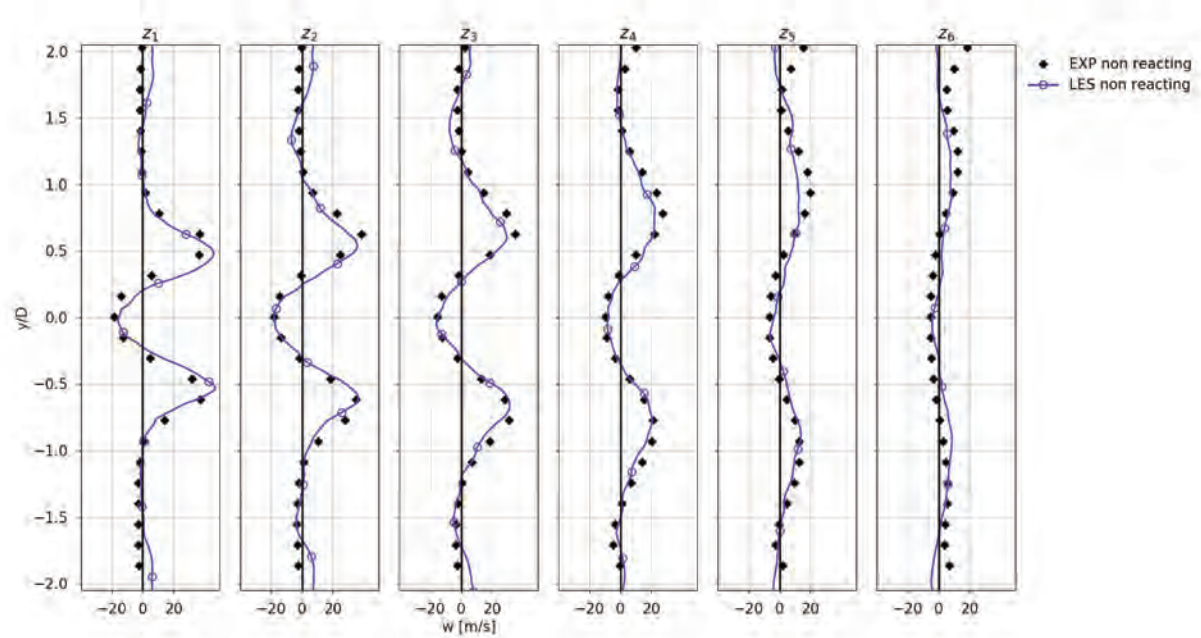
$$S_w = \frac{\int_0^{R_{ext}} \rho w u_\theta 2\pi r^2 dr}{R_{ext} \int_0^{R_{ext}} \rho w^2 2\pi r dr}. \quad (8.8)$$

where  $R_{ext} = D/2$  is the outer radius of injection, and  $u_\theta$  and  $w$  are respectively the azimuthal and axial velocity components. Herein, the swirl number is estimated inside the injection nozzle but after the junction of the first and second pre-heated inlet stages. Here  $S_w = 0.6$  which is slightly lower than the critical swirl number  $S_{w,c}$ .

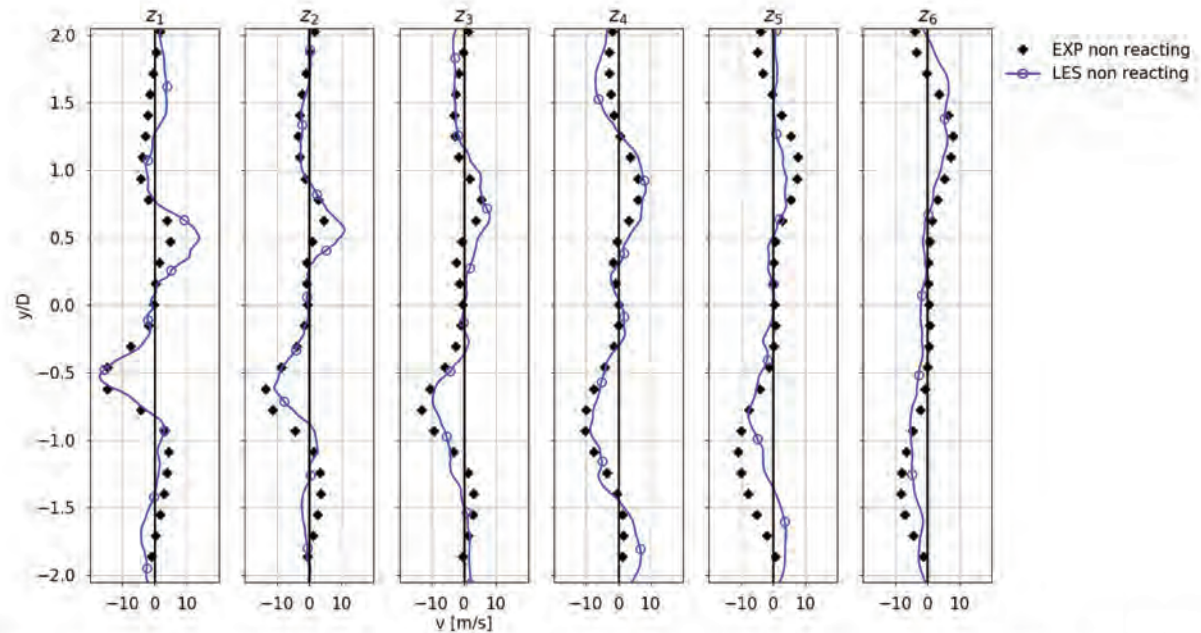
Figure 8.8 presents the radial profiles of the mean axial velocity component, showing a very good agreement with the measurements: the length and width of the IRZ are well predicted as well as the mean axial velocity magnitude. The only difference occurs close to the windows cooling films ( $y/D = 2$  and  $y/D = -2$ ) for the last three profiles where the mean axial velocity is under-predicted.

Figure 8.9 presents the radial profiles of the mean radial velocity component showing an overall good agreement with experiments. Regarding the mean radial velocity magnitude and the opening width of the swirled flow, one can note that the mean radial velocity field is correctly predicted. It means that the pre-heated air mass flow rate split between the two injector stages is recovered, and that removing the plenum from the original geometry does not have any effect on the simulation. Also note that unlike LES, the experimental profiles are not symmetrical.

Figures 8.10 and 8.11 respectively compare the radial profiles of RMS axial and radial velocity fluctuations from  $z_1$  to  $z_6$ : both are well captured by the LES (note that only the RMS fluctuations of the resolved field are considered).



**Fig. 8.8.** radial profiles of mean axial velocity component at measurement planes  $z_1 - z_6$  of Fig. 8.2 for the non-reacting case.



**Fig. 8.9.** Radial profiles of mean radial velocity component at measurement planes  $z_1 - z_6$  of Fig. 8.2 for the non-reacting case.

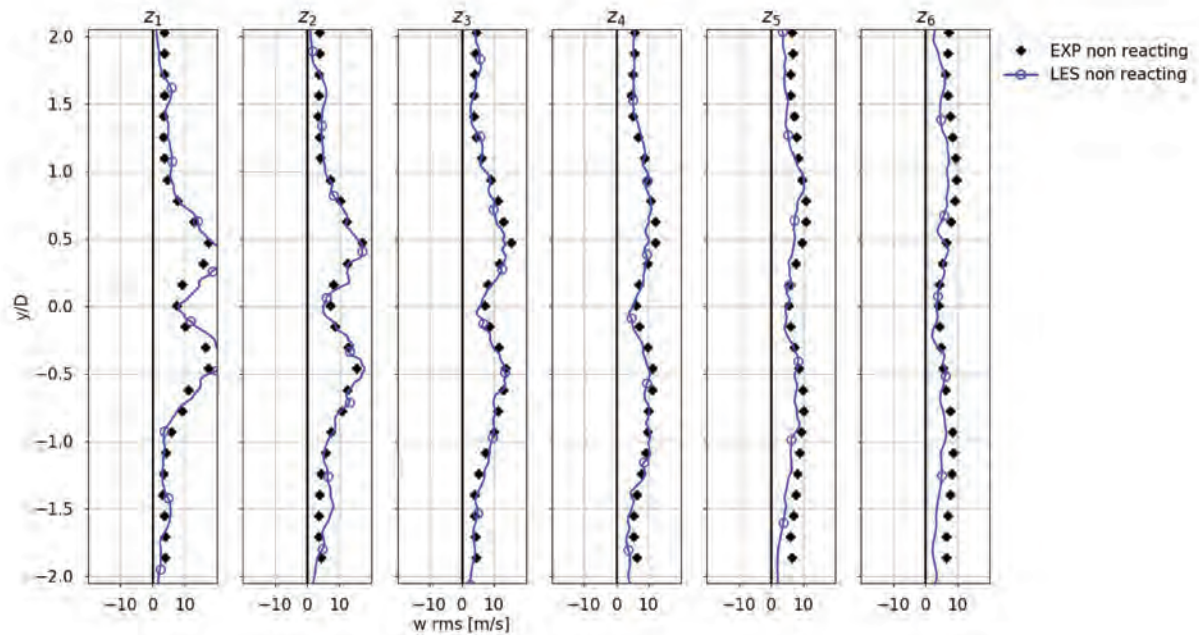


**Fig. 8.10.** Radial profiles of RMS axial velocity component at measurement planes  $z_1 - z_6$  of Fig. 8.2 for the non-reacting case.

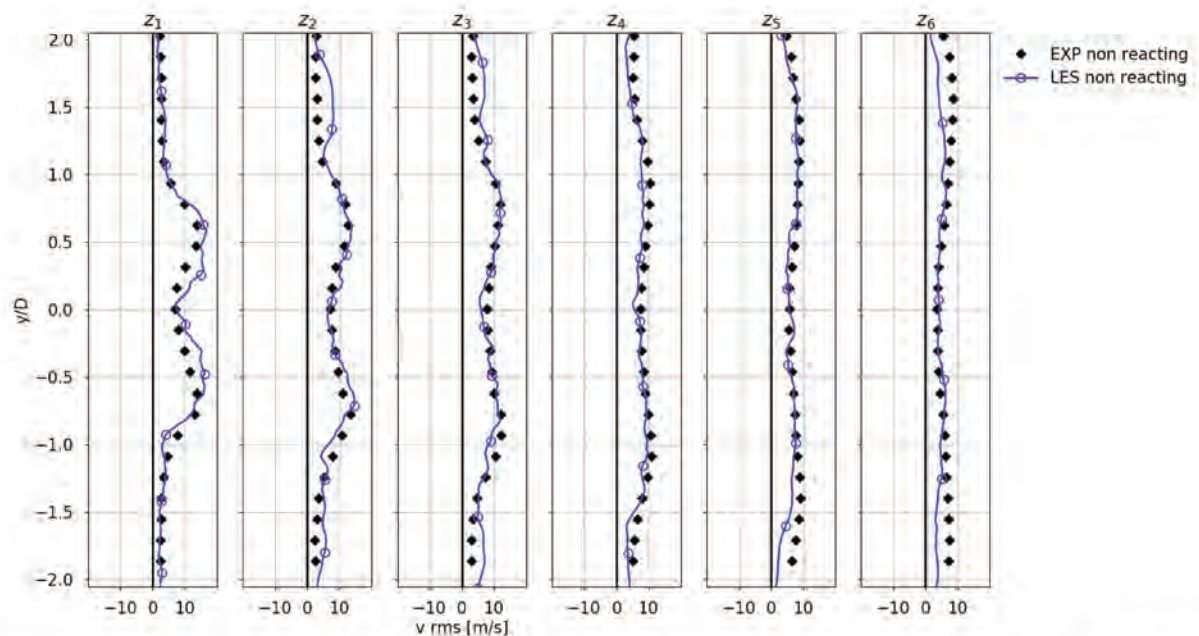


**Fig. 8.11.** Radial profiles of RMS radial velocity component at measurement planes  $z_1 - z_6$  of Fig. 8.2 for the non-reacting case.

Simulations	Injection distribution	SMD [ $\mu\text{m}$ ]	Flame sensor
A	Rosin-Rammler, $q = 3.1$	15	Standard
B	Rosin-Rammler, $q = 3.1$	15	Generic
C	Rosin-Rammler, $q = 3.1$	5	Standard
D	Rosin-Rammler, $q = 3.1$	25	Standard
E	Rosin-Rammler, $q = 3.1$	50	Standard
F	Rosin-Rammler, $q = 3.1$	100	Standard

**Tab. 8.3.** Summary of simulated cases.

To conclude for the non-reacting case, the mean and RMS velocity fields are well predicted by the LES. Reacting simulations are further performed using the same numerical setup as the non-reacting one. The only difference stands in the injection of liquid fuel and the use of the combustion model.

### 8.3.3 Reacting case

For the reacting case and as no measurements are available inside the injection nozzle, several questions arise: is the flame burning in premixed, diffusion or partially premixed mode? What droplet size distribution should be injected? Should the liquid properties be the same for the surrounding and central injection holes? As a first step, the same liquid injection properties are applied to both injection holes (surrounding and central). To characterize the effect of the injection droplet diameters on the flame, several test cases have been investigated varying the SMD of the liquid distribution. These cases are summarized in Tab. 8.3.

For all cases of Tab. 8.3 the obtained numerical flame has a V-shape rather than the expected tulip-shape. Moreover for case C, droplets evaporate as soon as they are injected. As a result the flame is gaseous which is not coherent with the experimental observations (droplets are still present at station  $z_2$ ). On the other hand, for cases E and F, droplets are too large. The flame is fully controlled by the evaporation process and is not able to burn close to the injection nozzle, which is once again not coherent with the experimental observations (cf. Fig 8.3). An observation about case F is that all droplets injected with the surrounding holes impact the wall separating the first and second air inlet stages. For this case the characteristic evaporation time of the droplets is too large to provide enough fuel vapor to the flame. Note that applying more complex liquid boundary conditions taking into account splash and re-atomization processes would be interesting to investigate.

Cases A and D correspond to the injected size distribution provided by SAFRAN Helicopter Engines. In both cases the stabilization process and the shape of the flame are the same, but the flame for case D is located more downstream than for case A, which is less coherent with experimental measurements. Therefore, case A is retained to investigate (1) the impact of the new generic thickening methodology on a realistic turbulent spray flame, and (2) the effect of a different thickening approach on the results (case B).

To determine the burning mode of the flame, a snapshot of the heat release field plotted with the Takeno index is presented in Fig. 8.12, as well as a focus on the flame structure along the spatial profiles A (Fig. 8.13) and B (Fig. 8.14) in Fig. 8.12. Black and orange iso-contours respectively refer to positive and negative Takeno indices, whereas the discontinuous line is an iso-contour of axial velocity  $w = 0\text{ m/s}$ . The flame burning regime is typical of lean premixed burners: the flame front mainly burns in a premixed regime, but is sometime followed by a diffusion flame resulting from the excess of oxidiser and liquid fuel evaporating through the premixed flame front (cf. Takeno index in Fig. 8.12). The tip of the flame is located inside the

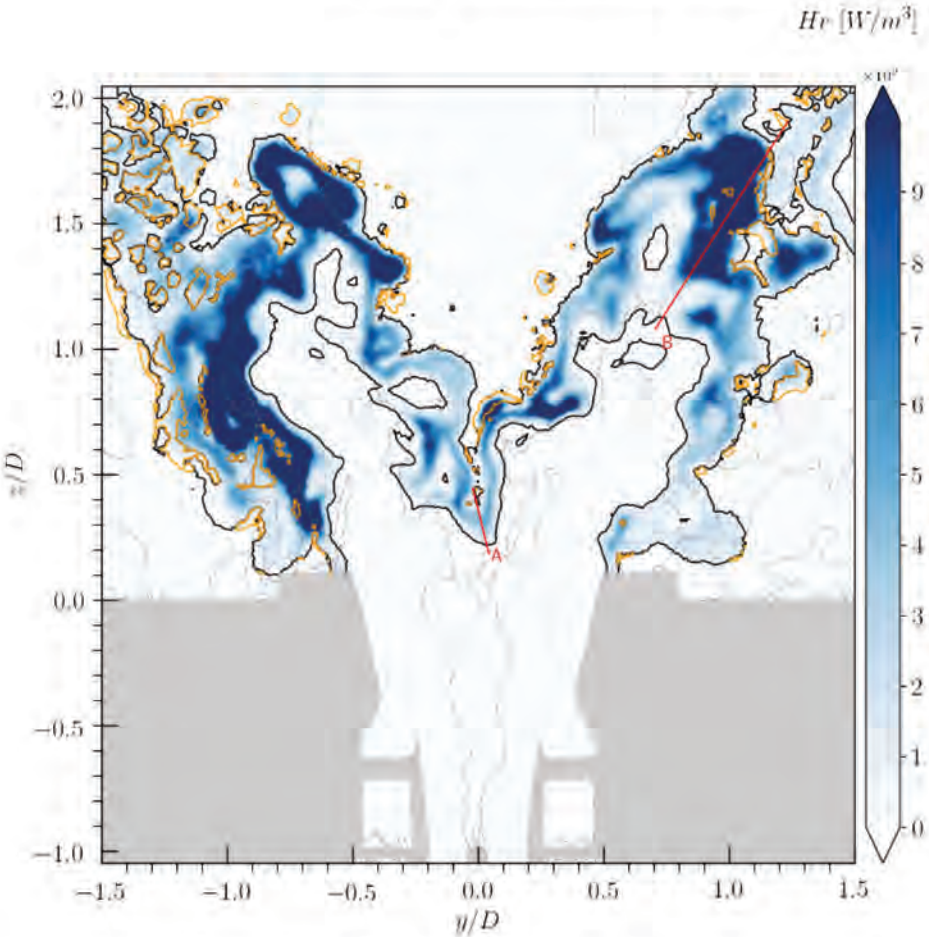
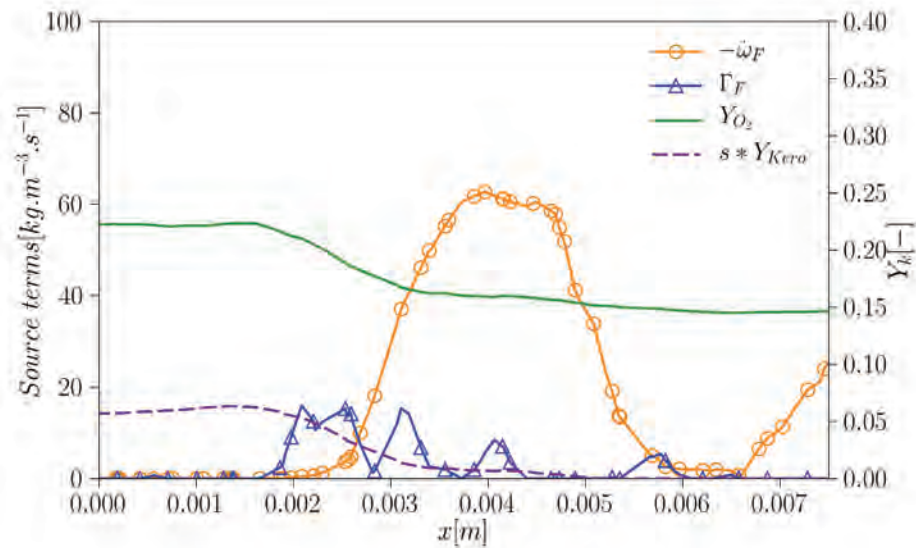


**Fig. 8.12.** Instantaneous field of heat release for the reacting case A. Black and orange iso-contours respectively refer to positive and negative Takeo indices, whereas the discontinuous line is an iso-contour of axial velocity  $w = 0 m/s$ .

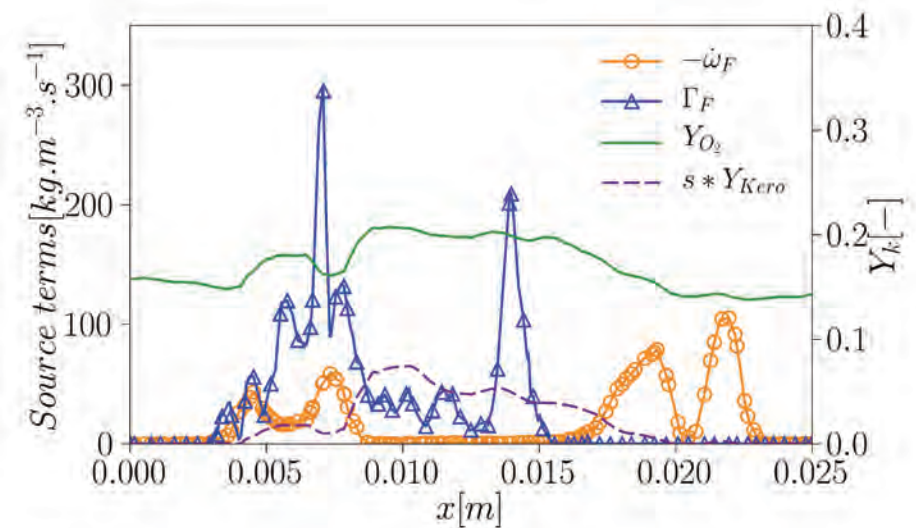
IRZ whereas the tail of the flame passes through the recirculation zone to burn large droplets which are still evaporating. Figure 8.13 shows the fuel consumption  $\omega_F$  and evaporation  $\Gamma_F$  rates as well as the mass fraction profiles of O<sub>2</sub> and Kerosene at the tip of the flame (cf. station A in Fig. 8.12). At this location, few droplets evaporate inside the flame front (low  $\Gamma_F$ ): the flame strongly depends on the local gaseous conditions. Herein the gaseous equivalence ratio is close to the lean flammability limit ( $\phi_g \approx 0.3$ ). At this location, the stabilization process is mainly controlled by the gaseous properties of the flow.

Figure 8.14 shows the fuel consumption  $\omega_F$  and evaporation  $\Gamma_F$  rates as well as the mass fraction profiles of O<sub>2</sub> and Kerosene at the tail of the flame (cf. station B in Fig. 8.12). At this location, the flame is stabilized thanks to the droplets evaporating inside the flame front:  $\Gamma_F$  is high and no gaseous fuel is located in front of the flame. The stabilization process is therefore different than the one at station A.

As the flame burns in a premixed mode, the use of the thickened flame model is justified, as well as the efficiency function to take into account the flame interactions with the turbulence. The spatial evolution of the  $\beta$  parameter along the flame front computed with the dynamic model is shown in Fig. 8.15. The black line is an iso-contour of heat release  $hr = 2 * 10^9 W/m^3$ , whereas the discontinuous line is an iso-contour of axial velocity  $w = 0 m/s$  delimiting the recirculation zones. Note that  $\beta$  is computed over the entire computational domain whereas the efficiency function is restricted to the flame front: the reader should look at the values of  $\beta$  in between the iso-contour of heat release.  $\beta$  drives the capacity of the flame front to wrinkle



**Fig. 8.13.** Instantaneous axial profile of species mass fractions  $Y_k$ , fuel consumption  $\omega_F$  and evaporation  $\Gamma_F$  source terms at station A in Fig. 8.12 for case A.



**Fig. 8.14.** Instantaneous axial profile of species mass fractions  $Y_k$ , fuel consumption  $\omega_F$  and evaporation  $\Gamma_F$  source terms at station B in Fig. 8.12 for case A.

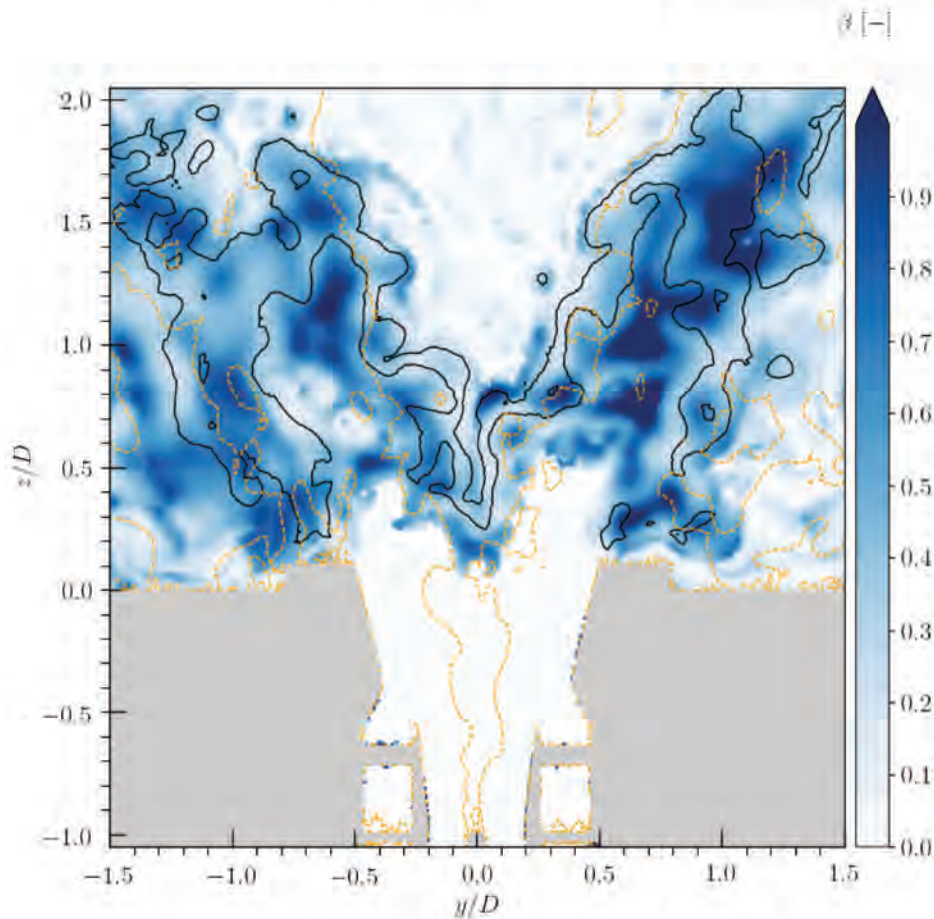


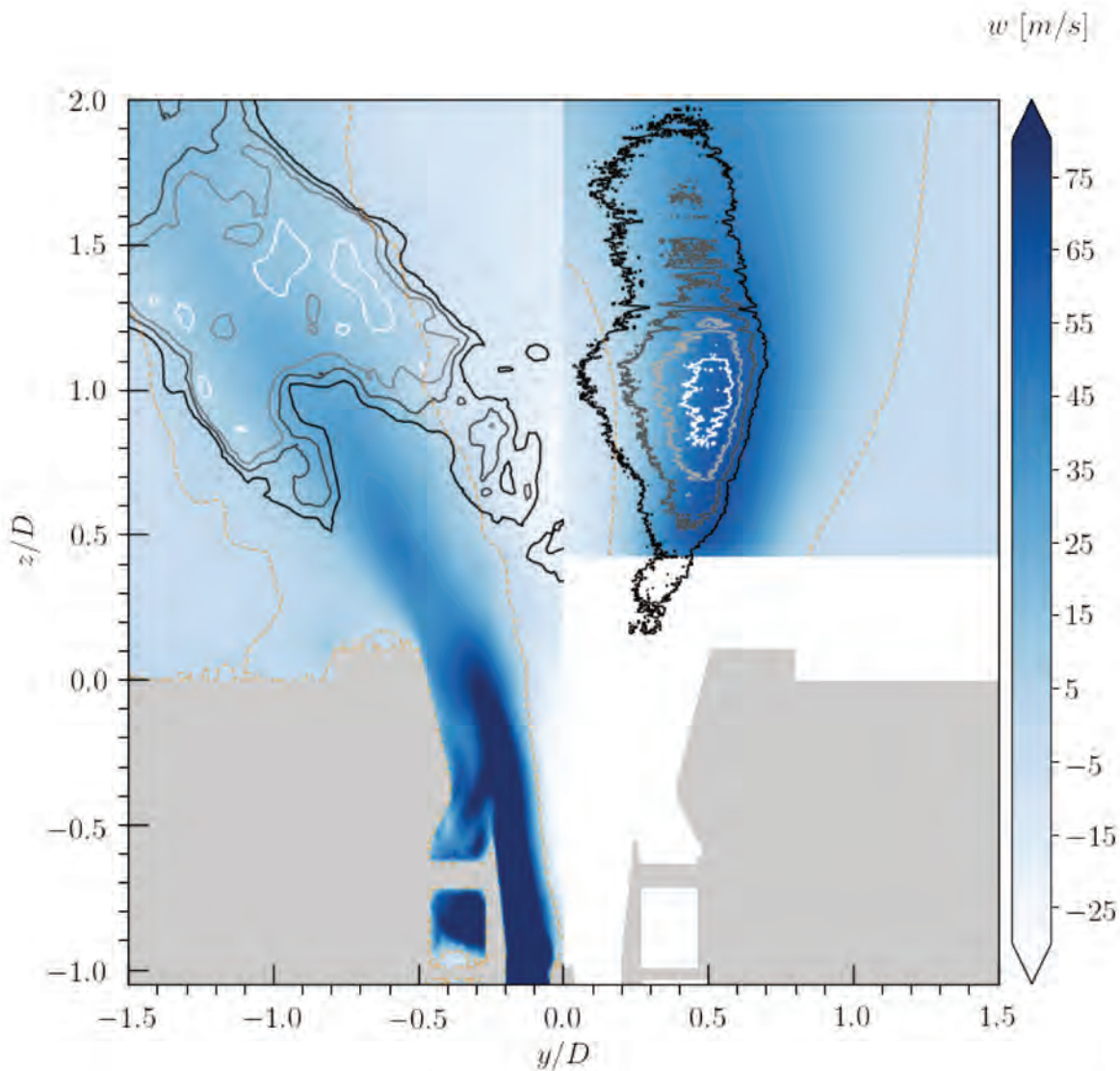
**Fig. 8.15.** Instantaneous field of  $\beta$  parameter for the reacting case A. The Black line is an iso-contour of heat release ( $hr = 2 * 10^9 W/m^3$ ) The discontinuous line is an iso-contour of axial velocity  $w = 0m/s$ .

when facing turbulent structures. Herein,  $\beta$  strongly changes along the flame front leading to a heterogeneous response of the flame to turbulence. Without the use of the dynamic model, the flame front is not able to accurately interact with vortices.

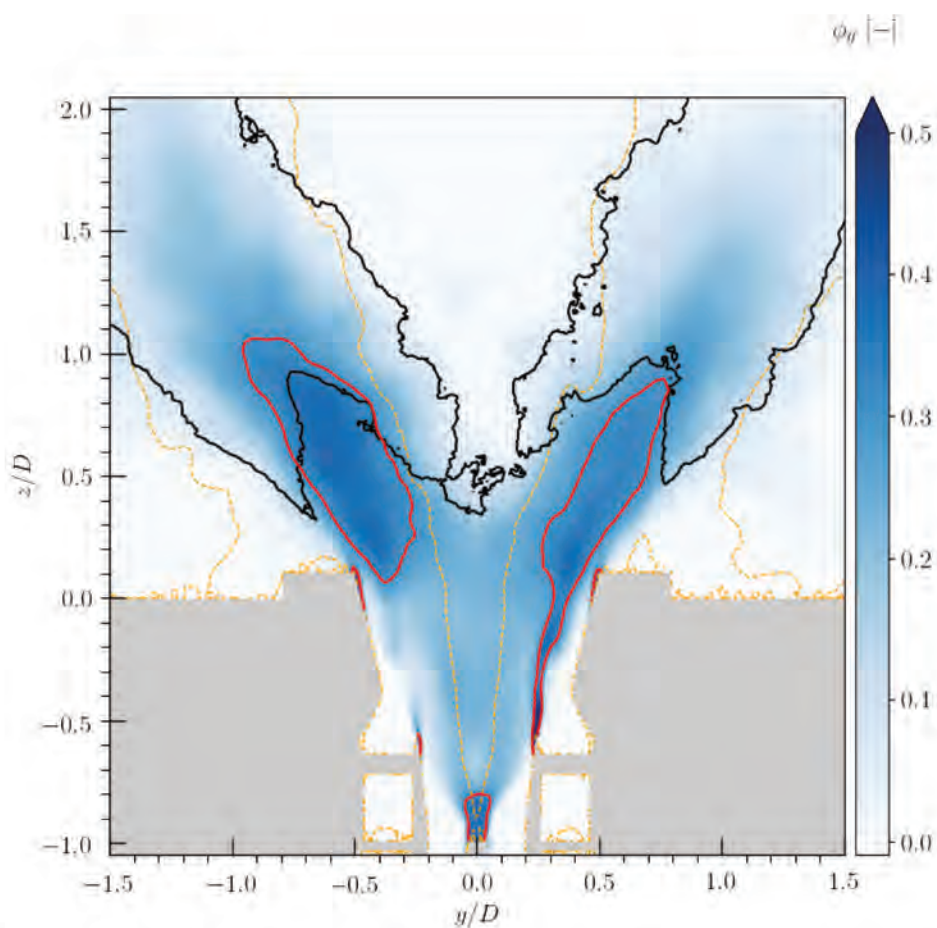
Figure 8.16 shows an averaged field of axial velocity for the LES (left) and experiment (right). Iso-contours of heat release obtained with the LES are qualitatively compared to iso-contours of OH measurements from the experiments. The discontinuous line delimits the recirculation zones and corresponds to an iso-contour of axial velocity  $w = 0m/s$ . The opening angle of the LES swirled jet is the same as the experimental one. However, the length of the IRZ predicted by LES is much longer: the flame does not have the correct shape (V-shape (Fig. 8.3) rather than the expected tulip-shape) and does not allow the recirculation zone closing. Indeed, the flame in experiments (cf. Fig. 8.16(right)) is stabilized in between the IRZ and the high velocity region of the swirled jet, making it possible to close the recirculation thanks to the burnt gas expansion. Also note that despite a different shape, the length of the flame is almost the same as in the experiment.

Fig. 8.17 presents an averaged field of gaseous equivalence ratio. The black line is an iso-contour of heat release  $hr = 2 * 10^9 W/m^3$ , the discontinuous line delimits the recirculation zones whereas the red line corresponds to an iso-contour of gaseous equivalence ratio equal to 0.3. With only vaporized fuel, the flame cannot get closer to the injector since the gaseous equivalence ratio is close to the lean flammability limit.

Indeed, when looking at Fig. 8.18 showing the averaged total (i.e liquid and gaseous) equivalence ratio  $\phi_{tot}$  with the same iso-contours as Fig. 8.17, one can note that the liquid



**Fig. 8.16.** Mean LES (left) and experimental (right) fields of axial velocity plotted with mean heat release iso-contours (left) and mean OH iso-contours (right). The discontinuous line delimits the recirculation zones (iso-contour of axial velocity  $w = 0\text{m/s}$ ).



**Fig. 8.17.** Averaged field of gaseous equivalence ratio for the reacting case A. Black and red lines respectively refer to heat release ( $hr = 2 \times 10^9 \text{ W/m}^3$ ) and gaseous equivalence ratio ( $\phi_g = 0.3$ ) iso-contours, whereas the discontinuous line is an iso-contour of axial velocity  $w = 0 \text{ m/s}$ .

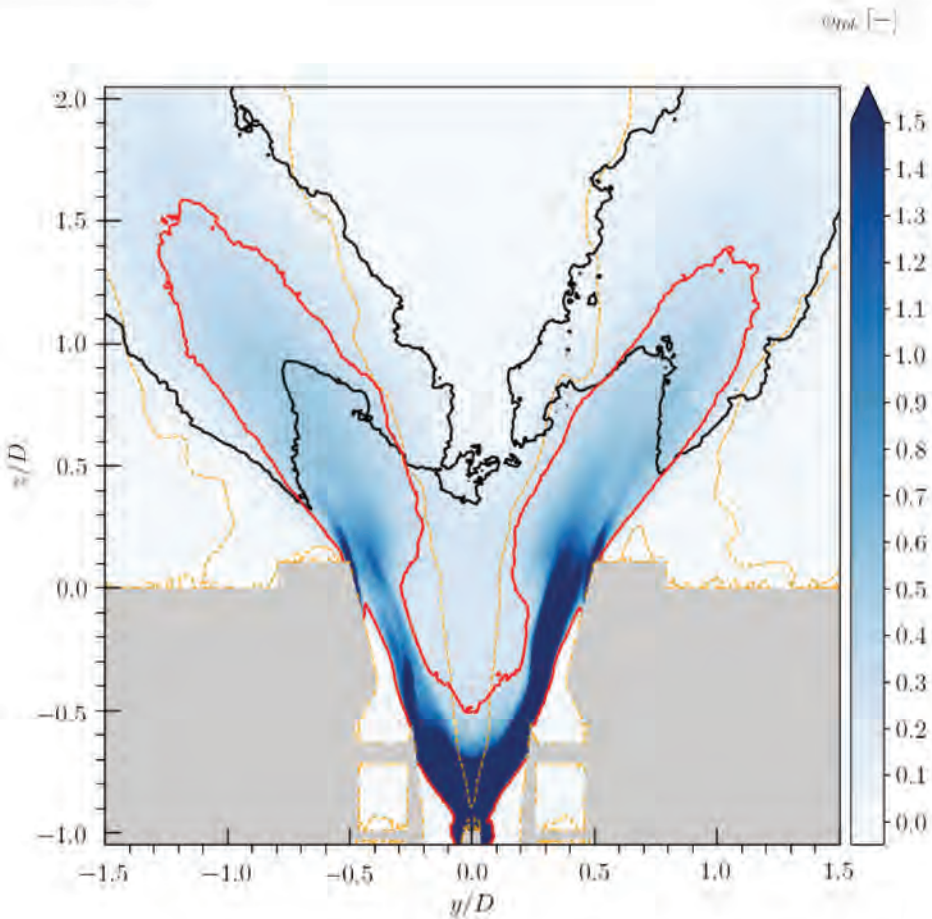
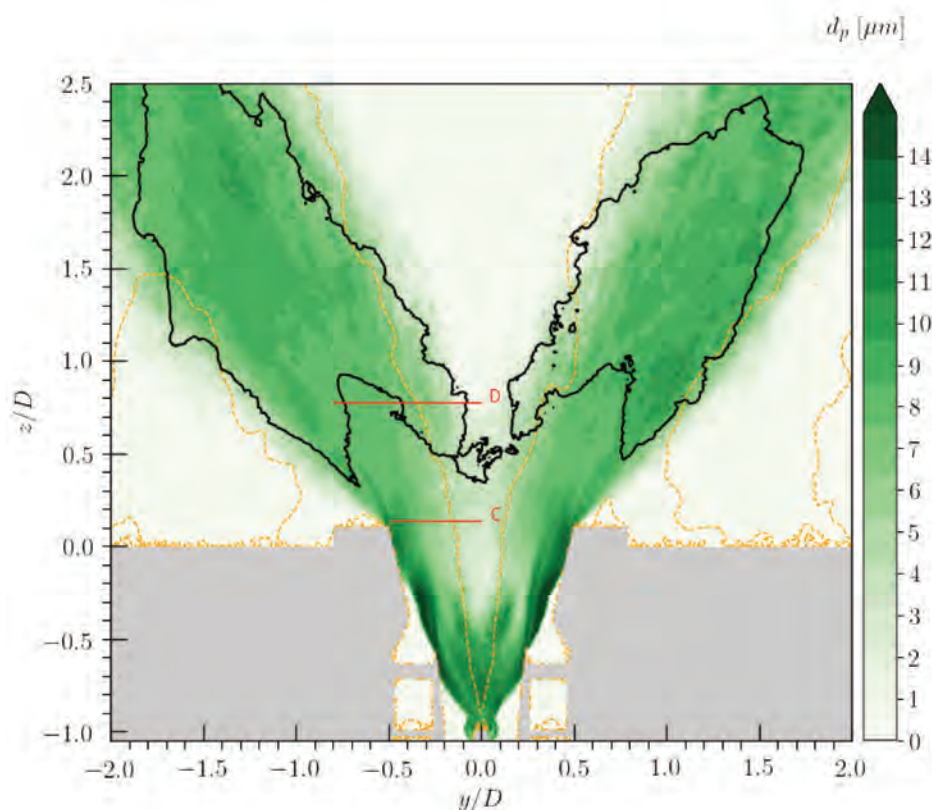


**Fig. 8.18.** Averaged field of total equivalence ratio for the reacting case A. Black and red lines respectively refer to heat release ( $hr = 2 * 10^9 \text{ W/m}^3$ ) and gaseous equivalence ratio ( $\phi_g = 0.3$ ) iso-contours, whereas the discontinuous line is an iso-contour of axial velocity  $w = 0 \text{ m/s}$ .

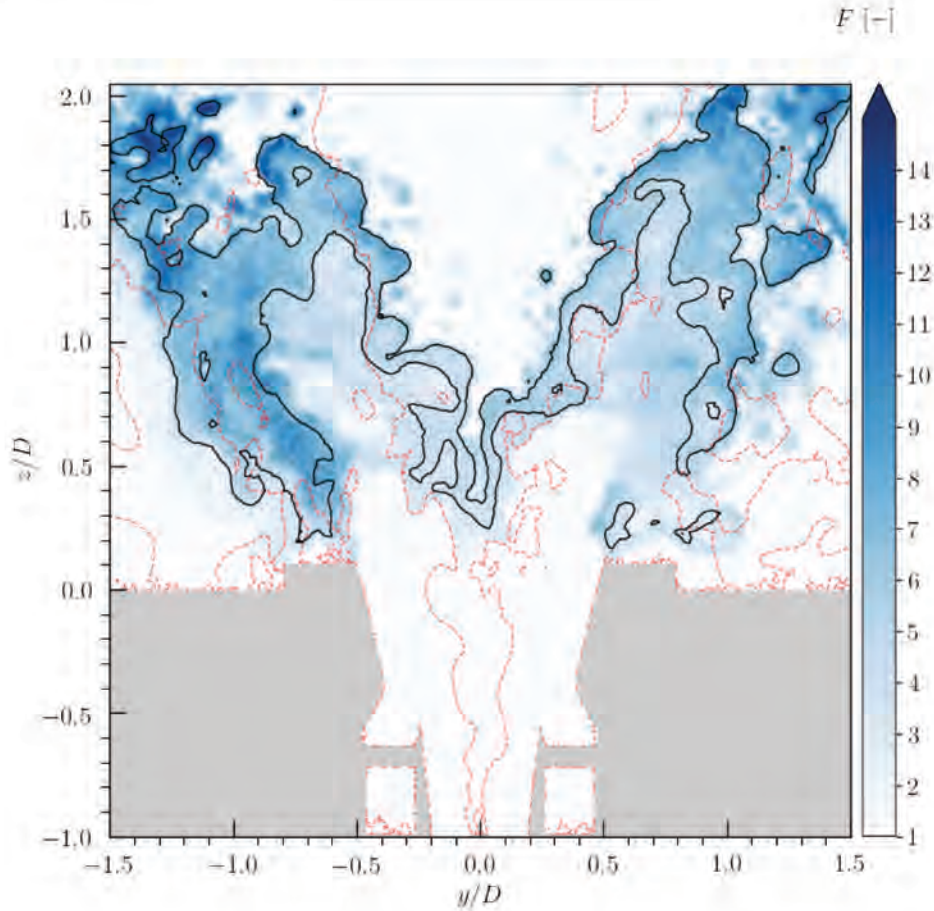
contribution plays a key role in the stabilization and the shape of the flame.

Figure 8.19 presents an averaged field of droplet diameters. The black line is an iso-contour of heat release  $hr = 2 * 10^9 \text{ W/m}^3$ , whereas the discontinuous line delimits the recirculation zones. Large droplets ( $dp \approx 15 \mu\text{m}$ ) are quickly dispersed from the injector onto the walls of the fuel injection nozzle by the swirl motion. These large evaporating droplets are then burnt by the tail of the flame: the flame encompasses regions where droplet diameters are higher than  $10 \mu\text{m}$  (which is coherent with observations made in Fig. 8.14). Therefore, the shape of the flame strongly depends on the spatial size distribution of the droplets whereas the length of the flame depends on the characteristic evaporation time. Using  $\tau_{ev}$  and the averaged axial droplet velocity, one can predict a liquid penetration length  $l_p$  equal to  $l_p/D \approx 3.4$  which almost corresponds to the distance between the injection holes and the tail of the flame.

Also note that some of the droplets are still evaporating downstream of the flame front. As observed in Fig. 8.20 showing an instantaneous thickening field, this is linked to the application of a higher thickening factor downstream of the flame front. Due to the coupling between both, the scaling of the Lagrangian source terms with a higher thickening factor, and a too sensitive standard flame sensor that activates thickening even in low chemical activity regions, the evaporation and drag processes are slowed down. In the present case, in order to limit this phenomenon, the parameter  $Nc$  (corresponding to the number of points requested in the flame front) has been set to  $Nc = 3$ , i.e., lower than the recommended value of  $Nc = 5$ . This corresponds to the best compromise between having a sufficiently high thickening factor



**Fig. 8.19.** Averaged field of droplet diameter for the reacting case A. The black line refers to a heat release iso-contour ( $hr = 2 * 10^9 \text{ W/m}^3$ ) whereas the discontinuous line is an iso-contour of axial velocity  $w = 0 \text{ m/s}$ .



**Fig. 8.20.** Instantaneous field of thickening factor  $F$  obtained with the standard flame sensor for the reacting case A. The black line corresponds to an iso-contour of heat release  $hr = 2 \times 10^9 \text{ W/m}^3$  whereas the discontinuous line is an iso-contour of axial velocity  $w = 0 \text{ m/s}$ .

in the flame, and the lowest as possible thickening factor downstream of the flame. Values of  $F$  downstream of the flame front are high since the mesh elements are large. The regions identified by the thickening sensor depend on the parameter  $\Omega_0$ . For two-phase flows, the  $\Omega_0$  parameter used in the estimation of  $S$  (Eq. 3.75) is tabulated as a function of the local equivalence ratio. The more the equivalence ratio decreases, the lower  $\Omega_0$ . As the operating point is lean, the flame sensor is very sensitive. These issues have motivated the development of the generic flame sensor. Results obtained with this generic approach are presented in Sect. 8.4.

Figures 8.21 and 8.22 show averaged profiles of droplet diameters  $D_{10}$  respectively plotted at station B ( $z = 0.001 \text{ m}$ ) and C ( $z = 0.015 \text{ mm}$ ) in Fig. 8.19. The "LES" profile is an arithmetic averaged between the "surrounding holes" and the "central hole" profiles. At station C, the trend of the LES surrounding holes profile is in good agreement with the experimental measurements, which is not the case for the LES central hole profile. Droplets from this last one are less homogeneously distributed along the radial direction. As a result, the LES averaged profile exhibits smaller droplets at the center of the burner ( $y/D \approx 0$ ) and larger droplets at the exit wall of the injection nozzle ( $y/D = -0.5$ ).

At station D, on the contrary, the trend of the averaged central hole droplet diameter profile is closer to experiments whereas the one resulting from the surrounding holes are slightly higher.

Finally, for both stations the "LES" mean droplet diameter profiles are of the same order

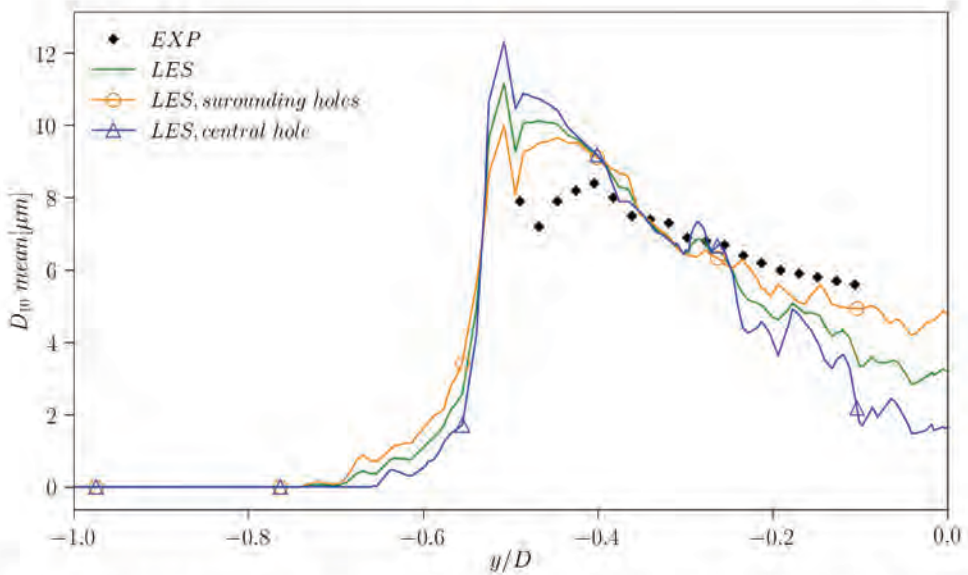


**Fig. 8.21.** Radial profile of mean droplet diameter at station C in Fig. 8.19 for case A. The "LES central hole" profile corresponds to the mean droplet diameter profile obtained with droplets injected by the central hole, whereas the "LES surrounding holes" profile corresponds to the mean droplet diameter profile obtained with droplets injected by the surrounding holes. Finally, the "LES" profile is an arithmetic averaged between the "surrounding holes" and the "central hole" profiles.

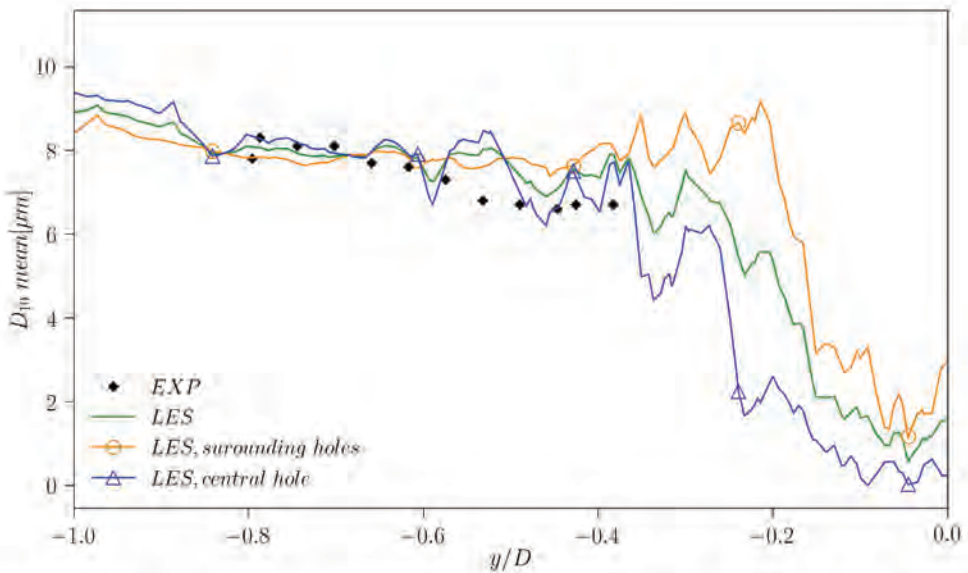


**Fig. 8.22.** Radial profile of mean droplet diameter at station D in Fig. 8.19 for case A. The "LES central hole" profile corresponds to the mean droplet diameter profile obtained with droplets injected by the central hole, whereas the "LES surrounding holes" profile corresponds to the mean droplet diameter profile obtained with droplets injected by the surrounding holes. Finally, the "LES" profile is an arithmetic averaged between the "surrounding holes" and the "central hole" profiles.

## 8.4 Application of the new generic thickening approach

---

of magnitude than in the experiment, meaning that (1) the initial droplet size distribution is close to the real one, and (2) the evaporation and drag processes are well modeled. However, correctly predicting the mean droplet diameter at two stations does not imply that the overall spatial distribution or the density of the spray are good. Moreover, the available experimental data are not sufficient to determine the liquid injection properties, or the spatial distribution of the droplets inside the combustion chamber. Nevertheless, changing the spatial distribution of large droplets downstream of station D will influence the shape of the flame. To change this spatial distribution, several tracks could be investigated:

- Droplets are injected assuming  $\alpha_l = 1$ . By decreasing  $\alpha_l$ , the liquid injection velocity increases. This will change the spatial distribution of the droplets at the tip of the injector and how these last ones are dragged into the swirled jet.
- Droplets in Fig. 8.19 impact the walls of the injection nozzle on which slip liquid boundary conditions are applied. Using more complex liquid boundary conditions that models splash and re-atomization processes will modify the droplet distribution.
- In the current work the liquid mass flow rate  $\dot{m}_l$  is proportionally distributed in between the injection holes and the same droplet distribution is applied to the central and the surrounding holes. Setting the liquid injection properties will also modify the droplet distribution.

### 8.4 Application of the new generic thickening approach

One of the objectives of the generic thickening method is to overcome the issues pointed out in the previous section. In the generic approach, as the thickening value is locally estimated as a function of a flame front thickness estimation  $\delta$ , the thickening factor is expected to be lower downstream of the flame front than at the location of flame. Indeed, as the generic flame sensor is based on the first forward reaction rate, and as the remaining burning droplets are located in burnt gases, the thinnest part of the flame should be the premixed flame front. A first test is performed with the same  $Nc = 3$  as the one used previously with the standard flame sensor. For  $Nc = 3$ , the thickening factor is found equal to unity which is correct since, as observed in Figs. 8.23 and 8.24 showing the instantaneous heat release field, the thinnest part of the flame front is discretized on more than 3 points. Indeed, the generic flame sensor is based on the estimation of the real thickness of flame, it does not depend on the local equivalence ratio, neither on any other parameters related to chemical kinetics.

Note that the two-phase flame is already thickened by the evaporating droplets crossing the flame front: the flame is still premixed and there is enough oxidizer (lean mixture) to burn the evaporating droplets. As observed in Fig. 8.25 showing the averaged field of droplet diameters obtained with the generic sensor and  $Nc = 3$ , the shape of the flame is different from the one obtained with the standard approach. The heat release is anchored at the exit of the injection nozzle and outside of the swirled jet, but the flame stabilization process is the same: the flame burns at the location where the largest droplets exit the injection nozzle. Indeed, as  $F = 1$  the Lagrangian source terms are not affected by the thickening and droplets quickly evaporate: the flame is able to burn the large droplets exiting the fuel injection nozzle (cf. Fig. 8.19 and Fig 8.21). But, as  $F = 1$  the turbulent sub-grid scale contribution to the flame wrinkling is neglected, meaning that  $S_T = S_L^0$ . Therefore, the flame can not stabilize itself in high velocity regions anymore (i.e inside the swirled jet).

To improve the results, the recommended value for flame resolution  $Nc = 6$  is now used for both thickening methods. Figure 8.26 shows the thickening factor field obtained with the standard flame sensor and  $Nc = 6$ . As expected, the order of magnitude of the overall thickening field is higher and the evaporation and drag processes are even more slowed down.

Figure 8.27 shows the thickening factor field obtained with the generic flame sensor and

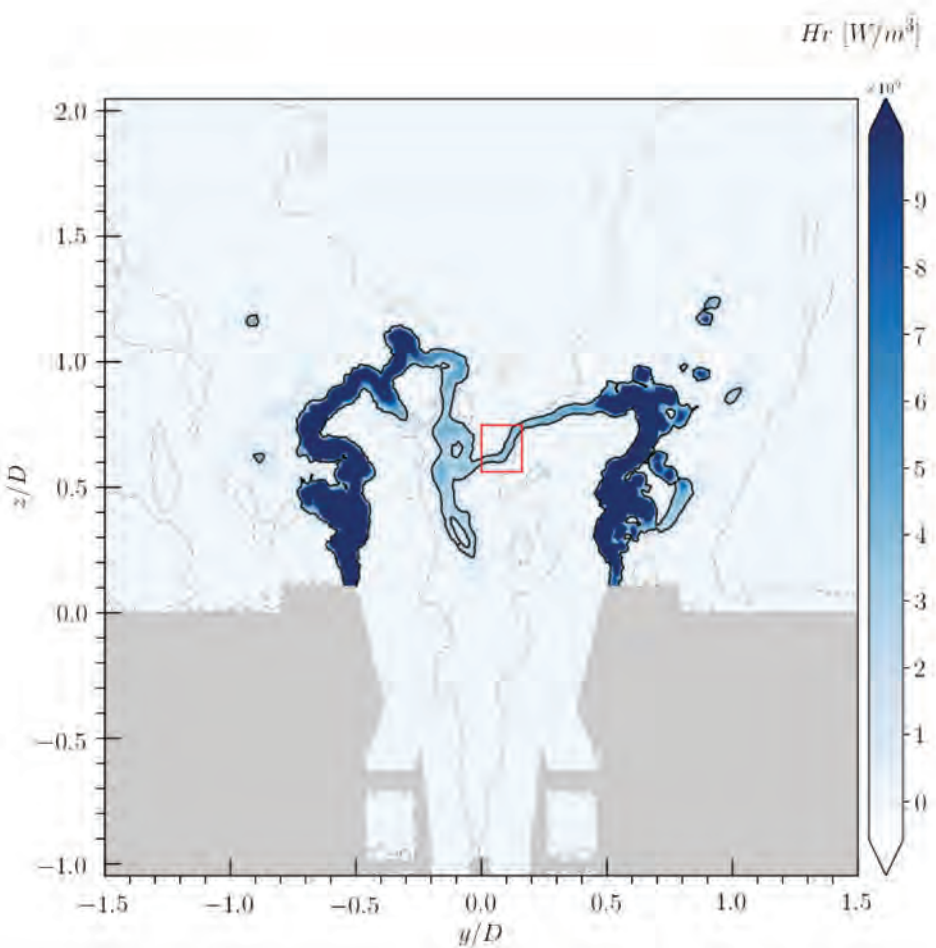


**Fig. 8.23.** Instantaneous field of heat release  $H_r$  obtained with the generic flame sensor for the reacting case. The black line corresponds to an iso-contour of heat release  $h_r = 2 \times 10^9 \text{ W/m}^3$  whereas the discontinuous line is an iso-contour of axial velocity  $w = 0 \text{ m/s}$ .

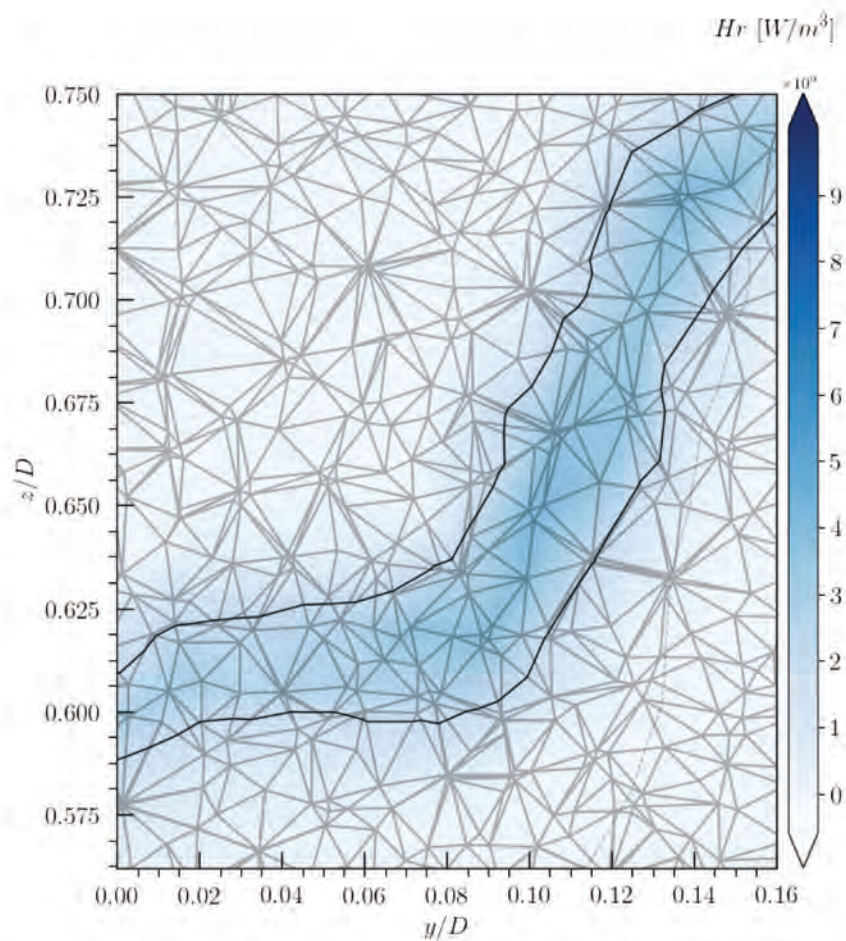


**Fig. 8.24.** Focus made on a restricted part (red box in Fig. 8.23) of the instantaneous field of heat release  $H_r$  obtained with the generic flame sensor for the reacting case. The black line corresponds to an iso-contour of heat release  $h_r = 2 \times 10^9 \text{ W/m}^3$  whereas the discontinuous line is an iso-contour of axial velocity  $w = 0 \text{ m/s}$ .

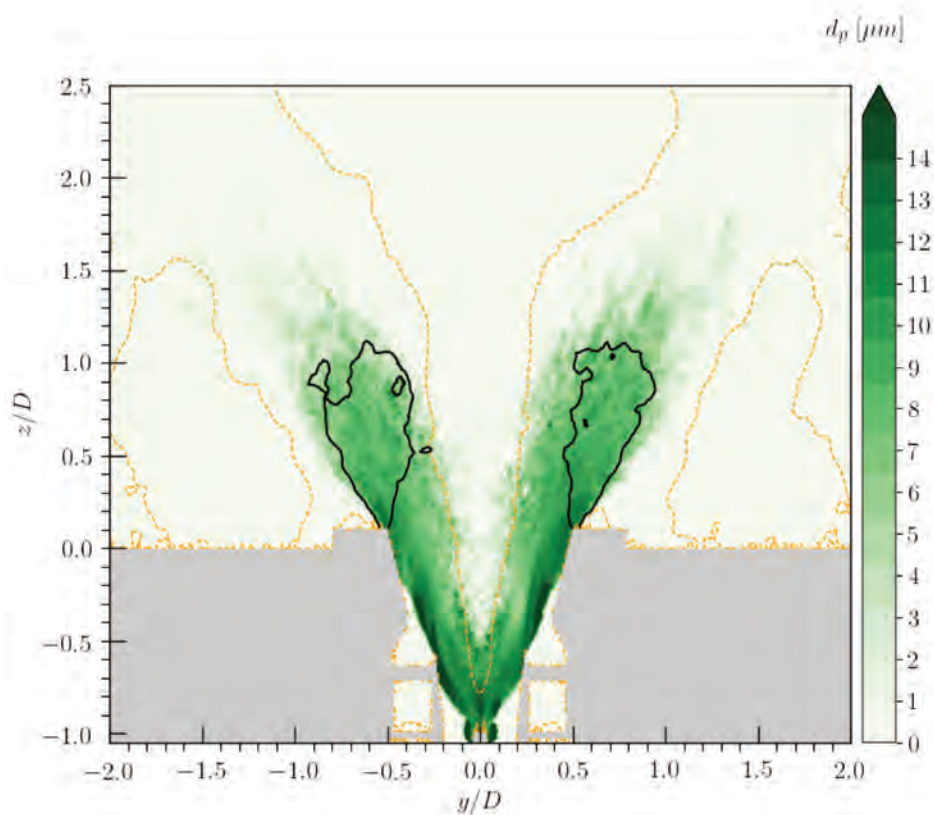


**Fig. 8.25.** Averaged field of droplet diameter obtained with the generic sensor and  $N_c = 3$ . The black line refers to a heat release iso-contour ( $hr = 2 * 10^9 \text{ W/m}^3$ ) whereas the discontinuous line is an iso-contour of axial velocity  $w = 0 \text{ m/s}$ .

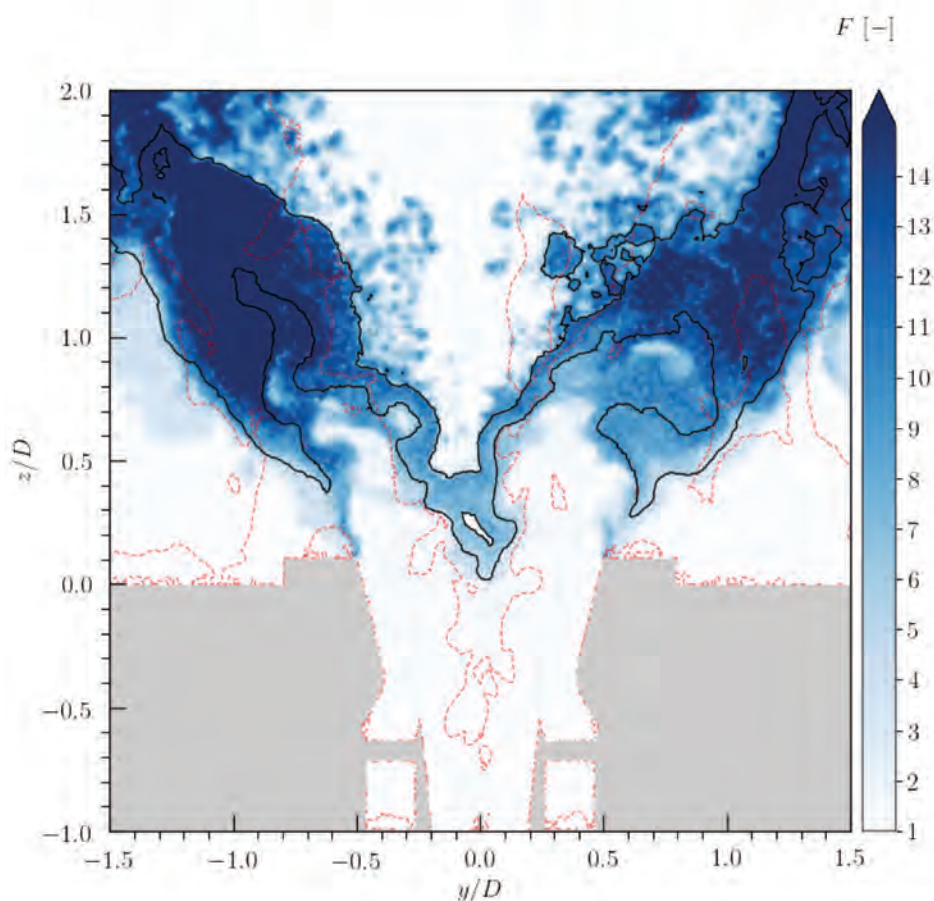


**Fig. 8.26.** Instantaneous field of thickening factor  $F$  obtained with the standard flame sensor for the reacting case and  $N_c = 6$ . The black line corresponds to an iso-contour of heat release  $hr = 2 \times 10^9 \text{ W/m}^3$  whereas the discontinuous line is an iso-contour of axial velocity  $w = 0 \text{ m/s}$ .

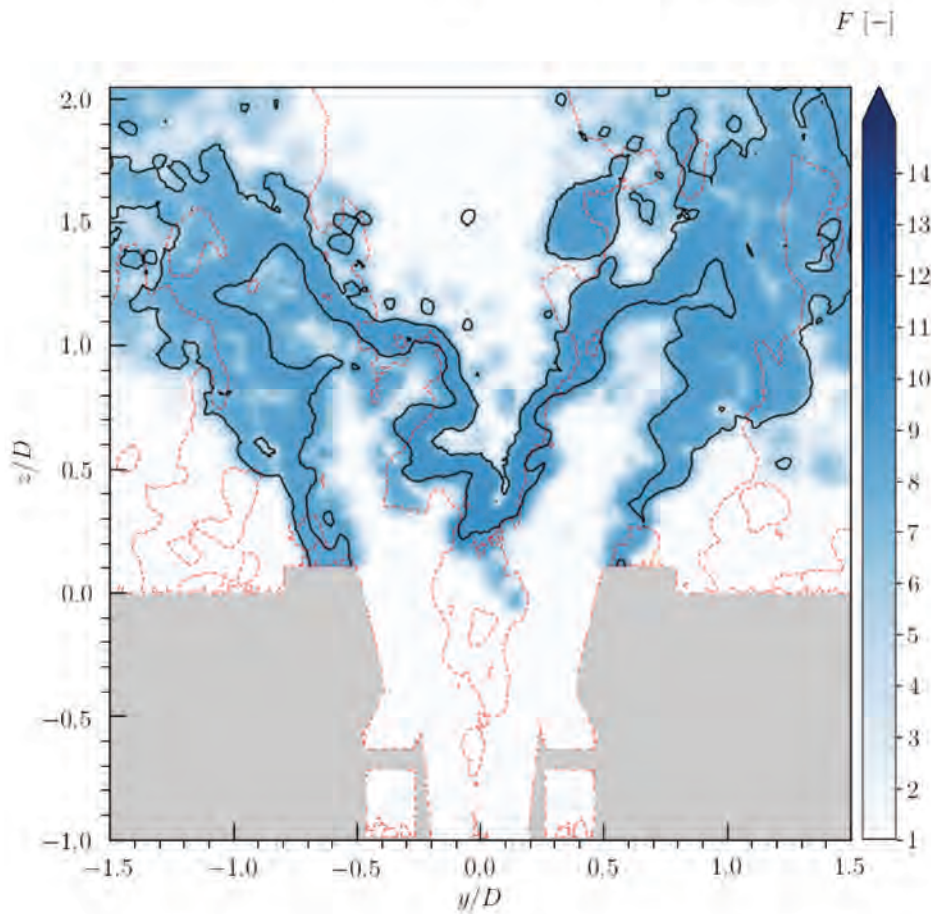


**Fig. 8.27.** Instantaneous field of thickening factor  $F$  obtained with the generic flame sensor for the reacting case and  $Nc = 6$ . The black line corresponds to an iso-contour of heat release  $hr = 2 \times 10^9 \text{ W/m}^3$  whereas the discontinuous line is an iso-contour of axial velocity  $w = 0 \text{ m/s}$ .

$Nc = 6$ . At the location of the flame, the thickening factor is of the same order of magnitude as for the standard flame sensor, meaning that once again the flame front thickness estimation is correct. Moreover, the generic flame sensor detects that the reacting regions downstream of the flame front are not as sharp as this last one. As a result the thickening factor applied downstream of the flame front is lower, which is the expected behavior.

Figure 8.28 presents the radial profiles of the mean axial velocity component for the standard and generic cases. For both cases as the flame still does not have a tulip-shape, the mean axial velocity profiles do not match the experimental data. The length of the IRZ is much longer, as well as the opening angle of the swirled flow. Results obtained with both sensors are almost the same, meaning that the generic flame sensor is at least capable to predict the flame with the same results accuracy than the standard one.

Figure 8.29 presents the radial profiles of the mean radial velocity component for the standard and generic cases. The radial velocity component mainly depends on the stabilization point location of the swirled flame. Herein, the classical and generic flames are stabilized at the same location: the mean radial velocity profiles are the same. Note that the magnitude of the last three profiles are higher than measurements since the length of the swirled jet (delimited by the IRZ) is longer.

Figures 8.30 and 8.31 respectively compare the radial profiles of RMS axial and radial velocity fluctuations from  $z_1$  to  $z_6$ . Results obtained with both flame sensors are identical. For the first three profiles  $w_{rms}$  and  $v_{rms}$  are almost well captured by the LES (note that only the

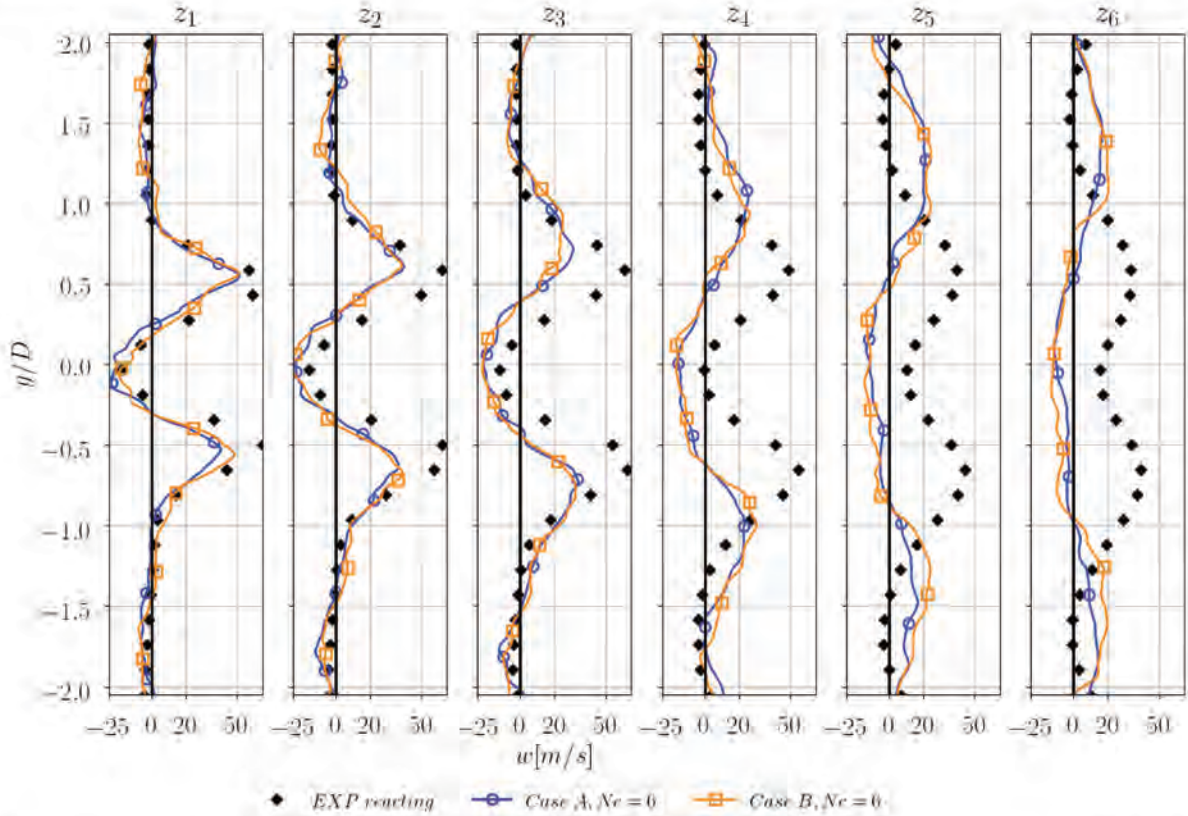


**Fig. 8.28.** Radial profiles of mean axial velocity component at measurement planes  $z_1$  –  $z_6$  of Fig. 8.2 for the reacting cases.

RMS fluctuations of the resolved field are considered). The main difference with experimental measurements lies in the three last profiles where RMS values at the center of the domain are under-predicted. Once again, this is explained by the shape of the flame and the stabilization location.

## 8.5 Conclusion

The first objective of this chapter was to simulate and analyze the structure of the HERON turbulent spray flame. The HERON test rig is an optically accessible combustor built to study lean combustion concepts under high pressure and temperature conditions. The experimental campaign exhibits several features making the HERON burner a challenging configuration for LES: (1) the shape of the flame depends on the operating conditions of the combustion chamber, (2) a part of the flame is stabilized inside the injection nozzle where no measurements are available, and (3) the liquid injection properties have not yet been characterized. On the operating point studied in this manuscript, the flame is known to have a tulip-shape. However, among the whole range of test cases performed in this PhD where the injection droplet diameter has been varied, none of the simulated flames recovered a tulip-shape. To begin with, the numerical setup has been validated with a non-reacting case which exhibits an accurate prediction of the cold flow. Then, the case showing closer results to experiments has been chosen to study the flame structure and analyze the mechanisms controlling the shape of the flame. The V-shape of the flame results from two processes. At the center of the recirculation zone, the flame is mainly gaseous and burns a lean premixed mixture. Inside the swirled jet, the flame is controlled by the evaporating droplets and is at the same location as the largest droplets exiting the injection nozzle. To change the droplet spatial distribution,

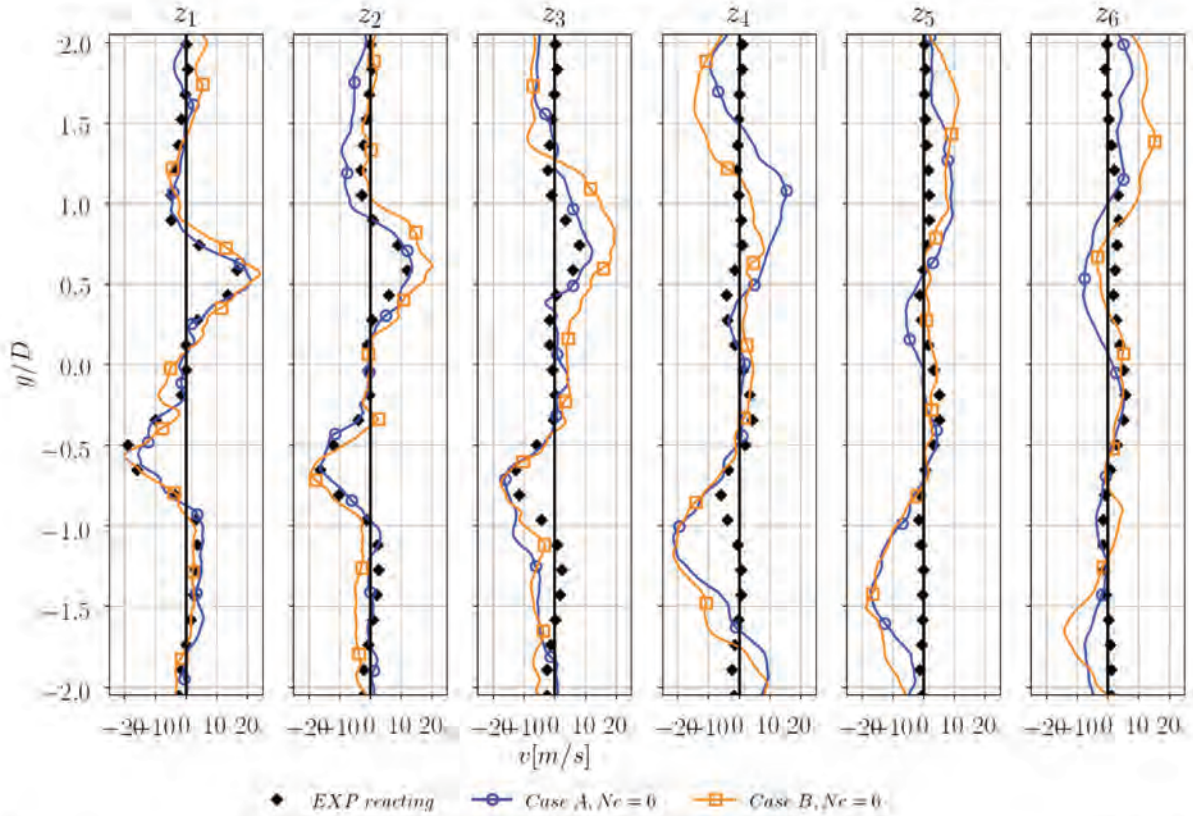


**Fig. 8.29.** radial profiles of mean radial velocity component at measurement planes  $z_1 - z_6$  of Fig. 8.2 for the reacting cases.

several options may be investigated in future works: increase the liquid injection velocity, use more complex liquid boundary conditions that model splash and re-atomization processes and set different liquid injection properties depending on the injection holes.

The second objective was to test the generic sensor developed in this thesis on a realistic turbulent spray flame. Note again that the only user-defined parameter used by the generic methodology is the number of points requested inside the flame front  $N_c$ . The results show that the use of the generic sensor is a good solution for the issues related to the slow down of drag and evaporation processes outside the reaction zones. On the HERON flame and at the studied operating conditions, the use of the generic approach leads to the same flow results as the ones obtained with the standard flame sensor, demonstrating the capacity of the generic flame sensor to thicken turbulent spray flames in realistic operating conditions.

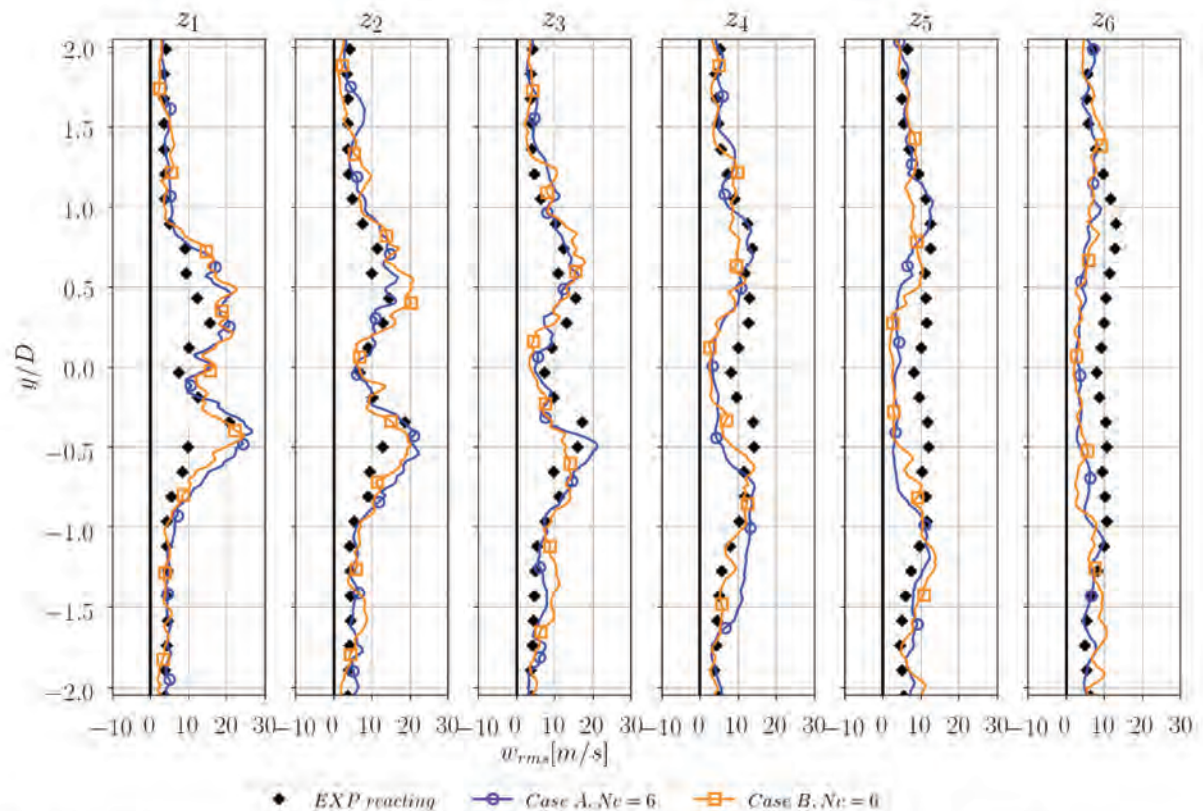


**Fig. 8.30.** radial profiles of RMS axial velocity component at measurement planes  $z_1 - z_6$  of Fig. 8.2 for the reacting cases.

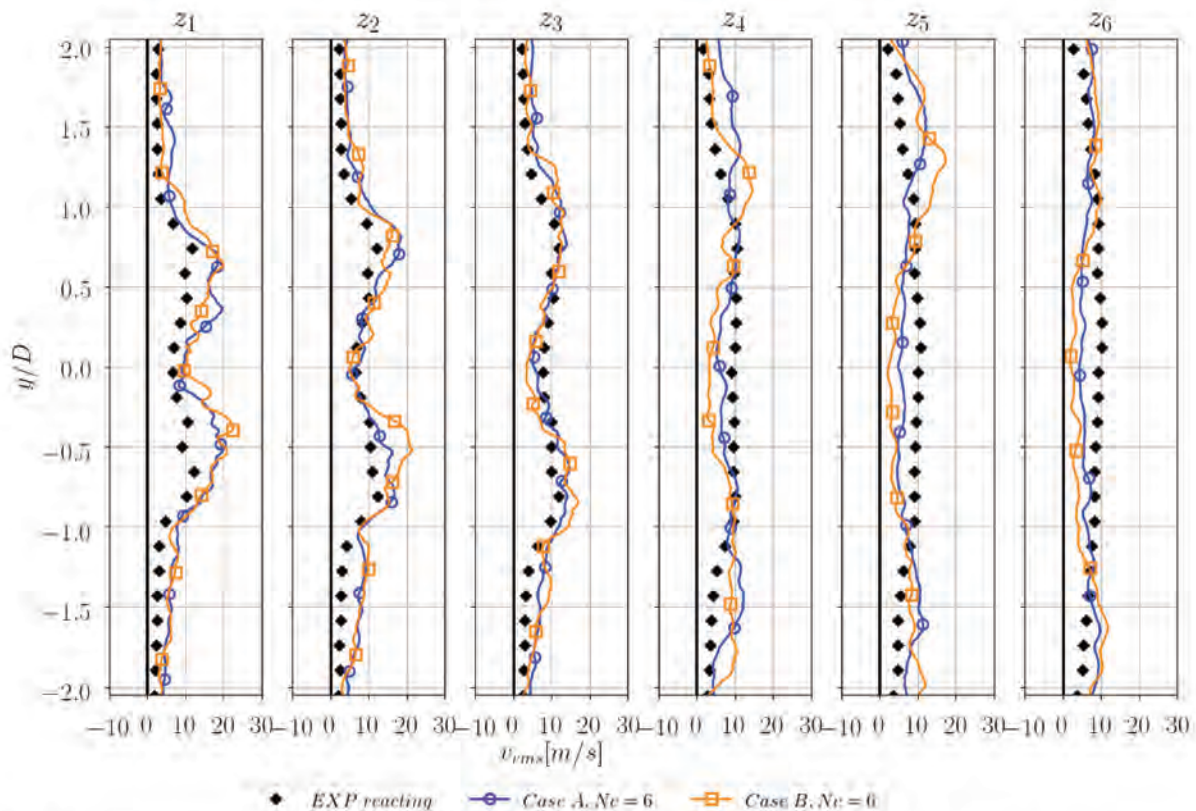


**Fig. 8.31.** radial profiles of RMS radial velocity component at measurement planes  $z_1 - z_6$  of Fig. 8.2 for the reacting cases.

# **V Conclusion and perspectives**



# Conclusion and perspectives

This PhD thesis was first an opportunity to apply and test the state-of-the-art TFLES models on complex turbulent gaseous and two-phase reacting configurations. The effects of chemistry description, sub-grid scale flame/turbulence interaction and spatial accuracy of the numerical method were first studied on the Volvo flame that is known to be a numerical challenging configuration. The pros and cons of these models were investigated to contribute to the understanding of the mechanisms related to turbulent combustion, and to propose a LES modeling strategy to improve the fidelity of reactive simulations. Then, numerical simulations of a turbulent spray flame using the LES-DPS approach were performed in a new burner build at CORIA laboratory, the Heron burner. The first attempts of simulations have demonstrated the difficulty to numerically predict such flames. Thanks to the analysis of the turbulent spray flame structure, the mechanisms controlling this flame were understood.

Another important contribution of this PhD thesis is the improvement of the accuracy and the genericity of the combustion modeling in the framework of the TFLES model. Indeed, a generic and self-adapting method for flame front detection and thickening has been developed. This approach relies on geometric considerations and unlike previous thickening methods does not need any parameterization nor preliminary calibration. The method was developed and implemented in an unstructured and massively parallel environment and is therefore directly usable for the computation of complex configurations. This method has been validated against configurations of increasing complexity and then applied to the burners previously studied. Apart from an easier use, and the reduction of user input only to one parameter ( $N_c$ ), this approach is critical to apply TFLES to complex cases with varying local conditions, complex chemistry or liquid fuel. Indeed the use of the generic thickening method in the Heron burner has demonstrated a more accurate thickening in post-flame regions.

Finally, this PhD thesis has contributed to the understanding of the spray/flame interaction for the peculiar case of homogeneous spray flames where the dispersed phase has a relative velocity compared to the carrier phase. Based on the numerical simulations of one-dimensional two-phase laminar flames, two burning regimes were identified. The first one, observed for lean mixtures, is similar to a corresponding gaseous premixed flame in terms of burnt gas temperature profiles. In this case the relative velocity increases the flame thickness and decreases the laminar flame speed. The second one, identified for rich mixtures, is more complex. The flame burns at a lower equivalence ratio that can be closer to stoichiometry, leading to higher local gas temperature and higher flame speed than the gaseous premixed flame at the same total equivalence ratio. However if the relative velocity is too high or droplets are too large, the local equivalence ratio at which the flame burns may be very low and the two-phase flame is slower than the gaseous flame.

From the detailed analysis of these flames, two analytical formulations for the spray flame propagation speed have been proposed and validated. The agreement between the overall trend of both the measured/estimated spray flame speeds demonstrates that the model and its parameters correctly take into account the main physical mechanisms controlling laminar spray flames.

In addition to contribute to the understanding of turbulent spray flames, the estimation of the two-phase laminar flame speed using these analytical formulations may also benefit to turbulent spray combustion models using so far gaseous laminar flame speeds and thicknesses as parameters. An interesting perspective to this thesis would be to use these correlations in the Heron simulations for both turbulent spray combustion modeling and flame analysis.

Although this PhD thesis has contributed to improve the accuracy of the turbulent spray flame simulations with a more accurate and generic sensor and a better prediction of two-phase laminar flame speeds, difficulties are still encountered in the Heron simulations, due in particular to the lack of data on the liquid injection parameters. Such uncertainties have a strong impact on the accuracy of numerical results and must be resolved. One promising approach is the Uncertainty Quantification (UQ) analysis on the liquid injection properties, which could be applied to determine the missing injection parameters.

# **VI Bibliography**



- 
- [1] J. Watkinson. 6 - Engines and transmissions. Edited by John Watkinson. Oxford. Butterworth-Heinemann (2004), 191 –257. (Cited on page 3).
  - [2] A. H. Lefebvre. Gas Turbines Combustion. Taylor & Francis (1999). (Cited on page 6).
  - [3] P. Jenny, D. Roekaerts, and N. Beishuizen. Modeling of turbulent dilute spray combustion. *Prog. Energy Comb. Sci.* 38 (6) (2012), 846–887. (Cited on page 7).
  - [4] P. Fede, P. Février, and O. Simonin. Numerical study of the effect of the fluid turbulence microscales on particle segregation and collision in gas-solid turbulent flows. 5th Int. Conf. Multiphase Flow. ICMF Yokohama, Japan. (2004). (Cited on page 7).
  - [5] P. Chassaing. Mécanique des fluides, Éléments d'un premier parcours. Cépaduès-Éditions (2000). (Cited on page 8).
  - [6] S. B. Pope. Turbulent flows. Cambridge University Press (2000). (Cited on pages 8, 44).
  - [7] J. Smagorinsky. General circulation experiments with the primitive equations: 1. The basic experiment. *Mon. Weather Rev.* 91 (1963), 99–164. (Cited on page 8).
  - [8] D. K. Lilly. The representation of small-scale turbulence in numerical simulation experiments. Proceedings of the IBM Scientific Computing Symposium on Environmental Sciences. Yorktown Heights, USA. (1967). (Cited on page 8).
  - [9] M. Boileau, G. Staffelbach, B. Cuenot, T. Poinsot, and C. Bérat. LES of an ignition sequence in a full helicopter combustor. *To be submitted to AIAA Journal* (2007). (Cited on page 8).
  - [10] D.C. Haworth and K. Jansen. Large-eddy simulation on unstructured deforming meshes: towards reciprocating IC engines. *Comput. Fluids* 29 (2000), 493–524. (Cited on page 8).
  - [11] S. Balachandar and J.K. Eaton. Turbulent Dispersed Multiphase Flow. *Annu. Rev. Fluid Mech.* 42 (2010), 111–133. (Cited on pages 11, 12).
  - [12] J. K. Eaton and J. R. Fessler. Preferential concentration of particles by turbulence. *Int. J. Multiphase Flow* 20 (1994), 169–209. (Cited on page 11).
  - [13] A.M. Wood, W. Hwang, and J.K. Eaton. Turbulent Dispersed Multiphase Flow. *Int. journal of Multiphase Flow* 31 (2005), 1220–1233. (Cited on page 13).
  - [14] R. G. Abdel-Gayed, D. Bradley, M. N. Hamid, and M. Lawes. Lewis number effects on turbulent burning velocity. *Proc. Combust. Inst.* 20 (1984), 505–512. (Cited on page 15).
  - [15] O. Gulder. Turbulent premixed flame propagation models for different combustion regimes. 23rd Symp. (Int.) on Comb. (1). Orleans. The Combustion Institute, Pittsburgh (1991), 743–750. (Cited on pages 15, 54).
  - [16] V. Yakhot, C. G. Orszag, S. Thangam, T. B. Gatski, and C. G. Speziale. Development of turbulence models for shear flows by a double expansion technique. *Phys. Fluids* 4 (7) (1992), 1510. (Cited on page 15).
  - [17] N. Peters. The turbulent burning velocity for large-scale and small-scale turbulence. *J. Fluid Mech.* 384 (1999), 107 –132. (Cited on pages 15, 77).
  - [18] F. Williams. Combustion Theory. 2nd ed. The Benjamin/Cummings Publishing Company (1985). (Cited on pages 15, 16, 39, 50, 69).
  - [19] M. Matalon and B. J. Matkowsky. Flames as gasdynamic discontinuities. *J. Fluid Mech.* 124 (1982), 239. (Cited on page 15).
  - [20] S. M. Candel and T. Poinsot. Flame stretch and the balance equation for the flame surface area. *Combust. Sci. Tech.* 70 (1990), 1–15. (Cited on page 15).
  - [21] W. Bush and F. Fendell. Asymptotic analysis of laminar flame propagation for general Lewis numbers. *Combust. Sci. Tech.* 1 (1970), 421. (Cited on page 16).

- 
- [22] J. Buckmaster and G. Ludford. Theory of laminar flames. Cambridge University Press (1982). (Cited on page 16).
  - [23] P. Pelce and P. Clavin. Influence of hydrodynamics and diffusion upon stability limits of laminar premixed flames. *J. Fluid Mech.* 124 (1982), 219. (Cited on page 16).
  - [24] P. Clavin and F. A. Williams. Theory of premixed-flame propagation in large scale turbulence. *J. Fluid Mech.* 56 (1979), 81–95. (Cited on page 16).
  - [25] P. Clavin and P. Garcia. The influence of the temperature dependence of diffusivities on the dynamics of flame fronts. *J. Mécanique* 2 (1983), 245–263. (Cited on page 16).
  - [26] T. Poinsot and D. Veynante. Theoretical and Numerical Combustion. Third Edition ([www.cerfacs.fr/elearning](http://www.cerfacs.fr/elearning)) (2011). (Cited on pages 17, 24, 33, 39, 44, 50, 52, 69, 114).
  - [27] C. Mueller, J. F. Driscoll, D. Reuss, M. Drake, and M. Rosalik. Vorticity generation and attenuation as vortices convect through a premixed flame. *Combust. Flame* 112 (1998), 342–358. (Cited on page 18).
  - [28] F. A. Williams. Theory of combustion in laminar flows. *Ann. Rev. Fluid Mech.* 3 (1971), 171–188. (Cited on page 18).
  - [29] J. Réveillon and L. Vervisch. Analysis of weakly turbulent diluted-spray flames and spray combustion regimes. *J. Fluid Mech.* 537 (2005), 317–347. (Cited on pages 19, 21, 30).
  - [30] A. R. Kerstein and C. K. Law. Percolation in combustion sprays I: Transition from cluster combustion to percolate combustion in non-premixed sprays. *Proc. Combust. Inst.* 19 (1982), 961–969. (Cited on page 19).
  - [31] H. H. Chiu, H. Y. Kim, and E. J. Croke. Internal group combustion of liquid droplets. *Proc. Combust. Inst.* 19 (1982), 971–980. (Cited on page 21).
  - [32] K. K. Kuo. Principles of Combustion. New York. John Wiley (1986). (Cited on page 21).
  - [33] K. Annamalai and W. Ryan. Interactive processes in gasification and combustion? Part I: liquid drop arrays and clouds. *Prog. Energy Comb. Sci.* 18 (1992), 221–295. (Cited on page 21).
  - [34] W. A. Sirignano. Advances in droplet array combustion theory and modeling. *Prog. Energy Comb. Sci.* 42 (2014), 54–86. (Cited on page 21).
  - [35] A. Umemura and S. Takamori. Percolation theory for flame propagation in non- or less-volatile fuel spray : A conceptual analysis to group combustion excitation mechanism. *Combust. Flame* 141 (2005), 336–349. (Cited on pages 21–23).
  - [36] R. Borghi. Background on droplets and sprays. Combustion and turbulence in two phase flows, Lecture Series 1996-02. Von Karman Institute for Fluid Dynamics (1996). (Cited on page 22).
  - [37] M. Mikami, S. Miyamoto, and N. Kojima. Counterflow diffusion flame with polydisperse sprays. *Proc. Combust. Inst.* 29 (2002), 593–599. (Cited on page 22).
  - [38] M. Mikami, Y. Mizuta, Y. Tsuchida, and N. Kojima. Flame structure and stabilization of lean-premixed sprays in a counterflow with low-volatility fuel. *Proc. Combust. Inst.* 32 (2) (2009), 2223–2230. (Cited on pages 22, 23).
  - [39] J. H. Burgoyne and L. Cohen. The Effect of Drop Size on Flame Propagation in Liquid Aerosols. *Proceedings of the Royal Society of London A: Mathematical, Physical and Engineering Sciences* 225 (1162) (1954), 375–392. (Cited on pages 23, 113).
  - [40] C. E. Polymeropoulos. Flame Propagation in a One-Dimensional Liquid Fuel Spray. *Combustion Science and Technology* 9 (5-6) (1974), 197–207. (Cited on pages 23, 113).

- 
- [41] D. R. Ballal and A. H. Lefebvre. Flame propagation in heterogeneous mixtures of fuel droplets, fuel vapor and air. *Proc. Combust. Inst.* 18 (1981), 321–327. (Cited on pages 23, 113).
  - [42] G. D. Myers and A. H. Lefebvre. Flame propagation in heterogeneous mixtures of fuel drops and air. *Combust. Flame* 66 (2) (1986), 193–210. (Cited on pages 23, 113).
  - [43] I. Silverman, J. B. Greenberg, and Y. Tambour. Stoichiometry and polydispersity effects in premixed spray flames. *Combust. Flame* 93 (1993), 97–118. (Cited on pages 23, 113).
  - [44] F. A. Williams. Spray combustion and atomization. *Phys. Fluids* 1 (1958), 541–546. (Cited on page 23).
  - [45] T. H. Lin, C. K. Law, and S. H. Chung. Theory of laminar flame propagation in off-stoichiometric dilute sprays. *Int. J. Heat and Mass Transfer* 31 (1988), 1023–1034. (Cited on page 23).
  - [46] G.A. Richards and P.E. Sojka. A model of H<sub>2</sub>-enhanced spray combustion. *Combustion and Flame* 79 (3) (1990), 319–332. (Cited on page 23).
  - [47] T. H. Lin and Y. Y. Sheu. Theory of laminar flame propagation in near-stoichiometric dilute sprays. *Int. J. Heat and Mass Transfer* 84 (1991), 333–342. (Cited on page 23).
  - [48] J. B. Greenberg, I. Silverman, and Y. Tambour. A new heterogeneous burning velocity formula for the propagation of a laminar flame front through a polydisperse spray of droplet. *Combust. Flame* 104 (1996), 358–368. (Cited on page 23).
  - [49] I. Silverman, J. B. Greenberg, and Y. Tambour. Asymptotic analysis of premixed polydisperse spray flame. *SIAM J. Appl. Math.* 51 (1991), 1284–1303. (Cited on page 23).
  - [50] J. B. Greenberg, I. Silverman, and Y. Tambour. On the origin of spray sectional conservation equations. *Combust. Flame* 93 (1993), 90–96. (Cited on page 23).
  - [51] M. Mikami, H. Oyagi, N. Kojima, and Y. Wakashima. Microgravity experiments on flame spread along fuel-droplet arrays at high temperatures. *Combust. Flame* 146 (2006), 391–406. (Cited on page 23).
  - [52] A. Neophytou and E. Mastorakos. Simulations of laminar flame propagation in droplet mists. *Combust. Flame* 156 (8) (2009), 1627–1640. (Cited on pages 23, 24, 113).
  - [53] S. Hayashi, S. Kumagai, and T. Sakai. Propagation velocity and structure of flames in droplet-vapor-air mixtures. *Combust. Sci. Tech.* 15 (1976), 169–177. (Cited on pages 23, 24, 113).
  - [54] M. Zhu and B. Rogg. Modelling and simulation of sprays in laminar flames. *Meccanica* 31 (1996), 177–193. (Cited on pages 24, 113).
  - [55] R. F. Dakhlia. Combustion stationnaire et instationnaire de mélanges diphasiques. PhD Thesis. Laboratoire d’Energétique Moléculaire et Macroscopique, Combustion (EM2C) du CNRS et de l’École Centrale de Paris, (2001). (Cited on pages 24, 113).
  - [56] J. Reveillon. Direct Numerical Simulation of Sprays: Turbulent Dispersion , Evaporation and Combustion. *Multiphase Reacting Flows: Modelling and Simulation* 492 (1981) (1988), 229–269. (Cited on pages 24, 25, 42).
  - [57] O. Delabroy, F. Lacas, B. Labegorre, and J.-M. Samaniego. Paramètres de similitude pour la combustion diphasique. *Rev. Gén. Therm.* (37) (1998), 934–953. (Cited on page 25).
  - [58] T. Takeno, M. Murayama, and Y. Tanida. Fractal analysis of turbulent premixed flame surface. *Experiments in Fluids* 10 (1990), 61–70. (Cited on page 26).
  - [59] S.K. Marley, E.J. Welle, K.M. Lyons, and W.L. Roberts. Effects of leading edge entrainment on the double flame structure in lifted ethanol spray flames. *Experimental Thermal and Fluid Science* 29 (2004), 23–31. (Cited on pages 26, 27, 30).

- 
- [60] H.W. Ge, I. Duwel, H. Kronemayer, R.W. Dibble, E. Gutheil, C. Schulz, and J. Wolfgram. Laser-based experimental and Monte Carlo PDF numerical investigation of an ethanol/air spray flame. *Combust. Sci. Tech.* 180 (8) (2008), 1529–1547. (Cited on page 26).
- [61] C. Pichard, Y. Michou, C. Chauveau, and I. Gokalp. Average Droplet Vaporization Rates in Partially Prevaporized Turbulent Spray Flames. *Proc. Combust. Inst.* 29 (2002), 527–533. (Cited on pages 27, 28).
- [62] A.N Karpetis and A. Gomez. An experimental study of well defined turbulent non-premixed spray flames. *Combust. Flame* 121, 1–23. (Cited on page 27).
- [63] J. F. Widmann and C. Presser. A benchmark experimental database for multiphase combustion model input and validation. *Combust. Flame* 129 (1) (2002), 47–86. (Cited on page 29).
- [64] M. Sanjosé, T. Lederlin, L. Gicquel, B. Cuenot, H. Pitsch, N. García-Rosa, R. Lecourt, and T. Poinsot. LES of two-phase reacting flows. *Proc. of the Summer Program* (2008), 251–263. (Cited on page 29).
- [65] D. E. Cavaliere, J. Kariuki, and E. Mastorakos. A comparison of the blow-off behaviour of swirl-stabilized premixed, non-premixed and spray flames. *Flow, Turb. and Combustion* 91 (2) (2013), 347–372. (Cited on page 29).
- [66] M. Uhlmann. An Immersed Boundary Method with Direct Forcing for the Simulation of Particulate Flows. *J. Comput. Phys.* 209 (2005), 448–476. (Cited on page 29).
- [67] B. Duret, G. Luret, J. Reveillon, T. Menard, A. Berlemont, and F. X. Demoulin. DNS analysis of turbulent mixing in two-phase flows. *Int. J. Multiphase Flow* 40 (2012), 93–105. (Cited on page 29).
- [68] M. R. G. Zoby, S. Navarro-Martinez, A. Kronenburg, and A. J. Marquis. Evaporation rates of droplet arrays in turbulent reacting flows. *Proc. Combust. Inst.* 33 (2) (2011), 2117–2125. (Cited on page 30).
- [69] M. R. G. Zoby, S. Navarro-Martinez, A. Kronenburg, and A. J. Marquis. Turbulent mixing in three-dimensional droplet arrays. *Int. J. Heat Fluid Flow* 32 (3) (2011), 499–509. (Cited on page 30).
- [70] Guang Wu and William A. Sirignano. Transient convective burning of a periodic fuel-droplet array. *Proc. Combust. Inst.* 33 (2) (2011), 2109–2116. (Cited on page 30).
- [71] Guang Wu and William A. Sirignano. Transient convective burning of interactive fuel droplets in double-layer arrays. *Combust. Flame* 158 (12) (2011), 2395–2407. (Cited on page 30).
- [72] Guang Wu and William A. Sirignano. Transient convective burning of interactive fuel droplets in single-layer arrays. *Combust. Theory and Modelling* 15 (2) (2011), 227–243. (Cited on page 30).
- [73] B. Wang, A. Kronenburg, G. L. Tufano, and O. T. Stein. Fully resolved DNS of droplet array combustion in turbulent convective flows and modelling for mixing fields in inter-droplet space. *Combust. Flame* 189 (2018), 347–366. (Cited on page 30).
- [74] J. Reveillon and F. X. Demoulin. Evaporating droplets in turbulent reacting flows. *Proc. Combust. Inst.* 38 (4) (2010), 679–686. (Cited on page 31).
- [75] K. Luo, H. Pitsch, M. G. Pai, and O. Desjardins. Direct numerical simulations and analysis of three-dimensional n-heptane spray flames in a model swirl combustor. *Proc. Combust. Inst.* 33 (2) (2011), 2143–2152. (Cited on page 31).
- [76] P. Fede and O. Simonin. Numerical study of the subgrid fluid turbulence effects on the statistics of heavy colliding particles. *Phys. Fluids* 18 (045103) (2006). (Cited on page 32).

- 
- [77] J. Pozorski and S. V. Apte. Filtered particle tracking in isotropic turbulence and stochastic modeling of subgrid-scale dispersion. *Int. J. Multiphase Flow* 35 (2) (2009), 118–128. (Cited on page 32).
- [78] W. P. Jones, C. Lettieri, A. J. Marquis, and S. Navarro-Martinez. Large Eddy Simulation of the two-phase flow in an experimental swirl-stabilized burner. *Int. J. Heat Fluid Flow* 38 (2012), 145–158. (Cited on page 32).
- [79] W. P. Jones, A. J. Marquis, and K. Vogiatzaki. Large-eddy simulation of spray combustion in a gas turbine combustor. *Combust. Flame* 161 (1) (2014), 222–239. (Cited on page 32).
- [80] B. Shotorban and F. Mashayek. Modeling subgrid-scale effects on particles by approximate deconvolution. *Phys. Fluids* 17 (2005), 081701. (Cited on page 32).
- [81] S. B. Pope. Pdf methods for turbulent reactive flows. *Prog. Energy Comb. Sci.* 19 (11) (1985), 119–192. (Cited on page 32).
- [82] A. Y. Klimenko and R. W. Bilger. Conditional moment closure for turbulent combustion. *Prog. Energy Comb. Sci.* 25 (6) (1999), 595–687. (Cited on page 33).
- [83] M. Mortensen and R. W. Bilger. Derivation of the conditional moment closure equations for spray combustion. *Combust. Flame* 156 (2009), 62–72. (Cited on page 33).
- [84] S. Navarro-Martinez, A. Kronenburg, and F. Di Mare. Conditional moment closure for large eddy simulations. *Flow, Turb. and Combustion* 75 (1-4) (2005), 245–274. (Cited on page 33).
- [85] M. Boileau, G. Staffelbach, B. Cuenot, T. Poinsot, and C. Bérat. LES of an ignition sequence in a gas turbine engine. *Combust. Flame* 154 (1-2) (2008), 2–22. (Cited on page 33).
- [86] J. M. Senoner, M. Sanjosé, T. Lederlin, F. Jaegle, M. García, E. Riber, B. Cuenot, L. Gicquel, H. Pitsch, and T. Poinsot. Evaluation of numerical strategies for two-phase reacting flows. *C. R. Acad. Sci. Mécanique* 337 (6-7) (2009), 528–538. (Cited on page 33).
- [87] D. Paulhiac. Modélisation de la combustion d'un spray dans un brûleur aéronautique. PhD thesis. INPT Toulouse, (2015). (Cited on pages 33, 34, 100, 114, 132).
- [88] J. Huang and H. Chiu. Multiple-state phenomena and hysteresis of a combusting isolated droplet. *Atomization and Sprays* 6 (1) (1996), 1–26. (Cited on page 33).
- [89] J. Huang and H. Chiu. Comparison of droplet combustion models in nonpremixed spray combustion. *AIAA Paper* (2002), 1–11. (Cited on page 33).
- [90] F. Wang, B. Hu, and Y. Huang. A two-phase turbulent combustion model and its validation for spray flames. *Fuel* 113 (2013), 280–286. (Cited on page 33).
- [91] S. De and S. H. Kim. Large eddy simulation of dilute reacting sprays: Droplet evaporation and scalar mixing. *Combust. Flame* 160 (10) (2013), 2048–2066. (Cited on page 34).
- [92] R. W. Bilger. A mixture fraction framework for the theory and modeling of droplets and sprays. *Combust. Flame* 158 (2) (2011), 191–202. (Cited on page 34).
- [93] T. Schønfeld and M. Rudgyard. Steady and Unsteady Flows Simulations Using the Hybrid Flow Solver AVBP. *AIAA Journal* 37 (11) (1999), 1378–1385. (Cited on pages 34, 77, 100, 115).
- [94] L. F. Richardson and P. Lynch. Weather prediction by numerical process. 2nd edition. Cambridge Mathematical Library. Cambridge University Press (2007). (Cited on page 37).
- [95] A. N. Kolmogorov. The Local Structure of Turbulence in Incompressible Viscous Fluid for Very Large Reynolds Numbers. *Proc. R. Soc.* 434 (1991), 9–13. (Cited on page 37).

- 
- [96] K. K. Kuo. Principles of combustion. Edited by Inc. John Wiley & Sons. 2nd Ed. John Wiley & Sons, Inc. (2005). (Cited on pages 39, 41, 71, 134).
  - [97] S. Chapman and T. G. Cowling. The Mathematical Theory of Non-uniform Gases. Cambridge University Press, 3rd edition (1970). (Cited on page 40).
  - [98] W. Sutherland. The viscosity of gases and molecular force. *Philosophical Magazine* 36 (223) (1893), 507–531. (Cited on page 40).
  - [99] C. K. Westbrook and F. L. Dryer. Simplified Reaction Mechanisms for the Oxidation of Hydrocarbon Fuels in Flames. *Combust. Sci. Tech.* 27 (1981), 31–43. (Cited on page 41).
  - [100] P. Chassaing. Turbulence en mécanique des fluides, Analyse du phénomène dans une perspective de modélisation à l'usage de l'ingénieur. Edited by Cépaduès-Editions. Institut National Polytechnique de Toulouse (2000). (Cited on page 42).
  - [101] P. Sagaut. Large Eddy Simulation for Incompressible Flows. Berlin. Springer (1998). (Cited on page 44).
  - [102] J. Boussinesq. Essai sur la théorie des eaux courantes. 26ème édn. *Acad. Sci. Paris* (1877). (Cited on page 45).
  - [103] A. N. Kolmogorov. The local structure of turbulence in incompressible viscous fluid for very large Reynolds numbers. *C. R. Acad. Sci., USSR* 30 (1941), 301. (Cited on page 45).
  - [104] P. Sagaut. Large eddy simulation for incompressible flows. Springer (2002). (Cited on page 45).
  - [105] F. Nicoud, H. Baya Toda, O. Cabrit, S. Bose, and J. Lee. Using singular values to build a subgrid-scale model for large eddy simulations. *Phys. Fluids* 23 (8) (2011), 085106. (Cited on page 45).
  - [106] F. Nicoud and F. Ducros. Subgrid-scale stress modelling based on the square of the velocity gradient. *Flow, Turb. and Combustion* 62 (3) (1999), 183–200. (Cited on pages 45, 46).
  - [107] P. Dagaut and M. Cathonnet. The ignition, oxidation, and combustion of kerosene: A review of experimental and kinetic modeling. *Prog. Energy Comb. Sci.* 32 (1) (2006), 48–92. (Cited on page 47).
  - [108] J. Luche, M. Reuillon, J-C. Boettner, and M. Cathonnet. Reduction of large detailed kinetic mechanisms: application to kerosene / air combustion. *Combust. Sci. Tech.* 176 (2004), 1935–1963. (Cited on pages 47, 134, 135).
  - [109] P. Pepiot-Desjardins and H. Pitsch. An efficient error-propagation-based reduction method for large chemical kinetic mechanisms. *Combust. Flame* 154 (2008), 67–81. (Cited on pages 47, 71).
  - [110] T. Jaravel, E. Riber, B. Cuenot, and G. Bulat. Large Eddy Simulation of an industrial gas turbine combustor using reduced chemistry with accurate pollutant prediction. *Proc. Combust. Inst.* 36 (2016), 3817–3825. (Cited on pages 47, 70).
  - [111] A. Felden. Development of analytically reduced chemistries and applications in Large Eddy Simulations of turbulent combustion. PhD thesis. INPT Toulouse, (2017). (Cited on pages 47, 70).
  - [112] B. Franzelli, E. Riber, M. Sanjose, and T. Poinsot. A two-step chemical scheme for kerosene-air premixed flames. *Combust. Flame* 157 (2010), 1364–1373. (Cited on pages 48, 134).
  - [113] W. P. Jones and R. P. Lindstedt. Global Reaction Schemes for Hydrocarbon Combustion. *Combust. Flame* 73 (1988), 222–233. (Cited on page 48).

- 
- [114] M. Cailler, N. Darabiha, D. Veynante, and B. Fiorina. Building-up virtual optimized mechanism for flame modeling. *Proc. Combust. Inst.* 36 (1) (2017), 1251–1258. (Cited on page 48).
- [115] A. R. Kerstein, W. Ashurst, and F. A. Williams. Field equation for interface propagation in an unsteady homogeneous flow field. *Phys. Rev. A* 37 (7) (1988), 2728–2731. (Cited on page 48).
- [116] B. Fiorina, R. Vicquelin, P. Auzillon, N. Darabiha, O. Gicquel, and D. Veynante. A filtered tabulated chemistry model for LES of premixed combustion. *Combust. Flame* 157 (3) (2010), 465–475. (Cited on page 48).
- [117] O. Gicquel, N. Darabiha, and D. Thévenin. Laminar premixed hydrogen/air counterflow flame simulations using flame prolongation of ILDM with differential diffusion. *Proc. Combust. Inst.* 28 (2000), 1901–1908. (Cited on page 48).
- [118] J. A. van Oijen, F. A. Lammers, and L. P. H. de Goey. Modeling of premixed laminar flames using flamelet generated manifolds. *Combust. Sci. Tech.* 127 (2001), 2124–2134. (Cited on pages 48, 73).
- [119] M. Boger, D. Veynante, H. Boughanem, and A. Trouv . Direct Numerical Simulation analysis of flame surface density concept for Large Eddy Simulation of turbulent premixed combustion. *Proc. Combust. Inst.* 27 (1998), 917–927. (Cited on pages 49, 53).
- [120] C. Duwig. Study of a filtered flamelet formulation for large eddy simulation of premixed turbulent flames. *Flow Turbulence Combust* 379 (2007), 433–454. (Cited on page 49).
- [121] H. Boughanem and A. Trouv . The occurrence of flame instabilities in turbulent premixed combustion. *Proc. Combust. Inst.* 27 (1998), 971–978. (Cited on page 49).
- [122] M. Boger and D. Veynante. Large eddy simulations of a turbulent premixed V-shape flame. Advances in Turbulence VIII. Edited by C. Dopazo. Barcelona, Spain. CIMNE (2000), 449–452. (Cited on page 49).
- [123] T. D. Butler and P. J. O'Rourke. A numerical method for two-dimensional unsteady reacting flows. *Proc. Combust. Inst.* 16. (Cited on page 50).
- [124] P. J. O'Rourke and F. V. Bracco. Two Scaling Transformations for the Numerical Computation of Multidimensional Unsteady Laminar Flames. *J. Comput. Phys.* (Cited on page 50).
- [125] F. A. Williams. Combustion Theory. Menlo Park, CA. Benjamin Cummings (1985). (Cited on page 50).
- [126] J.-Ph. L gier, T. Poinsot, and D. Veynante. Dynamically thickened flame LES model for premixed and non-premixed turbulent combustion. *Proc. of the Summer Program* (2000), 157–168. (Cited on pages 50, 95).
- [127] Ludovic Durand and Wolfgang Polifke. Implementation of the Thickened Flame model for Large Eddy Simulation of turbulent premixed combustion in a commercial solver. *Proceedings of ASME Turbo Expo 2007* 2 (2007). (Cited on page 50).
- [128] G. Kuenne, A. Ketelheun, and J. Janicka. LES modeling of premixed combustion using a thickened flame approach coupled with FGM tabulated chemistry. *Combust. Flame* 158 (9) (2011), 1750–1767. (Cited on page 50).
- [129] F. Proch, P. Domingo, L. Vervisch, and A. M. Kempf. Flame resolved simulation of a turbulent premixed bluff-body burner experiment. Part II: A-priori and a-posteriori investigation of sub-grid scale wrinkling closures in the context of artificially thickened flame modeling. *Combust. Flame* 180 (2017), 340–350. (Cited on pages 50, 95).

- 
- [130] P. A. Strakey and G. Eggenspieler. Development and Validation of a Thickened Flame Modeling Approach for Large Eddy Simulation of Premixed Combustion. *J. Eng. Gas Turb. and Power* 132 (7) (2010), 071501. (Cited on pages 50, 95).
- [131] O. Colin, F. Ducros, D. Veynante, and T. Poinsot. A thickened flame model for large eddy simulations of turbulent premixed combustion. *Phys. Fluids* 12 (7) (2000), 1843–1863. (Cited on pages 51–54, 70, 91, 95).
- [132] C. Angelberger, D. Veynante, F. Egolfopoulos, and T. Poinsot. Large eddy simulations of combustion instabilities in premixed flames. *Proc. of the Summer Program* (1998), 61–82. (Cited on page 52).
- [133] F. Charlette, D. Veynante, and C. Meneveau. A power-law wrinkling model for LES of premixed turbulent combustion: Part I - non-dynamic formulation and initial tests. *Combust. Flame* 131 (2002), 159–180. (Cited on pages 52, 54).
- [134] G. Wang, M. Boileau, and D. Veynante. Implementation of a dynamic thickened flame model for large eddy simulations of turbulent premixed combustion. *Combust. Flame* 158 (11) (2011), 2199–2213. (Cited on pages 54, 73, 79).
- [135] F. Gouldin, K. Bray, and J. Y. Chen. Chemical closure model for fractal flamelets. *Combust. Flame* 77 (1989), 241–259. (Cited on page 54).
- [136] D. Veynante and V. Moureau. Analysis of dynamic models for large eddy simulations of turbulent premixed combustion. *Combust. Flame* 162 (12) (2015), 4622–4642. (Cited on pages 54, 55, 73, 107).
- [137] O. Vermorel, P. Quillatre, and T. Poinsot. LES of explosions in venting chamber: A test case for premixed turbulent combustion models. *Combust. Flame* 183 (2017), 207–223. (Cited on page 55).
- [138] G. Wang, M. Boileau, D. Veynante, and K. Truffin. Large eddy simulation of a growing turbulent premixed flame kernel using a dynamic flame surface density model. *Combust. Flame* 159 (8) (2012), 2742–2754. (Cited on pages 55, 73).
- [139] S. Mouriaux, O. Colin, and D. Veynante. Adaptation of a dynamic wrinkling model to an engine configuration. *Proc. Combust. Inst.* 36 (3) (2017), 3415–3422. (Cited on page 55).
- [140] P. S. Volpiani, T. Schmitt, and D. Veynante. A posteriori tests of a dynamic thickened flame model for large eddy simulations of turbulent premixed combustion. *Combust. Flame* 174 (2016), 166–178. (Cited on pages 55, 73, 79, 107).
- [141] P. S. Volpiani, T. Schmitt, and D. Veynante. Large eddy simulation of a turbulent swirling premixed flame coupling the TFLES model with a dynamic wrinkling formulation. *Combust. Flame* 180 (2017), 124–135. (Cited on pages 55, 69, 73, 107).
- [142] M. Germano. A proposal for a redefinition of the turbulent stresses in the filtered Navier-Stokes equations. *Phys. Fluids* 29 (7) (1986), 2323–2324. (Cited on page 55).
- [143] M. Germano, U. Piomelli, P. Moin, and W. Cabot. A dynamic subgrid-scale eddy viscosity model. *Phys. Fluids* 3 (7) (1991), 1760–1765. (Cited on page 55).
- [144] M. Germano. Turbulence: the filtering approach. *J. Fluid Mech.* 238 (1992), 325–336. (Cited on page 55).
- [145] D. K. Lilly. A proposed modification of the germano sub-grid closure method. *Phys. Fluids* 4 (3) (1992), 633–635. (Cited on page 55).
- [146] F. Charlette, C. Meneveau, and D. Veynante. A Power-Law Flame Wrinkling Model for LES of Premixed Turbulent Combustion Part II: Dynamic Formulation. *Combust. Flame* 197 (2002), 181–197. (Cited on pages 55, 91, 107).

- 
- [147] D. Veynante, T. Schmitt, and M. Boileau. Analysis of dynamic models for turbulent premixed combustion. *Proc. of the Summer Program* (2012), 387–396. (Cited on page 55).
- [148] C. Crowe, M. Sommerfeld, and Y. Tsuji. Multiphase Flows with Droplets and Particles. Taylor & Francis (1998). (Cited on page 59).
- [149] L. Schiller and A. Nauman. A drag coefficient correlation. *VDI Zeitung* 77 (1935), 318–320. (Cited on pages 59, 116, 132).
- [150] D. B. Spalding. The combustion of liquid fuels. The Combustion Institute, Pittsburgh volume 4 (1953), 847–864. (Cited on pages 60, 62).
- [151] W. A. Sirignano. Fluid dynamics and transport of droplets and sprays. Cambridge University Press (1999). (Cited on page 60).
- [152] W. E. Ranz and W. R. Marshall. Evaporation from drops. *Chem. Eng. Prog.* 48 (4) (1952), 173. (Cited on page 65).
- [153] B. Abramzon and W. A. Sirignano. Droplet vaporisation model for spray combustion calculations. *Int. J. Heat and Mass Transfer* 9 (1989), 1605–1618. (Cited on pages 65, 132).
- [154] B. Rochette, F. Collin-Bastiani, L. Gicquel, O. Vermorel, D. Veynante, and T. Poinsot. Influence of chemical schemes, numerical method and dynamic turbulent combustion modeling on LES of premixed turbulent flames. *Combust. Flame* 191 (2018), 417–430. (Cited on pages 69, 107–109).
- [155] K. N. C. Bray. The interaction between turbulence and combustion. The Combustion Institute, Pittsburgh volume 17 (1979), 223–233. (Cited on page 69).
- [156] N. Peters. Turbulent combustion. Cambridge University Press (2001), 304. (Cited on page 69).
- [157] H. Pitsch. Large Eddy Simulation of Turbulent Combustion. *Ann. Rev. Fluid Mech.* 38 (2006), 453–482. (Cited on page 69).
- [158] P. Moin and S. V. Apte. Large-eddy simulation of realistic gas turbine combustors. *AIAA Journal* 44 (4) (2006), 698–708. (Cited on page 69).
- [159] N. Gourdain, L. Gicquel, G. Staffelbach, O. Vermorel, F. Duchaine, J-F. Boussuge, and T. Poinsot. High performance parallel computing of flows in complex geometries - part 2: applications. *Comput. Sci. Disc.* 2 (1) (2009), 28pp. (Cited on page 69).
- [160] W. Meier, P. Weigand, X.R. Duan, and R. Giezendanner-Thoben. Detailed characterization of the dynamics of thermoacoustic pulsations in a lean premixed swirl flame. *Combust. Flame* 150 (1-2) (2007), 2–26. (Cited on page 69).
- [161] S. Roux, G. Lartigue, T. Poinsot, U. Meier, and C. Bérat. Studies of mean and unsteady flow in a swirled combustor using experiments, acoustic analysis and Large Eddy Simulations. *Combust. Flame* 141 (2005), 40–54. (Cited on page 69).
- [162] Benedetta Franzelli, Eleonore Riber, Laurent Y.M. Gicquel, and Thierry Poinsot. Large Eddy Simulation of combustion instabilities in a lean partially premixed swirled flame. *Combust. Flame* 159 (2) (2012), 621–637. (Cited on page 69).
- [163] V. Moureau, P. Domingo, L. Vervisch, and D. Veynante. DNS analysis of a Re=40000 swirl burner. *Proc. of the Summer Program* (13) (2010), 209–298. (Cited on page 69).
- [164] V. Moureau, P. Domingo, and L. Vervisch. From Large-Eddy Simulation to Direct Numerical Simulation of a lean premixed swirl flame: Filtered laminar flame-PDF modeling. *Combust. Flame* 158 (7) (2011), 1340–1357. (Cited on page 69).
- [165] J.-M. Lourier, M. Stohr, B. Noll, S. Werner, and A. Fiolitakis. Scale Adaptive Simulation of a thermoacoustic instability in a partially premixed lean swirl combustor. *Combust. Flame* 183 (2017), 343–357. (Cited on page 69).

- 
- [166] A. Sjunnesson, C. Nilsson, and E. Max. LDA Measurements of velocities and turbulence in a bluff body stabilized flame. *4th International Conference on Laser Anemometry - Advances and Application*, ASME 3 (1991), 83–90. (Cited on pages 69, 75, 77, 79, 91, 107).
  - [167] A. Sjunnesson and P. Henrikson. CARS measurements and visualization of reacting flows in a bluff body stabilized flame. *28th Joint Propulsion Conference and Exhibit*, AIAA 92-3650 (1992). (Cited on pages 69, 75, 77, 91, 107).
  - [168] A. Sjunnesson, S. Olovsson, and B. Sjöblom. Validation Rig-A tool for flame studies. *10th International Symposium on Air Breathing Engines* (1991), 385–393. (Cited on pages 69, 75, 77, 91, 107).
  - [169] Peter A T Cocks, Marios C Soteriou, and Vaidyanathan Sankaran. Impact of numerics on the predictive capabilities of reacting flow LES. *Combust. Flame* 162 (2015), 3394–3411. (Cited on pages 69, 107).
  - [170] A. Ghani, T. Poinsot, L. Gicquel, and G. Staffelbach. LES of longitudinal and transverse self-excited combustion instabilities in a bluff-body stabilized turbulent premixed flame. *Combust. Flame* 162 (2015), 4075–4083. (Cited on pages 69, 71, 77, 107).
  - [171] N Zettervall, K Nordin-Bates, E J K Nilsson, and C Fureby. Large Eddy Simulation of a premixed bluff body stabilized flame using global and skeletal reaction mechanisms. *Combust. Flame* (2017), 1–22. (Cited on pages 69, 70, 77, 107).
  - [172] S. Jerzembeck, N. Peters, P. Pepiot-desjardins, and H. Pitsch. Laminar burning velocities at high pressure for primary reference fuels and gasoline : Experimental and numerical investigation. *Combust. Flame* 156 (2) (2009), 292–301. (Cited on pages 71–73).
  - [173] H.J. Curran, P. Gaffuri, W.J. Pitz, and C.K. Westbrook. A Comprehensive Modeling Study of n-Heptane Oxidation. *Combust. Flame* 114 (1) (1998), 149–177. (Cited on page 71).
  - [174] H.J. Curran, P. Gaffuri, W.J. Pitz, and C.K. Westbrook. A comprehensive modeling study of iso-octane oxidation. *Combust. Flame* 129 (3) (2002), 253–280. (Cited on page 71).
  - [175] T. Løvs, D. Nilsson, and F. Mauss. Automatic reduction procedure for chemical mechanisms applied to premixed methane/air flames. *Proc. Combust. Inst.* 28 (2) (2000), 1809–1815. (Cited on page 71).
  - [176] K. Bray, M. Champion, and P. Libby. Mean reaction rates in premixed turbulent flames. *Proc. Combust. Inst.* 22 (1988), 763–769. (Cited on page 73).
  - [177] K. N. C. Bray. Studies of the turbulent burning velocity. *Proc. R. Soc. Lond. A* 431 (1990), 315–335. (Cited on page 73).
  - [178] Nedunchezhian Swaminathan and Kenneth Bray. *Turbulent Premixed Flames*. Cambridge University Press (2011). (Cited on page 73).
  - [179] B. Fiorina, O. Gicquel, L. Vervisch, S. Carpentier, and N. Darabiha. Approximating the chemical structure of partially-premixed and diffusion counter-flow flames using FPI flamelet tabulation. *Combust. Flame* 140 (2005), 147–160. (Cited on page 73).
  - [180] M. A. Singer and S. B. Pope. Exploiting ISAT to solve the equations of reacting flow. *Combust. Theory and Modelling* 8 (2) (2004), 361–383. (Cited on page 73).
  - [181] P. Quillatré. Simulation aux grandes échelles d'explosions en domaine semi-confiné. PhD thesis. INPT Toulouse, (2014). (Cited on page 73).
  - [182] P. D. Lax and B. Wendroff. Difference schemes for hyperbolic equations with high order of accuracy. *Commun. Pure Appl. Math.* 17 (1964), 381–398. (Cited on pages 74, 100).
  - [183] O. Colin and M. Rudgyard. Development of high-order Taylor-Galerkin schemes for unsteady calculations. *J. Comput. Phys.* 162 (2) (2000), 338–371. (Cited on pages 74, 132).

- 
- [184] R.-H. Ni. A multiple grid scheme for solving the Euler equations. *AIAA Journal* 101 (1982), 1565–1571. (Cited on page 74).
- [185] L. Quartapelle and V. Selmin. High-order Taylor-Galerkin methods for non-linear multidimensional problems. *Finite Elements Fluids* 76 (90) (1993). (Cited on page 74).
- [186] F.R.S. Rayleigh. On the resultant of a large number of vibrations of the same pitch and of arbitrary phase. *Philosophical Magazine* 10 (60) (1880), 73–78. (Cited on page 75).
- [187] H. Li, P. Khare, H. Sung, and V. Yang. A Large-Eddy-Simulation Study of Combustion Dynamics of Bluff-Body Stabilized Flames. *Combust. Sci. Tech.* 188 (6) (2016), 924–952. (Cited on page 77).
- [188] J. Kim and S. B. Pope. Effects of combined dimension reduction and tabulation on the simulations of a turbulent premixed flame using a large-eddy simulation/probability density function method. *Combust. Theory and Modelling* 18 (3) (2014), 388–413. (Cited on page 77).
- [189] H. Wu, P. C. Ma, Y. Lv, and M. Ihme. MVP-Workshop Contribution: Modeling of Volvo Bluff Flame Experiment. *AIAA Journal* 55 (2017), 1–16. (Cited on page 77).
- [190] T. Poinsot and S. Lele. Boundary conditions for direct simulations of compressible viscous flows. *J. Comput. Phys.* 101 (1) (1992), 104–129. (Cited on pages 77, 132).
- [191] N. Guezennec and T. Poinsot. Acoustically nonreflecting and reflecting boundary conditions for vorticity injection in compressible solvers. *AIAA Journal* 47 (2009), 1709–1722. (Cited on pages 77, 107).
- [192] T. Kitano, K. Kaneko, R. Kurose, and S. Komori. Large-eddy simulations of gas- and liquid-fueled combustion instabilities in back-step flows. *Combust. Flame* 170 (2016), 63–78. (Cited on page 95).
- [193] O. Monga and S. Benayoun. Using Partial Derivatives of 3D Images to Extract Typical Surface Features. *Computer Vision and Image Understanding* 61 (2) (1995), 171 –189. (Cited on page 96).
- [194] A. Walbron, S. Chupin, D. Rochais, R. Abraham, and M. Bergounioux. 3D Image Segmentation and Cylinder Recognition for Composite Materials. Proceedings of the 2nd International Congress on 3D Materials Science. Cham. Springer International Publishing (2016), 47–52. (Cited on page 96).
- [195] A. Walbron. Fast analysis of heterogeneous materials 3D-images : mediums structure identification and application to their multiscale characterization. PhD thesis. Université d'Orléans, (2016). (Cited on page 96).
- [196] A. Haselbacher, F.M. Najjar, and J.P. Ferry. An efficient and robust particle-localization algorithm for unstructured grids. *J. Comput. Phys.* 225 (2007), 2198–2213. (Cited on pages 97, 98).
- [197] E. Riber, V. Moureau, M. Garcia, T. Poinsot, and O. Simonin. Evaluation of numerical strategies for large eddy simulation of particulate two-phase recirculating flows. *J. Comput. Phys.* 228 (2) (2009), 539 –564. (Cited on page 97).
- [198] F. Shum-Kivan, J. Marrero Santiago, A. Verdier, E. Riber, B. Renou, G. Cabot, and B. Cuenot. Experimental and numerical analysis of a turbulent spray flame structure. *Proc. Combust. Inst.* 36 (2) (2017), 2567 –2575. (Cited on page 97).
- [199] Y. Ling and S. Balachandar. Simulation and scaling analysis of a spherical particle-laden blast wave. *Shock Waves* 28 (3) (2018), 545–558. (Cited on page 97).
- [200] L. Hervo, J. M. Senoner, A. Biancherin, and B. Cuenot. Large-Eddy Simulation of Kerosene Spray Ignition in a Simplified Aeronautic Combustor. *Flow, Turbulence and Combustion* 101 (2) (2018), 603–625. (Cited on page 97).

- 
- [201] B. Rochette, E. Riber, and B. Cuenot. Effect of non-zero relative velocity on the flame speed of two-phase laminar flames. *Proc. Combust. Inst.* 37 (3) (2019), 3393–3400. (Cited on page 113).
  - [202] B. Franzelli, E. Riber, M. Sanjosé, and T. Poinsot. A two-step chemical scheme for Large-Eddy Simulation of kerosene-air flames. *Combust. Flame* 157 (7) (2010), 1364–1373. (Cited on pages 114, 134).
  - [203] K. Kumar, J. E. Freeh, C. J. Sung, and Y. Huang. Laminar Flame Speeds of Preheated iso-Octane/O<sub>2</sub>/N<sub>2</sub> and n-Heptane/O<sub>2</sub>/N<sub>2</sub> Mixtures. *Journal of Propulsion and Power* 23 (2) (2007), 428–436. (Cited on pages 114, 115).
  - [204] F. Jaegle, J.-M. Senoner, M. Garcia, F. Bismes, R. Lecourt, B. Cuenot, and T. Poinsot. Lagrangian and eulerian simulations of evaporating fuel spray in an aeronautical multipoint injector. *Proc. Combust. Inst.* 33 (2011), 2099–2107. (Cited on pages 115, 132).
  - [205] P. Malbois, L. Bouheraoua, E. Salaün, F. Frindt, G. Cabot, B. Renou, F. Grisch, H. Verdier, and S. Richard. Experimental investigation with optical diagnostics of a lean-premixed aero-engine injection system under relevant operating conditions. Proceedings of the ASME turbo expo: Turbine Technical Conference and Exposition. Charlotte, United States. (2017). (Cited on pages 129, 131).
  - [206] P. Malbois. Experimental investigation by laser diagnostics of the kerosene/air mixing and high-pressure swirl-stabilized lean premixed combustion from a low-NO<sub>x</sub> injection system. Theses. Normandie Université, (2017). (Cited on page 129).
  - [207] J. M. Beer and N. A. Chigier. Combustion aerodynamics. Malabar, Florida. Krieger (1983). (Cited on page 136).
  - [208] P. Billant, J.-M. Chomaz, and P. Huerre. Experimental Study of Vortex Breakdown in Swirling Jets. *J. Fluid Mech.* 376 (1998), 183–219. (Cited on page 136).
  - [209] T. Ivanic, E. Foucault, and J. Pecheux. *J. Exp Fluids* 35 (2003), 317–324. (Cited on page 136).